This is to certify that the
dissertation entitled

THE INCLUSIVE JET CROSS SECTION IN PROTON-ANTIPROTON COLLISIONS AT A CENTER OF MASS ENERGY OF 1.96 TeV

presented by

GENE U. FLANAGAN

has been accepted towards fulfillment
of the requirements for the

Ph.D degree in PHYSICS

Joey M Huston
Major Professor's Signature

4/11/05
Date

THE INCLUSIVE JET CROSS SECTION IN $p\bar{p}$ COLLISIONS AT $\sqrt{s} = 1.96$ TeV

By

Gene U. Flanagan

A DISSERTATION

Submitted to
Michigan State University
in partial fulfillment of the requirements
for the degree of

DOCTOR OF PHILOSOPHY

Department of Physics and Astronomy

2005

ABSTRACT

THE INCLUSIVE JET CROSS SECTION IN $p\bar{p}$ COLLISIONS AT $\sqrt{s} = 1.96$ TeV

By

Gene Flanagan

The following work presents a preliminary measurement of the inclusive jet cross section for jet transverse momenta from 61 to 620 GeV in the rapidity range $0.1 < |Y| < 0.7$. The result is based on 218 pb^{-1} of data collected by the CDF detector at the Fermi National Accelerator Lab. The data are consistent with NLO pQCD predictions based on the CTEQ6.1 parton distribution functions.

ACKNOWLEDGEMENTS

I would like to thank everybody who has been involved with the analysis for their help, advice and direct contributions.

Many thanks to my supervisor, Joey Huston, for his insight, guidance, assistance and patience with me throughout the analysis. I would also like to thank Carl Bromberg, who assisted me in a number of ways during my time at Michigan State University.

There are a number of people who not only contributed to the analysis but also to my continuing education: Anwar Bhatti, who took on the unenviable task of helping me learn and use C++ and for his guidance and assistance throughout the analysis; Frank Chlebana, Kenechi Hatakeyama and Giuseppe Latino for their assistance, advice and contributions.

I would also like to thank the CDF collaboration in its entirety–it takes a lot of effort by many people to make any analysis possible.

Finally I thank my family: my wife Amy, who has been incredibly supportive and has had to endure the analysis as much as anybody else–in some ways more as she doubled as my editor, my parents, Kevin and Elizabeth, and my brother, Jack, who have always been supportive and without whom I would not have come this far.

Contents

List of Tables

List of Figures

Chapter 1

QCD Theory

1.1 Introduction

Our understanding of the physical universe is contained in the Standard Model, which describes the interactions between the known particles. These interactions are governed by the four fundamental forces:

- strong
- weak
- electromagnetic
- gravitational.

The fundamental constituents of the known particles and therefore of matter are quarks and leptons, both of which occur in three generations. Leptons are described by the following quantum numbers: spin, charge, baryon number, isospin and mass. Quarks too have these quantum numbers but additionally they carry a colour charge. In the case of quarks the baryon number is always $\pm 1/3$. Quarks are the constituents of hadrons; hadrons are colourless particles that carry integer charge and baryon number. Hadrons are either mesons (quark-antiquark states, *e.g.* $\pi^+(ud)$) or baryons (3 quark configurations, *e.g.* $p(uud)$ and $n(udd)$). Baryons are fermions with a

baryon number 1, whereas mesons are bosons with a baryon number 0. In addition to the valence quarks, hadrons also have a sea of quark-antiquark pairs and gluons, where the gluons are the force-mediating bosons of Quantum Chromo Dynamics (QCD).

QCD is the accepted theory of strong interactions, which take place between quarks which make up the hadrons.

1.2 The QCD Lagrangian

QCD is defined as a field theory by its Lagrange density:

$$L_{eff}^{QCD}[\psi_{f(x)}, A(x), c(x); g, m_f] = L_{invar} + L_{gauge} + L_{ghost}, \tag{1.1}$$

which is a function of the quark field ψ_f, the gluon field A, the ghost field c, the coupling strength g and the fermion mass m_f. The subscripts f label the distinct quark fields. L_{invar} is the classical density which is invariant under $SU(N_c)$ gauge transformations. For QCD the number of colours describing quarks is 3 and so $N_c = 3$. The classical density was originally written by Yang and Mills [1] in the form:

$$\begin{aligned} L_{invar} &= \sum_f \overline{\psi}_f [i \not{D}[A] - m_f]\psi_f - \frac{1}{4}F^2[A] \\ &= \sum_{f=1}^{n_f} \sum_{\alpha=1}^{4} \sum_{\beta=1}^{4} \sum_{i,j=1}^{N_c} \overline{\psi}_{f,\beta,j} [i(\gamma)^{\mu}_{\beta\alpha} D_{\mu,ji}[A] - m_f \delta_{\beta\alpha}\delta_{ji}]\psi_{f,\alpha,i} \\ &\quad -\frac{1}{4} \sum_{\mu,\nu=0}^{3} \sum_{a=0}^{N_c^2-1} F_{\mu\nu,a}[A] F_a^{\mu\nu}[A], \end{aligned} \tag{1.2}$$

where f is the flavour, α and β are Dirac spinor labels, i and j are the colour labels, μ and ν are Lorentz indices and a labels the colour adjoint. In the above we have used the notation:

$$D_{\mu,ij}[A] \equiv \partial_\mu \delta_{ij} + igA_{\mu a}(T_a)_{ij}, \tag{1.3}$$

$$F_{\mu\nu,a}[A] \equiv \partial_\mu A_{\nu a} - \partial_\nu A_{\mu a} - gC_{abc}A_{\mu b}A_{\nu c}, \tag{1.4}$$

where $F_{\mu\nu,a}$ is the non-Abelian field strength tensor defined in terms of the gluon vector field A^μ_b, g is the strong coupling constant and the C_{abc}'s are real numbers which are the structure constants of the $SU(N_c)$ group. The Lie algebra is defined in terms of the commutation relations of the $N_c - 1$, $N_c \times N_c$ matrices, $(T_a)_{ij}$,

$$[T_a, T_b] = iC_{abc}T_c, \tag{1.5}$$

where the T_a's are matrices in the fundemental N_c-dimensional respresentation. Taking the T_a's to be hermitian in this representation makes QCD look very much like Quantum Electro Dynamics (QED).

$D^\mu_{ij}[A]$ is the covariant derivative in the N_c-dimensional representation of $SU(N_c)$, which acts on the spinor quark fields ψ, with colour indices $i = 1...N_c$. There are $n_f = 6$ independent quark fields in the Standard Model, they are labelled by flavour: $f(= u, d, c, s, t, b)$.

The quark fields (ψ_f) transform under local gauge transformations as

$$\psi'_{f,\alpha,j}(x) = U_{ji}(x)\psi_{f,\alpha,i}(x), \tag{1.6}$$

where

$$U_{ji}(x) = \left[exp\left\{ i \sum_{a=1}^{N_c^2-1} \beta_a(x)T_a \right\} \right]_{ji}. \tag{1.7}$$

For every value of x, U_{ij} is an element of the $SU(N_c)$ group, which is the local invariance that was built into the theory. The transformation of the gluon field is described in terms of the $N_c \times N_c$ matrix, $A_\mu(x)$,

$$[A_\mu(x)]_{ij} \equiv \sum_{a=1}^{N_c^2-1} A_{\mu a}(x)(T_a)_{ij}. \tag{1.8}$$

The gluon field is defined to transform according to

$$A'_\mu(x) = U(x)A_\mu(x)U^{-1}(x) + \frac{i}{g}[\partial_\mu U(x)]U^{-1}(x). \tag{1.9}$$

A mass gluon mass cannot be included in the Lagrangian, as a term of the form $m^2 A_\mu A^\mu$ would violate the gauge invariance of the theory. The gauge particle, the gluon, must be massless.

To facilitate the use of perturbation theory to make calculations of QCD quantities we need to fix the gauge. Without a gauge fixing term the gluon propagator has no inverse, rendering the use of perturbation theory impossible. There are different ways we can fix the gauge, all of them, however, break the gauge invariance of the theory. The breaking of the gauge invariance comes through the introduction of a parameter λ. It does not matter which choice of gauge fixing term is chosen, as physical quantities (scattering matrix terms) do not depend on λ, however, the intermediate steps of a calculation may look very different depending on the choice of gauge [2].

Gauge fixing can be achieved by either requiring a purely physical gauge or selecting the set of more general covariant gauges and introducing the associated ghost fields. The derivation of the form of the ghost field can be found with a path integral formulation [4, 6]. The ghost field will cancel the unphysical degrees of freedom that would otherwise propagate in a covariant gauge. The Lagrangians for the gauge fields are of the form:

$$L_{gauge}^{covariant} = \frac{\lambda}{2}\sum_{a=1}^{N_c^2-1}(\partial_\mu A_a^\mu)^2 \text{ and}$$

$$L_{gauge}^{physical} = \frac{\lambda}{2}\sum_{a=1}^{N_c^2-1}(n_a.A_a)^2, \tag{1.10}$$

where n is a vector, λ is a gauge parameter and A is the gluon field. The first of the above densities ($L_{gauge}^{covarient}$) defines a set of covariant gauges that can be added to the QCD Lagrangian (see equation 1.1). If this choice is made the ghost Lagrangian is of the form:

$$L_{ghost} = (\partial_\mu \bar{c}_a)(\partial^\mu \delta_{ad} - gC_{abd}A_b^\mu)c_d, \tag{1.11}$$

where c_a and $\bar{c}_a$ are the ghost and anti-ghost fields [9, 10]. The ghost fields anti-commute (even though they are scalar). Setting $\lambda = 1$ in the set of covarient gauges gives the *Feynman gauge*. The Feynman gauge has a fairly simple gluon propagator (see figure 1.1). The second of the densities defines the set of physical gauges [11]. With this choice, the limit $\lambda \to \infty$ eliminates the need for the introduction of a ghost density. The light-like n ($n^2 = 0$) selected from this set is known as the *light cone gauge*.

1.3 Green's Functions & Observables

1.3.1 Feynman Rules & Green's Functions

Choosing the generators T_a to be hermitian, and taking the Fourier transform associates everywhere $\partial_p \to -iq_p$, where q_p is the momentum flowing into the vertex, makes the quark-gluon vertex look like the electron-photon vertex of QED with an additional multiplicative factor T_a. The Feynman rules for the QCD vertices can be seen in figure 1.1.

The Feynman rules allow the construction of Green's functions in momentum space. These are the vacuum expectation values of the time ordered products of fields:

$$(2\pi)^4\delta(p_1..p_n)G_{\alpha_1...\alpha_n}(p_1,...,p_n) = \prod_{i=1}^{n}\int d^4x_i.e^{-ip_ix_i}.\langle 0|T[\phi_{\alpha_1}(x_1)...\phi_{\alpha_n}(x_n)]|0\rangle, \tag{1.12}$$

where the space, time and spin indices have all been absorbed into the α's. Green's functions contain all of the physical information of the theory. Green's functions are used to construct the Scattering matrix (S-matrix), thus the S-matrix will also have all of the physical information contained in the theory. $G_{\alpha_1...\alpha_n}(p_1,...,p_n)$ is just the sum of all of the Feyman diagrams contributing to the process of interest.

1.3.2 The S-Matrix and Cross Sections.

Green's functions are not always physical observables: there is no way of guaranteeing that the external particles are on mass shell. In addition, Green's functions need not be gauge invariant. A relationship exists between Green's Functions and observables, such as cross sections. Green's functions are related to observables through the S-matrix. It is helpful to consider a generic toy model using the scalar fields ϕ_a and a coupling g. A two point Green's Function $G_{\alpha\beta}$ has a pole at $p^2 - m^2$. Near this pole it has the form of a free propagating field times a scalar constant R_ϕ:

$$G_{\alpha\beta}(p) \rightarrow R_\phi G_{\alpha\beta}(p)^{free} + \text{finite terms.} \tag{1.13}$$

If the particles are hadrons then R_ϕ and the physical mass, M, cannot be calculated using perturbation theory. If instead of hadrons we consider the perturbative S-matrix for quarks, then R_ϕ and M can be calculated pertubatively in the coupling g:

$$R_\phi = 1 + O(g^2) \quad \text{and} \quad M = m + O(g^2). \tag{1.14}$$

We now wish to make the connection between Green's functions and observables. The connection between Green's functions and observables is the S-matrx. The S-matrix tells us the amplitude for the scattering of incoming momentum eigenstates into outgoing momentum eigenstates. The most important S-matrix for QCD is the matrix describing $2 \to 2$ processes. The S-matrix is derived from the Green's functions via reduction formulas which relate $G_{\alpha\beta} \to S$. The general form for the reduction formula is

$$S((p_1,s_1)+(p_2,s_2) \to (p_3,s_3)+...(p_n,s_n)) = \prod_i \psi(p_i,s_i)_{\alpha_i} \left[\frac{G_{\alpha_i\beta_i}(p_i)^{free}}{R_\phi^{1/2}}\right]^{-1}$$

$$\times G_{\beta_1...\beta_n}(p_1,p_2,-p_3,...-p_n), \tag{1.15}$$

where all of the quantum numbers, for example, spin of the particle i, are absorbed into the s_i's. $\psi(p_i,s_i)_\alpha$ represents the wave function of the external particle i . $G_{\alpha_i\beta_i}(p_i)^{free}$ is the free propagator for the field i. After multipling by $G^{-1}_{\alpha\beta}$ one can set all of the p_i's on mass-shell ($p_i^2 = m_i^2$). From the S-matrix the Transition Matrix (T-matrix) is defined as:

$$S = I + iT, \tag{1.16}$$

where I is the identity matrix in the space of momentum eigenstates. In the case of momentum eigenstates the T-matrix contains explicit momentum conserving delta functions. These delta functions can be separated from the rest of the T-matrix:

$$iT((p_i,s_i)+(p_2,s_2) \to (p_3,s_3)+...(p_n,s_n)) = (2\pi)^4\delta^4(p_1+p_2-p_3...-p_n)$$

$$\times M((p_i,s_i)+(p_2,s_2) \to (p_3,s_3)+...(p_n,s_n)). \tag{1.17}$$

The cross section can be found by integrating the differential cross section which is a function of the M-matrix over the n-particle phase-space

$$d\sigma((p_i,s_i)+(p_2,s_2)\rightarrow(p_3,s_3)+...(p_n,s_n)) = \frac{dPS_n}{4\sqrt{(p_1.p_2)^2-m_1^2m_2^2}}\times|M((p_i,s_i)+(p_2,s_2)\rightarrow(p_3,s_3)+...(p_n,s_n))|^2, \quad (1.18)$$

where

$$dPS_n=\prod_i\frac{d^3p_i}{2\omega_i(2\pi)^3}N_i(2\pi)^4\delta^4(p_1+p_2-\sum_{j=3}^{n}p_j). \quad (1.19)$$

The N_i's depend on the normalisation of the wave functions; if $\overline{u}(p,s)u(p,s)=2m$ then $N_i=1$ for vector, scalar and fermions. If $\overline{u}(p,s)u(p,s)=1$ then $N_i=2m$ for fermions.

In the next section we will discuss the treatment of divergences and how they effect the calculation of observable quantities.

1.3.3 Divergences and Renormalisation Schemes

Until now we have assumed that the Green's functions, and therefore observables, were free of divergent terms. This is not true when processes with loop diagrams are included. The inclusion of loop diagrams in the un-modified Green's functions lead to ultraviolet divergences. Loop diagrams are associated with virtual states in which energy conservation is violated by an arbitrarily large amount. The momentum is conserved at each vertex of a Feyman diagram. The loop momentum, is unrestricted. The loop momentum, k, is not observable so we need to sum over all possible values. This introduces a $\int d^4k$ in loop diagrams/Green's functions. These integrals over the loop momentum are often divergent. There are renormalisation schemes that can be used within perturbation theory that remove these divergences. As an example we

consider a scalar field for which the un-renormalised loop integral (loop momentum k) is given by:

$$\Gamma^{un}(p) = \int \frac{d^4k}{(2\pi)^4} \frac{1}{(k^2-m^2)((p-k)^2-m^2)} \tag{1.20}$$

$$= \int_0^1 dx \int \frac{d^4k}{(2\pi)^4} \frac{1}{(k^2-2xp.k+xp^2-m^2)^2} \tag{1.21}$$

$$= \int_0^1 dx \int \frac{d^4k}{(2\pi)^4} \frac{1}{(k^2+x(1-x)p^2-m^2)^2}. \tag{1.22}$$

Going from 1.20 to 1.21 is referred to as Feynman parameterisation. There is a change of variable in the last line $k' = k - xp$. The integral is still divergent in the limit $k \to \infty$ (the ultraviolet region) in the present form. The divergence can be understood by considering a generic one loop integral:

$$\Gamma^{un}(p) \equiv \int \frac{d^4k}{(2\pi)^4} \frac{1}{(k^2-M^2(p))^2}, \tag{1.23}$$

where k is the loop momentum and we have absorbed all of the external momentum dependence into $M(p)$. This integral is undefined due to a logarithmic divergence at infinity. To maintain simplicity the momentum dependance of the Dirac traces and vector indices in the numerator are neglected as they do not effect the renormalisation. Logarithmically divergent integrals can be evaluated using *dimensional regularisation*. In dimensional regularisation the UV loop divergences are regulated by reducing the number of space-time dimensions to $n < 4$:

$$\frac{d^4k}{(2\pi)^4} \to (\mu)^{2\epsilon} \frac{d^{4-2\epsilon}k}{(2\pi)^{4-2\epsilon}}, \tag{1.24}$$

where $\epsilon = 2 - n/2$. The renormalisation scale, μ, preserves the dimensions of the couplings and the fields. Within this regularisation method loop integrals like 1.23

lead to poles at $\epsilon = 0$. The minimal subtraction renormalisation prescription (see below) is to subtract off the poles and replace the bare coupling by the renormalised coupling $g(\mu^2)$. This leads to expressions such as:

$$\Gamma^{(un)}(p) \rightarrow \Gamma^{(ren)}(p,\mu) = \frac{i}{(4\pi)^2} ln(\frac{M^2(p)}{\mu^2}), \tag{1.25}$$

where a mass scale μ is introduced which is not present in the original QCD Lagrangian. So far there is nothing preventing the mass scale from differing between integrals.

We must determine a set of rules to define μ for each divergent diagram. The choice of rules used are referred to as the renormalisation scheme. There are two common sets of rules or schemes:

- Momentum subtraction scheme: choose

$$\Gamma^{(ren)}(P_0) = 0, \tag{1.26}$$

  where the P_0 are a fixed set external momenta, and Γ a specific divergent vertex function. This approach is often used in QED. In this scheme all of the one loop and higher order corrections to the electron-photon vertex go to zero as the momentum transfer goes to zero. P_0 is where the photon momentum goes to zero and the electrons are on shell.

- Minimal subtraction scheme: μ is chosen to be the same for all divergent integrals and is left as free parameter in the renormalised Green's function. In this scheme μ will be present in all physical observables calculated from the Green's functions/M-matrix at any fixed order in perturbation theory. This approach is typically used in pQCD.

When the measured inclusive jet cross section is compared to the NLO pQCD prediction we will make a choice of which value of μ to use, introducing an unavoidable uncertainty in the comparison to data to NLO pQCD.

1.3.4 Renormalisation Scale and Experimental Results

Using the minimal subtraction scheme we are left with an arbitrary parameter, μ, in the theory, requiring a method to determine unique experimental predictions from this theory. If we take the simple case of massless particle and a single coupling constant g, we can compute a cross section, σ, from the renormalised perturbative series

$$\sigma(p,\mu) = \sum_{n=1}^{A} a_n(p,\mu) g(\mu)^{2n}, \tag{1.27}$$

where A is the highest order term that can be computed. By measuring $\sigma(p,\mu)$ for some momenta p^0 and fixing μ to some value we can solve for $g(\mu)$. Having solved for g, the cross section σ can be computed for any p. Since the cross section, $\sigma(p,\mu)$, is an observable it must be independent of the choice of μ:

$$\mu \frac{d}{d\mu} \sigma(p,\mu) = 0. \tag{1.28}$$

This is exact if we perform the computation using all orders of perturbation theory. By computing $\sigma(p,\mu)$ to finite order we introduce errors of the order of the first uncomputed term in the perturbation expansion. Provided the coupling is small, leading order or next to leading order should provide a reasonable description of measured observables. The size of the coupling and therefore the applicability of perturbative QCD is closely is related to asymptotic freedom.

1.4 Asymptotic Freedom

The use of QCD to describe the strong interaction is underpinned by two properties: asymptotic freedom and confinement. We consider hadron spectra to see why these two properties are very important in the success of QCD. Hadron spectra can be described by quark models even though quarks have never been seen in isolation. Although quarks are produced in high energy physics experiments, they hadronize before being detected. Mesons and baryons and/or their decay products are detected. From the hadronization time one can see that the forces between quarks are strong. However, certain high energy cross sections are well described by models in which the quarks do not interact at all (the parton model). Asymptotic freedom refers to the weakness of the forces between quarks at short distances. Confinement arises from the strength of the forces at large distances.

QCD allows for both of these behaviours by making the force between quarks a function of the distance. At some distance it becomes easier to create new quark and anti-quark pairs which combine into hadrons than it is to continue to work against the increasing force.

1.4.1 Forces in QCD

Asymptotic freedom and confinement arise from the effective forces that are implicit in the Feynman rules of QCD. It is easier to discuss force and potential in the context of QED as it provides insight to QCD processes in a simpler environment. There are differences between QED and QCD: the QCD Lagrangain field tensor has a different structure from the QED analogue. QED has no term for the photon-photon interaction. However in QCD the gluons couple through the colour charge resulting in a gluon-gluon interaction term. For QED we have:

$$A_\mu \to A_\mu + (1/e)\partial_\mu \alpha \tag{1.29}$$

and for QCD we have

$$G^a_\mu \to G^a_\mu - (1/g)\partial_\mu \alpha_a - C_{abc}\alpha_b G^c_\mu. \tag{1.30}$$

The additional term in G^a_μ means the field strength tensor has a more complicated form than the QED counterpart. For QCD the field strength tensor has the form:

$$G^a_{\mu\nu} = \partial_\mu G^a_\nu - \partial_\nu G^a_\mu - g f_{abc} G^b_\mu G^c_\nu, \tag{1.31}$$

the QED field strength tensor has no

term of the form $g f_{abc} G^b_\mu G^c_\nu$. The additional term in the QCD Lagrangian means the kinetic energy term is now not purely kinetic but includes a self interaction between the gauge bosons (gluons).

The electrostatic Coulomb force is derived from the potential between two charged particles;

$$V(Q_1, Q_2, \mathbf{r}) = \frac{1}{4\pi}\frac{Q_1 Q_2}{|\mathbf{r}|}, \tag{1.32}$$

where Q_1 and Q_2 represent the size of the two charges separated by a vector $\mathbf{r}$. In QED this potential arises from the scattering of two heavy charged particles. If the particles are sufficiently heavy the energy transfer can be ignored as it is much smaller than the momentum transfer (in the non relativistic approximation ($p^2/2M \ll M$)). The potential is the spatial fourier transform of the gauge field propagator, multiplied by the coupling constant at the vertices and divided by $-i$. If the charges are equal $Q_1 = Q_2 = e$ the potential is:

$$V(\mathbf{r}) = -e^2 \int \frac{d^3\mathbf{k}}{(2\pi)^3} e^{-i\mathbf{k}.\mathbf{r}} \frac{1}{-\mathbf{k}^2}$$

$$= -e^2 \frac{2}{(2\pi)^2} \int_0^\infty dk \frac{sin(k|\mathbf{r}|)}{k|\mathbf{r}|}. \tag{1.33}$$

The lowest order Feynman diagram (tree level, figure 1.2 b) yields the potential. Even beyond tree level the potential is still the fourier transform of the scattering amplitude:

$$V(\mathbf{r}) = \int \frac{d^3\mathbf{k}}{(2\pi)^3} e^{-i\mathbf{k}.\mathbf{r}} A(\mathbf{k}^2). \tag{1.34}$$

In the previous example $A(\mathbf{k}^2)$ is given by single photon exchange $\sim O(e^2)$. Figure 1.2 c, d, e, f, g show the $O(e^4)$ graphs that contribute to the potential through perturbative corrections. The momentum dependence of the different contributions may differ from the lowest order term. These higher order diagrams require renormalization but it is instructive to assume it is done and consider the overall physical picture.

Experimentally, the contributions of various diagrams from the lowest order diagram cannot be separated. The higher order corrections modify the momentum dependence, and therefore the potential. To determine the electromagnetic coupling we define the amplitude at a fixed momentum transfer $-\mathbf{k}^2 = p_0$ to be

$$A(p_0) = \frac{\alpha(p_0)}{p_0}, \tag{1.35}$$

where the fine structure constant is equal to

$$\alpha = \frac{e^2}{4\pi}. \tag{1.36}$$

This tells us nothing about the momentum dependence of $A(p)$. The main contribution of the higher order diagrams comes from the process where the two incoming

charges are linked by a virtual photon inducing a self energy diagram of a fermion and anti-fermion pair. The net charge of the fermion/anti-fermion pair is zero and they act to screen each of the original charges from each other. We can think of the two heavy charges as being surrounded by a cloud of charge pairs. If the heavy charges are far apart they each see a large cloud which serves to decrease the effective charge of the other heavy charge. As p_0 increases the charges come closer together (uncertainty principle) and once inside the cloud the screening is less effective. This can be summarised as a statement, that, as the momentum transfer increases, the observed charge also increases:

$$\frac{d}{dp_0}e^2 > 0. \tag{1.37}$$

We define the effective charge for QCD as $g^2(p_0)$ and the effective fine structure 'constant' for QCD by

$$\alpha_s = \frac{g^2}{4\pi}. \tag{1.38}$$

The diagrams for QED are all present for QCD also, with photons replaced with gluons. There are additional diagrams due to three gluon vertices. As in QED the effect of the virtual corrections is to surround the now non-abelian charges with a charge cloud. The emission of a gluon does not leave the charge of the heavy charge unchanged. The total charge is still conserved but the charge of the heavy scatterer leaks into the surrounding charge cloud. As the two scatterers enter into each others virtual charge cloud they are less likely to see the true charge of each other [5]. This is the opposite of the QED situation. Here we have 'anti-screening':

$$\frac{d}{dp_0}g^2 < 0, \tag{1.39}$$

so as p_0 increases, the observed coupling decreases, giving *asymptotic freedom* (larger momentum transfer smaller coupling). Large momentum transfer corresponds to small distance scale, and therefore small coupling, which aids in the use/validity of the perturbative description.

1.4.2 The Renormalization Group and the Effective Coupling

To define $A(p_0)$ in perturbation theory it is necessary to introduce a renormalisation mass. This can be done via the inclusion of μ in $A(p_0) = \frac{\alpha(p_0)}{p_0}$. In terms of $\alpha_s(\mu^2)$, the amplitude is of the form

$$A(\mathbf{k}^2) = \alpha_s(\mu^2)\frac{1}{\mathbf{k}^2} + a_{21}\alpha_s^2(\mu^2)\frac{ln(\mathbf{k}^2/\mu^2)}{\mathbf{k}^2} + a_{20}\alpha_s^2(\mu^2) + ... \tag{1.40}$$

with a_{21} a number and a_{20} possibly a function of the masses and the infrared cutoff. The renormalisation group consists of the set of all possible rescalings of μ. The amplitude $A(\mathbf{k}^2)$ is a physical quantity and can therefore be measured experimentally. For this reason the amplitude cannot depend on the choice of μ^2:

$$\frac{d[pA(p)]}{d\mu} = 0. \tag{1.41}$$

Using equations 1.40 and 1.41 we see the μ dependence is described by:

$$\mu\frac{d\alpha_s(\mu^2)}{d\mu} = -a_{21}\alpha_s^2(\mu^2) + \quad \text{higher order terms.} \tag{1.42}$$

Given $a_{21} > 0$ the coupling decreases as the renormalisation scale μ increases. The asymptotic freedom can be expressed through the dependence of the linear coupling $g(\mu) = \sqrt{4\pi\alpha_s(\mu^2)}$, which yields:

$$\mu \frac{dg(\mu)}{d\mu} = \beta(g(\mu)), \tag{1.43}$$

where β is the power series:

$$\beta(g) = -g(\frac{\alpha_s}{4\pi}\beta_1 + (\frac{\alpha_s}{4\pi})^2\beta_2 + ..). \tag{1.44}$$

β_1 can be derived from a_{21} or from any physical quantity that depends on μ in perturbation theory. For QCD

$$\beta_1 = 11 - 2n_f/3 = (11N_c - 2n_f)/3, \tag{1.45}$$

where n_f is the number of flavours of quarks and N_c is the number of colours. The lowest order approximation to the dependence on the linear coupling in terms of α_2 is

$$\alpha_s(\mu^2) = \frac{\alpha_s(\mu_0^2)}{1 + (\beta_1/4\pi)\alpha_s(\mu_0^2)\ln(\mu^2/\mu_0^2)} \tag{1.46}$$

or equivalently

$$\alpha_s(\mu^2) = \frac{4\pi}{\beta_1 ln(\mu^2/\Lambda^2)} \tag{1.47}$$

where

$$\Lambda = \mu_0 e^{-2\pi/(\beta_1 \alpha_s(\mu_0^2))}, \tag{1.48}$$

this sets the scale for the running coupling otherwise known as Λ_{QCD}. By using higher terms in the β power series a more accurate result can be obtained.

$\alpha_s(\mu^2)$ can be expressed in an expansion of powers of

$$1/(ln(\mu^2/\Lambda^2)), \tag{1.49}$$

where the coefficients of the $1/(ln(\mu^2/\lambda^2))$ series is a polynomial in $ln(1/(ln(\mu^2/\lambda^2)))$. Keeping the first two β terms allows the determination of coeffecient of the $[1/(ln(\mu^2/\lambda^2))]^2$ term:

$$\frac{\alpha_s(\mu^2)}{4\pi} = \frac{1}{\beta_1 ln(\mu^2/\Lambda^2)} - \frac{\beta_2 ln(ln(\mu^2/\Lambda^2))}{\beta_1^3 ln^2(\mu^2/\Lambda^2)} + O(\frac{1}{ln^3(\mu^2/\Lambda^2)}), \tag{1.50}$$

where $\beta_2 = 102 - 38n_f/3$. We have set a renormalisation scale by the introduction of a unit of mass μ.

1.5 Infrared Safety

Using the solution to the running coupling discussed above we see asymptotic freedom can aid one in practical cases. For a given physical quantity $\sigma(p_i.p_j/\mu^2, m_i^2/\mu^2, g(\mu))$ that can be calculated in perturbation theory. It follows that:

$$\sigma(\frac{p_i.p_j}{\mu^2}, \frac{m_i^2}{\mu^2}, g(\mu)) = \sum_{n=0}^{\infty} a_n(\frac{p_i.p_j}{\mu^2}, \frac{m_i^2}{\mu^2})\alpha_s^n(\mu), \tag{1.51}$$

where the p_i denote the external momenta and m_i are the internal (quark) masses. It is not uncommon for the coefficients a_n to be large, regardless of the value of of $\alpha_s(\mu)$. Many cross sections in pQCD are infrared divergent due to the vanishing gluon mass. Infrared divergences either cancel or can be factorised into universal functions such as Parton Distribution Functions, which contain all of the low energy information. Infrared safe quantities are those that do not depend on the long distance behaviour of the theory. For the class of quantities that are infrared safe the coefficients a_n are infrared finite [17, 18] and also have a finite limit for vanishing m_i:

$$\sigma(\frac{p_i.p_j}{\mu^2}, \frac{m_i^2}{\mu^2}, g(\mu)) = \sigma(\frac{Q^2}{\mu^2}, 0, g(\mu)) \left\{1 + O(\frac{m_i^2}{Q^2})\right\}, \tag{1.52}$$

Q^2 is the scale of the large invariants along the $p_i.p_j$. For an infrared safe quantity equation 1.28 has the solution (upto mass corrections $\sim m^2/Q^2$)

$$\sigma(\frac{p_i.p_j}{\mu^2}, \frac{m_i^2}{\mu^2}, g(\mu)) = \sigma(1, 0, g(Q)), \tag{1.53}$$

all the momentum has been absorbed into the couplings. If Q is large the coupling decreases and the description offered by pQCD should impove.

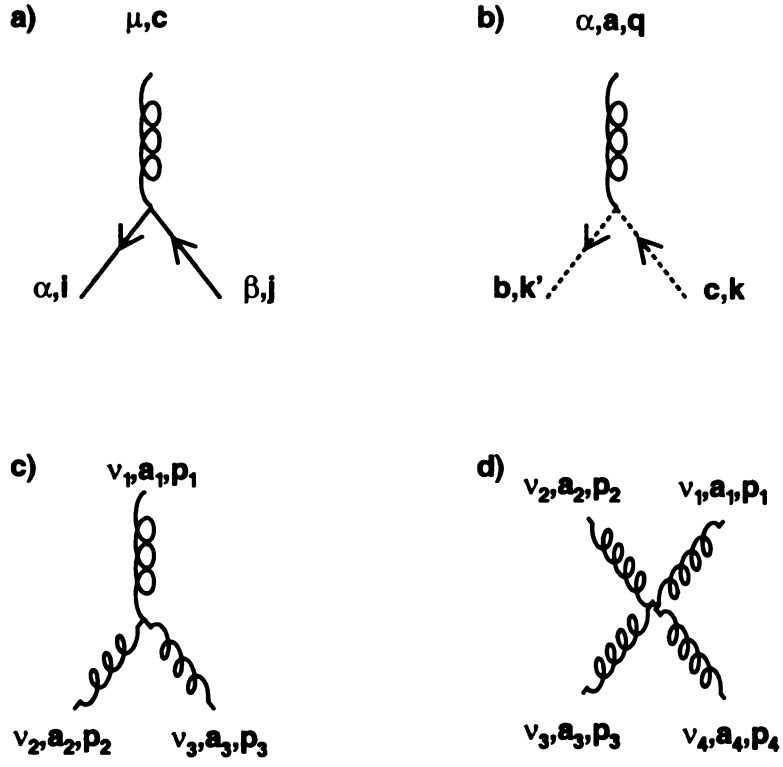

Figure 1.1: *Feynman diagrams/rules for the vertices. All momenta defined to flow into vertex.*

$$a) - ig(T_c^{(F)})_{ji}[\gamma_\mu]_{\beta\alpha} \tag{1.57}$$

$$b) g C_{abc} k'_\alpha \tag{1.58}$$

$$c) - gC_{a_1a_2a_3}[g^{\nu_1\nu_2}(p_1 - p_2)^{\nu_3} + g^{\nu_2\nu_3}(p_2 - p_3)^{\nu_1} + g^{\nu_3\nu_1}(p_3 - p_1)^{\nu_2}] \tag{1.59}$$

$$\begin{aligned} d) &- ig^2[C_{ea_1a_2}C_{ea_3a_4}(g^{\nu_1\nu_3}g^{\nu_2\nu_4} - g^{\nu_1\nu_4}g^{\nu_2\nu_3})] \\ &+(-ig^2)[C_{ea_1a_3}C_{ea_4a_2}(g^{\nu_1\nu_4}g^{\nu_3\nu_2} - g^{\nu_1\nu_2}g^{\nu_3\nu_4})] \\ &+(-ig^2)[C_{ea_1a_4}C_{ea_2a_3}(g^{\nu_1\nu_2}g^{\nu_4\nu_3} - g^{\nu_1\nu_3}g^{\nu_4\nu_2})] \end{aligned} \tag{1.60}$$

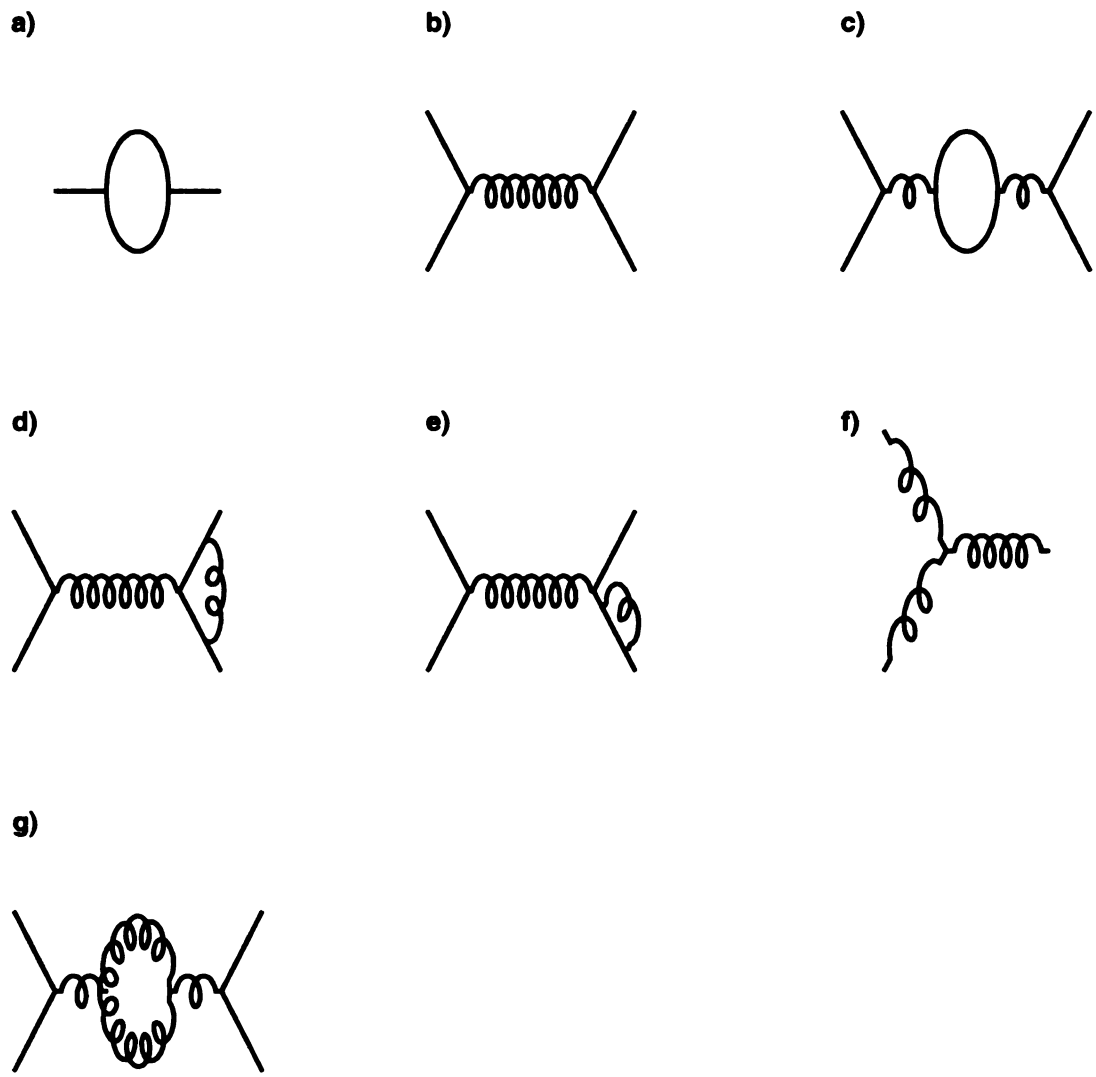

Figure 1.2: *a) An ultraviolet divergent one loop scalar diagram. b) Lowest order potential QED/QCD (tree level diagram).(c-e) Field theory corections to the potential in QCD which are also present in QED. (f-g) non abelian correction to the QCD potential (not present in QED).*

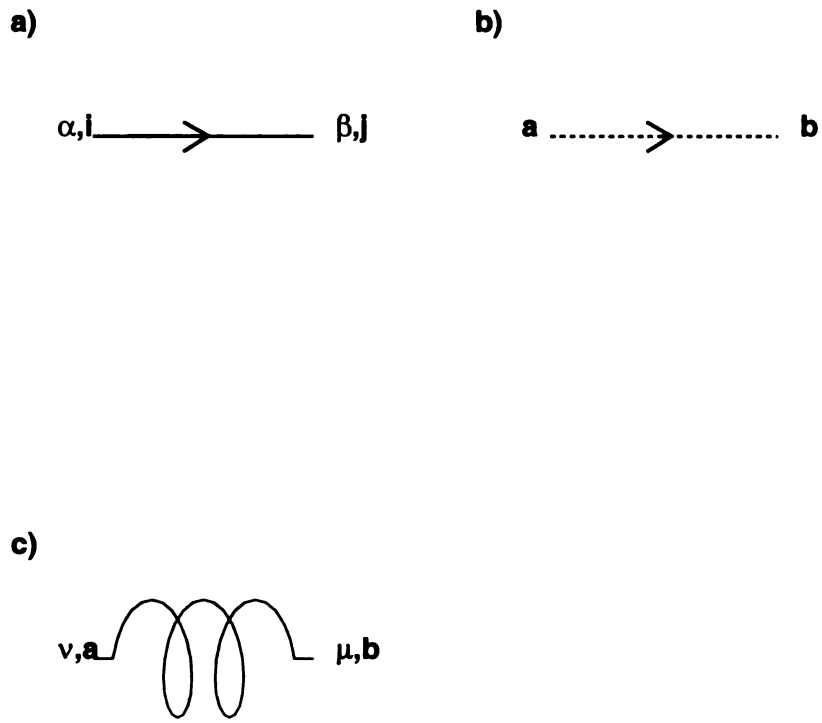

Figure 1.3: *Feynman rules for a) quark propagator, b) ghost propagator and c) gluon propagator.*

$$a) \quad i\frac{\delta_{ba}}{k^2 - m^2 + i\epsilon}[(\not{k} + m)]_{\alpha\beta} \tag{1.65}$$

$$b) \quad i\frac{\delta_{ba}}{k^2 + i\epsilon} \tag{1.66}$$

$$c)\ \textit{(Covariant gauge)} \quad i\frac{\delta_{ba}}{k^2 + i\epsilon}[-g^{\mu\nu} + (1 - \frac{1}{\lambda})\frac{k^\mu k^\nu}{k^2 + i\epsilon}] \tag{1.67}$$

$$c)\ \textit{(Physical gauge)} \quad i\frac{\delta_{ba}}{k^2 + i\epsilon}[-g^{\mu\nu} + \frac{k^\mu n^\nu + n^\mu k^\nu}{n.k} - n^2\frac{k^\mu k^\nu}{(n.k)^2}] \tag{1.68}$$

1.6 Jet Production

As discussed previously one of the most important QCD processes in $p\bar{p}$ collisions is the leading order process of $2 \rightarrow 2$ scattering. Two incoming partons interact and produce two outgoing partons. These outgoing partons hadronize to yield a jet of hadrons. The particles that make up the hadron jet deposit energy in the calorimeter. These energy deposits are what we measure (calorimeter jets). Figure 1.4 show the diagrams that contribute to jet production. All other diagrams that contribute to lowest order jet production are related to those shown via crossing.

At this point it is usefull to define some of the variables that will be used throughout the following work: E_T and P_T are the transverse energy and momentum of the partons/jets. In the limit of massless partons/jets $E_T = P_T$. The rapidity of jets and partons is defined as: $Y = \frac{1}{2} ln\left(\frac{E+P_z}{E-P_z}\right)$. The pseudo rapidity is defined as: $\eta = -ln(cot(\theta/2))$. In the massless limit $Y = \eta$.

The two-jet cross section can be expressed in terms of the parton distribution functions and a matrix element M [7]:

$$\frac{d^3\sigma}{dY_3 dY_4 dP_T^2} = \frac{1}{16\pi s^2} \sum_{i,j,k,l=q,\bar{q},g} \frac{f_i(x_1,\mu^2)}{x_1} \frac{f_i(x_2,\mu^2)}{x_2} \times \sum |M(ij \rightarrow kl)|^2 \frac{1}{1+\delta_{kl}}, \quad (1.69)$$

where P_T is the transverse momentum, the f_i represent the parton distribution functions and Y_3 and Y_4 are the rapidities of the outgoing partons. x_1 and x_2 are the momentum fractions $1/2x_T(e^{Y_3} + e^{Y_4})$ and $1/2x_T(e^{-Y_3} + e^{-Y_4})$ respectively, where $x_T = 2p_T/\sqrt{s}$. In the parton center of mass frame the subprocess scattering angle, θ^*, is related to the lab frame rapidity difference:

$$Y^* = \frac{1}{2}(Y_1 - Y_2) \text{ by } sin\theta^* = \frac{1}{cosh(Y^*)}. \tag{1.70}$$

Table 1.1 shows the square of the invariant matrix element ($|M|^2$) for $2 \rightarrow 2$ parton subprocesses contributing to jets. The value is given in terms of the Mandelstam variables: $\hat{s}, \hat{t}$ and $\hat{u}$.

$$\begin{aligned} \hat{s} &= (P_i + P_j)^2 \\ \hat{t} &= (P_i - P_1)^2 = -\frac{1}{2}\hat{s}(1 - cos\theta^*) \\ \hat{u} &= (P_j - P_1)^2 = -\frac{1}{2}\hat{s}(1 + cos\theta^*), \end{aligned} \tag{1.71}$$

where p_i and p_j are the initial state four-vectors and p_1 is an outgoing momentum four-vector. The Mandelstam variables obey the relation $\hat{s} + \hat{t} + \hat{u} = 0$. If we assume we have massless quarks and perfect jet algorithms ($P_{Jet} = P_{Parton}$) the single jet cross section can be found by integrating equation 1.69 over one of the jets:

$$\begin{aligned} \frac{E_{jet}d^3\sigma}{d^3P_{jet}} &= \frac{1}{16\pi^2 s} \sum_{i,j,k,l=q,\bar{q},g} \int_0^1 \frac{dx_1}{x_1}\frac{dx_2}{x_2} f_i(x_1,\mu^2) f_j(x_2,\mu^2) \\ &\times \sum |M(ij \rightarrow kl)|^2 \frac{1}{1+\delta_{kl}} \delta(\hat{s} + \hat{t} + \hat{u}). \end{aligned} \tag{1.72}$$

Predictions for the jet cross section as a function of P_T are obtained from the expression

$$\frac{E_{jet}d^3\sigma}{d^3P_{jet}} \equiv \frac{d^3\sigma}{d^2P_T dY} \rightarrow \frac{1}{2\pi P_T}\frac{d^2\sigma}{dP_T dY}, \tag{1.73}$$

where the last term arises from the assumption that jets and partons are massless ($E_T = P_T$ and $\eta = Y$).

Up to now our discussion of jet production was based on exclusive dijet production. Typical events seen at CDF have more than 2 jets. To understand the multijet final states we need to consider initial state radiation, final state radiation and higher order diagrams. The basic $2 \rightarrow 2$ interaction, or hard scatter, is a QCD interaction. In QCD however, the quarks and gluons can radiate gluons in both before and after the hard scatter. There can also be extra partons produced in the hard scatter, when this occurs the process is no longer $2 \rightarrow 2$ but is now $2 \rightarrow 3$, $2 \rightarrow 4$, etc. Experimentally, the inclusive jet cross section is defined as the number of jets in a bin of P_T, normalized by the acceptance and integrated luminosity. As an inclusive quantity all the jets in each event which fall within the acceptance region contribute to the cross section measurement.

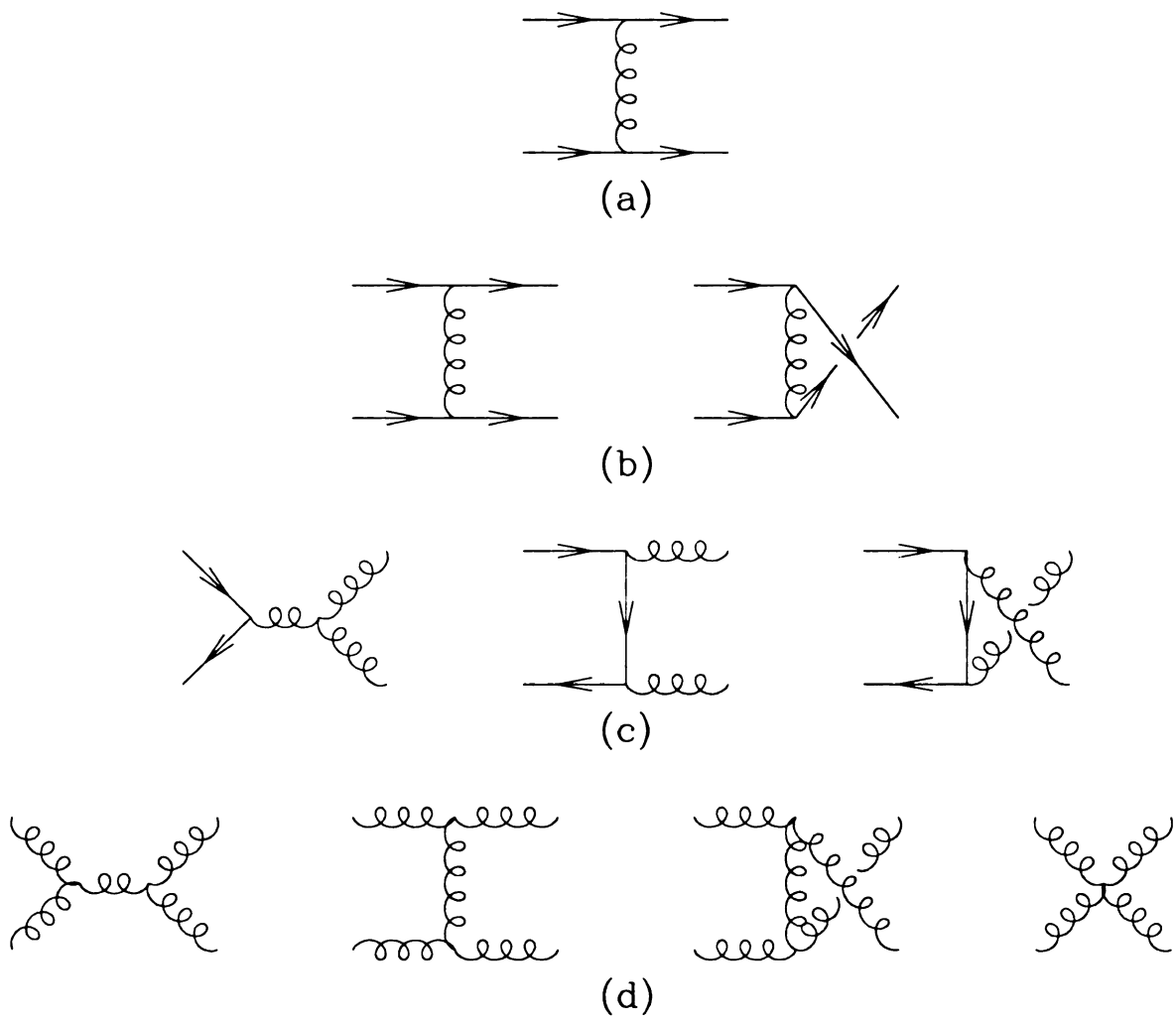

Figure 1.4: *Diagrams that contribute to jet production. All other lowest order jet production diagrams are related to this set by crossing. The low P_T cross section is dominated by qg and gg. The high P_T cross section is dominated by contributions from the qg and qq subprocesses. The Figure is taken from [8]*

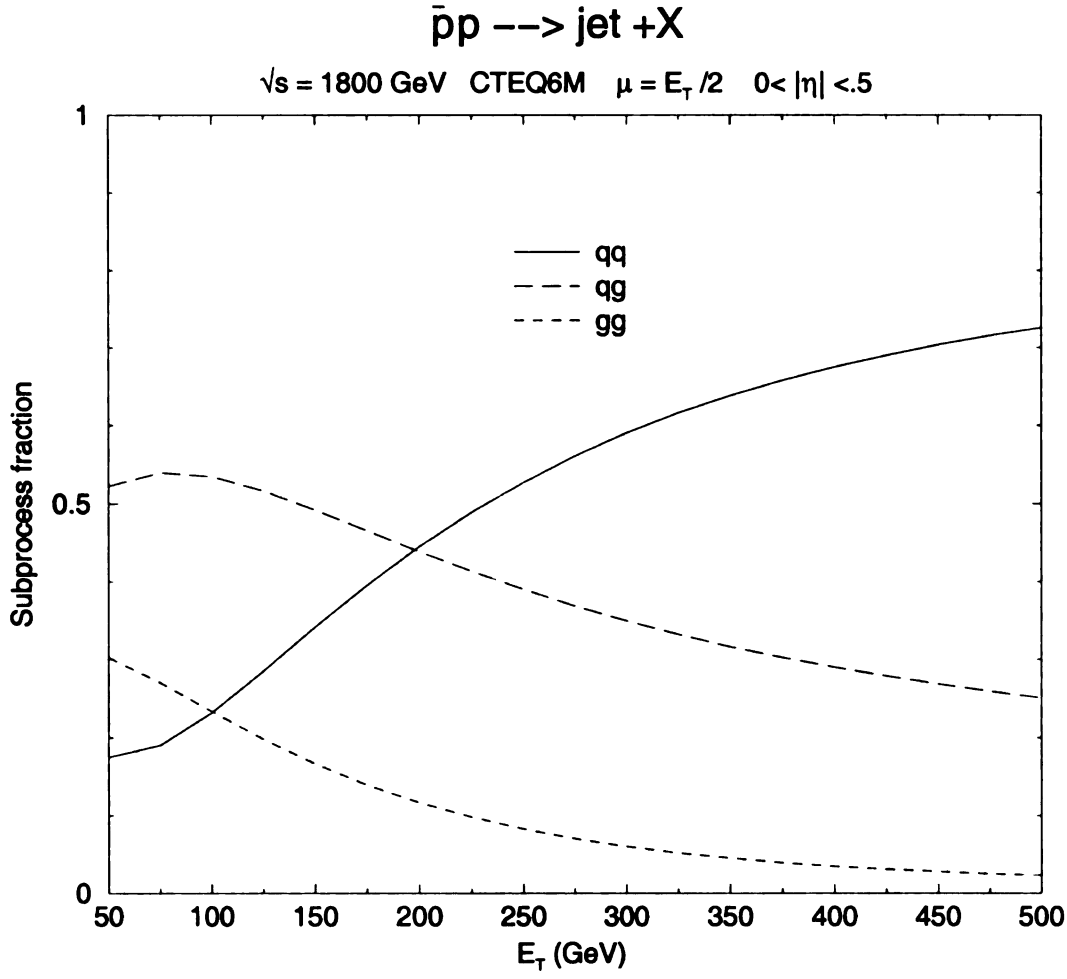

Figure 1.5: *QCD subprocess contributions. The figure describes the contributions for the subprocesses gg, gq and qq at* $\sqrt{s} = 1.8$ *TeV. We expect very similar contributions at 1.96 TeV.*

Process	$\sum \lvert M\rvert^2/g^4$	$\theta^* = \pi/2$
$qq' \to qq'$	$\frac{4}{9}\frac{\hat{s}^2+\hat{u}^2}{\hat{t}^2}$	2.22
$q\overline{q}' \to q\overline{q}'$	$\frac{4}{9}\frac{\hat{s}^2+\hat{u}^2}{\hat{t}^2}$	2.22
$qq \to qq$	$\frac{4}{9}\left(\frac{\hat{s}^2+\hat{u}^2}{\hat{t}^2} + \frac{\hat{s}^2+\hat{u}^2}{\hat{u}^2}\right) - \frac{8}{27}\frac{\hat{s}^2}{\hat{u}\hat{t}}$	3.26
$q\overline{q} \to q'\overline{q}'$	$\frac{4}{9}\frac{\hat{t}^2+\hat{u}^2}{\hat{s}^2}$	0.22
$q\overline{q} \to q\overline{q}$	$\frac{4}{9}\left(\frac{\hat{s}^2+\hat{u}^2}{\hat{t}^2} + \frac{\hat{t}^2+\hat{u}^2}{\hat{s}^2}\right) - \frac{8}{27}\frac{\hat{u}^2}{\hat{s}\hat{t}}$	2.59
$q\overline{q} \to gg$	$\frac{32}{27}\frac{\hat{s}^2+\hat{u}^2}{\hat{t}\hat{u}} - \frac{8}{3}\frac{\hat{t}^2+\hat{u}^2}{\hat{s}^2}$	1.04
$gg \to q\overline{q}$	$\frac{1}{6}\frac{\hat{s}^2+\hat{u}^2}{\hat{t}\hat{u}} - \frac{3}{8}\frac{\hat{t}^2+\hat{u}^2}{\hat{s}^2}$	0.15
$gq \to gq$	$-\frac{4}{9}\frac{\hat{s}^2+\hat{u}^2}{\hat{s}\hat{u}} + \frac{\hat{u}^2+\hat{s}^2}{\hat{t}^2}$	6.11
$gg \to gg$	$\frac{9}{2}\left(\frac{3}{1} - \frac{\hat{t}\hat{u}}{\hat{s}^2} - \frac{\hat{s}\hat{u}}{\hat{t}^2} - \frac{\hat{s}\hat{t}}{\hat{u}^2}\right)$	30.4

Table 1.1: *Leading order jet production matrix elements squared ($\sum \lvert M\rvert^2/g^4$). The spin and colour indices have been averaged (summed) over the initial (final) sates. The column labelled $\theta^* = \pi/2$ gives the size of the contribution from each of the subprocesses at $\theta^* = \pi/2$. Table adapted from [7, 12].*

Chapter 2

Jet Identification

2.1 Introduction

In this chapter we give a brief history of jet measurement and begin to link the theoretical concepts of QCD to the application of QCD as a predictive tool to be used in an experimental setting.

Searches for jet structure at the ISR pp collider ($\sqrt{s} = 63$ GeV), provided hints of two jet signatures. Extraction of the jet signal was difficult because the sharing of hadron momentum between the constituent partons reduced the available energy for parton scattering [13, 14, 15, 16]. In addition to the low jet energies, the remnants of the incident hadrons were a large background of low energy particles, another factor making jet identification difficult. The first clear evidence of two jet dominance was seen at the CERN $Sp\bar{p}S$ collider ($\sqrt{s} = 540$ GeV) [27, 21]. This was also the first measurement of the inclusive jet cross section.

Increases in the center of mass energies and improvements in accelerator/detector technology gave rise to larger sample sizes and increased collision energies. These improvements lead to production of jets of higher transverse energy. Producing jets at higher energy helps to distinguish jets from the underlying event (beam remnants from initial hadrons). The higher energies also reduced the transverse spreading of the

jets in space during fragmentation. Figures 2.1 and 2.2 show a dijet event resulting from a $p\bar{p}$ collision with $\sqrt{s} = 1.96$ TeV, seen at CDF. The figures illustrate very well the separation of the jet signal from the background and the 2 jet dominance of $p\bar{p}$ collisions with a large center of mass energy.

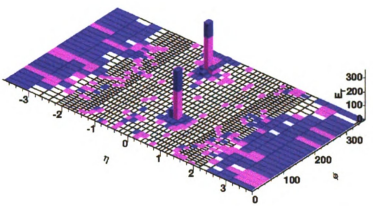

Figure 2.1: *Lego Plot of CDF dijet event. The display shows two well separated jets in the central calorimeter. The pink and blue colouring of the towers indicates the fraction of electromagnetic energy and hadronic energy respectively.*

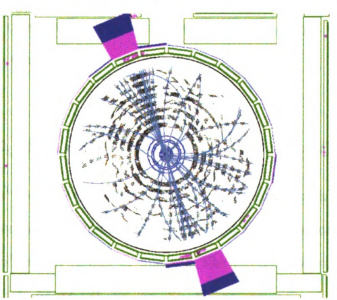

Figure 2.2: *Central outer tracker (COT) and calorimeter display of a CDF dijet event. The display highlights the back to back nature of the dijet event. COT superlayer hits and tracks are also seen in the display.*

Along with improvements in high energy experiments, there has also been progress towards more detailed and precise theoretical predictions. As the transverse energy of the jets increase, the value of the strong coupling constant α_s decreases, improving the validity of the perturbative expansion.

At leading order, $O(\alpha_s)$, one parton from each incident hadron participates in the collision producing two outgoing partons. More than two jets are observed in a typical collision at the Tevatron. To account for the multi-jet contributions, leading log Monte Carlo programs were developed to take the leading order Matrix Element predictions and add parton showering. The additional showering transition from partons to hadrons was based on empirical models of hadronisation and fragmentation and allowed for the description of multi-jet final states.

The cross section for hard scattering between two incident hadrons ($1 + 2 \rightarrow 3 + X$) to produce hadronic jets can be factorised into components from empirically determined Parton Distribution Functions (PDF's), $f_i(x, \mu_F^2)$ and the perturbatively calculated two-body scattering cross section $\hat{\sigma}$. A detailed discussion can be found in [22]. The hadronic cross section can be written as (using $\mu = \mu_r = \mu_f$, where μ_r is the renormalisation scale)

$$\sigma_{1+2\rightarrow 3+X} = \Sigma_{i,j} \int dx_1 dx_2 f_i(x_1, \mu^2) f_j(x_2, \mu^2) \times \hat{\sigma}_{i,j}(x_1 P, x_2 P, \alpha_s(\mu^2)). \quad (2.1)$$

The PDF's, $f_i(x, \mu^2)$, describe the initial parton momentum as a fraction x of the incident hadron momentum P and a function of the factorisation scale μ_F. The index refers to the type of parton (gluon or quark). The relative contribution of a given sub-process is shown in figure 1.6.

The PDF's are universal and can be derived from any process, *e.g.* Drell Yan, and applied to any other process. The PDF's are derived from global fits to scattering data

taken from a variety of experiments measuring different processes. Uncertainties in PDF's arise from uncertainty in the input data, the parameterisations of the parton momentum distributions and the extrapolation of the PDF's into other kinematic regions.

The hard two body parton level cross section, $\hat{\sigma}$, is only a function of the fractional momentum carried by the incident partons (x), the strong coupling constant (α_s) and the renormalisation scale that characterises the energy of the hard interaction (μ). The two body cross sections can be calculated with perturbative QCD at leading order (LO) [24] and next to leading order (NLO) [23, 25]. At leading order there are eight diagrams that describe the $2 \rightarrow 2$ scattering. The NLO calculations include diagrams with gluon emission as both an internal loop and final state parton.

The scales μ_R and μ_F are uncertainties which are intrinsic in fixed order perturbation theory. Although the choice of μ scale is arbitrary, a reasonable choice is related to a physical observable such as the jet P_T. In the following analysis we will compare the inclusive jet data to NLO QCD predictions.

Predictions for the jet cross section as a function of P_T are obtained from the general cross section given above:

$$\begin{aligned} \frac{Ed^3\sigma}{d^3p} &\equiv \frac{d^3\sigma}{d^2P_T dY} \\ &= \frac{1}{2\pi P_T}\frac{d^2\sigma}{dP_T dY}. \end{aligned} \tag{2.2}$$

Experimentally the inclusive jet cross section is defined as the number of jets in an P_T bin normalised by acceptance and integrated luminosity.

The fundamental step in the measurement of the inclusive jet cross section is the identification of jets. We need to be able to identify jets in a consistent way at

parton, hadron and calorimeter level. The parton level jet identification is required for comparison of data to theory. In a leading order (LO) calculation there are two partons in the final state, each of which will be associated with a jet. LO predictions have no dependence on the jet algorithm or on jet shape or size. When considering next to leading order (NLO) calculations there can be up to 3 partons in the final state and therefore there can be more than two jets in an event. The requirement to find jets in a consistent manner at parton, hadron and calorimeter level can be satisfied by the cone algorithms JetClu and MidPoint and also in the K_T clustering algorithm. There are subtle differences between the clustering scheme used at parton level and calorimeter level. At next to leading order parton level there are no overlapping jets, but at calorimeter level we may see multiple jets that do overlap. Jets that overlap are either split into 2 (or more) non-overlapping jets or merged into a single jet. The splitting and merging procedure depends on the algorithm. This splitting and merging feature is modelled in the parton level clustering by a parameter R_{sep}. Like μ, we will see that when comparing data to NLO pQCD we will need to make a choice for the value of R_{sep} to use. The details of the algorithms used in the current analysis are given in the following chapter.

Chapter 3

Jet Algorithms

3.1 Introduction

In the present analysis there are two cone algorithms used to reconstruct jets: Midpoint and JetClu. The JetClu algorithm is used in the Level-3 trigger and the Midpoint algorithm is used for jet reconstruction for the inclusive cross section measurement.

Cone algorithms form jets by grouping together particles whose trajectories, or towers, lie within a circle of radius R in $(\eta(Y), \phi)$ space, where $\eta(Y)$ is the pseudorapidity(rapidity) and ϕ is the azimuthal angle. How the towers are combined and how the jet properties are calculated depend on the specific algorithm.

In this section the ideal theoretical and experimental attributes of jet algorithms are outlined, followed by the outline of the recombination schemes used in the JetClu and Midpoint algorithms.

3.2 Theoretical Attributes of a Jet Algorithm

There are some desirable attributes we look for in jet clustering algorithms. These attributes may not be be present in an ideal form in practice due to the practicality of the implemention and/or computing limitations. Some desirable features are:

- Infrared safety: A jet algorithm should not only be infrared safe in the sense that infrared singularities do not appear in any perturbative calculations but it should also cluster partons, hadrons and calorimeter towers in a manner which is insensitive to soft radiation.

- Collinear safety: The algorithm needs to be collinear safe with respect to pertubative calculations and also find jets that are insensitive to collinear emission of radiation.

- Invariance under boosts: The algorithm should find the same solutions independent of boosts in the longitudinal (beam) direction. This is important in $p\bar{p}$ situation where the center of mass of the individual parton-parton interaction may be boosted with respect to the $p\bar{p}$ center of mass.

- Order Independence: The algorithm should find the same jets at parton, hadron and calorimeter level.

3.3 Experimental Attributes of a Jet Algorithm

After a jet has passed through the calorimeter the effects of showering, detector response, noise and multiple interactions will affect the performance of any jet algorithm. It is our goal to remove these effects and correct the measure cross section to the hadron and parton levels (removing detector effects). To aid in the correcting of the calorimeter level cross section to the hadron and parton levels the following attributes are desirable:

- The algorithm should not be detector dependent. There is a need to avoid or minimize any dependence of the algorithm on the segmentation of the calorimeter used to take the data.

- Resolution and angle bias: The algorithm should not amplify the effects of resolution smearing of the detector. Minimising this also helps to limit the size of the corrections that will be required to go from the calorimeter level cross section to the hadron level cross section.

- Stability with luminosity: The jet finding efficiency should not by strongly affected by multiple hard interactions associated with high luminosity. Also, the jet energy and angular resolution should not depend on luminosity.

- Fully specified: the algorithm should include specifications for clustering, energy and angle for reconstructed jets. In the case of overlapping jets the splitting and merging criteria need to be specified as well.

3.4 JetClu

The JetClu algorithm is used in the Level-3 trigger (discussed later) to reconstruct jets from energy deposits in the calorimeter towers. The algorithm consists of preclustering, clustering, splitting and merging, and the calculation of jet parameters. When used in the Level-3 trigger the tower energies are not corrected for the primary vertex Z. Below we outline the clustering steps.

3.4.1 PreClustering

- Merge the towers in the Foward and Plug calorimeters such that they have 24 segments in ϕ.
- Make E_T ordered list of towers with $E_T > 1$GeV.
- Associate the highest E_T tower with the first precluster.
- Loop over the tower list and add a tower to a precluster if it is within 7×7 towers of the seed tower and is adjacent to an existing tower in the precluster.

Otherwise, start a new precluster.

- Restore full segmentation of towers in the foward and plug calorimeters.

At this point a precluster consists of a contiguous set of towers with decreasing energy. Every tower with $E_T > 1$ GeV is assigned to one and only one precluster.

3.4.2 Clustering

- Make list of towers with $E_T > 100$ MeV.
- Order preclusters in E_T.
- Add tower to a precluster if the tower is within $\Delta R = 0.7$ of the cluster centroid.
- Iterate until tower list of the clusters is stable.
- Original towers in cluster are never dropped .

At this stage every precluster has an associated cluster. A tower may belong to more than one cluster.

3.4.3 Merging and Splitting

- E_T order the clusters.
- Using a double nested loop ($i = 1$,number of clusters,$j = 1, i - 1$), make a list of towers which are included in both clusters i and j.
- Merge two clusters if the common towers contain more than 75% of the E_T of the smaller cluster.
- If overlap contains less than 75% assign common towers to the closest cluster in an iterative fashion.

At this stage a tower is assigned to one and only one cluster, all clusters with $E_T >$ 1GeV are promoted to jets. The final jet energy and momentum is computed from the final list of towers:

$$\begin{aligned}
E_{Jet} &= \sum_i E_i \\
P_x &= \sum_i E_i sin(\theta_i) cos(\phi_i) \\
P_y &= \sum_i E_i sin(\theta_i) sin(\phi_i) \\
P_z &= \sum_i E_i cos(\theta_i) \\
\phi_{Jet} &= tan^{-1}(\frac{P_y}{P_x}) \\
sin(\theta_{Jet}) &= \frac{\sqrt{P_x^2 + P_y^2}}{\sqrt{P_x^2 + P_y^2 + P_z^2}} \\
E_T^{Jet} &= E_{Jet} sin(\theta_{Jet})
\end{aligned} \tag{3.1}$$

3.5 The Midpoint Jet Algorithm

In this analysis the Midpoint jet algorithm is used in the reconstruction of jets at the hadron and calorimeter level in Monte Carlo, and at calorimeter level in the data. The Midpoint algorithm has some advantages over the JetClu. Unlike JetClu, Midpoint does not use the calorimeter segmentation when clustering at the hadron level. This is very important as we use the hadron level clustering when deriving jet corrections. Both JetClu and Midpoint are seed based algorithms, they look for jets only around seed towers, which can lead to sensitivity to soft radiation. The Midpoint algorithm places additional seeds at the midpoint positions of stable cones:

$P_i + P_j$, $P_i + P_j + P_k$ *etc.* These additional seeds at the midpoints are used to define new initial search cones. The addition of these search cones lessens the sensitivity of the algorithm to soft radiation.

3.5.1 Clustering

The MidPoint algorithm makes use of 4-vectors throughout the clustering. The detector towers are sorted in descending P_T. Only towers passing a seed cut, $P_T^{Tower} > P_T^{Seed}$ are used as starting points for the initial jet cones. The seed threshold is choosen to be low enough such that variations of P_T^{Seed} lead to negligible variations in any jet observable. A tower or parton i is clustered into a cone and eventually a jet if the separation in (Y, ϕ) satisfies the following:

$$i \subset: \sqrt{(Y^i - Y^c)^2 + (\phi^i - \phi^c)^2} \leq R, \tag{3.2}$$

where c denotes the cone variables. For massless towers, particles or partons $Y = \eta$. The centroid corresponding to this cone is given by

$$\begin{aligned} P^c &= (E^c, \mathbf{P}^c) = \sum_{i \subset c} (E^i, P_x^i, P_y^i, P_z^i) \\ Y^c &= \frac{1}{2} ln(\frac{E^c + P_z^c}{E^c - P_z^c}) \\ \phi^c &= tan^{-1}(\frac{P_y^c}{P_x^c}). \end{aligned} \tag{3.3}$$

A jet arises from a stable cone, for which $\overline{Y}^c = Y^c = Y^{jet}$ and $\overline{\phi}^c = \phi^c = \phi^{jet}$, and the jet has the following kinematic properties:

$$\begin{aligned} P^{jet} &= (E^{jet}, \mathbf{P}^{jet}) = \sum_{i \subset J = c} (E^i, P_x^i, P_y^i, P_z^i) \\ Y^{jet} &= \frac{1}{2} ln(\frac{E^{jet} + P_z^{jet}}{E^{jet} - P_z^{jet}}) \end{aligned}$$

$$\phi^{jet} = tan^{-1}(\frac{P_y^{jet}}{P_x^{jet}}). \quad (3.4)$$

3.5.2 Splitting and Merging

The Midpoint algorithm has a different splitting and merging criteria from JetClu. In the MidPoint algorithm two jets are merged if the overlap energy is greater than 50% of the smaller jets energy. This splitting/merging is performed on an iterative basis.

Chapter 4

The Detector

4.1 Introduction

The inclusive jet cross section is measured from $p\bar{p}$ collisions in the Tevatron accelerator at Fermilab. The final state is measured using the Collider Detector at Fermilab (CDF). This chapter provides a brief description of the accelerator complex at Fermilab and of the subdetectors of CDF that are central in this analysis.

4.2 Experimental apparatus

4.2.1 The Accelerator Complex

The $p\bar{p}$ collisions at Fermilab are made possible by a series of accelerators culminating in the Tevatron. The Tevatron is currently the world's highest energy accelerator; during the data taking period of this analysis, the Tevatron produced collisions with a center of mass energy of $\sqrt{s} = 1.96$ TeV.

4.2.2 Protons

The proton source at Fermilab is composed of a 400 MeV linear accelerator (Linac) and an 8 GeV Booster. The Linac is accompanied by a H^- ion source Cockcroft-Walton accelerator (capacitor-diode voltage multiplying array). The process of proton

acceleration begins with a bottle of molecular hydrogen. The H^- is extracted electrostatically using a cesium walled chamber. The molecular hydrogen is ionised due to the low work function of the cesium. A 750 keV electric potential is applied to the resulting ions by a Cockcroft-Walton power supply. The H^- ions are accelerated electrostatically to 750 keV. Following this acceleration they enter a transfer station. The transfer station gives a bunch structure to the now continuous H^- beam and injects the bunches into the 150 m Linac. The Linac consists of 11 copper radio frequency (RF) cavities. A potential difference is applied to alternating cavities, this accelerates the H^- ions to 400 MeV. At the end of the Linac, a copper foil strips the electrons from the H^- ions leaving a bare proton. The protons are then injected into the Booster. The Booster is an alternating gradient synchrotron with 475 m circumference. The Booster accelerates the protons to 8 GeV. From the Booster the beam is transferred into the Main Injector (MI). In collider mode the MI, which is also a synchrotron, accelerates the proton beam to 150 GeV. It also performs the coalescing and cogging of the beam preparing it for injection to the Tevatron.

The Tevatron is a superconducting synchrotron with a circumference of $\sim$ 4 miles. This accelerates the beam to its final energy of 980 GeV.

4.2.3 Antiprotons

Antiproton production begins by extracting the 120 GeV proton beam from the MI and directing it onto a nickel target. In the resulting nuclear interactions, antiprotons are produced. The yield is approximately 1 antiproton for every 10^5 protons that hit the target. The resulting spray of particles is focused by a cylindrical lithium lens with an 0.5 MA pulsed axial current. The particles are then filtered by a pulsed dipole-magnet spectrometer resulting in an 8 GeV beam of antiprotons. The antiproton beam is directed toward the Debuncher, one of two rounded triangular synchrotrons

which make up the antiproton source. The Debuncher reduces the momentum spread of the antiproton beam by bunch rotation and stochastic cooling techniques. The cooling process converts narrow bunches with a large momentum spread into a broad beam with a small momentum spread. After the beam is cooled it is injected into the Accumulator, which is co-centric with the Debuncher. From the Accumulator the antiprotons are loaded into the main injector. From here they are loaded into the final stage of the Tevatron.

4.2.4 Collisions

For Run II the Tevatron operates with a 36 on 36 bunch structure, with a 396 ns bunch spacing. At two points on the Tevatron ring ($B0$ and $D0$) the beam is focused using quadrapole magnets to achieve a high luminosity at the interaction points inside the detectors. The luminosity of the beams is given by

$$\mathrm{L} = \frac{\gamma}{2\pi} f_0 N_{\overline{p}} N_p B \frac{H}{\beta^* \epsilon_p (1 + \frac{\epsilon_{\overline{p}}}{\epsilon_p})}, \tag{4.1}$$

where γ is the relativistic energy factor, f_0 is the revolution frequency, N_p ($N_{\overline{p}}$) are the number of protons (anti-protons) per bunch, B is the number of bunches of each type, β^* is the beta function at the center of the interaction region, ϵ_p ($\epsilon_{\overline{p}}$) are the proton (anti-proton) 95% normalised emittances and H is the form factor associated with the bunch length.

4.3 The CDF Detector

CDF is a general purpose detector located at the B0 interaction point of the Tevatron. It is cylindrically symmetric around the beam axis and has back-foward symmetry about the nominal interaction point. It is designed to make precise position, mo-

mentum and energy measurements of particles originating from the $p\bar{p}$ collision. This section describes the Run II configuration of the CDF detector. A more complete description can be found in the technical design report [34]. The components of the detector that are central to this analysis such as the Calorimetry, Cherenkov luminosity counters (CLC) and central outer tracker (COT) will be outlined in the following sections.

CDF uses a right-handed coordinate system: $\hat{x}$ points away from the center of the Tevatron (north), $\hat{y}$ points upward, and $\hat{z}$ points along the beam direction (east). Due the cylindrical symmetry of the detector it is useful to use cylindical coordinates for the physical quantities used in measurements. Using r, the radial distance from the z axis, ϕ is the azimuthal angle (0 radians lies on the x axis) and θ is the polar angle relative to the z axis.

The rapidity ($Y = \frac{1}{2}ln(\frac{E+P_Z}{E-P_Z})$) is a relativistic invariant for boosts along the beam axis. In the ultra relativistic regime the rapidity can be approximated by the purely geometric quantity psuedo-rapidity ($\eta = -ln(cot\frac{\theta}{2})$).

The CDF detector is a combination of tracking systems inside a 1.4 T solenoidal magnetic field surrounded by electromagnetic and hadronic calorimeters and a muon system. The measurement of the inclusive jet cross section uses the calorimeters for measurement of the jet energy/momentum. The tracking system provides the position of the $p\bar{p}$ collision vertex. This vertex is used in the offline reconstruction of jets.

Closest to the beam pipe is the Silicon Vertex Detector (SVX). It is roughly 60cm long and covers the radial region 3.0 cm out to 7.9 cm. The $r-\phi$ tracking information is provided by the SVX allows precise determination of the transverse position of the event vertex and contributes to the track momentum resolution. Surrounding the

SVX is the Vertex Drift Chamber (VTX). This detector provides $r - Z$ information used to determine the position of the $p\bar{p}$ in z. The SVX and VTX are inside a 3.2 m long drift chamber called the Central Tracking Chamber (CTC). The CTC covers the radial region from 31.0 cm to 132 cm. The momentum resolution of the SVX-CTC system is $\delta P/P = [(0.0009P_T)^2 + (0.0066)^2]^{1/2}$ where P_T has units of GeV/c.

Outside the tracking system there is the combination of electromagnetic and hadronic calorimeters. Calorimetery is used to measure the energy of incident particles. The central calorimeters ($|\eta| < 1.1$) consist of projective towers of dimension $\Delta\eta \times \Delta\phi = 0.1 \times 15^o$. The inner section is an electromagnetic compartment designed to measure the electromagnetic energy of incident particles. The outer compartment is hadronic. Each tower consists of a unique piece of the solid angle and the calormetric information within that piece of the solid angle. CDF has several interface regions between calorimetry detectors of varying ϕ and η segmentation. There are regions where the electromagnetic segmentation is finer than the hadronic segmentation. There are nine distinct types of tower:

4.3.1 Central Outer Tracker

The Central Outer Tracker (COT) is an open cell drift chamber which provides tracking coverage for the region $|\eta| < 1$. The COT is segmented into 8 layers moving out radially from $r = 40$ to 137 cm. Each layer holds a number of cells, the cells contain a 50 : 50 mixture of Ar-Et gas and a trace amount isopropyl alcohol. The Ar-Et and isopropyl alcohol combination has a drift velocity of $\sim 200\mu$m/ns. The maximum drift length for a given cell is approximately 0.9 cm and the maximum drift time $\sim$ 175ns in the drift field of 1.9 kV/cm. For high P_T tracks the beam constrained momentum resolution of the COT is $\delta P_T/P_T^2 \leq 0.001$ (GeV/c)$^{-1}$.

4.3.2 Magnetic Field

The CDF detector has a 1.4 T axial magnetic field throughout the tracking volume which enables measurements of charge and momentum via the tracking detectors. The field points in the $-\hat{z}$ direction of the CDF global coordinate system. The solenoid used to generate the field is superconducting and is constructed of an aluminum stabalised NbTi conductor. The normal operating field of 1.4 T corresponds to a persistent current of 4650 Amps. The cooling of the solenoid is done indirectly using liquid helium. The soleniod is supported by an aluminum structure and an iron return yoke.

4.3.3 Calorimetry

The calorimeter systems at CDF surround the tracking volume and the solenoid. They provide the energy measurement of electrons, photons and jets. Each calorimeter system covers 2π in azimuth, and a large range in η.

Electromagnetic

The central electormagnetic calorimeter (CEM) is a lead-scintillator sampling calorimeter consisting of a stack of 1/8" thick lead plates separated by 5 mm thick polystyrene scintillator. They sample the electromagnetic shower in the regions bounded by the lead plates. Electromagnetic particles interact with the lead causing showering of electrons and photons in the calorimeter. The electrons produce blue light in the scintillators. The total amount of light observed at a photomultipler tube (PMT) is proportional to the energy of the initial electron or photon. The light is collected by acrylic wavelength shifting fibres at both azimuthal tower boundries and guided to the PMT's. In order to maintain a constant radiation thickness of $X_0 = 18$ (X_0 is the radiation length) as a function of η, the layers of lead are replaced with acrylic.

At $|\eta| = 0.06$ there are 30 layers of lead; at $|\eta| = 1.0$ there are 20 layers of lead.

Hadronic

The Central Hadronic (CHA) and End Wall Hadronic (WHA) calorimeters are made up of layers of 2.5 cm thick steel separated by 1 cm thick plastic scintillator.

The central electromagnetic calorimeter (CEM) is followed at larger radius by the the central hadronic calorimeters (CHA and WHA). The CEM absorber is lead and the CHA/WHA absorber is 4.5 interaction lengths of iron; scintillator is the active medium in both types of calorimeter. Two phototubes bracket each tower in ϕ and the geometric mean of the energy of the two tubes is used to determine the ϕ position of the energy deposited in the tower.

4.3.4 Resolution of the calorimeters

The CEM has an energy resolution of

$$\frac{\sigma(E)}{E} = \frac{14.0\%}{\sqrt{E_T}} \oplus 2\%, \tag{4.2}$$

where $\oplus$ indicates addition in quadrature. At a depth of about 6 X_0, the CEM contains a shower maximum detector called the CES. This employs a proportional strip and wire counters in a fine-grained array to provide precise position and shape information ($\sim$ 2 mm) for electromagnetic cascades.

The CHA is an iron-sintillator sampling calorimeter, approximately 4.5 interaction lengths in depth and has an energy resolution of

$$\frac{\sigma(E)}{E} = \frac{50.0\%}{\sqrt{E_T}} \oplus 3\%. \tag{4.3}$$

The WHA is also an iron-scintillator sampling calorimeter covering the psuedorapidity range $0.7 < |\eta| < 1.3$. Like the CHA the WHA has a depth of ~ 4.5 interaction lengths, however the resolution is somewhat poorer with a resolution of

$$\frac{\sigma(E)}{E} = \frac{75.0\%}{\sqrt{E_T}} \oplus 3\%. \tag{4.4}$$

4.3.5 Cherenkov Luminosity Counters (CLC)

The Cherenkov luminosity counters are used to measure the luminosity at CDF. The counters provide the trigger requirement for the minimum bias data sample used in this analysis. The CLC consists of two conical shaped volumes containing isobutane as a radiator. These volumes are located on both ends of the experiment in the three degree hole between the end plug calorimeter and the beam pipe. Each of the volumes is divided into 48 conically shaped mylar counters that are arranged into three concentric rings around the beam pipe. The CLC counters accept particles from the collision point in the psuedo-rapidity range $3.7 < |\eta| < 4.7$. The CLC samples a large fraction of the total inelastic cross section. The min bias trigger is based on coincidence triggers from the east and west CLC modules using a 15ns time window centered on the bunch crossing time $t - 20$ ns..

4.3.6 Segmentation

Name	Rapidity	$\phi - \eta$ segmentation
CEM	0.0-1.1	
CHA	0.0-0.9	$15^o \times 0.1$
WHA	0.7-1.3	

Table 4.1: Segmentation of the central calorimeters

Chapter 5

The CDF Trigger

5.1 Introduction

The trigger plays an important role at CDF as the collision rate is much higher than the rate at which data can be stored and many of the collisions do not contain interesting physics. The role of the trigger is to extract the most interesting physics events from a large number of minimum bias events (see chapter 6). The trigger can be used to preferentially select high transverse energy jet events while rejecting the more numerous minimum bias, or zero bias events. This allows us to obtain a large number of events covering a large jet E_T range without saturating the bandwidth with uninteresting events or low E_T jets. In this chapter we give an overview of the CDF trigger system and describe the jet triggers used in the analysis. A more complete description of the trigger system can be found in the Technical Design Report [34].

5.2 The CDF Trigger Architecture

The CDF trigger has a three level architecture with each level providing a rate reduction large enough to allow processing at the next trigger stage, the reduction is achieved by requiring an event has specific properties at each trigger stage. The Level-1 trigger uses hardware to find physics objects based on a subset of the avail-

able detector information. The Level-2 trigger uses hardware to do limited event reconstruction in programmable processors. The Level-3 trigger uses the full detector information to reconstruct events in a processor farm.

5.2.1 The Level 1 Trigger

The Level-1 hardware finds calorimeter objects, and tracks in the central tracking chamber. The decision on whether the event satisfies a trigger is made every 132ns.

Level 1 Calorimeter Hardware

The Level-1 calorimeter hardware triggers on electrons, photons, total event transverse energy, missing transverse energy, and jets. The calorimeter triggers are divided into two types: object triggers (jets, electrons and photons) and global triggers (ΣE_T and missing transverse energy $\not\!\!E_T$). The object triggers are formed by applying thresholds to individual calorimeter towers. Electron and photon triggers are formed by applying thresholds to the electromagnetic energy of a tower. The jet triggers are formed by applying the thresholds to the electromagnetic and hadronic energies of the tower.

The Level-1 jet triggers require a single trigger tower $\approx 0.2 \times 0.3$ in (η, ϕ) space to be above an E_T threshold. There are two Level-1 triggers that feed the jet triggers: STT5 and STT10. STT5 requires a single trigger tower above 5 GeV and STT10 requires a single trigger tower above 10 GeV. These thresholds are typically $\leq 33\%$ of the Level-2 cluster E_T requirment and thus have a negligible effect on the combined trigger efficiency.

Prescales and Rate Limiting

In addition to imposing the aforementioned requirements to select out interesting physics events from the minimum bias events, triggers can be prescaled. The prescaling can be done either by simply accepting a predefined fraction of the events that satisfy the trigger or by limiting the rate at which the trigger events are recorded. The jet triggers are prescaled by accepting a fixed fraction of events.

5.2.2 The Level 2 Trigger

Jets are not fully contained in a single calorimeter tower. A single tower will only contain a fraction of the total jet energy. The Level-1 thresholds must be set lower than the jet energy to provide an efficient trigger. To avoid saturating the Level-2 bandwidth while spanning a wide range of E_T, four jet trigger samples were collected using Level-2 cluster thresholds of 15,40,60 and 90 GeV and nominal prescale factors of 240,50,20 and 1. These are used to form the jet trigger samples, Jet20, Jet50, Jet70 and Jet100 respectively. The clusters are found by the Level-2 cluster finder. In this algorithm contiguous regions of calorimeter towers with non trivial energy are clustered together. Each cluster starts with a tower above a seed threshold and all towers above a second, somewhat lower threshold that form a contiguous region with the seed tower are added to the cluster. The size of the cluster expands until no towers adjacent to the cluster have energy over the second threshold. Once the entire cluster is found, the tower energies are removed from the list and the next seed tower found and the algorithm is repeated. For each cluster found the total EM and HAD energies are calculated and recorded with the number of towers and the (η, ϕ) of the seed tower.

The data from the calorimeter are collected and processed by the Level-1 trigger.

The towers are summed on the detector into trigger towers of $0.2 \times 15\,\text{deg}$ in (η, ϕ). This is a 24×24 array (1152 towers , 576 EM, 576 HAD). The tower energies are weighted by $\sin\theta$ and are gain and offset corrected.

5.2.3 The Level 3 Trigger

CDF uses the JetClu algorithm in the Level-3 jet trigger software. Here we outline the implementation of the algorithm in the trigger.

The CDF calorimeter has 84 pseudo-rapidity (η) annuli covering the η range $-4.2 \geq \eta \geq 4.2$. These η annuli are divided into 24 azimuthal (ϕ) segments in the $|\eta| \geq 1.2$ regions and 72 segments in the $|\eta| \leq 1.2$ regions. The JetClu algorithm consists of 4 stages: preclustering, clustering, splitting/merging and the calculation of jet parameters. This is done using $Z = 0.0$.

L1 Trigger	L2 Trigger	L3 Trigger
ST5 (20)	CL15 (12, 25)	J20
	CL40 (1)	J50
ST10 (1)	CL60 (8)	J70
	CL90 (1)	J100

Table 5.1: *The trigger paths and prescales (given in parenthesis) used in the analysis.*

5.3 Trigger Efficiency

The efficiency of the jet triggers is dominated by the Level-2 triggers. The Level-2 clustering algorithm is a nearest neighbour clustering algorithm. The Level-2 clustering and the JetClu algorithm which is used in the Level-3 trigger are quite different. We now further complicate things by using the Midpoint algorithm which differs from both the Level-2 clustering and the Level-3 JetClu clustering.

For each of the jet triggers the efficiency of the Level-2 cluster E_T cut is measured

as a function of the Midpoint algorithm jet P_T. The overlap of separate trigger samples allows the derivation of the trigger efficiency curves. As an example consider the Jet50 trigger efficiency. The efficiency curve ($\epsilon_{trig}(P_T)$) for this trigger can be found by dividing the P_T distribution of Jet20 events that satisfy the Level-2 requirement ($E_T^{Level-2\ cluster} > 40$GeV) by the full Jet20 P_T distribution:

$$\epsilon_{trig} = \frac{M_{trig}}{M_{total}}, \tag{5.1}$$

where M_{trig} is the number of events in the subsample that passed the Level-2 cluster E_T requirement. M_{total} is the total number of events in the parent sample. The uncertainty in a given trigger efficiency bin is calculated binomially:

$$\delta\epsilon = \sqrt{\frac{\epsilon(1-\epsilon)}{M_{total}-1}}. \tag{5.2}$$

The efficiency of the Level-3 E_T cut is found in the same way as the efficiency of the Level-2 cut. The Level-3 E_T requirements are not very different from the Level-2 cluster requirement, thus the difference between Level-2 and Level-3 trigger efficiencies is not very large.

The trigger efficiency curves are calculated and fitted to the function

$$\epsilon(P_T) = \frac{1}{1+e^{(-P_1(P_T+P_2))}}. \tag{5.3}$$

We select the P_T regions of the jet trigger samples that satisfy $\epsilon_{trig}(Level-3) > 0.995$ using equation 5.3.

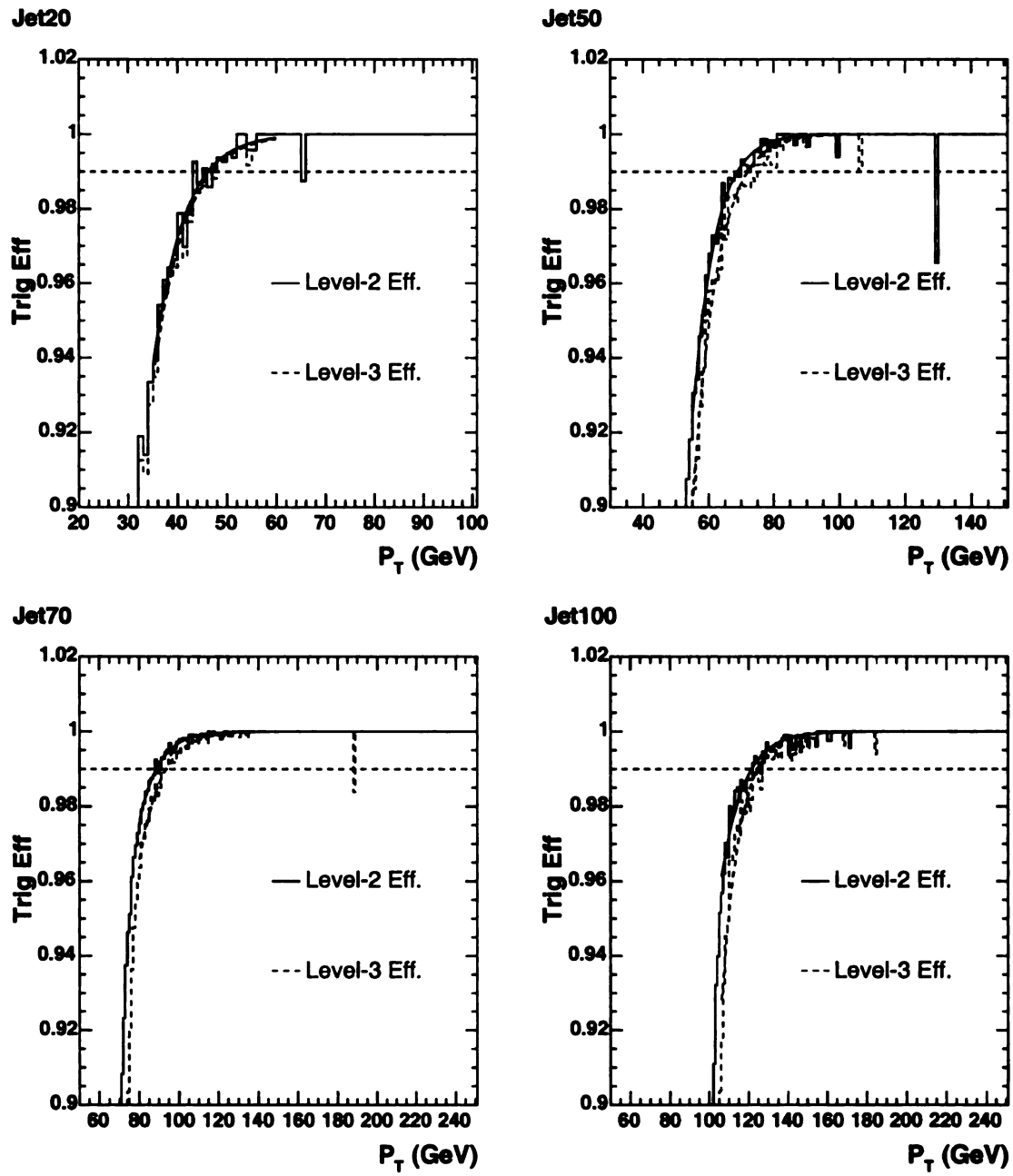

Figure 5.1: *Trigger efficiencies for the jet samples used in the analysis. Both the Level-2 and Level-3 efficiencies are shown. The Jet20 efficiency was measured from the STT5 sample. The 99% and 98% efficiency values for Level-2 and Level-3 E_T cuts are listed in table 5.2.*

Sample	Jet20	Jet50	Jet70	Jet100
L3 99% Eff (GeV)	47.04	72.67	93.59	124.52
L3 98% Eff (GeV)	42.69	67.46	86.17	118.25
L2 99% Eff (GeV)	46.20	69.48	88.67	121.67
L2 98% Eff (GeV)	42.02	64.59	82.04	113.86
PreScale	413	20	8	1

Table 5.2: *Trigger efficiencies and prescales for jet triggers. The analysis requires the Level 3 efficiency to be* > 0.99. *Once we know the* P_T *value corresponding to that efficiency we begin using the trigger sample in the range* $P_T(\epsilon > 0.99) + 5\%$ *to account for the jet energy scale uncertainty.*

5.4 Prescales

The Jet triggers are prescaled at Level 1 and Level 2 (see 5.1). We measure the combined Level 1 and Level 2 prescales from the data. This allows us to combine and use the four Jet samples to construct the inclusive jet cross section as a function of P_T.

The effective prescale is determined for each of the low E_T trigger samples by normalisation to the next highest E_T sample in the P_T range where both samples have full trigger efficiency. It is important that these datasets do not contain any bad runs, especially so in the lower E_T trigger. Any bad run may lead to a non statistical effect in the high P_T region where the number of events may be small. If this happens it may become difficult to distinguish statistical effects from systematic problems. At lower P_T this will be less important as the physics cross section is large enough that a few bad runs will not make an appreciable difference. The prescales for Jet50, Jet70 and Jet100 are consistent with the nominal values. The Jet20 prescale was changed at run 153067 so an effective prescale which depends on the data sample is used.

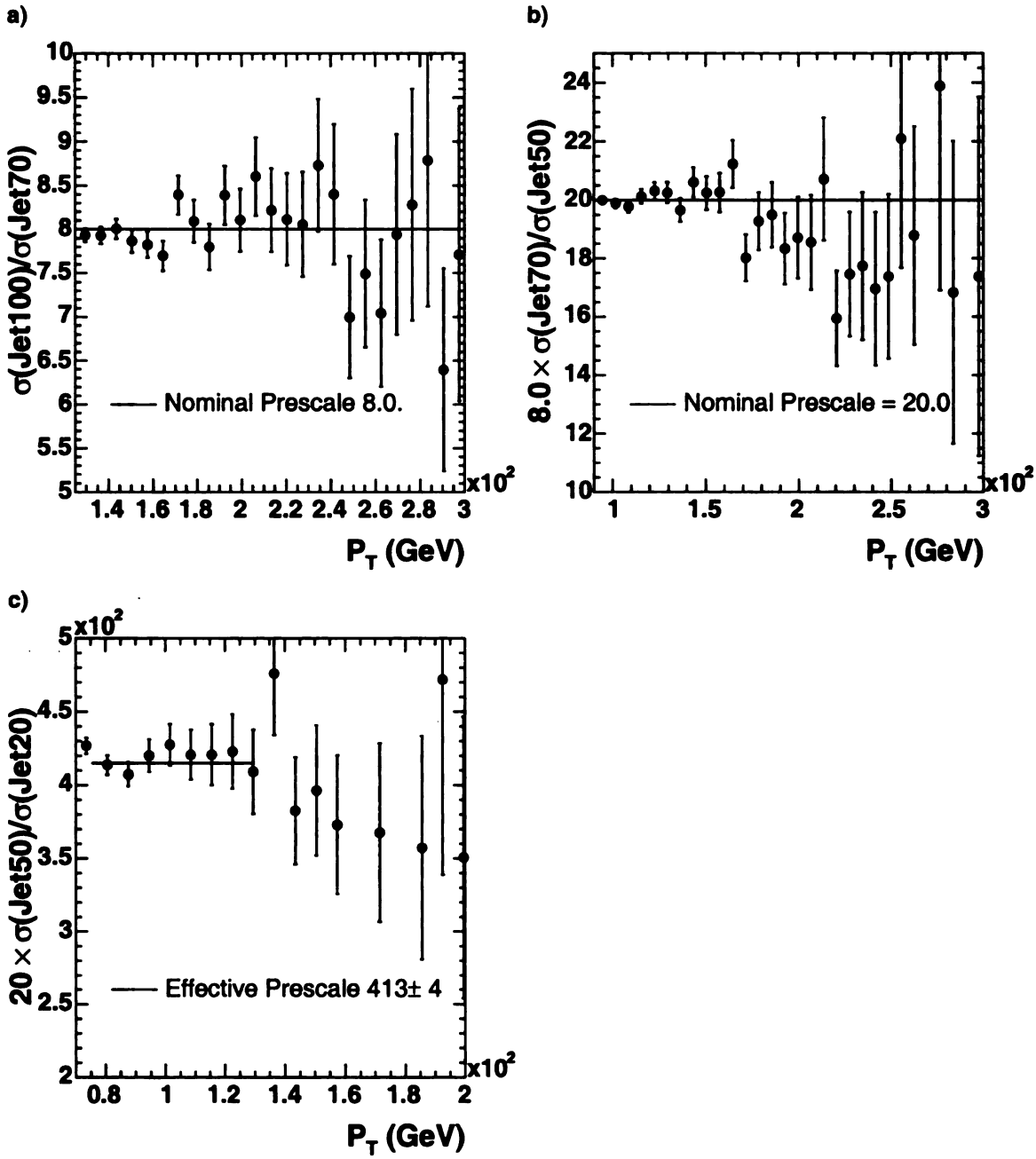

Figure 5.2: *Normalised prescale factor for Jet20, Jet50, Jet70 and Jet100 triggers as a function of P_T. The nominal prescale factors are included prior to the fit. These prescale factors are used to correct the cross section in such a way that all the triggers are normalised to the Jet100 trigger. Deviations of the ratio from unity can arise from missing data and in the case of the Jet20 sample the L2 prescale was changed during the run period.*

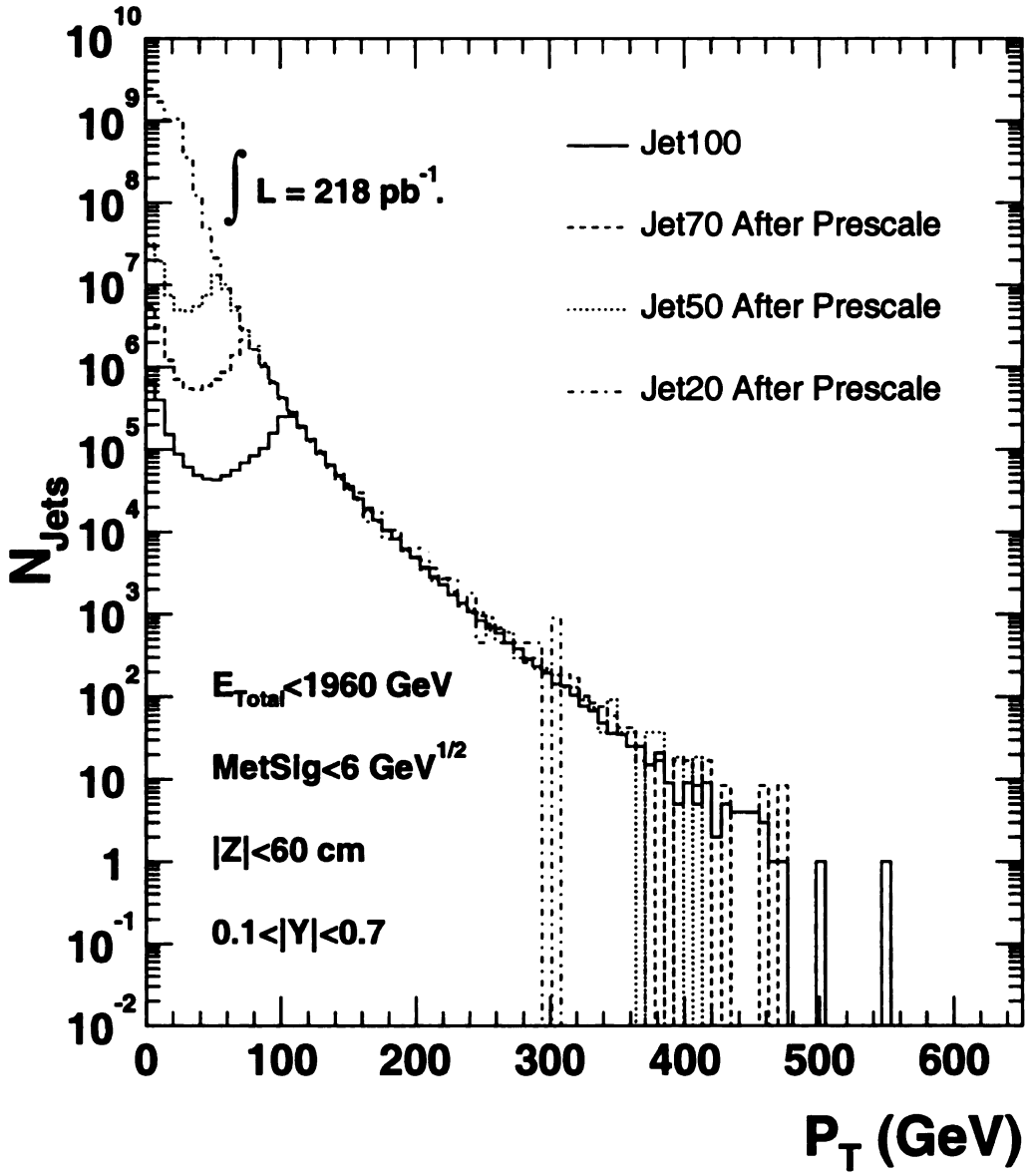

Figure 5.3: *Inclusive jet P_T spectrum for Jet20, Jet50, Jet70 and Jet100 after applying prescales. All triggers are normalised to the Jet100 trigger which has no prescale.*

Chapter 6

Multiple Interactions & Underlying Event

6.1 Introduction

The inclusive jet analysis uses the Midpoint jet clustering algorithm for jet reconstruction. In each event, spectator interactions can contribute energy to the jet cone. This energy must be subtracted in order to compare to LO and NLO perturbative QCD models that do not contain multiple interactions and/or underlying event. In the following chapter we present the measurement of the multiple interaction and underlying event contribution to jets. The multiple interaction correction derived from the data is used to correct the jets; however, the underlying event correction we use is taken from Monte Carlo. The underlying event study from the data, including the $P_T(\pm 90^o)$ cone study is included for completeness only.

Most of the inelastic $p\overline{p}$ collisions from the Tevatron result in soft collisions with most of the particles going in a direction only slightly deviated from the original p or $\overline{p}$ directions. Such events are triggered on using the CLC (see section 4.3.5) and make up the minimum bias sample.

In addition to these events there are hard scattering events which produce jets. The underlying event is everything except the hard scattered jets, it contains beam

remnant plus contributions from initial and final state radiation. In addition to the soft spectator interactions there can be multiple hard interactions associated with a single bunch crossing.

6.2 Data Set

In this measurement of the multiple interaction correction and the underlying event momentum we use the tower P_T and jet P_T which has been corrected using the primary vertex as the interaction point. The event properties of the minimum bias sample are shown in figures 6.1 and 6.2. The events are required to pass the following cuts:

- $|Z_{vertex}| < 60$ cm
- Missing $E_T < 30$ GeV.

The data span the same running period as the data sample used in the inclusive jet analysis. This ensures the measurment samples the same or at least similar instantaneous luminosity as the jet samples that it is used to correct.

6.3 Method

6.3.1 Minimum Bias Momentum in a Random Cone

The multiple interaction correction is measured in the data and applied to the raw jet energy. The absolute corrections are derived from the Monte Carlo, as are the underlying event corrections as well. The application of these later two corrections are discussed in chapter 9.

The multiple interaction correction is measured by considering the minimum bias momentum in a cone placed randomly in (Y, ϕ) with the constraint that $0.1 < |Y| < 0.7$. The cone energy is measured as a function of the number of quality 12 vertices (NQ12Zv) in the event. Quality 12 vertices are required to have ≥ 2 COT tracks. The slope, A_1, of the straight line fit to $\langle P_T \rangle_{cone}$ *versus* number of NQ12Zv is the energy that needs to be removed from the raw jet P_T when more than one vertex is seen in a jet event. The correction has the form:

$$UEM(R) = A_1 \times (NQ12Zv - 1). \tag{6.1}$$

6.3.2 Summing of Tower Momentum in a Cone

The towers that are within the cone must be summed in a manner consistent with the Midpoint jet algorithm clustering. The summation of towers uses the following prescription: for each tower construct the 4-vectors for the hadronic and electromagnetic compartments:

$$\begin{aligned} \mathbf{P}^{tower} &= (P_x, P_y, P_z, E)_{Had} + (P_x, P_y, P_z, E)_{EM} \\ Y^{tower} &= \frac{1}{2} ln(\frac{E^{tower} + P_z^{tower}}{E^{tower} - P_z^{tower}}) \end{aligned} \tag{6.2}$$

where:

$$\begin{aligned} P_x(had/em) &= E_{had/em} sin(\theta_{had/em}) cos(\phi) \\ P_y(had/em) &= E_{had/em} sin(\theta_{had/em}) sin(\phi) \\ P_z(had/em) &= E_{had/em} cos(\theta_{had/em}) \\ (P_T)^2 &= (\sum P_x)^2 + (\sum P_y)^2 \end{aligned} \tag{6.3}$$

where $\theta_{had/em}$ are the angles calculated with the correct Z vertex. The azimuthal angle ϕ is the same for the hadronic and electromagnetic tower compartments.

6.3.3 Effect of Single Tower Threshold

In the Midpoint algorithm all towers with a $P_T > 100$ MeV, within a radius $R = 0.7$ of the jet centroid, are included in the jet momentum. The non-jet momentum can contribute to this momentum in two ways: a non-jet tower above the threshold is just added to the jet momentum or a non-jet tower below the threshold can contribute if it overlaps with a jet tower and the combined P_T is above threshold. Instead of doing a full study by mixing jet events with minimum bias events, we compare the momentum in the $R = 0.7$ cone using three different single tower thresholds; 50 MeV, 100 MeV and 150 MeV. The mean number of towers in a midpoint jet is approximately 20 with a maximum ~ 50. We see in this study that the mean number of towers ($P_T^{Tower} > 50$ MeV) in a $R = 0.7$ cone in a minbias event is ~ 3.86, this tower occupancy decreases to 2.78 towers for a 100 MeV tower threshold and to 2.05 for a 150 MeV tower threshold. The corresponding change in the average P_T found in the cones is 0.96 GeV for the 50 MeV threshold and drops to 0.88 GeV and then to 0.80 GeV for the 100 MeV and 150 MeV thresholds respectively. Note that these numbers have no requirement on the number of Z vertices seen in the event.

6.4 Multiple Interaction and Underlying Event Subtraction

In the context of the full jet correction machinery, the corrected jet energy is given as:

$$P_T^{corr}(R) = (P_T^{raw}(R) \times f_{rel}(R) - UEM(R)) \times f_{abs} - UE(R) + OC(R), \quad (6.4)$$

where $P_T^{raw}(R)$ is the raw P_T of the jet. The relative correction (f_{rel}) is used to map the $0.7 < |\eta| < 0.1$ calorimeter response to the response of the central calorimeter. In the current analysis, only the central calorimetery is used so the relative corrections are not required. The absolute correction (f_{abs}) corrects for the energy from a hadron that is not sampled in the detector. The multiple interaction correction (UEM) removes contributions to the jet energy due to additional hard interactions in a single crossing. The underlying event correction UE removes the contribution to the jet energy from soft spectator interactions and beam remnants. The out of cone correction ($OC(R)$) corrects for energy lost out of the clustering cone by adding energy back in. All corrections depend on cone size (R).

6.5 Results

Here we sumarise the measurement of the underlying event energy and the multiple interaction energy. The correction that is applied in the inclusive analysis is based on the 100 MeV tower threshold measurement.

$NQ12Zv$	$\langle P_T \rangle$ (GeV)(50MeV)	$\langle P_T \rangle$ (GeV)(100MeV)	$\langle P_T \rangle$ (GeV)(150MeV)
0	0.268424 ± 0.0002	0.23546 ±0.00021	0.201907 ±0.00020
1	1.01558 ± 0.00038	0.93705 ±0.00037	0.847977 ±0.00036
2	2.00251 ± 0.00140	1.86343 ±0.0013	1.70014 ±0.0013
3	2.99476 ± 0.00512	2.80485 ±0.0050	2.57705 ±0.0049
4	3.97096 ± 0.01722	3.7401 ±0.016	3.45628 ±0.016
5	4.96319 ± 0.04768	4.70266 ±0.047	4.37765 ±0.046
6	5.61756 ± 0.10616	5.33413 ±0.105	4.9803 ±0.10
7	6.56919 ± 0.23632	6.27037 ±0.234	5.87383 ±0.23
8	7.90464 ± 0.49985	7.57915 ±0.497	7.15621 ±0.49
Slope	0.987 ± 0.001	0.928 ± 0.001	0.855 ± 0.001

Table 6.1: *The $NQ12Zv = 1$ row is a measure of the underlying event for the three tower thresholds. The slope of the linear fit to $\langle P_T \rangle$ versus $NQ12Zv$ is the multiple interaction correction.*

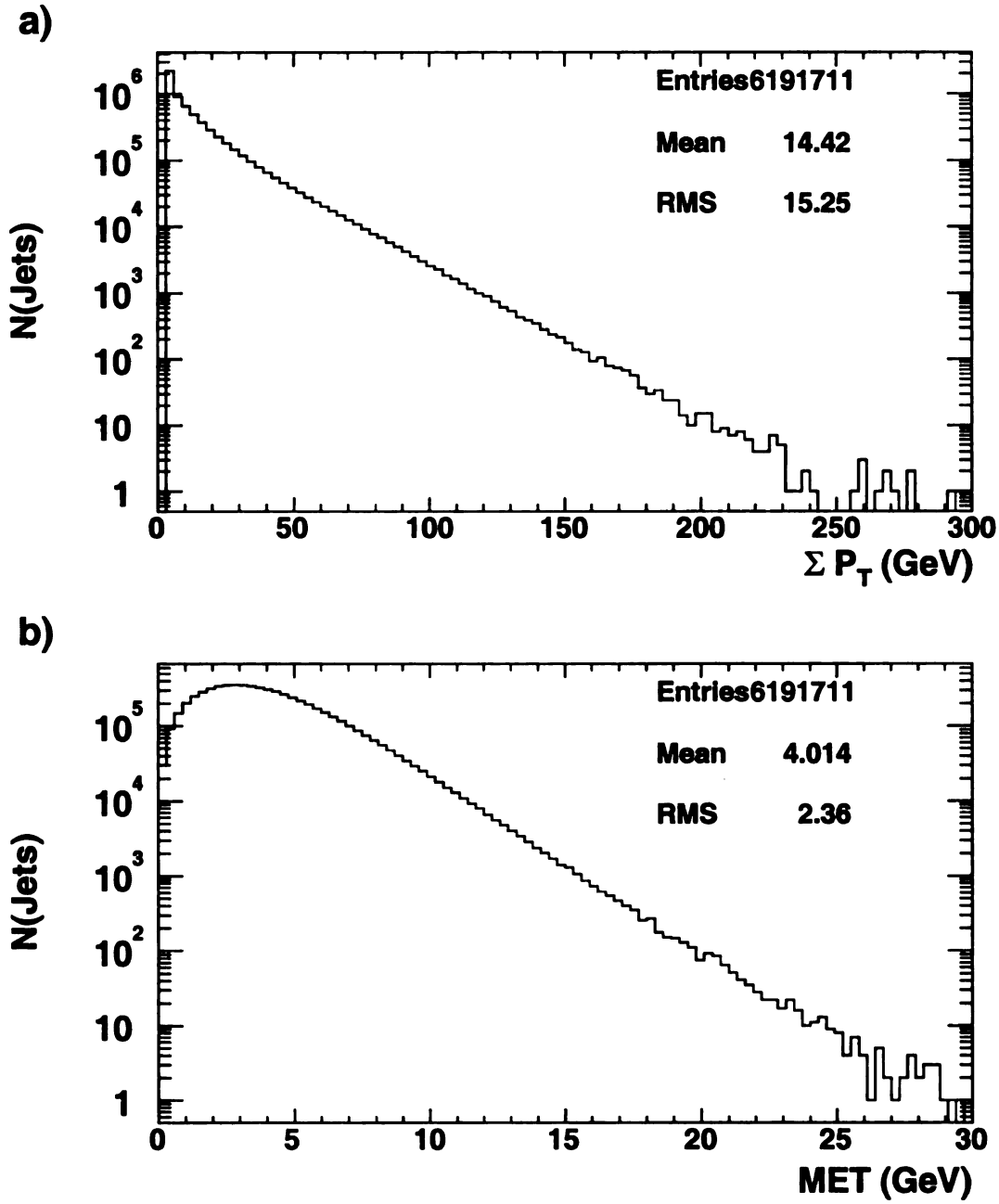

Figure 6.1: *Event properties of the minimum bias sample: a) ΣP_T, b) Missing E_T, c) leading jet P_T and d) the jet multiplicity. The events are required to pass a Z_{vertex}, missing E_T and lead jet P_T cut.*

figure 6.1 continued.

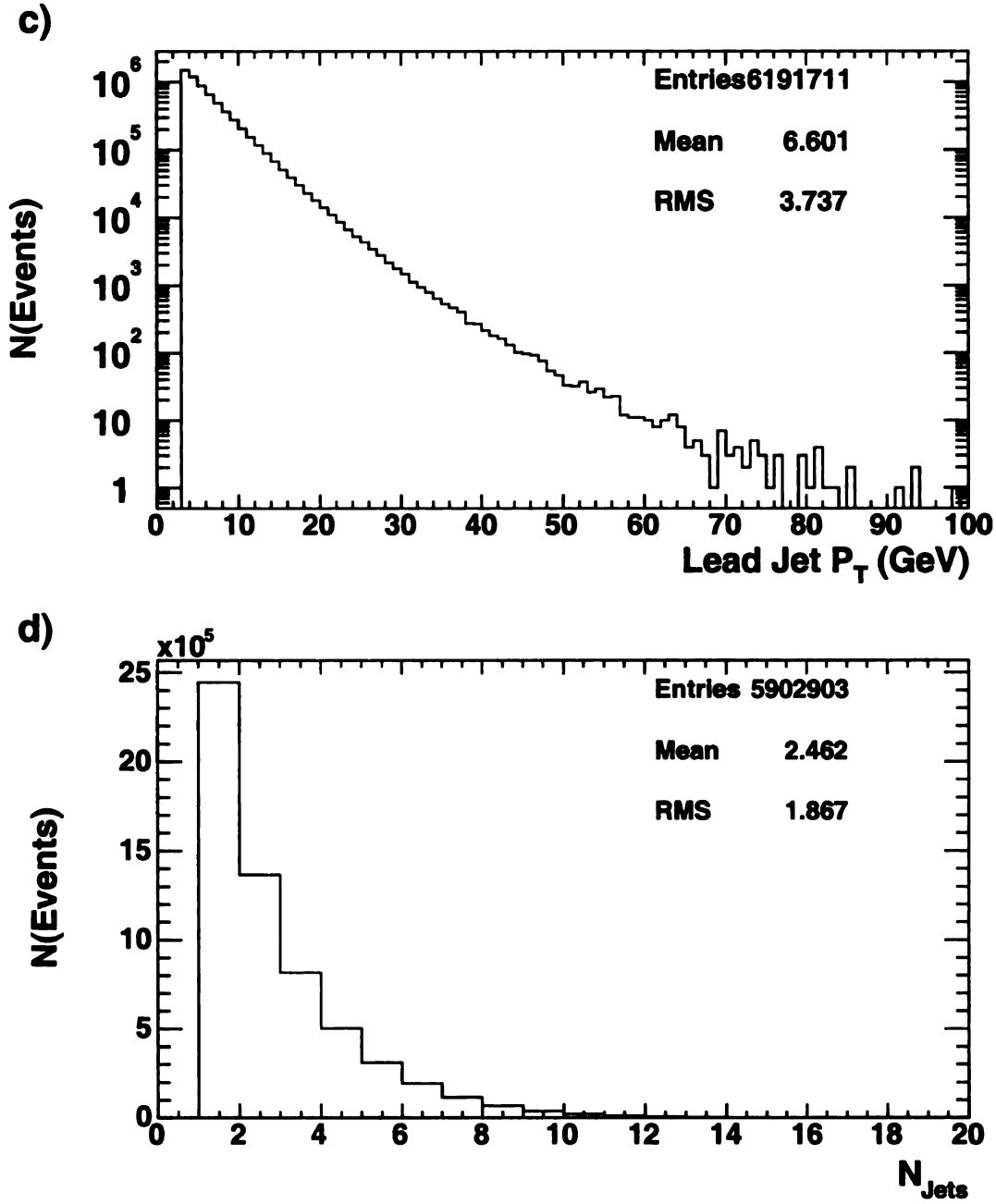

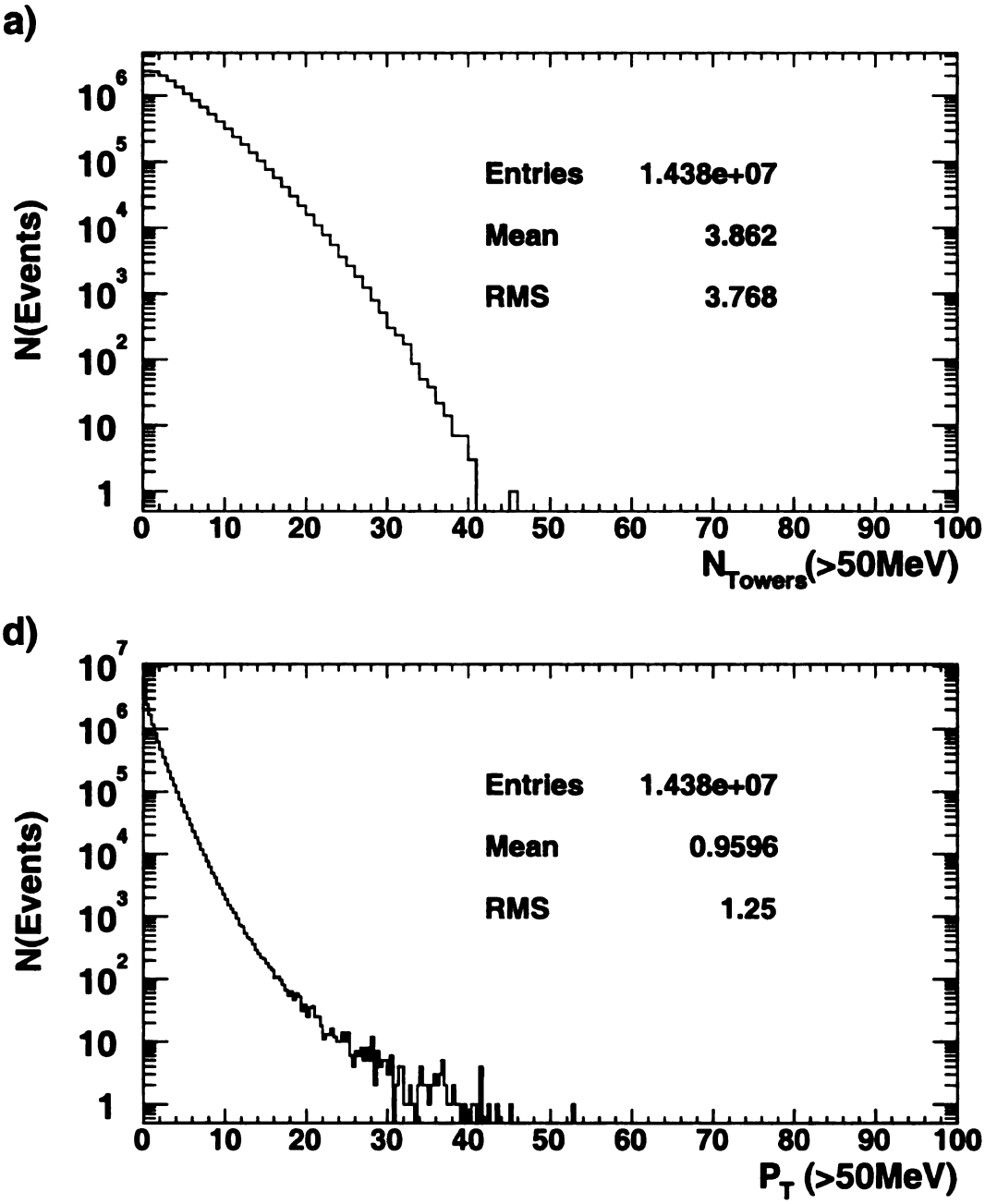

Figure 6.2: *Effect of tower threshold on the minimum bias momentum (d-e) and number of towers (a-c) in a random cone. Increasing the single tower threshold from 50 to 100 MeV then to 150 MeV gives a decrease in $\langle P_T \rangle$ in the random cone of 75 MeV and 85 MeV respectively.*

figure 6.2 continued.

b)

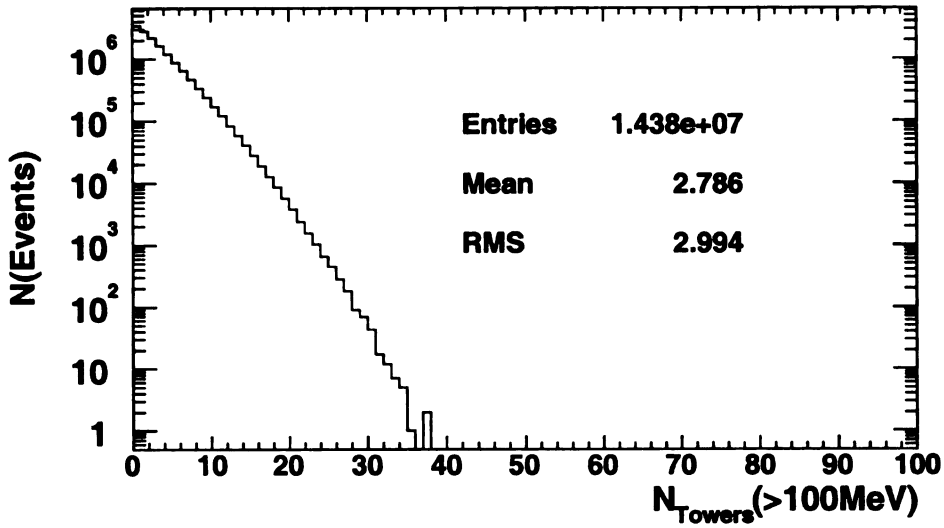

e)

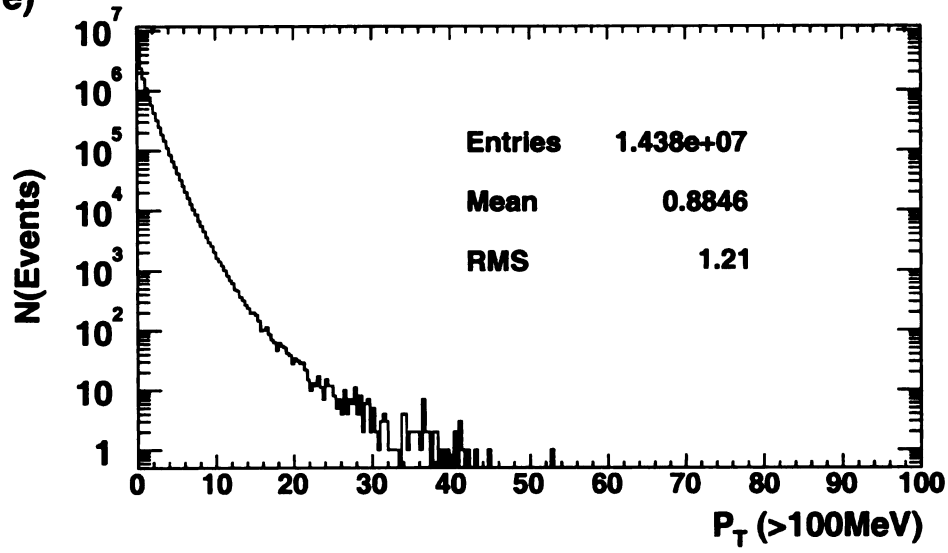

figure 6.2 continued.

c)

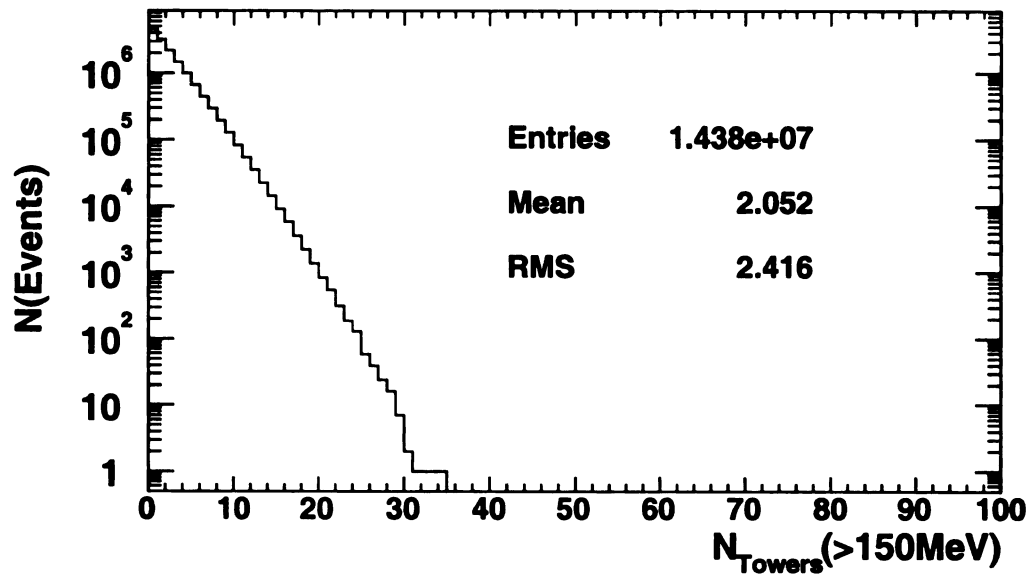

f)

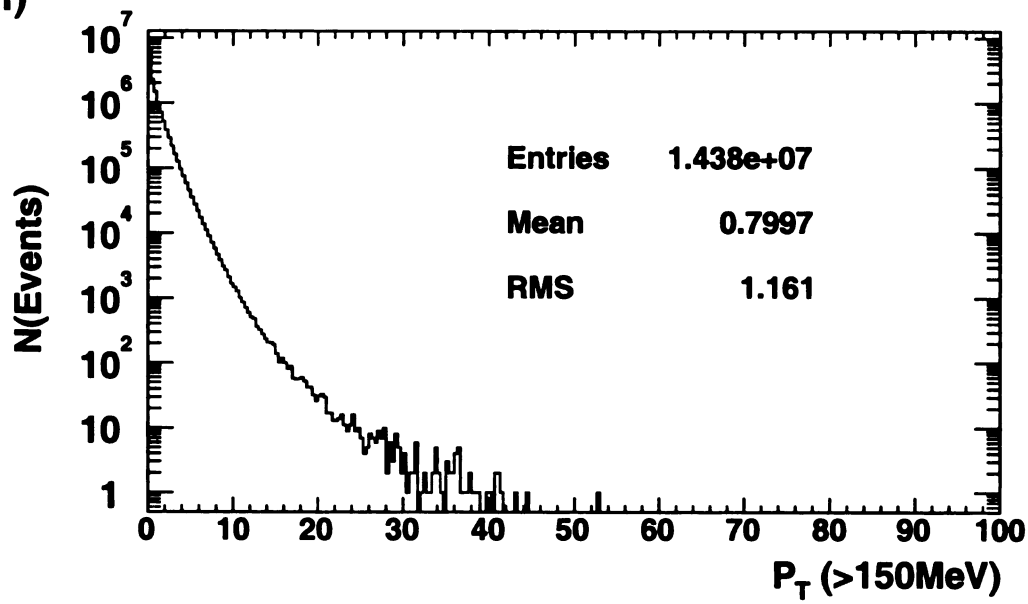

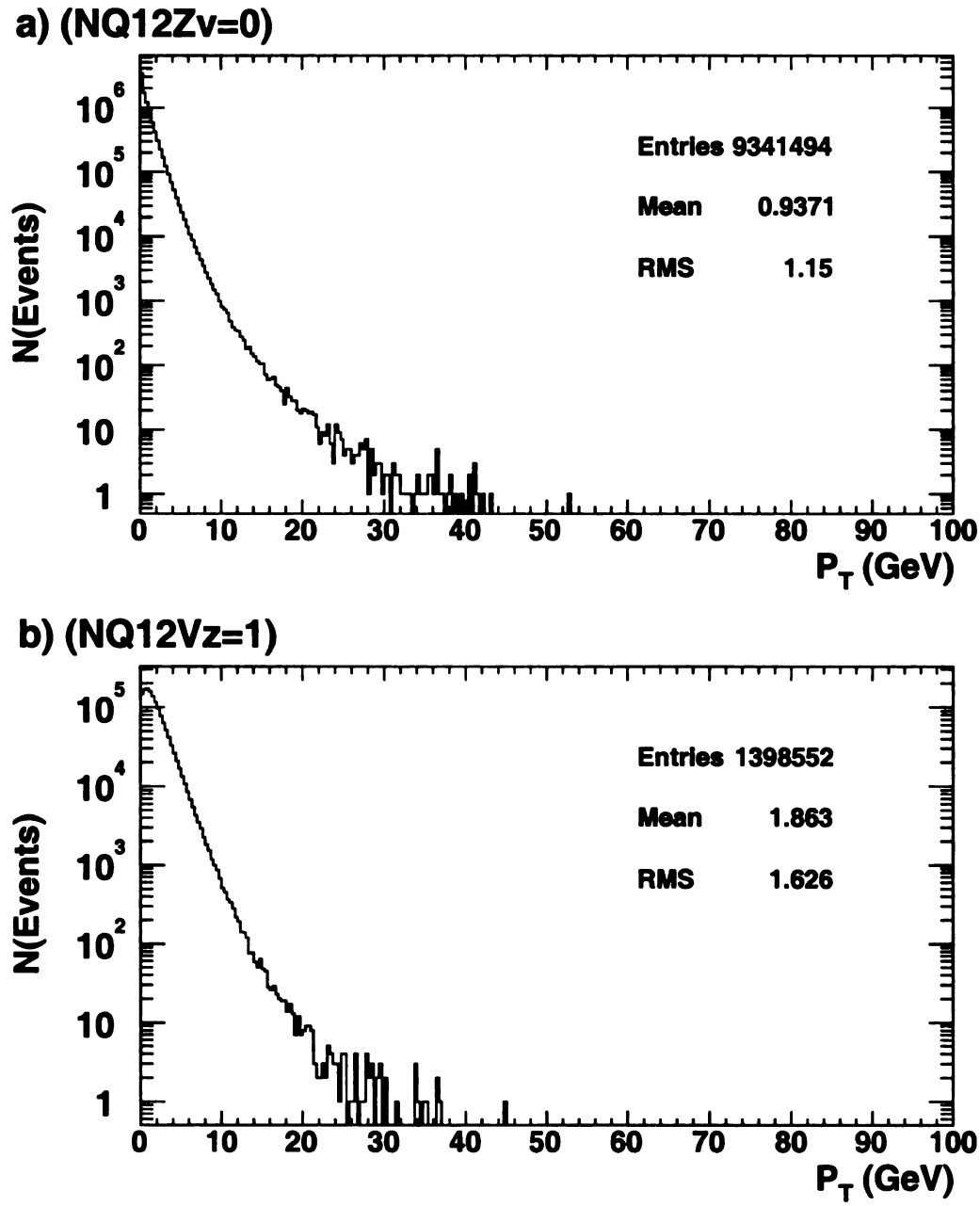

Figure 6.3: *P_T in random cone $R = 0.7$ with quality 12 vertex multiplicity requirements (tower threshold 100 MeV).*

figure 6.3 continued.

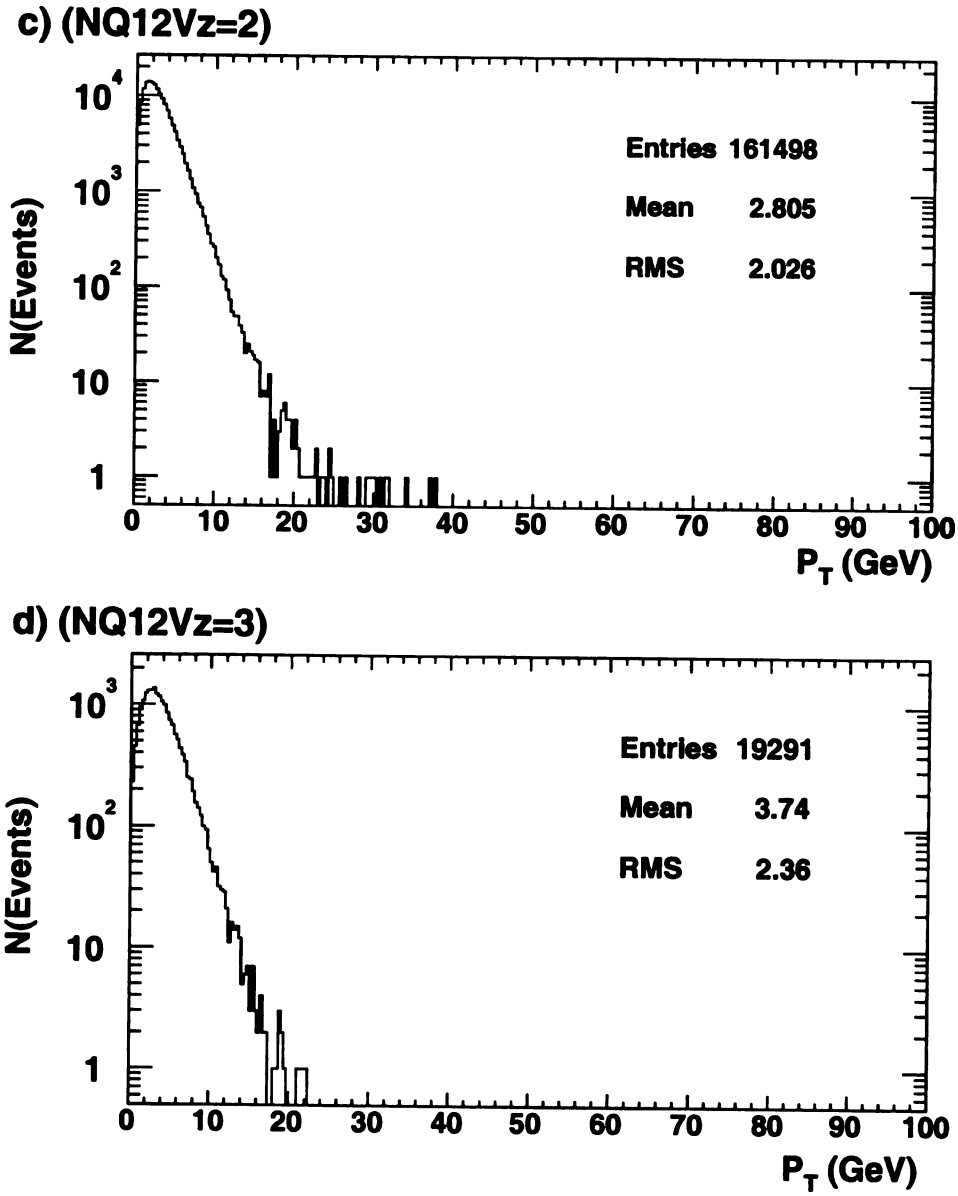

figure 6.3 continued.

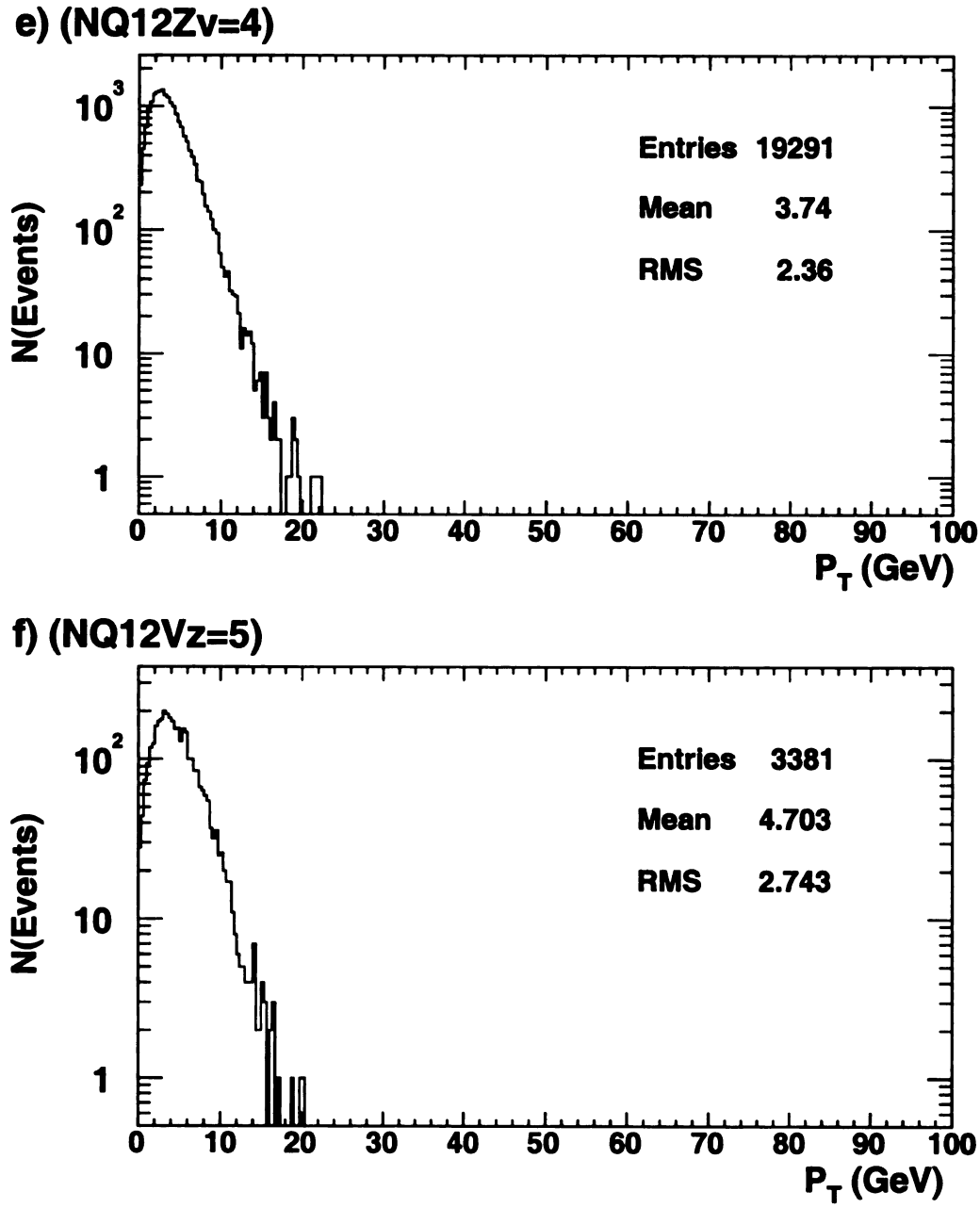

figure 6.3 continued.

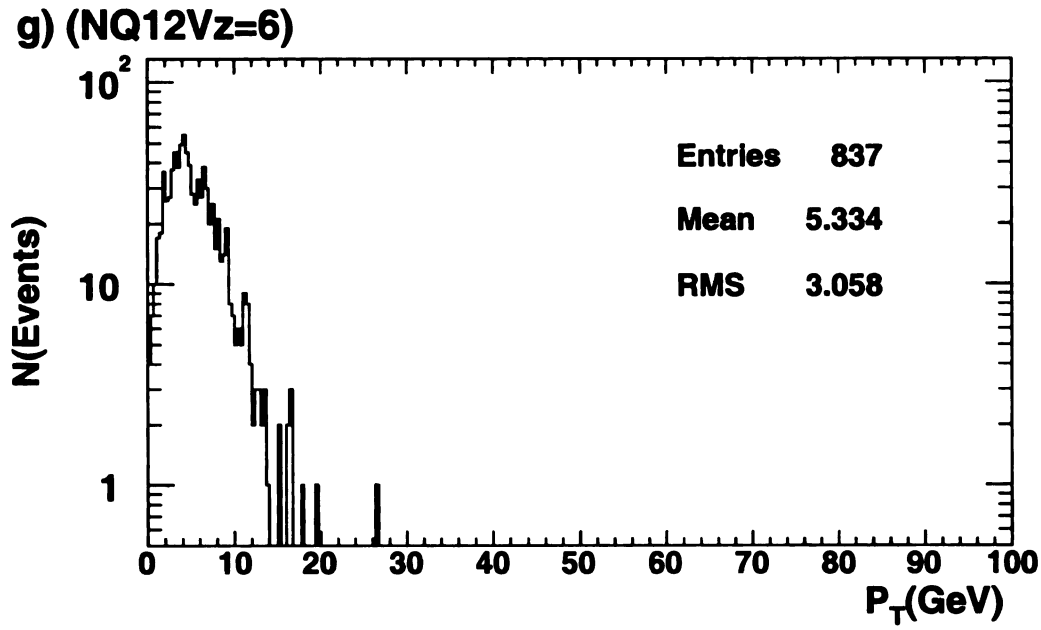

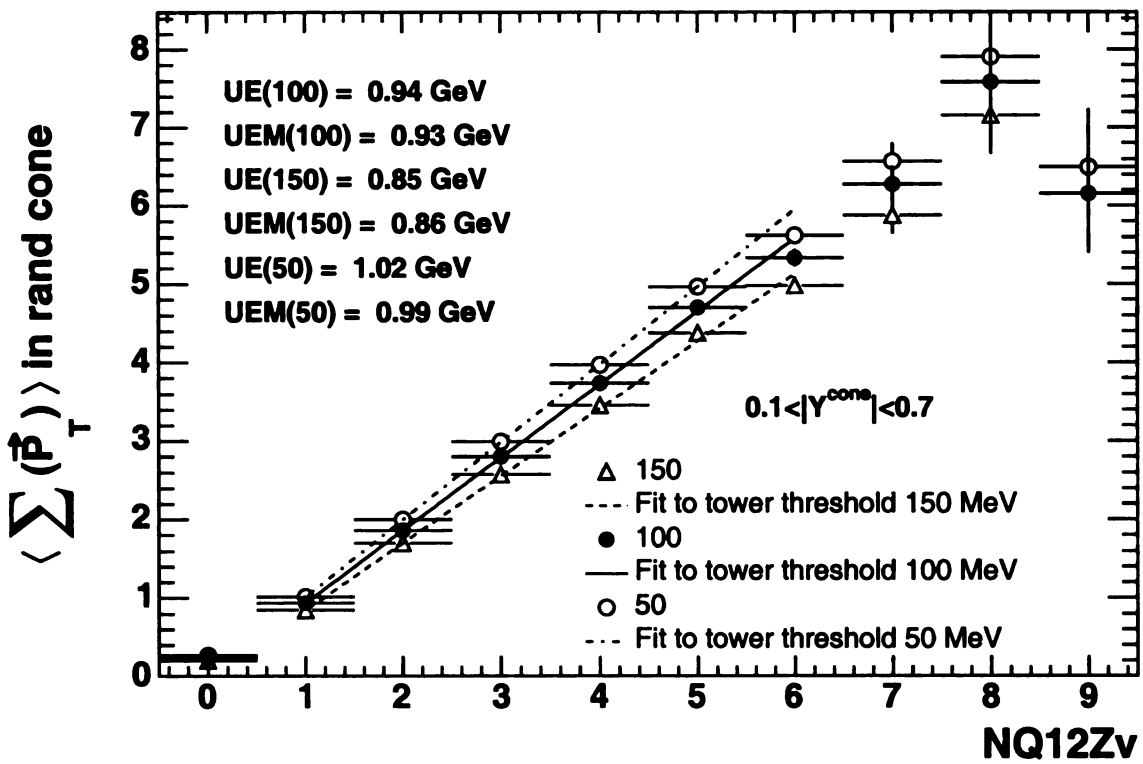

Figure 6.4: *Linear fit to minimum bias momentum versus number of quality 12 vertices for tower thresholds of 50, 100 and 150 MeV .*

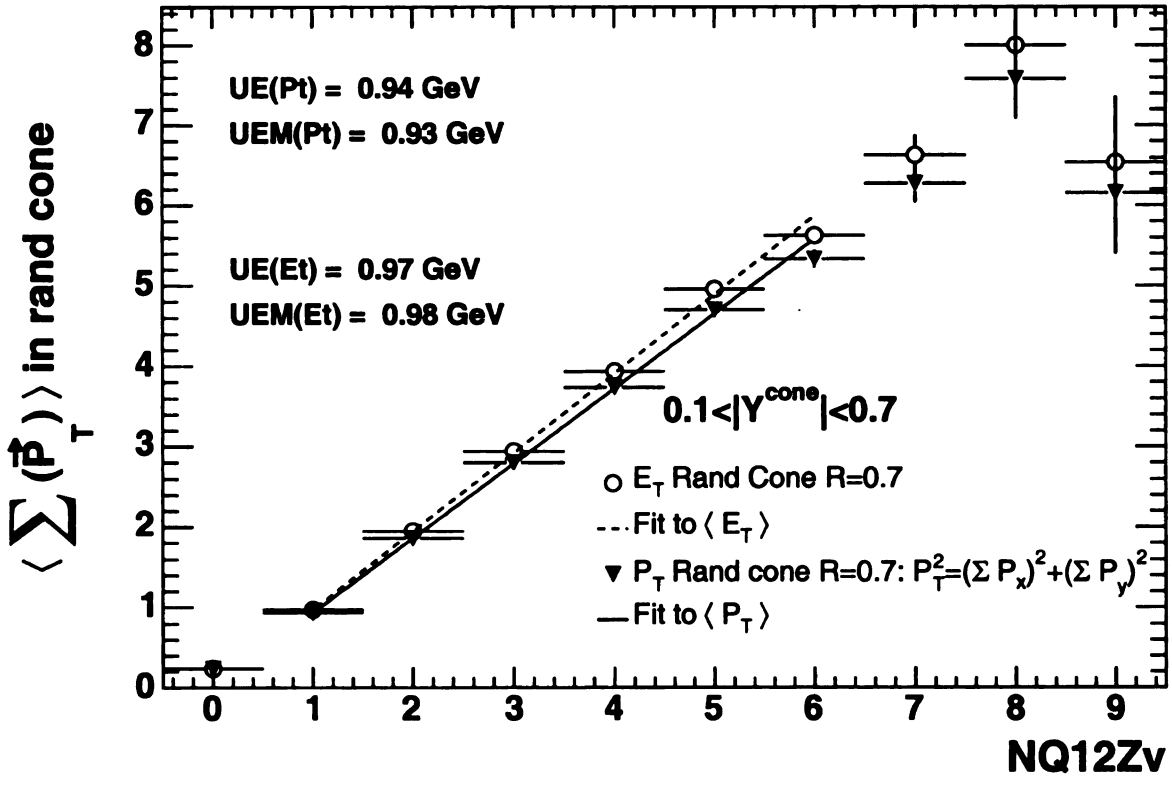

Figure 6.5: *Linear fit to minimum bias momentum and energy versus number of quality 12 vertices for tower threshold of 100 MeV.*

6.5.1 Corrections Versus Instantaneous Luminosity

In this section we recalculate the UE and UEM corrections in 6 bins of instantaneous luminosity and check that the number of observed vertices is directly proportional to the instantaneous luminosity. The proportionality of the number of quality 12 vertices to the instantaneous luminosity is consistent with the assumption that these vertices characterise the number of interactions observed in a given event. This is true when the number of vertices in the event is less than 4-5; above this there may be a problem with fake rate. The jet samples are dominated by events with ≤ 2 vertices so any non-linearity seen with a large number of vertices in an event should not effect the cross section correction. We also observe that there is only a very weak dependence of the correction factors on the instantaneous luminosity.

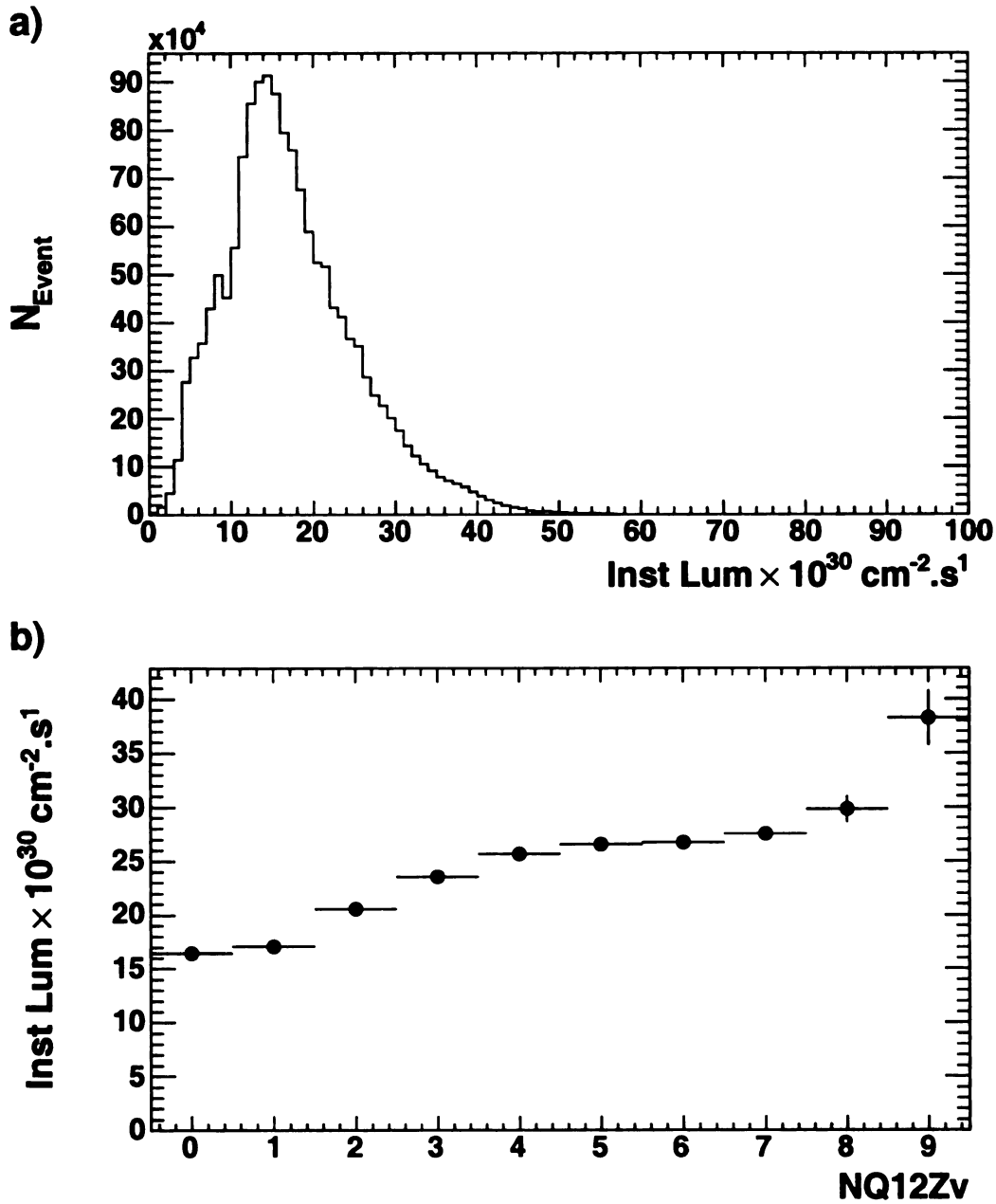

Figure 6.6: *a) Instantaneous luminosity for the min bias sample for the same running period as the jet triggers used in the cross section analysis. b) Instantaneous luminosity as a function of number of quality 12 vertices. c) Average number of towers in a random cone $R = 0.7$ as a function of the instantaneous luminosity and d) average P_T in a random cone $R = 0.7$ as a function of the instantaneous luminosity.*

figure 6.6 continued.

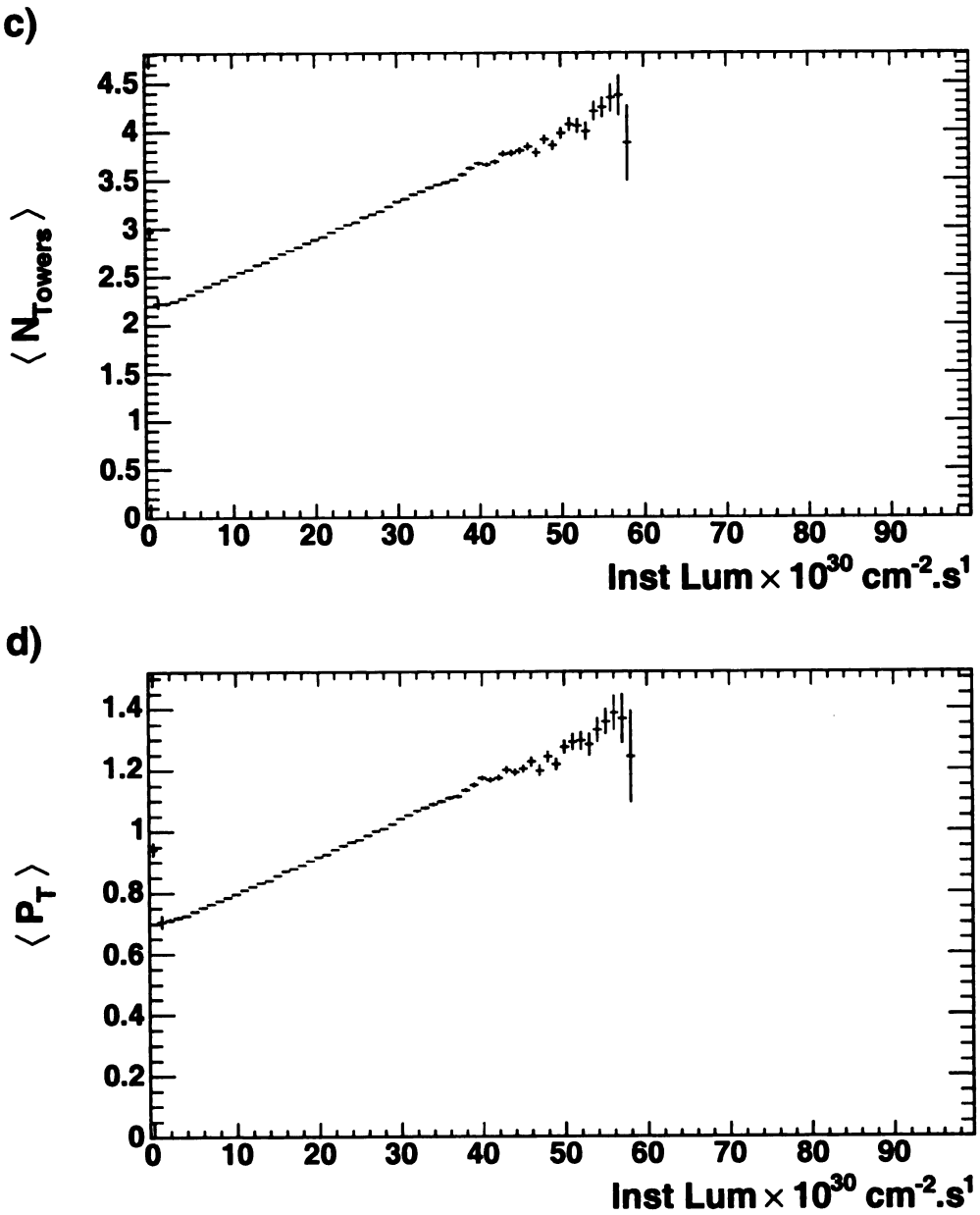

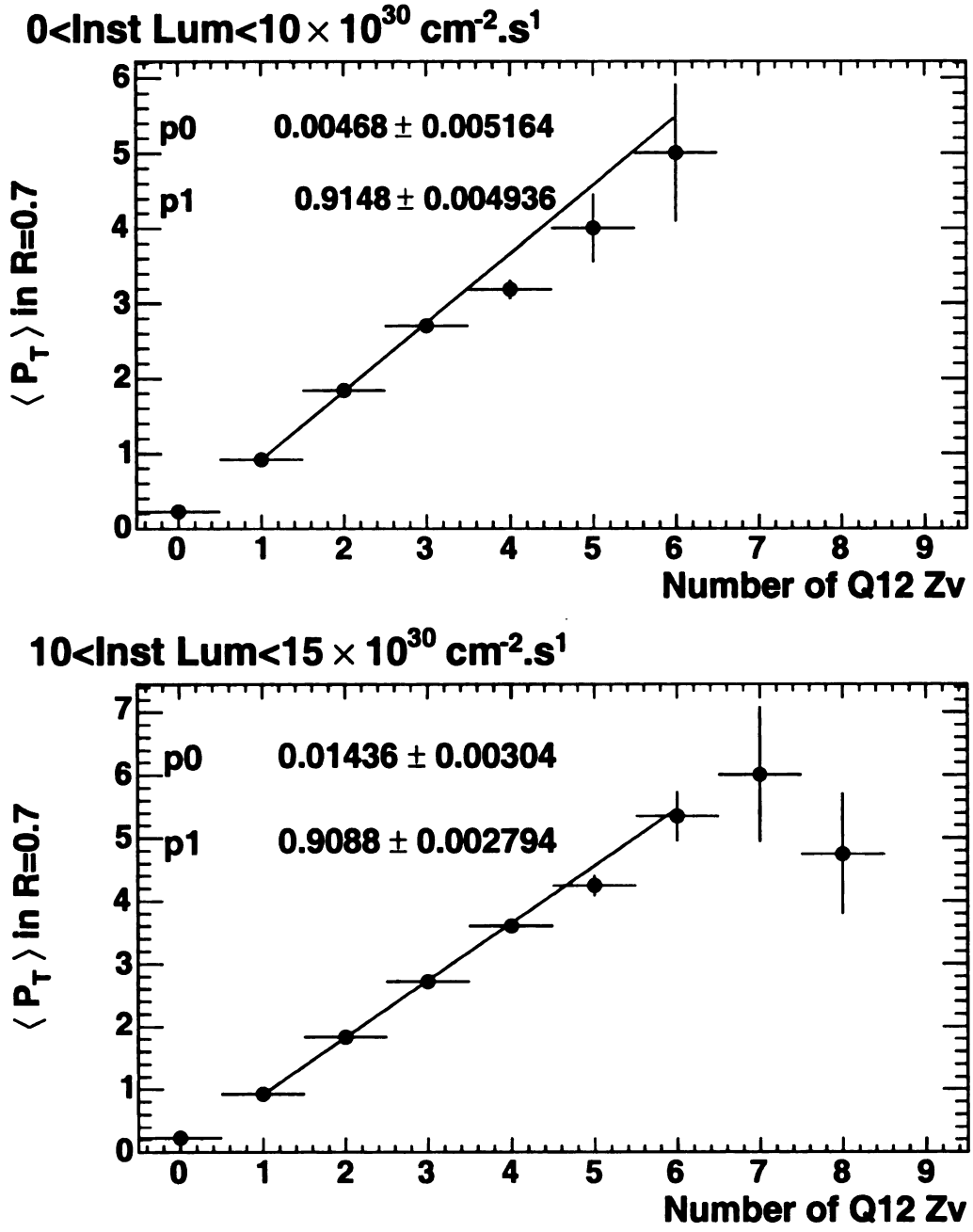

Figure 6.7: *Minimum bias energy in a random cone of* $R = 0.7$ *(*$P_{Tower} > 100$ *MeV) as a function of number of quality 12 vertices. Fit is to* $p_0 + p_1 \times NQ12Vz$*. The slope gives the multiple interation correction. The fits are done in 6 bins of instantaneous luminosity, see table for details.*

Figure 6.7 continued.

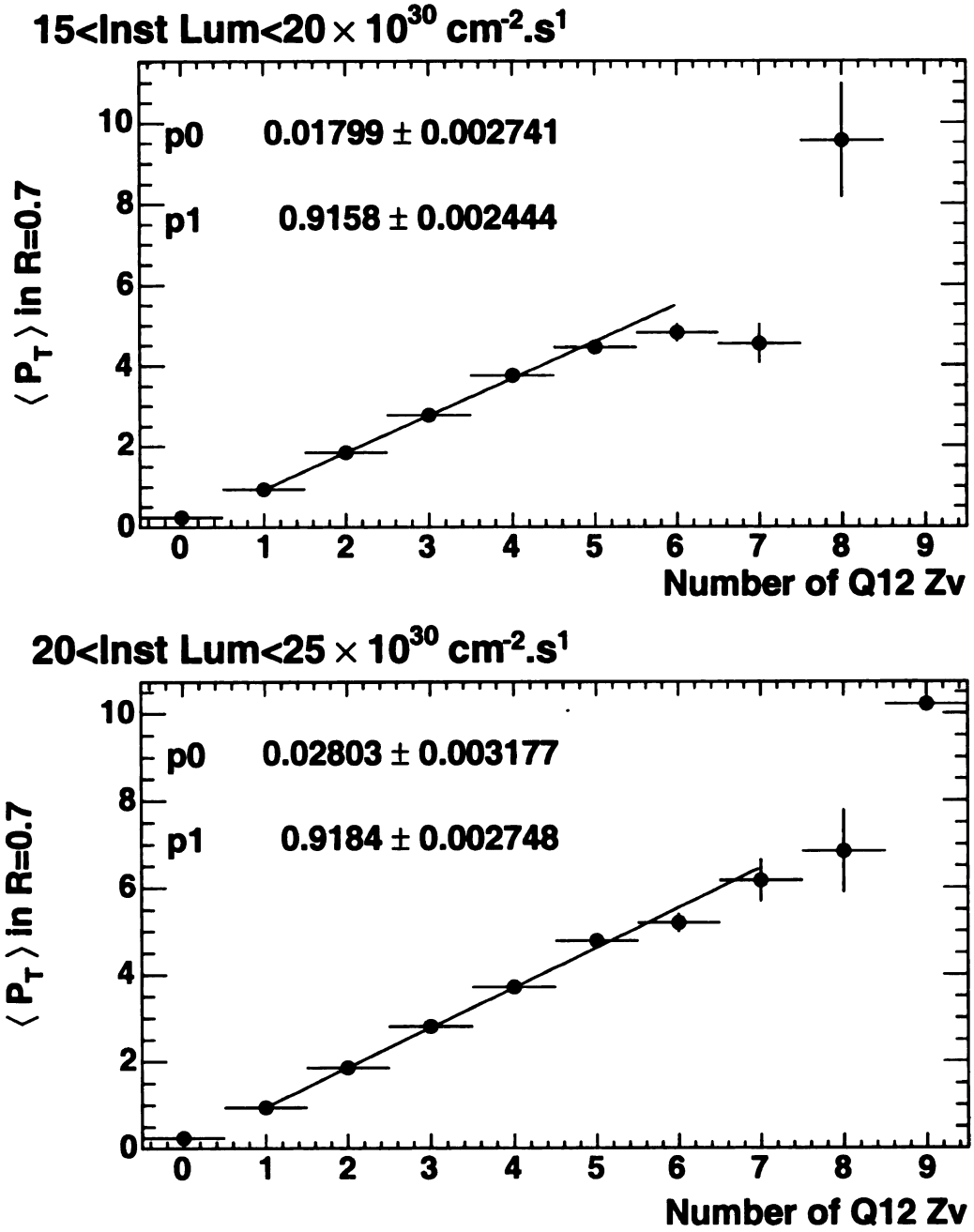

Figure 6.7 continued.

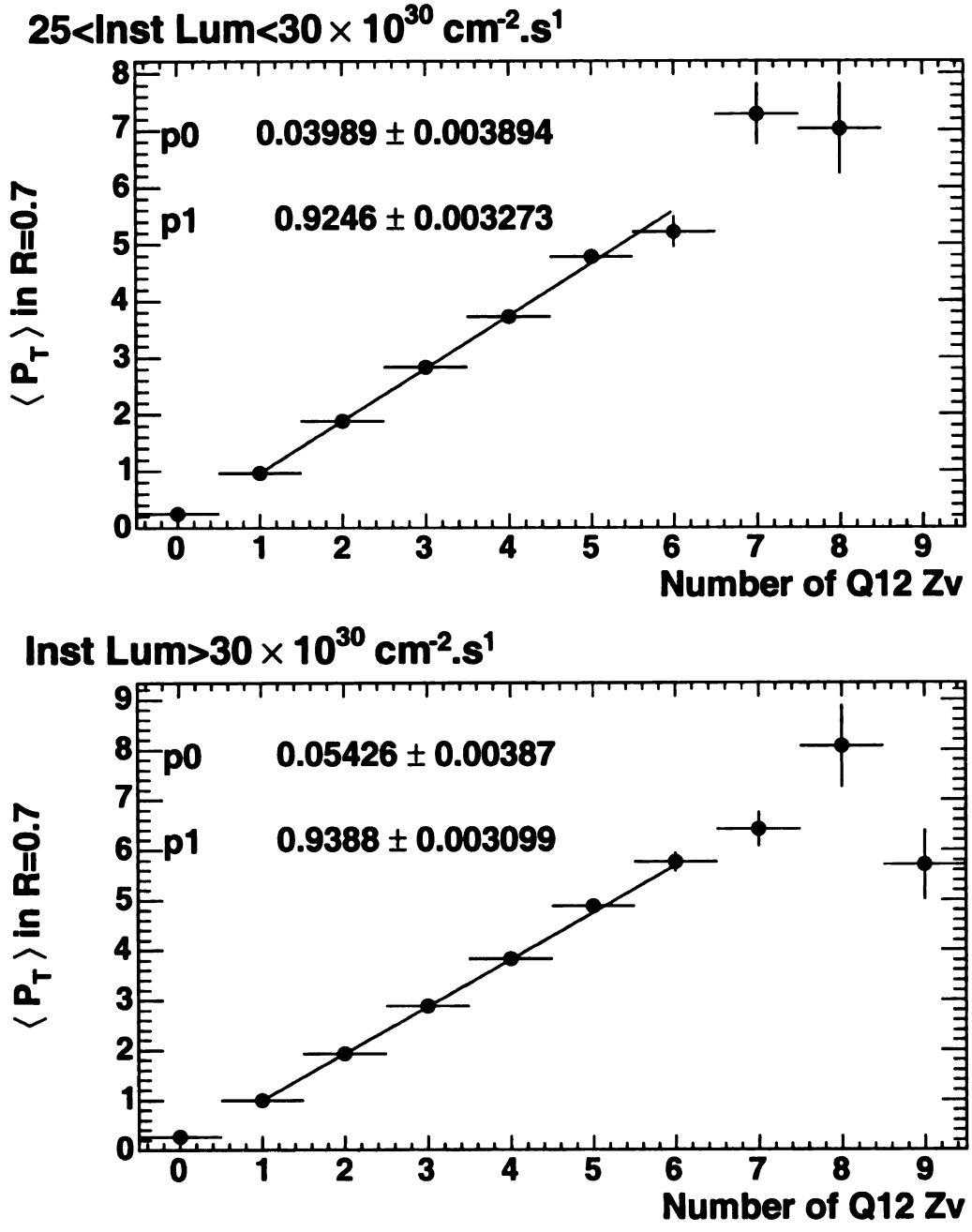

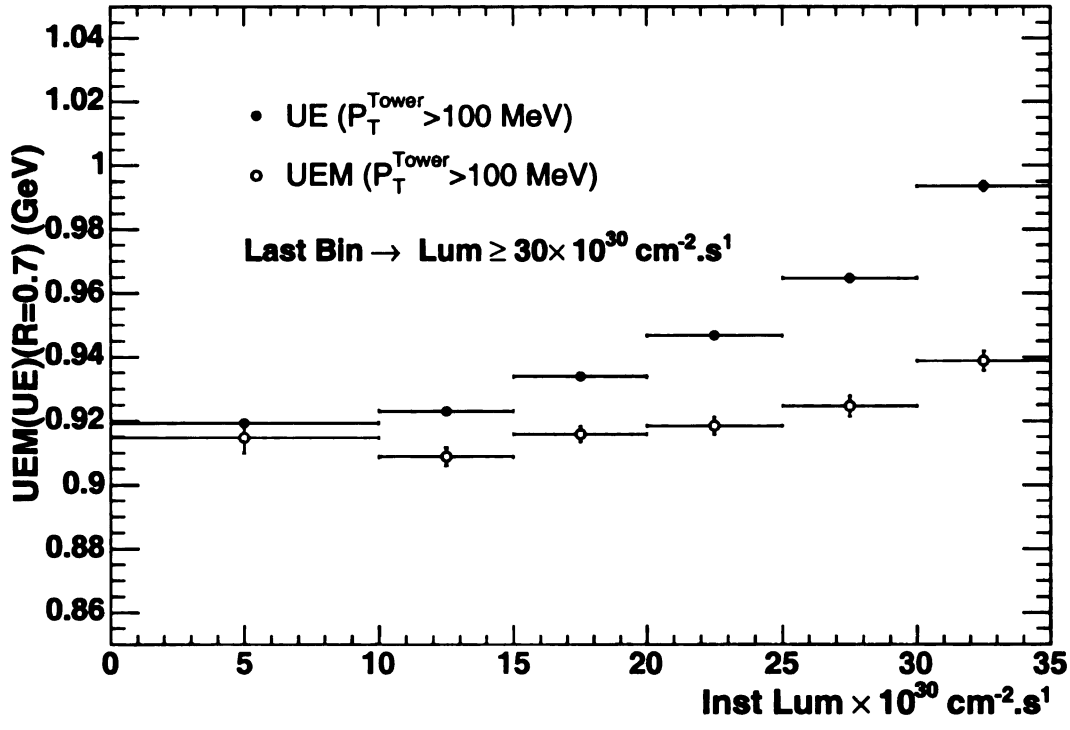

Figure 6.8: *Multiple interaction correction and underlying event as a function of the instantaneous luminosity. We see a weak dependance on the luminosity. The effect of the luminosity dependence is accounted for in the systematic assigned to the multiple interaction correction (see chapter 12).*

6.5.2 Instantaneous Luminosity & Number of Quality 12 Vertices in Jet Samples

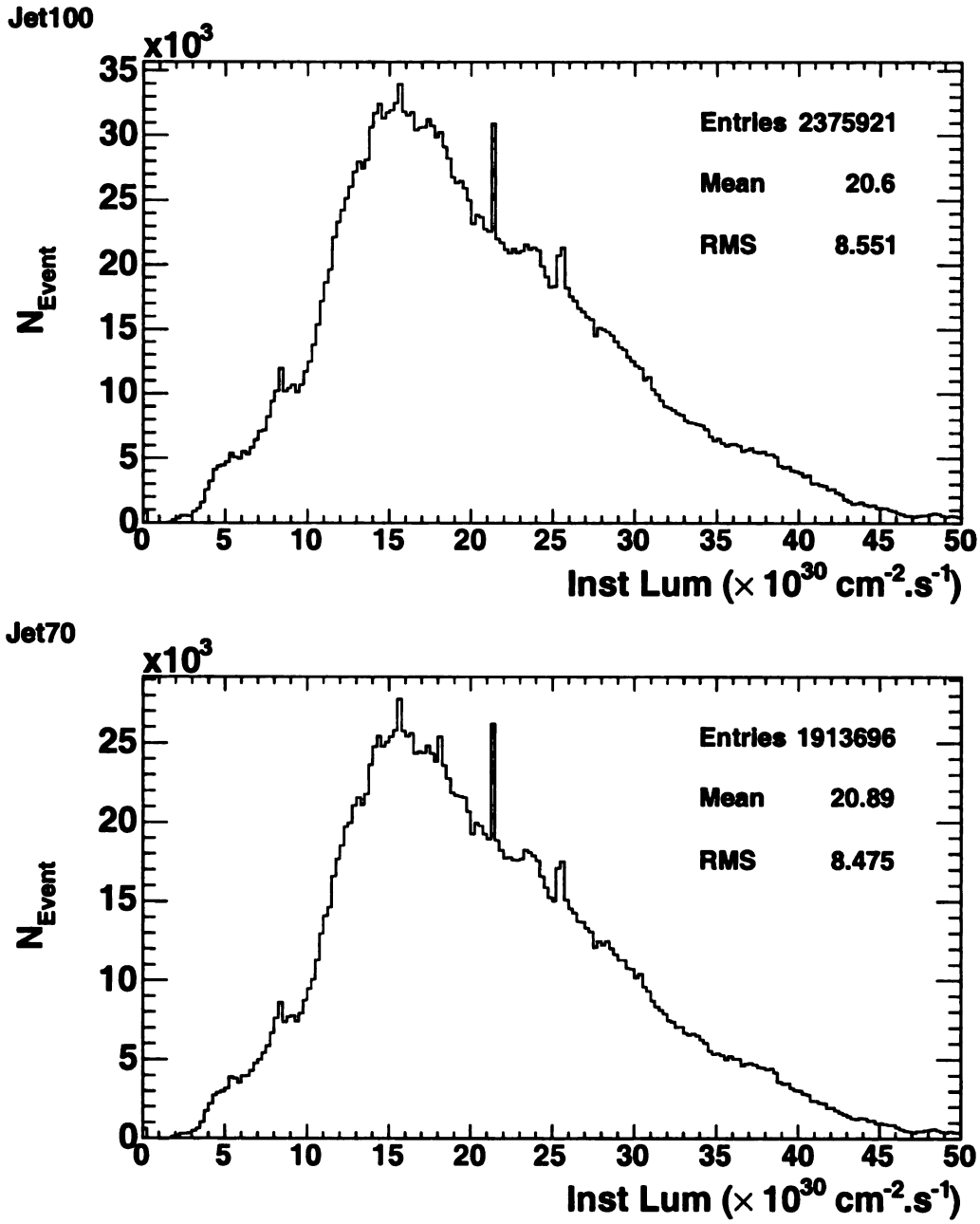

Figure 6.9: *Instantaneous Luminosity of the jet trigger samples. These distributions are consistent with the corresponding minimum bias distribution that was used to determine the multiple interaction correction.*

Figure 6.9 continued.

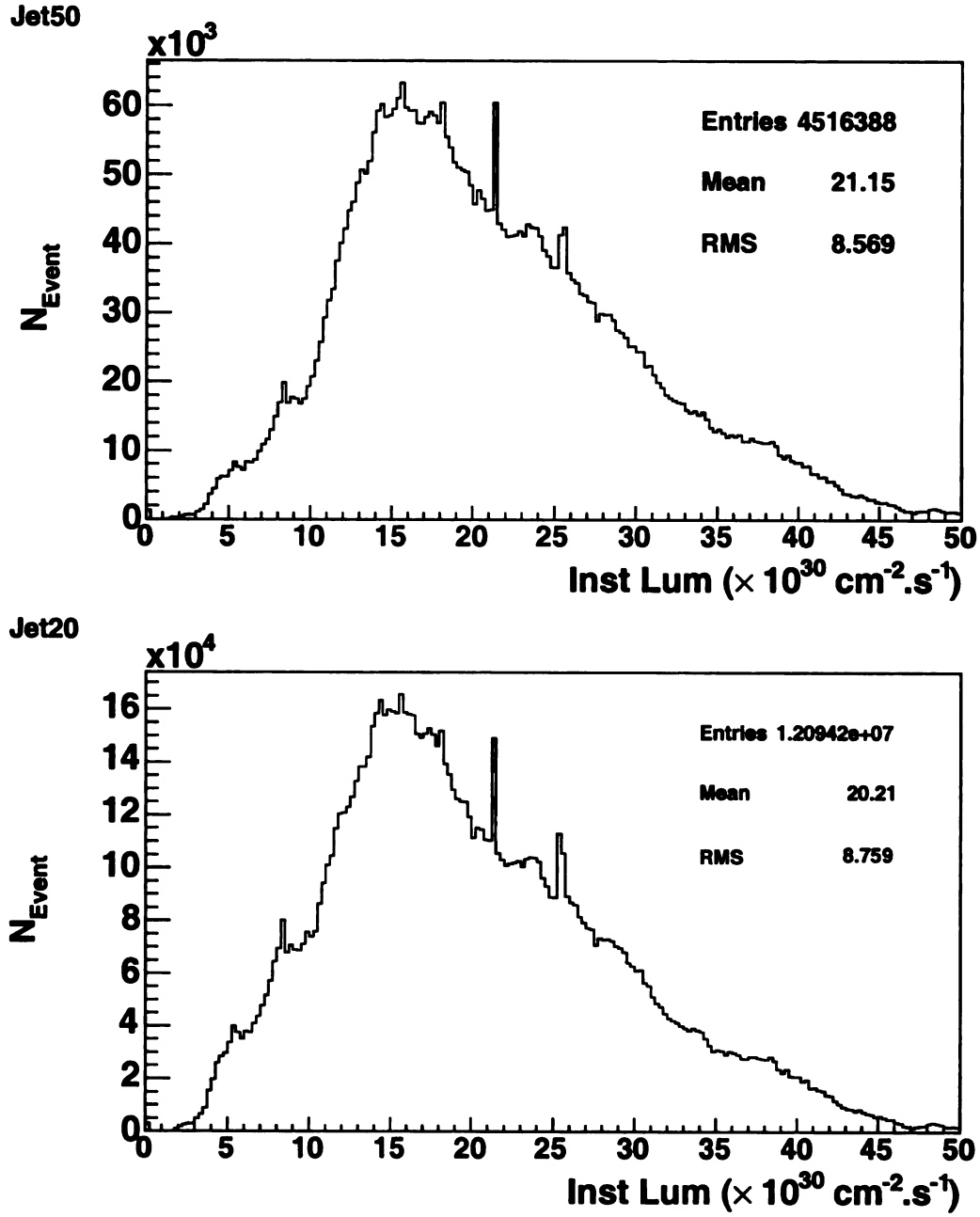

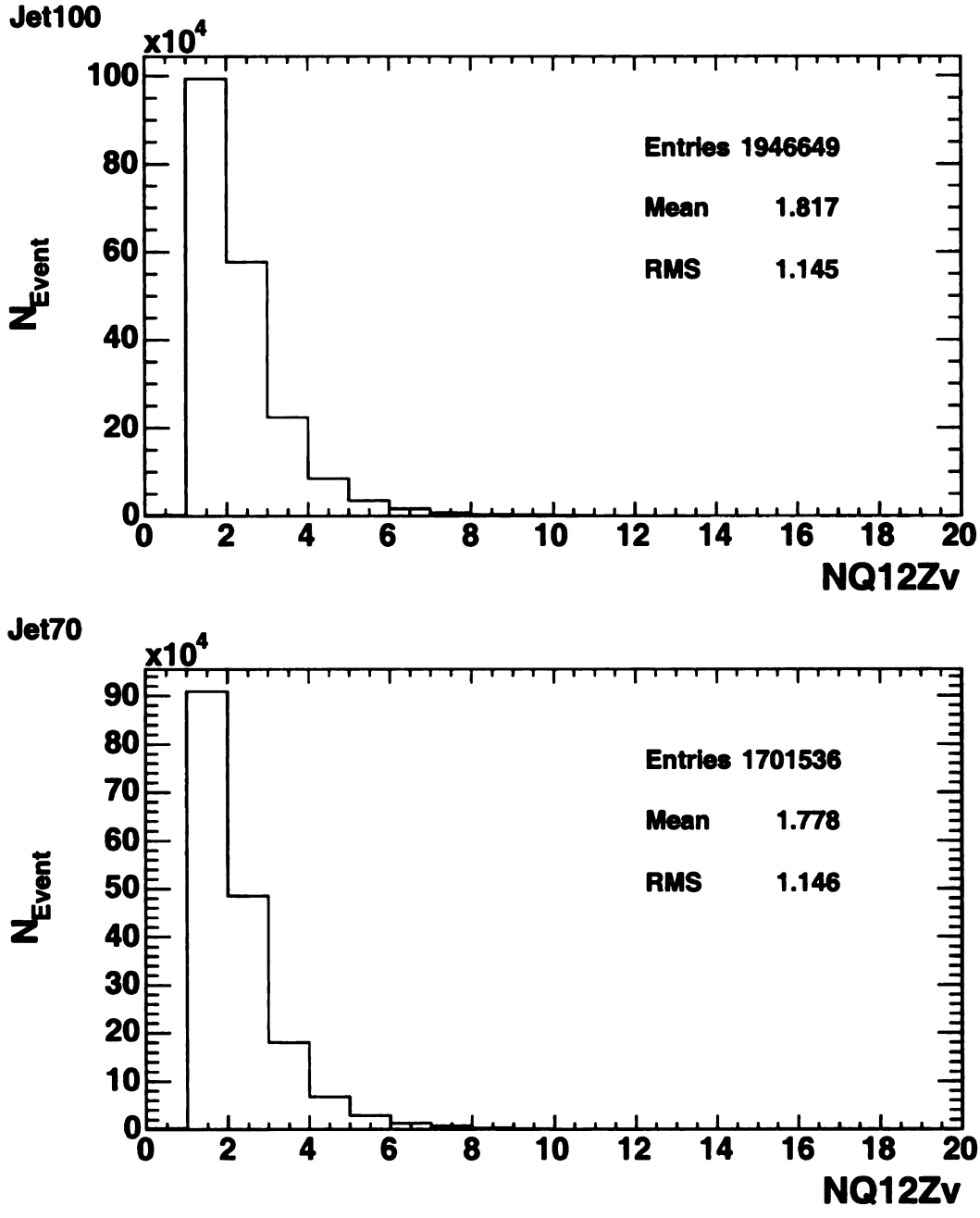

Figure 6.10: *Number of vertices per event in the jet samples and minbias sample. The jet samples are dominated by NQ12Zv of 1 and 2. So any non-linearity of the correction correction quantity ($\langle P_T \rangle$ versus NQ12Zv) should not affect the corrected cross section.*

figure 6.10 continued.

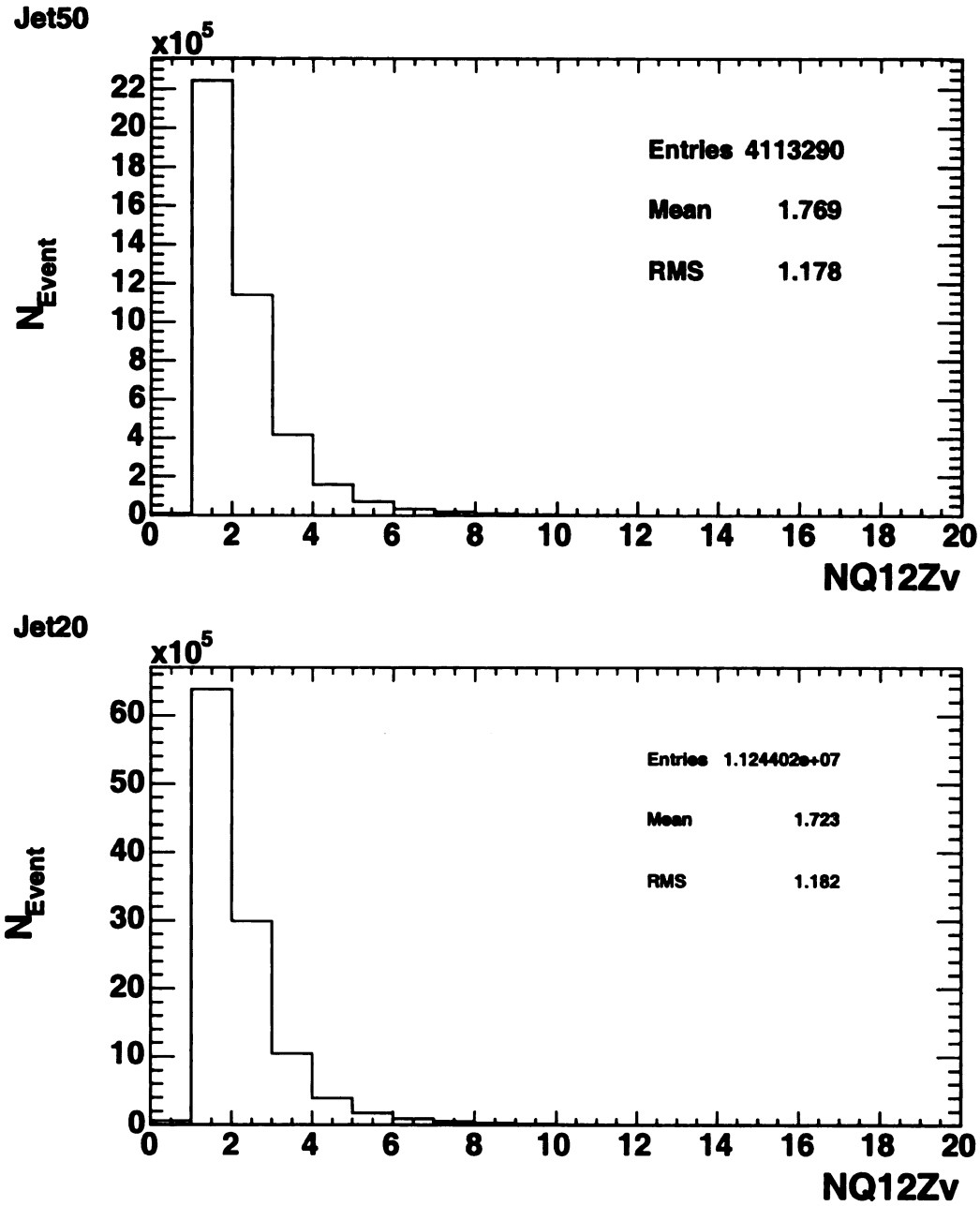

figure 6.10 continued.

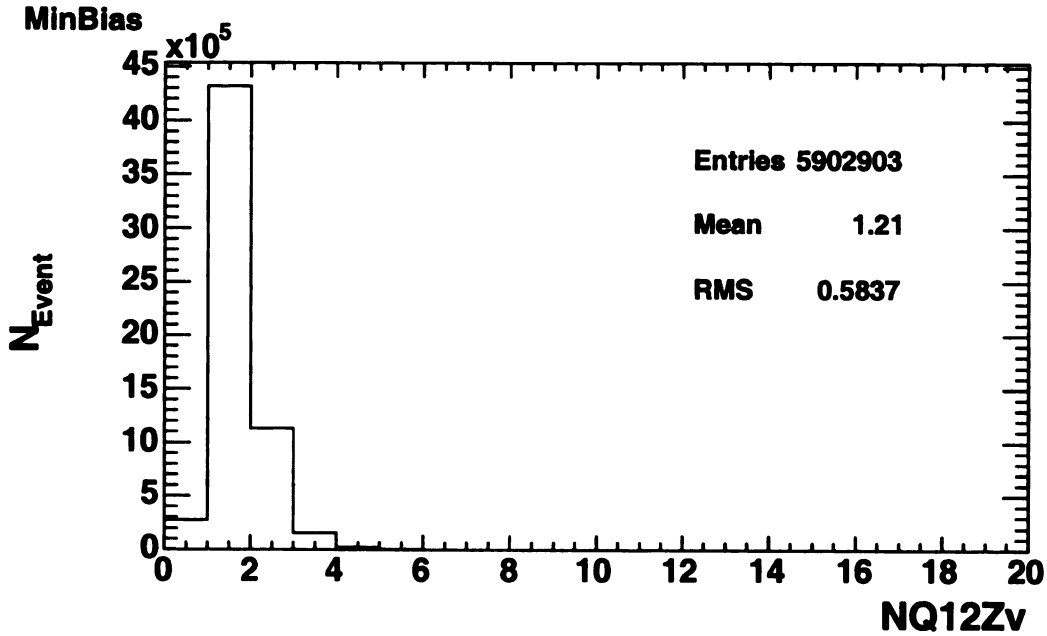

6.6 90^o Transverse Momentum (P_T^{90}) in Jet Events

For each event, the transverse momentum and the number of towers in a cone $R = 0.7$ centered at $\eta = \eta^{jet1}$, $\phi = \phi^{jet1} \pm 90^o$ is calculated. We use the same two tower thresholds as in the previous sections (50 and 100 MeV). Here we still use the minimum bias sample and select a "jet sample" from it by requiring that an event has a central jet with $P_T^{Jet} > 5$ GeV. This sub-sample of the min bias data is used to study the P_T^{90} in the low energy jet events. The 90^o cones includes energy from (a) jet activity, (b) energy from soft interactions from spectator partons and (c) additional interactions occuring in the same bunch crossing. In order to isolate the contribution from the jet activity we consider the $\phi + 90^o$ and the $\phi - 90^o$ cones. The difference of these cones is related to the jet activity [33]. We wish to compare the P_T^{90} of the "min-cone" with the underlying event found from the full minimum bias sample using the random cone study.

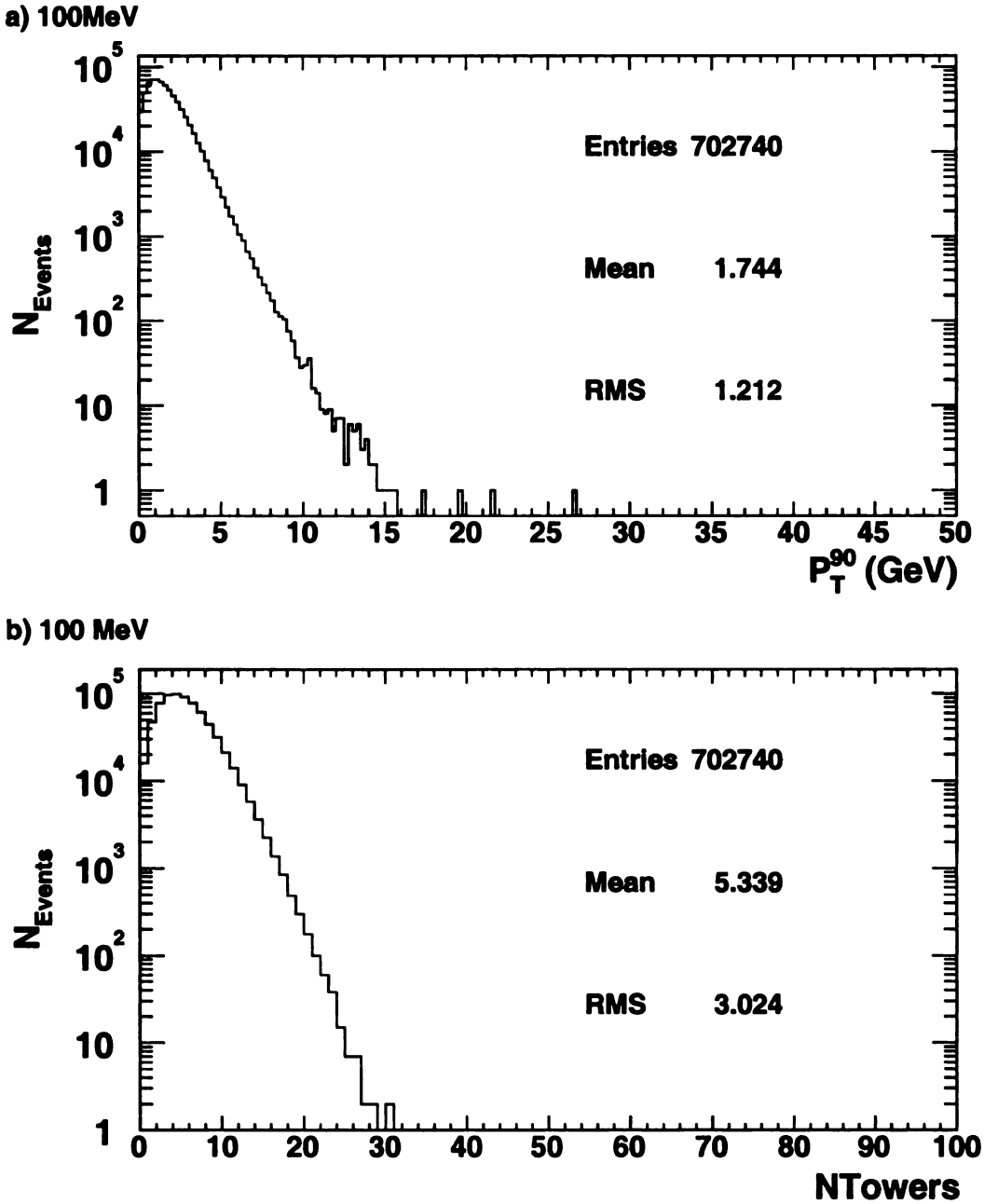

Figure 6.11: P_T^{90} *and number of towers for 50-100 MeV tower thresholds*

figure 6.11 continued.

c) 50 MeV

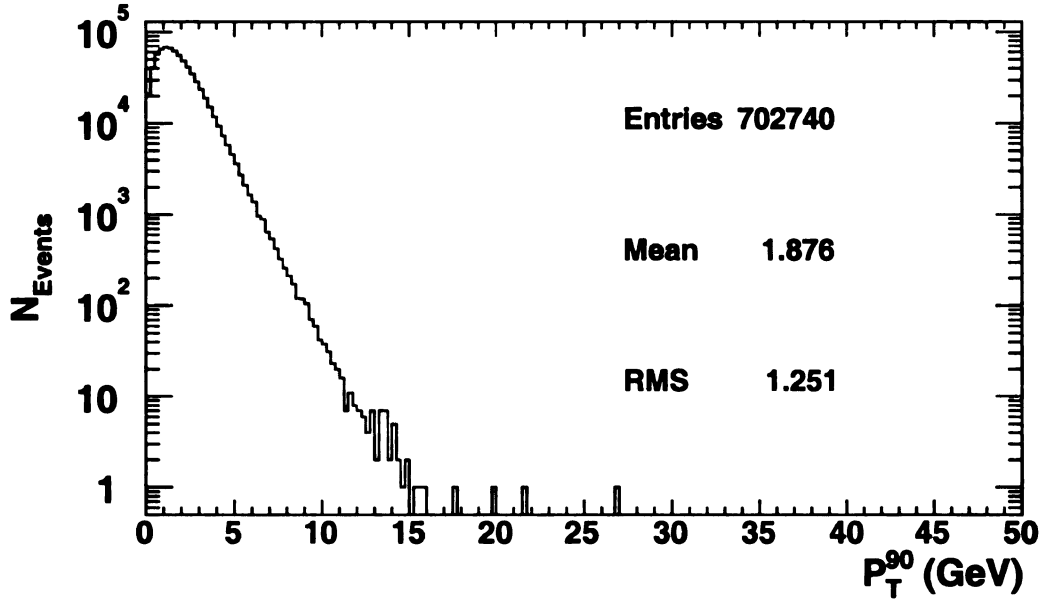

d) 50 MeV

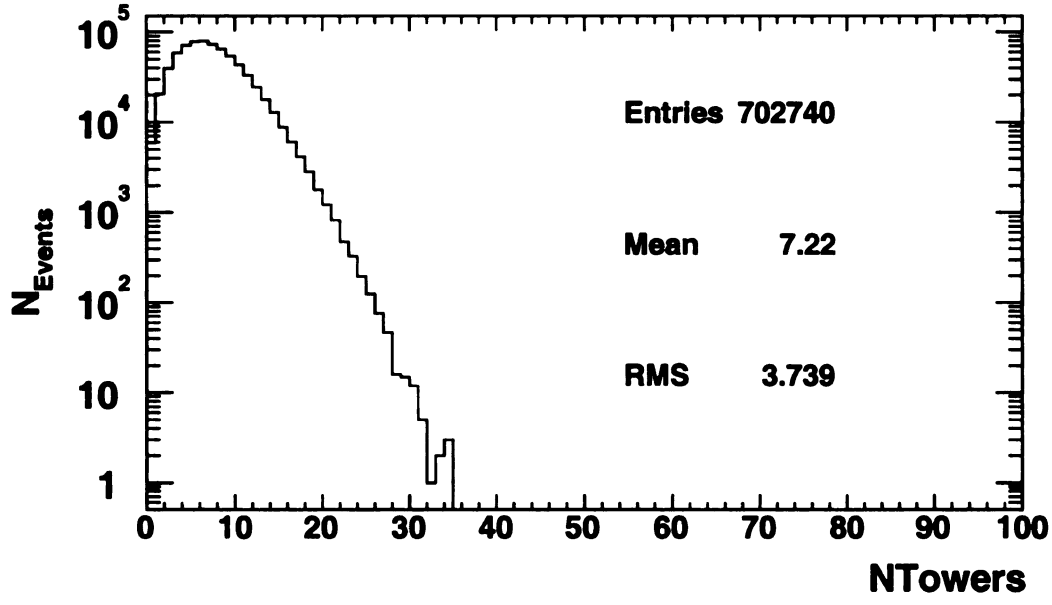

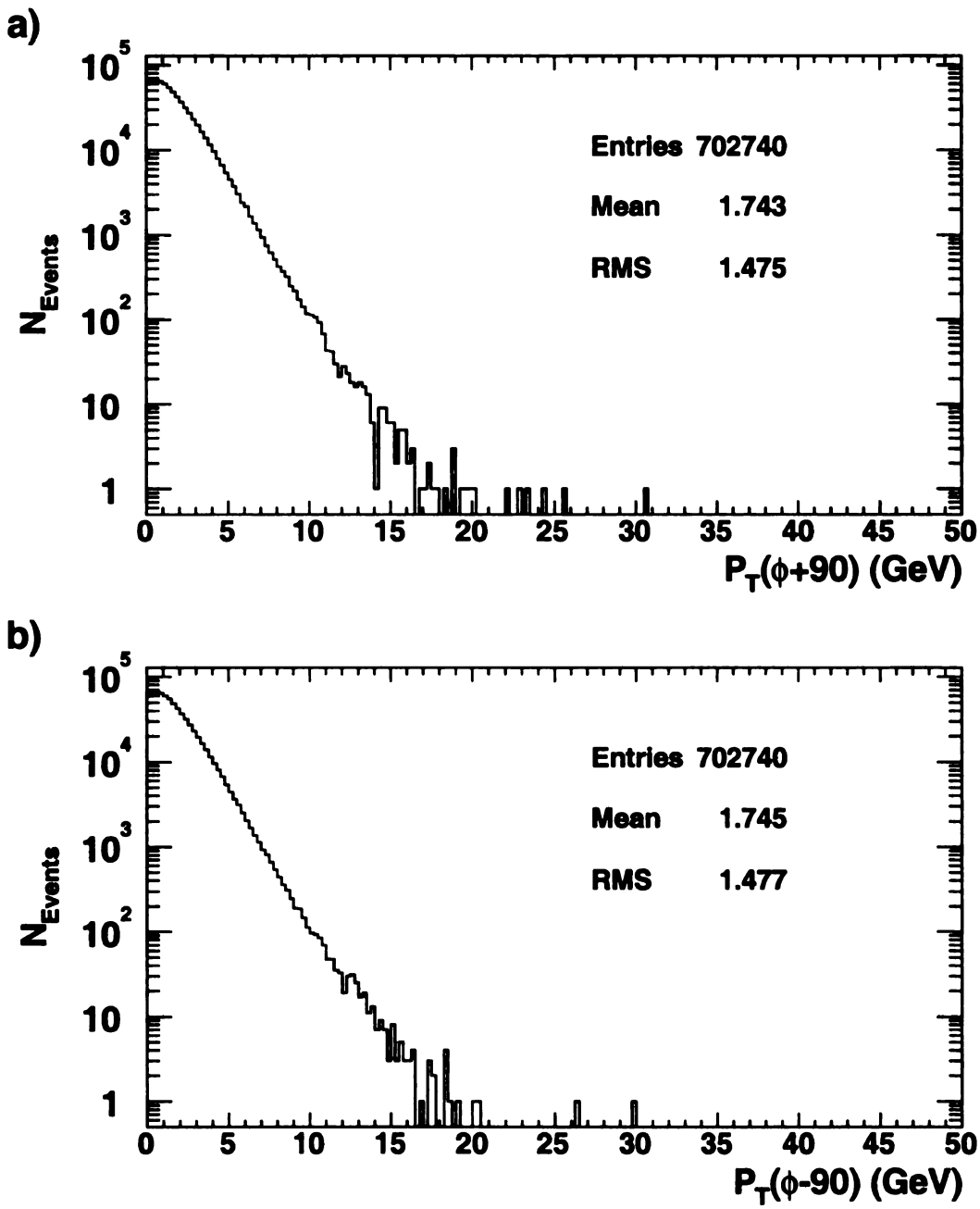

Figure 6.12: $P_T^{90}(\phi+90), P_T^{90}(\phi-90), P_T^{90}(max), P_T^{90}(min), P_T^{90}(ave)$ *and* $P_T^{90}(diff)$ *for* $P_T^{Tower} > 100\ MeV$

Figure 6.12 continued.

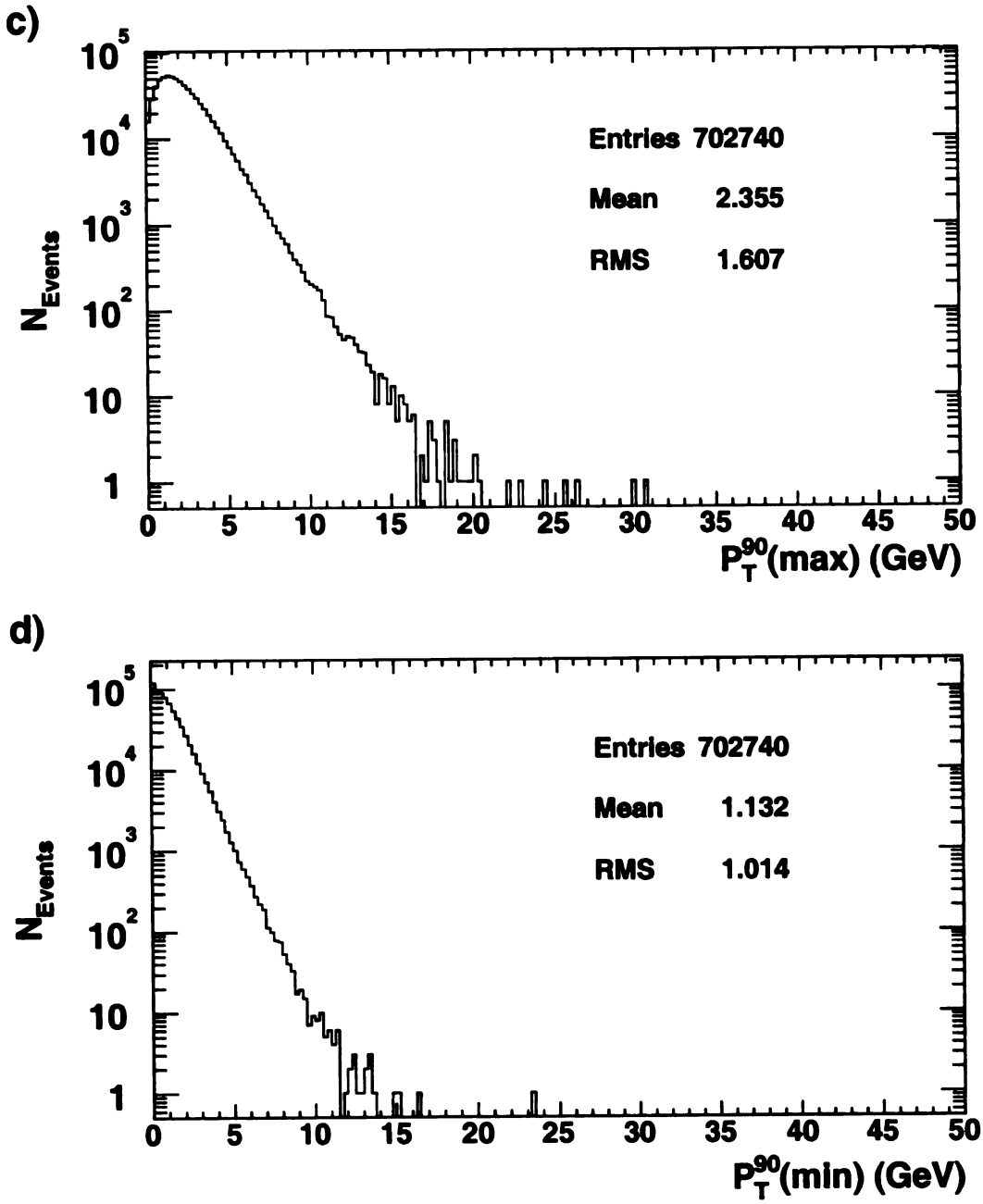

Figure 6.12 continued.

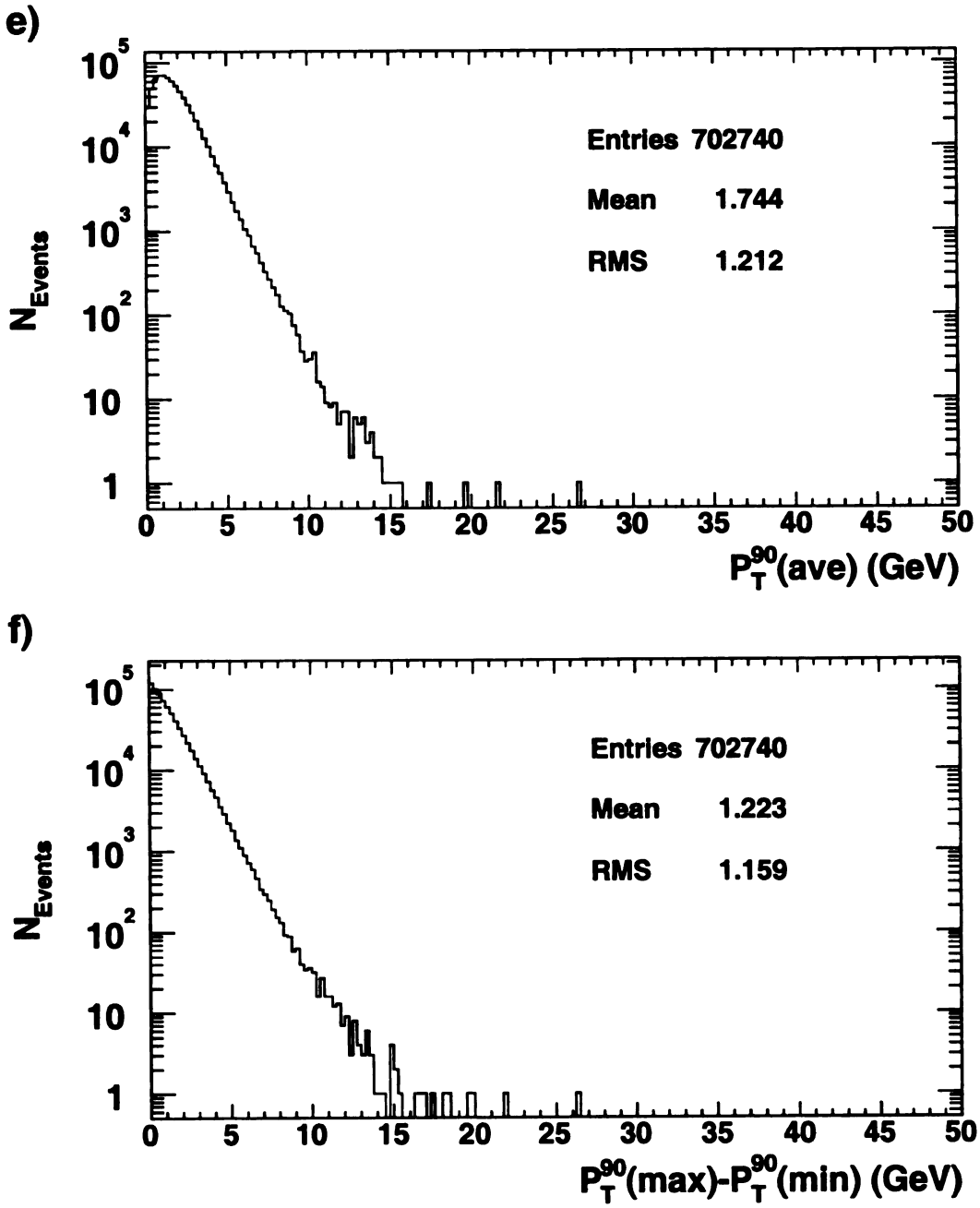

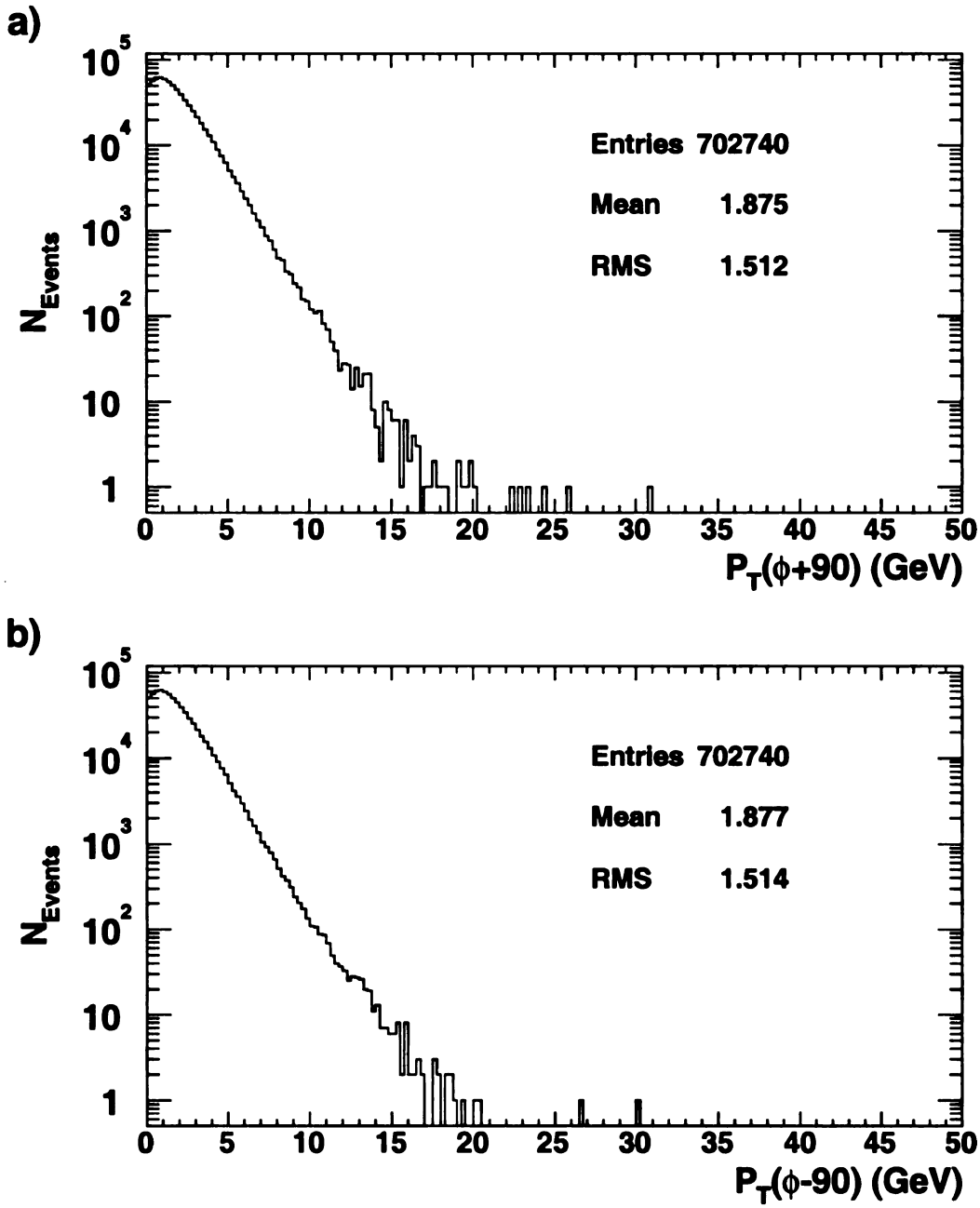

Figure 6.13: $P_T^{90}(\phi+90), P_T^{90}(\phi-90), P_T^{90}(max), P_T^{90}(min), P_T^{90}(ave)$ *and* $P_T^{90}(diff)$ *for* $P_T^{Tower} > 50\ MeV$

Figure 6.13 continued.

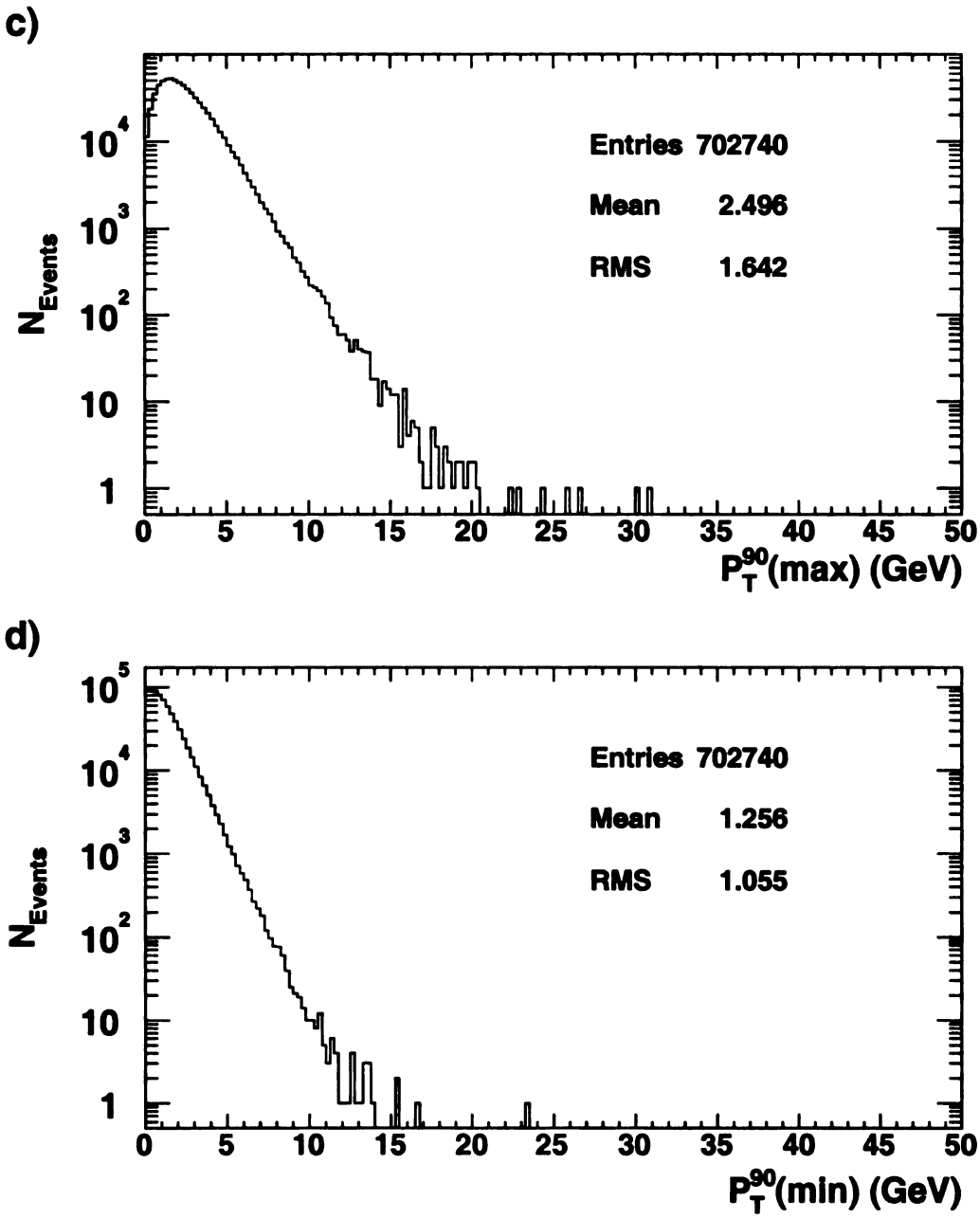

Figure 6.13 continued.

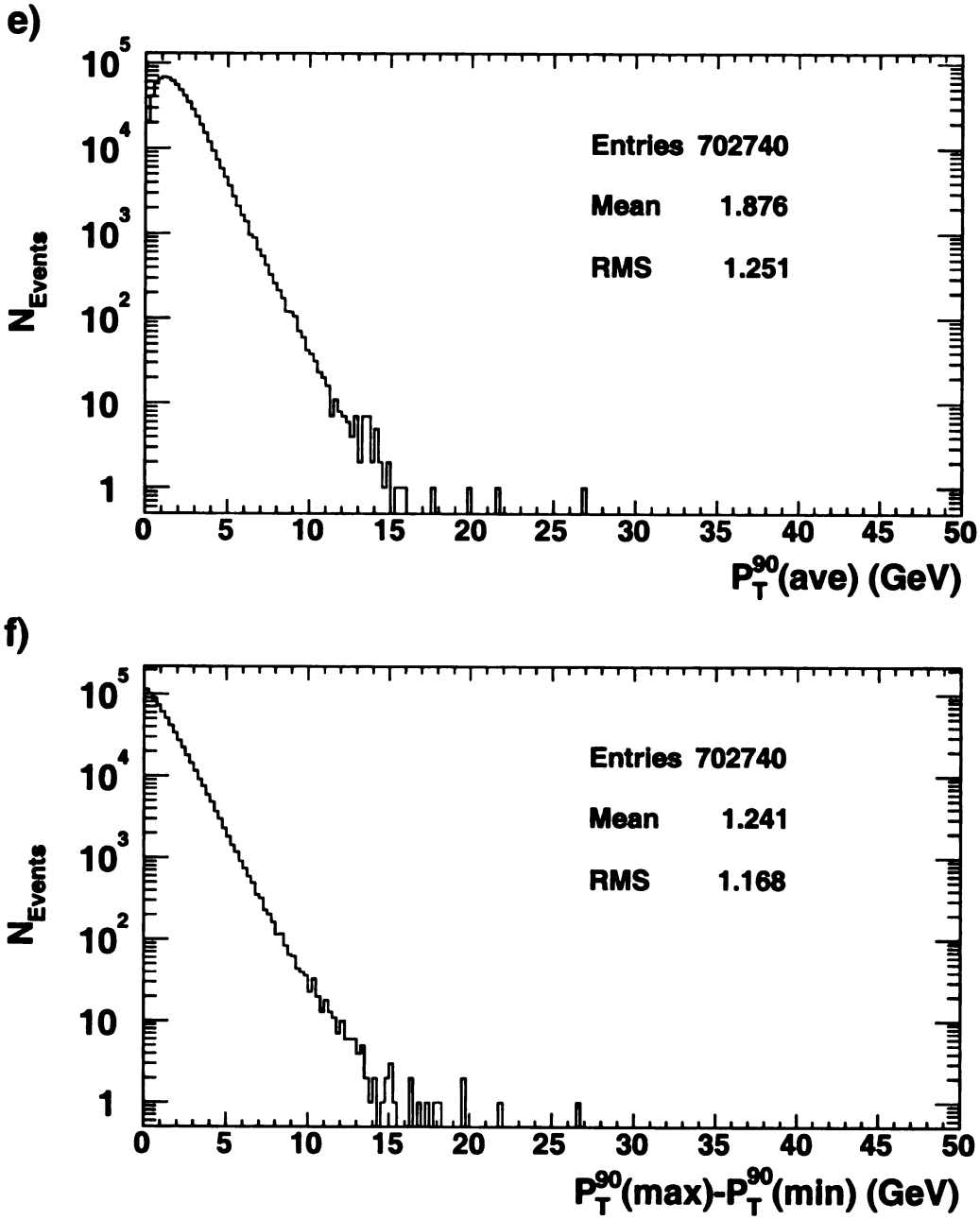

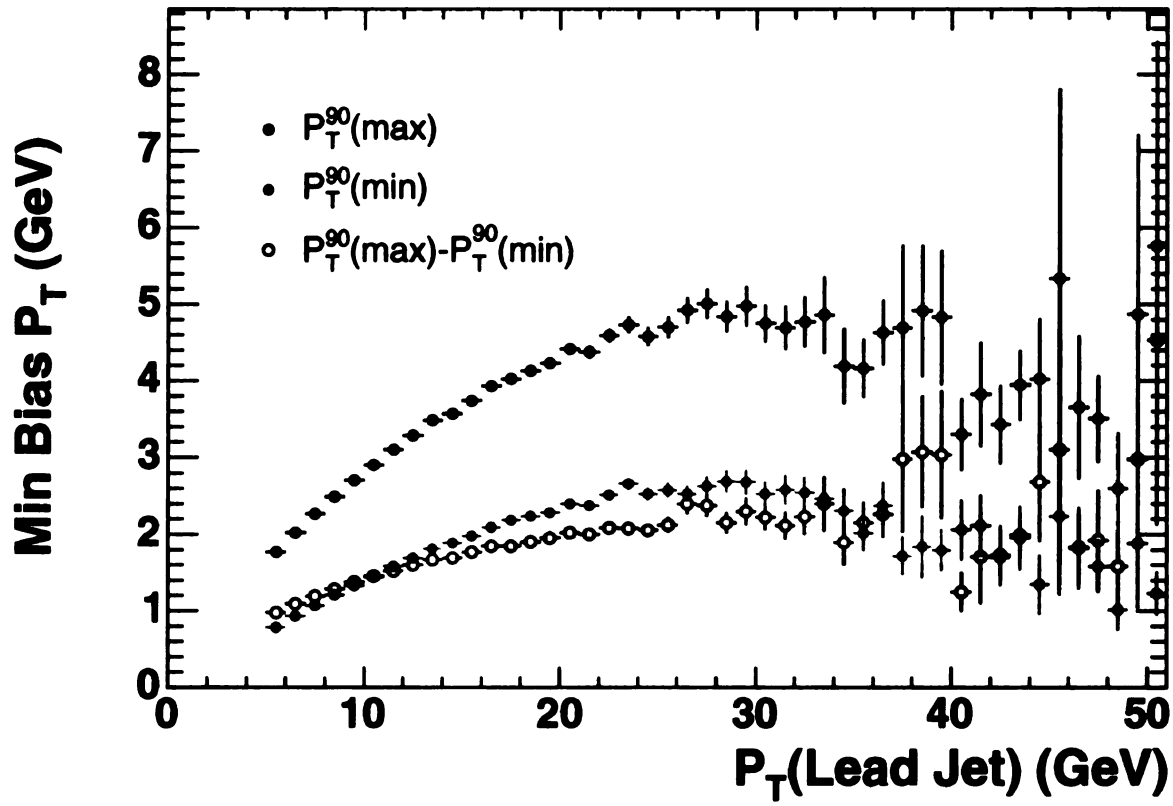

Figure 6.14: $P_T^{90}(max)$, $P_T^{90}(min)$ *and* $P_T^{90}(diff)$ *for* $P_T^{Tower} > 100$ *MeV as function of lead jet* P_T

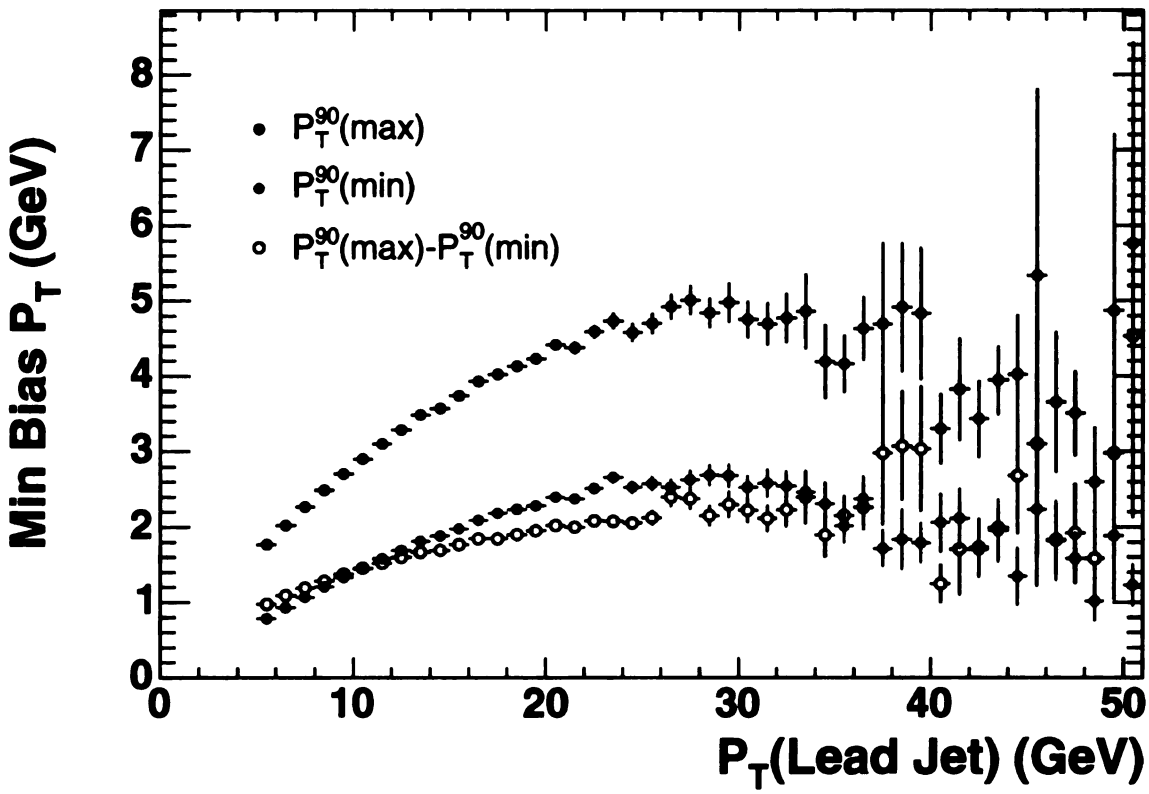

Figure 6.15: $P_T^{90}(max), P_T^{90}(min)$ *and* $P_T^{90}(diff)$ *for* $P_T^{Tower} > 50$ *MeV as function of lead jet* P_T

6.7 Conclusion

We have studied the energy/momentum deposition in a $R = 0.7$ cone in the minimum bias data and compared it to the 90^o P_T in the subset of minimum bias events that satisfy $P_T^{Jet} > 5.0$ GeV. It was found for a cone $R = 0.7$:

- On average the underlying event contribution to a jet in the central region is 0.9375 GeV. The value is measured from minimum bias data having $|Z| < 60.0$ cm with a tower threshold of 100 MeV, using events with a single quality 12 vertex.

- The multiple interaction correction was found to be 0.928 GeV/Vertex for a 100 MeV tower threshold.

- Decreasing the tower threshold from 100 to 50 MeV increases $P_T^{R=0.7}$ by $\sim$ 100.0 MeV.

- The minimum P_T^{90} in the jet events is weakly dependent on the lead jet P_T in the event. The $\langle P_T^{90}(min)\rangle$ of the minbias events that have a 5.0 GeV jet is 1.13 GeV (average over full run range).

- The maximum P_T^{90} in the jet events increases slowly with the lead jet P_T over the range included in this study. The $P_T^{90}(min)$ and $P_T^{90}(max) - P_T^{90}(min)$ both have weak dependence on the lead jet P_T.

Chapter 7

Jet Energy Resolution

7.1 Introduction

To measure the jet energy resolution we use the technique of P_T *balance*, first introduced by UA2 [19]. For a $2 \rightarrow 2$ event in a perfect calorimeter, momentum conservation requires the P_T of the first jet to be equal to the P_T of the second. Calorimeter resolution and QCD radiation produce fluctuations in P_T which can result in a P_T imbalance for an event. This imbalance is related to the single jet resolution and it is what we measure.

A vector $\vec{K}_T$ is defined for the dijet system as the vector sum of the transverse momenta of the two leading jets in the event. In the absence of initial state radiation, conservation of momentum requires the total transverse momentum of the event (hard-scattered jets) to be conserved. In a pure dijet event this implies that $\vec{K}_T = 0$. Detector resolution and QCD radiation can produce a momentum imbalance in the event causing $\vec{K}_T$ to deviate from zero.

The coordinate system for the dijet $\vec{K}_T$ is defined so that the perpendicular direction ($\hat{\perp}$) is the direction that bisects the azimuthal angle between the two jets. The parallel direction ($\hat{\parallel}$) is orthogonal to ($\hat{\perp}$): $\hat{\parallel} \times \hat{\perp} = \hat{z}$, where z is the positive z axis in the detector coordinate system (beam line). From these definitions we have:

$$K_{T||} = (P_{T1} - P_{T2}) \sin(\frac{\phi_{12}}{2}), \tag{7.1}$$

$$K_{T\perp} = (P_{T1} + P_{T2}) \cos(\frac{\phi_{12}}{2}), \tag{7.2}$$

where ϕ_{12} is the angle between the two jets. The width of the $K_{T||}$ distribution ($\sigma_{||}$) and the $K_{T\perp}$ distribution ($\sigma_{\perp}$) are related to the jet resolution: the perpendicular component is dominated by QCD radiation effects and the parallel component is a combination of radiation effects and detector resolution. The detector resolution can be extracted from $\sigma_{\perp}$ and $\sigma_{||}$ by:

$$\sigma_{RMS} = \frac{\sqrt{\sigma_{||}^2 - \sigma_{\perp}^2}}{\sqrt{2}}. \tag{7.3}$$

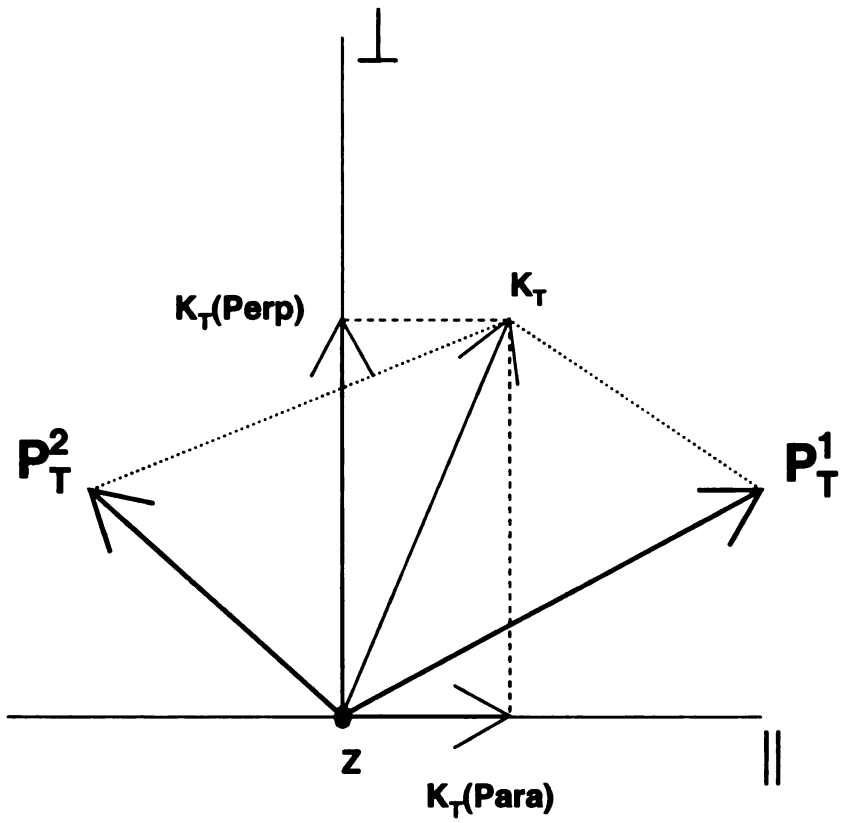

Figure 7.1: *P_T balance technique. The P_T vectors of the two leading central jets in the transverse plane are shown. The $\perp$ axis is the perpendicular bisector of the angle between the two jets (ϕ_{12}). The $\parallel$ axis is orthogonal to the $\perp$ axis in the transverse plane. K_T, the vector sum of P_{T1} and P_{T2} is shown with its components along the $\perp$ and $\parallel$ axis.*

7.2 Method

We measure the $K_{T\parallel}$ and $K_{T\perp}$ distributions in the data and Pythia. The data-Pythia comparison of σ_{RMS} gives an indication of how well Pythia+CDFSIM is modelling the resolution and QCD radiation. The discrepancy between data and Pythia can be used to set the size of the resolution systematic uncertainty on the cross section.

Dijet events are selected so that at least one of the jets lies within the rapidity range $0.1 < Y < 0.7$. This jet is referred to as the "trigger" jet The remaining jet is referred to as the "probe" jet. When considering the central calorimeter resolution it is also required that the probe jet satisfies the Y cut. The distributions $K_{T\parallel}$ and $K_{T\perp}$ are constructed for central-central jet pairs.

The Monte Carlo is divided into subsamples of the total available sample. The division is based on the P_T coverage relative to the jet trigger we want to compare to. For example the Jet20 data is compared to a sample made up from Pythia $\hat{P}_T$ $\geq$18,40,60 and 90 GeV subsamples. The subsamples are weighted by luminosity for the study.

The data are required to pass the good run requirement, database-ntuple event count matching and the following cuts:

- $E_{total} < 1960$ GeV
- $\tilde{\not{E}}_T < XX$
- $|z| < 60$cm
- $0.1 < |Y^{trigger/probe}| < 0.7$
- $\Delta\phi_{12} > 2.7$ radians
- $P_T^{3rd\ jet} < 0.1 \times P_T^{Average}$, where XX is 3.5, 5.0, 5.0 and 6.0 for Jet20, Jet50, Jet70 and Jet100 respectively. A further selection cut is made on the average P_T of

the leading two jets to minimise any bias in the measurement.

	Jet20	Jet50	Jet70	Jet100
P_{T1}^{Min} (GeV)	50	75.0	95.0	130.0
$\langle P_{dijet} \rangle$ (GeV)	30-45	45-81	81-100	100+

Table 7.1: *The P_T^{Min} cuts is used to ensure the Pythia samples and the data are away from generation and trigger thresholds respectively.*

7.3 Results

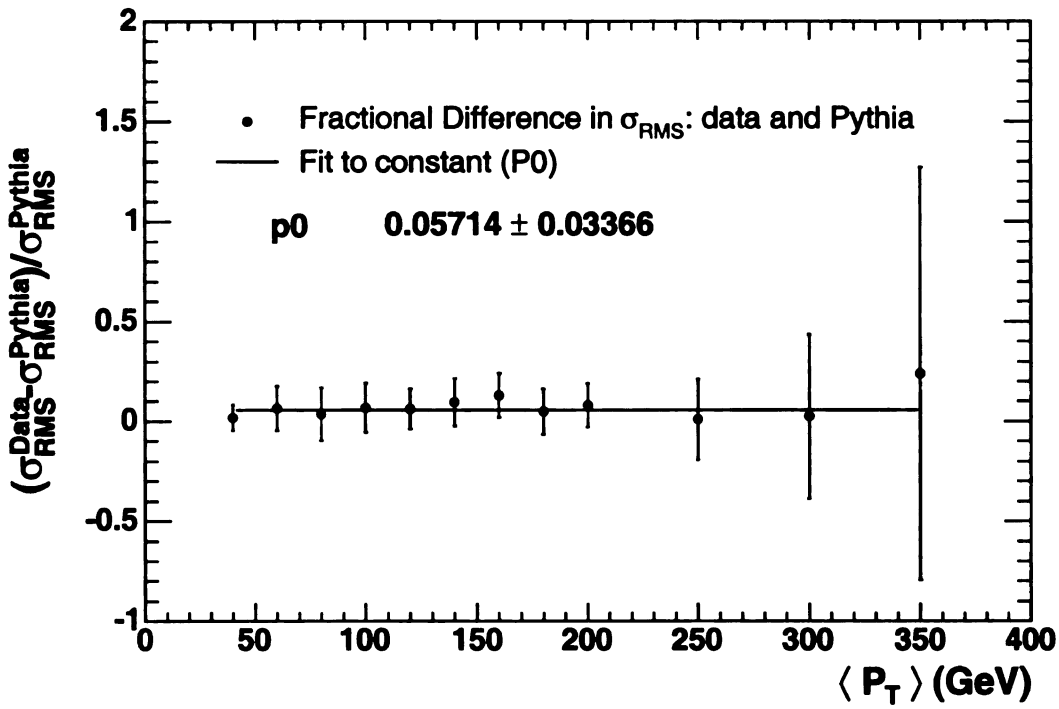

Figure 7.2: *Data-Pythia Resolution difference versus* $\langle P_T^{Dijet} \rangle$.

$\langle P_T^{Min} \rangle - \langle P_T^{Max} \rangle$ (GeV)	$K_{\|}^{Data}$	$\delta K_{T\|}^{Data}$	$K_{T\|}^{Pythia}$	$\delta K_{T\|}^{Pythia}$
60-40	0.247	0.021	0.242	0.032
80-60	0.252	0.011	0.237	0.032
100-80	0.177	0.012	0.170	0.027
120-100	0.566	0.027	0.606	0.109
140-120	0.264	0.008	0.247	0.031
160-140	0.173	0.007	0.158	0.021
180-160	0.172	0.010	0.153	0.017
200-180	0.161	0.015	0.152	0.016
250-200	0.157	0.016	0.145	0.012
300-250	0.135	0.035	0.135	0.010
350-300	0.132	0.071	0.132	0.015
400-350	0.106	0.174	0.126	0.028

Table 7.2: $K_{T\|}$ *for data and Pythia as a function of the average dijet energy.*

$\langle P_T^{Min} \rangle - \langle P_T^{Max} \rangle$ (GeV)	$K_{\perp}^{Data}$	$\delta K_{T\perp}^{Data}$	$K_{T\perp}^{Pythia}$	$\delta K_{T\perp}^{Pythia}$
60-40	0.063	0.021	0.059	0.032
80-60	0.053	0.011	0.050	0.032
100-80	0.049	0.012	0.042	0.027
120-100	0.072	0.027	0.065	0.109
140-120	0.067	0.008	0.057	0.031
160-140	0.063	0.007	0.058	0.021
180-160	0.060	0.010	0.056	0.017
200-180	0.057	0.015	0.049	0.016
250-200	0.055	0.016	0.048	0.012
300-250	0.049	0.035	0.044	0.010
350-300	0.051	0.071	0.044	0.015
400-350	0.055	0.174	0.038	0.028

Table 7.3: $K_{T\perp}$ *for data and Pythia as a function of the average dijet energy.*

$\langle P_T^{Min} \rangle - \langle P_T^{Max} \rangle$ (GeV)	σ_{RMS}^{Data}	$\delta\sigma_{RMS}^{Data}$	σ_{RMS}^{Pythia}	$\delta\sigma_{RMS}^{Pythia}$
40-60	0.169	0.010	0.166	0.016
60-80	0.174	0.005	0.163	0.016
80-100	0.120	0.006	0.116	0.013
100-120	0.397	0.013	0.426	0.054
120-140	0.180	0.004	0.169	0.015
140-160	0.114	0.003	0.104	0.010
160-180	0.114	0.005	0.101	0.008
180-200	0.106	0.007	0.101	0.008
200-250	0.104	0.008	0.096	0.006
250-300	0.089	0.017	0.090	0.005
300-350	0.086	0.035	0.088	0.007
350-400	0.064	0.087	0.084	0.014

Table 7.4: *Jet energy resolution (σ_{RMS}) for data and Pythia.*

$\langle P_T^{Min} \rangle - \langle P_T^{Max} \rangle$ (GeV)	$(\sigma_{RMS}^{Data} - \sigma_{RMS}^{Pythia})/\sigma_{RMS}^{Pythia}$	*Err*
40-60	0.016	0.064
60-80	0.064	0.112
80-100	0.035	0.132
100-120	0.068	0.124
120-140	0.062	0.101
140-160	0.096	0.118
160-180	0.130	0.109
180-200	0.048	0.114
200-250	0.079	0.108
250-300	0.010	0.203
300-350	0.024	0.411
350-400	0.240	1.032

Table 7.5: *Jet energy resolution (σ_{RMS}) fractional difference detween data and Pythia.*

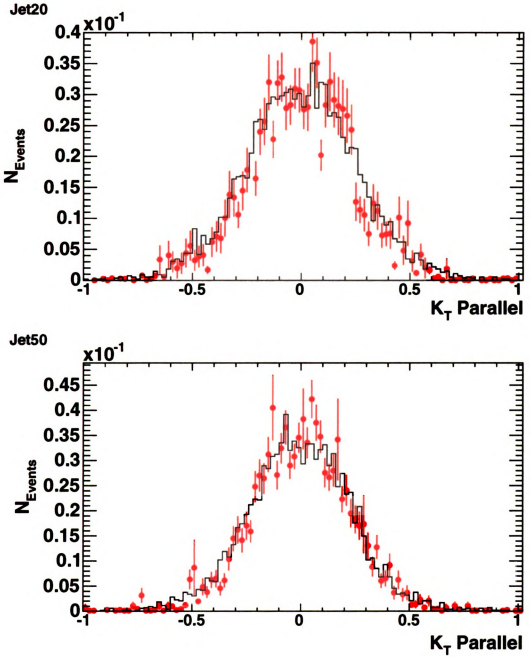

Figure 7.3: $K_{T\|}$ *for data (histogram) and Pythia (points). This quantity is sensitive to both QCD radiation and detector resolution. All distributions are normalised to unity.*

Figure 10.6 continued.

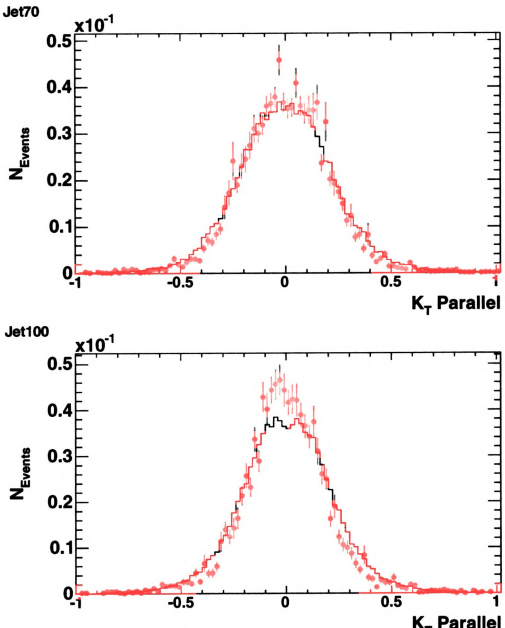

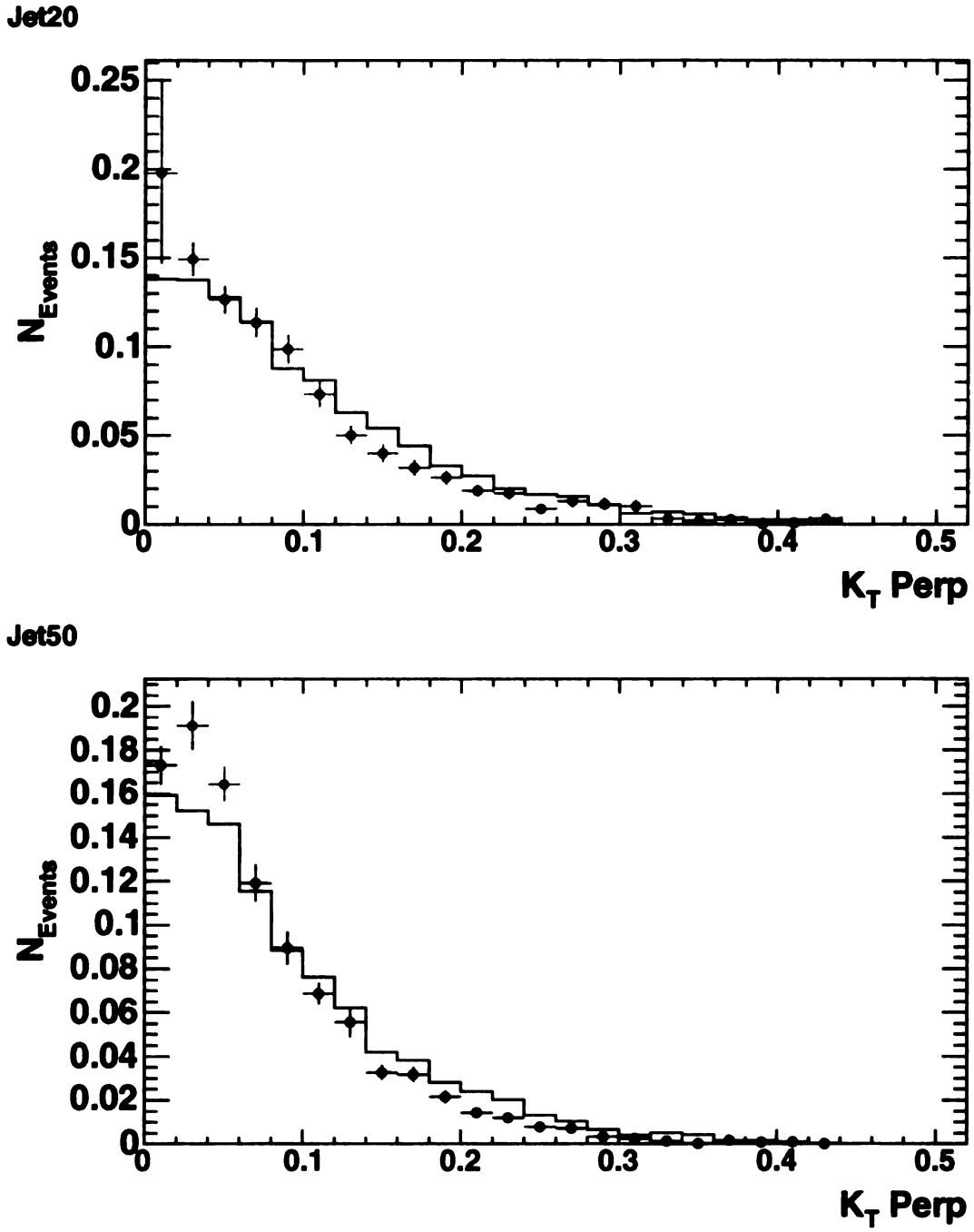

Figure 7.4: *$K_{T\perp}$ for data (histogram) and Pythia (points). This quantity is dominated by QCD radiation. All distributions are normalised to unity.*

Figure 10.7 continued.

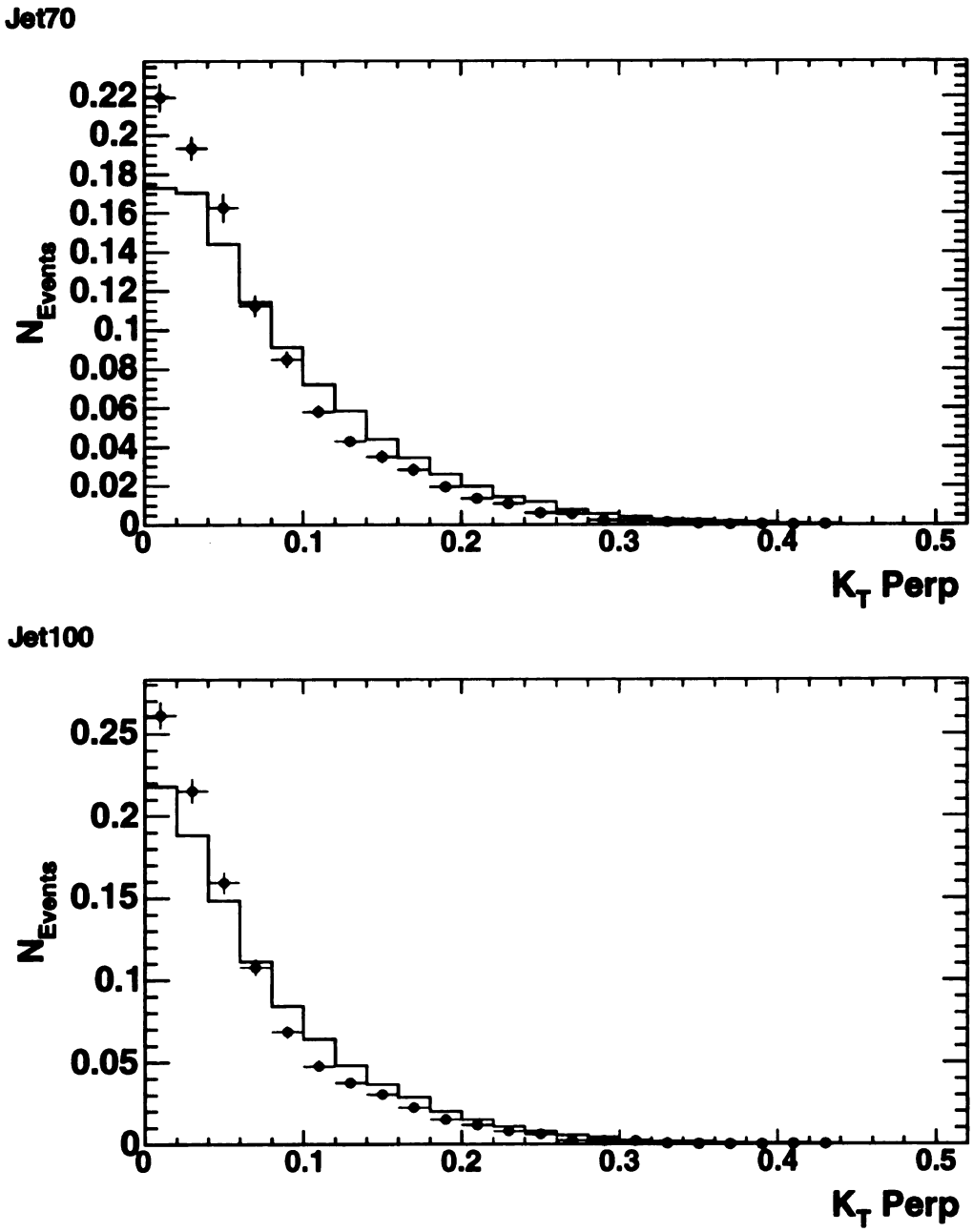

7.4 Conclusion

Pythia reproduces the $K_{T||}$ distributions found in the data reasonably well. The $K_{T\perp}$ distributions found in Pythia appear to be slightly narrower that those found in the data. This suggests the 3rd jet content of the data is different from Pythia. We compute the single jet resolution (σ_{RMS}) and find that the agreement between data and Pythia is good. The data is systematically higher than Pythia by $\sim$ 6% (see figure 7.2). This systematic difference will be propagated into the inclusive jet cross section systematics.

Chapter 8

The Raw Inclusive Jet Cross Section

8.1 Introduction

Jet production at the Tevatron probes the highest momentum transfers currently available, this corresponds to large x and size scale of $\sim 10^{-17}$ cm. This analysis is restricted to the central region, similar to that of previous CDF inclusive jet cross section publications. This chapter will describe the data sample, analysis cuts, jet kinematics, jet backgrounds and the raw inclusive jet cross section.

8.2 Data Sample

The analysis uses data collected over the running period of Feb 2002 until Feb 2004. Over this period $275pb^{-1}$ of data was collected with the jet triggers (Jet20, Jet50, Jet70 and Jet100). The data are processed in version 5.3.3 of the CDF offline software. The Midpoint algorithm used for jet reconstruction uses a cone of $R = 0.7$ and $f_{merge} = 50\%$.

8.2.1 Run Selection

Runs are required to pass the "good run criteria". The good run list was composed by querying the database with the following requirements:

```
SHIFTCREW_STATUS   = 1
RUNCONTROL_STATUS = 1
OFFLINE_STATUS     = 1
RUNNUMBER   >= 138815
CLC_STATUS   = 1
L1T_STATUS   = 1
L2T_STATUS   = 1
L3T_STATUS   = 1
CAL_STATUS   = 1
CAL_OFFLINE = 1
(COT_STATUS = 1 OR COT_OFFLINE = 1).
```

In addition, there is a check to make sure that the number of events in the ntuple is in agreement with the number of events recorded in the database for each run that is used. This insures the luminosity taken from the run summary provides a fair measure of the integrated luminosity. This is important to the analysis as the luminosity sets the overall normalisation of the inclusive cross section.

Sample	Jet20	Jet50	Jet70	Jet70
OffLine Luminosity $(pb)^{-1}$	275	275	275	275
Nevents	19009663	5824615	2621059	3089196
GoodRun Selection	14669594	5091120	2177599	2611157
DataBase Event Matching	11867876	4516388	1827810	2310033
Number of runs for analysis	1134	1204	1170	1167
Lum for analysis $(pb)^{-1}$	206.826	225.83	207.301	218.513

Table 8.1: *Number of events for each Jet trigger used in the analysis and how many pass the good run list (DQM version 5)and database-stntuple event matching.*

8.3 Event Selection

The raw inclusive jet cross section is required to satisfy the following cleanup cuts. These are designed to remove background events coming from detector noise and cosmics. They also ensure the jets used in the analysis are contained in a region with good tracking coverage:

- Good run selection (DQM version 5, no silicon)
- $E_{total} < 1960$ GeV
- $\tilde{\not{E}_T} < XX$
- $|Z| < 60$cm
- $0.1 < |Y| < 0.7$

Where XX is 3.5, 5, 5, 6 for the jet20, jet50, jet70 and jet100 samples respectively.

Number events pass cut	Jet20	Jet50	Jet70	Jet70
Total	11867876	4516308	1827810	2310033
$\not\!\!E_T$	11840114	4431622	1762526	2052939
$\|Z\| < 60.$ cm	11036107	4087286	1625560	1892625
$E_{Total} < 1960$ GeV	11035915	4087095	1625497	1892525

Table 8.2: *Number of events passing event selection cuts for the jet triggers (E_{Total}, $\not\!\!E_T$ and Z vertex). The total number of events here is after requireing the good run requirements.*

8.3.1 Z-Vertex Cut

The protons and antiprotons are distributed in bunches which extend ~ 50 cm in the Z or beampipe direction. This means the resulting $p\bar{p}$ interactions can occur over a wide range of Z values. Putting it another way, there is a large luminous region. The Z vertex information used for reconstructing the jets comes primarily from the COT. The distribution is approximately gaussian with $\sigma \approx 30$ cm, centered near $Z = 0.0$ cm. To ensure good coverage events used in the analysis are required to satisfy the condition $|Z| < 60.0$ cm. The efficiency of this cut is determined from a fit to minimum bias data using beam shape parameters [26]. Here the efficiency of the cut is also measured for each of the four jet trigger samples used in the analysis. For the jet triggers, the efficiency of the cut is measured by applying the vertex cut after all of the other event cuts have been applied. Then the efficiency is defined by as the number that pass all of the cuts divided by the number of events that passed all cuts before the vertex cut.

The efficiency of this selection cut enters the raw cross section as a luminosity efficiency correction and is uniform for all of the jet triggers.

Sample	Jet20	Jet50	Jet70	Jet100
% Eff of $\|Z\| < 60$ cm	93	92	92	92
% events with no vertex	0.4	0.1	0.1	0.1

Table 8.3: *Efficiency of Z vertex cut in the jet triggers and fraction of events that satisfy the event selection cuts but have no vertex. The Z-vertex correction is taken from the beam fit parameters: the value was* 95% *[26]*

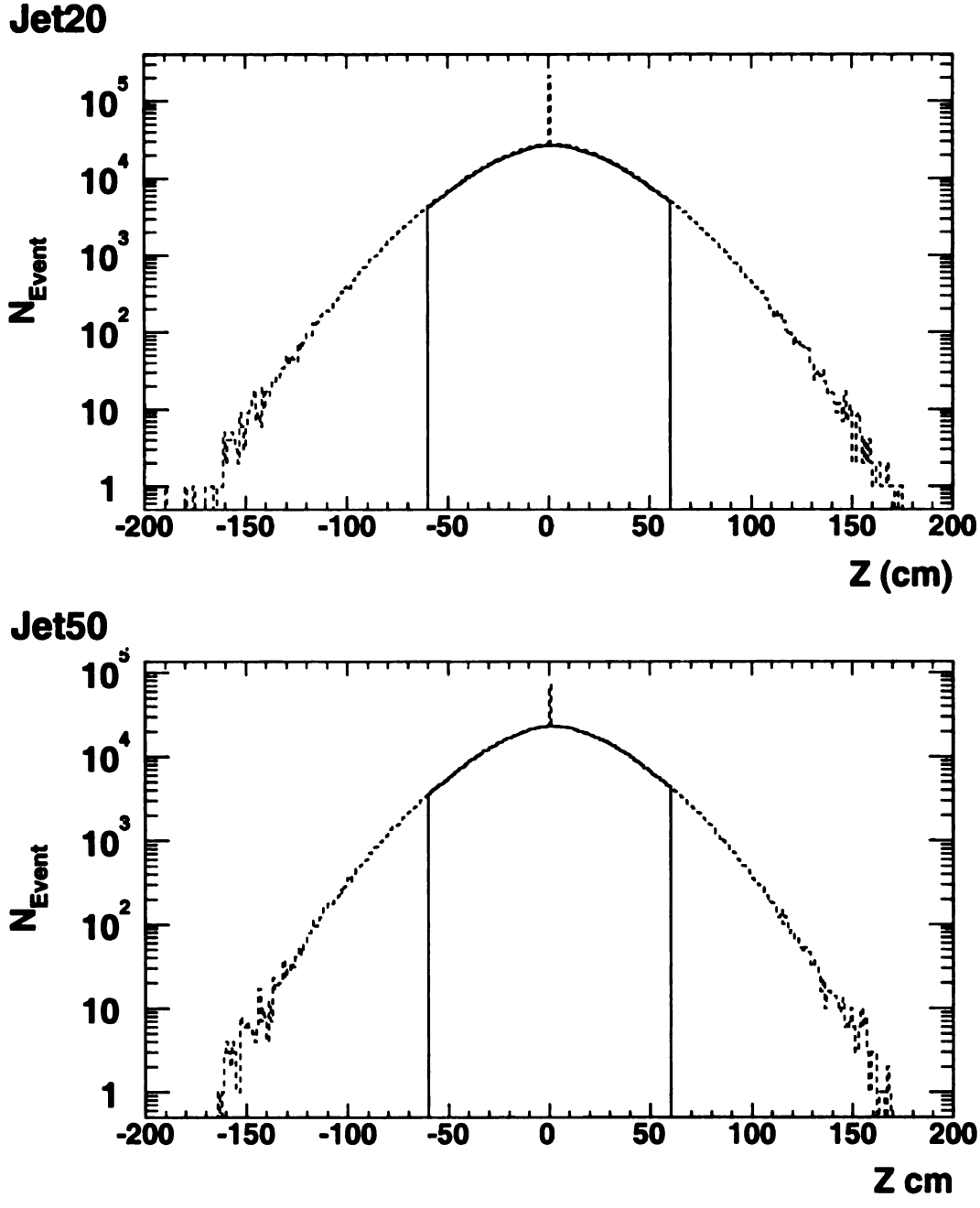

Figure 8.1: *Z vertex of the four jet triggers before and after selection cuts. The peak at $Z = 0.0$ cm in the before plot is due to cosmics and is removed by the missing E_T significance cut.*

figure 8.1 continued.

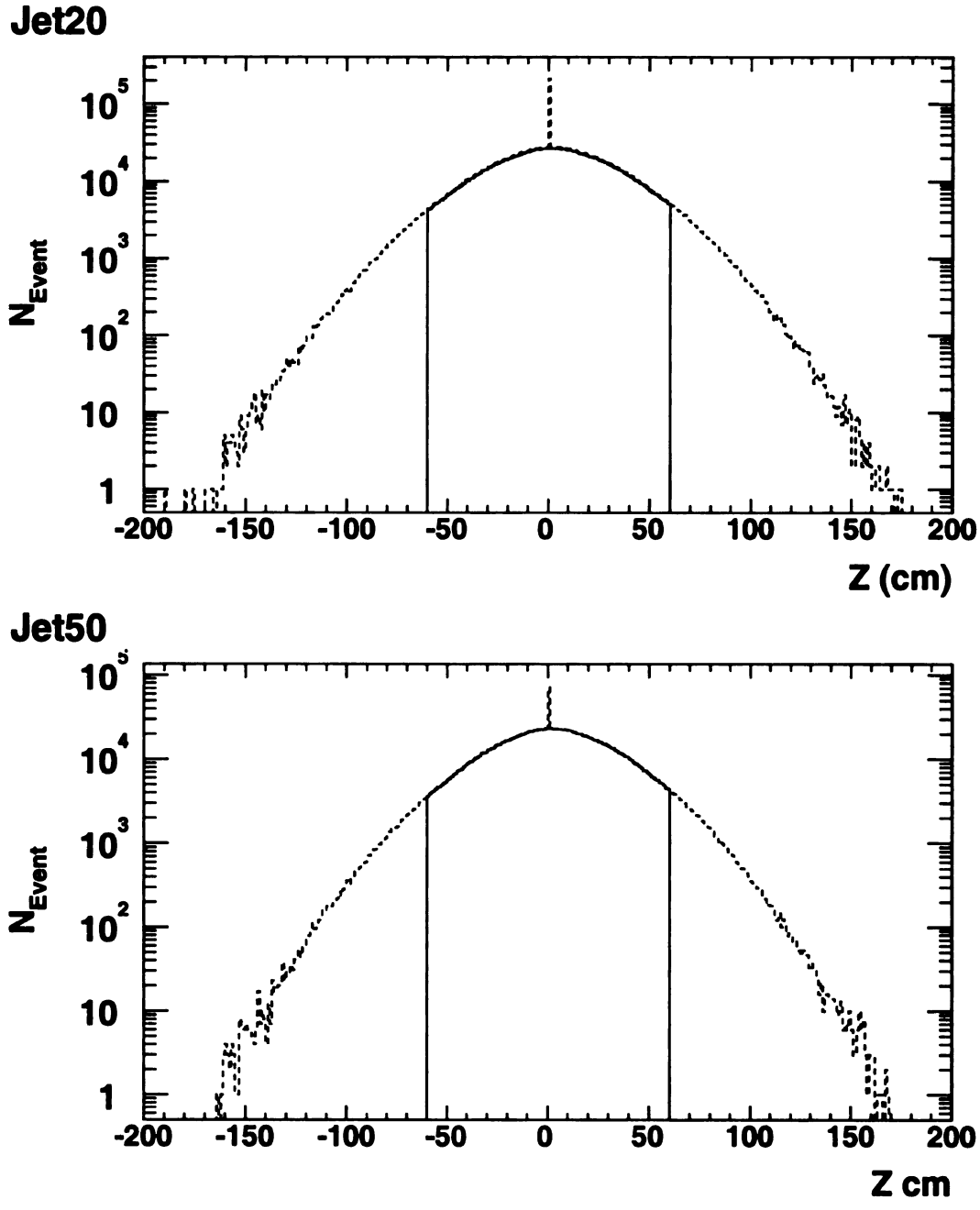

8.4 Kinematics

In this section, we plot the event properties that are used in or are related to the selection cuts for events and jet kinematic quantities. All of the plots show distributions before event cuts and after the final selection cuts. Note however, that not all entries in the plots make it into the inclusive cross section due to the matching of trigger samples.

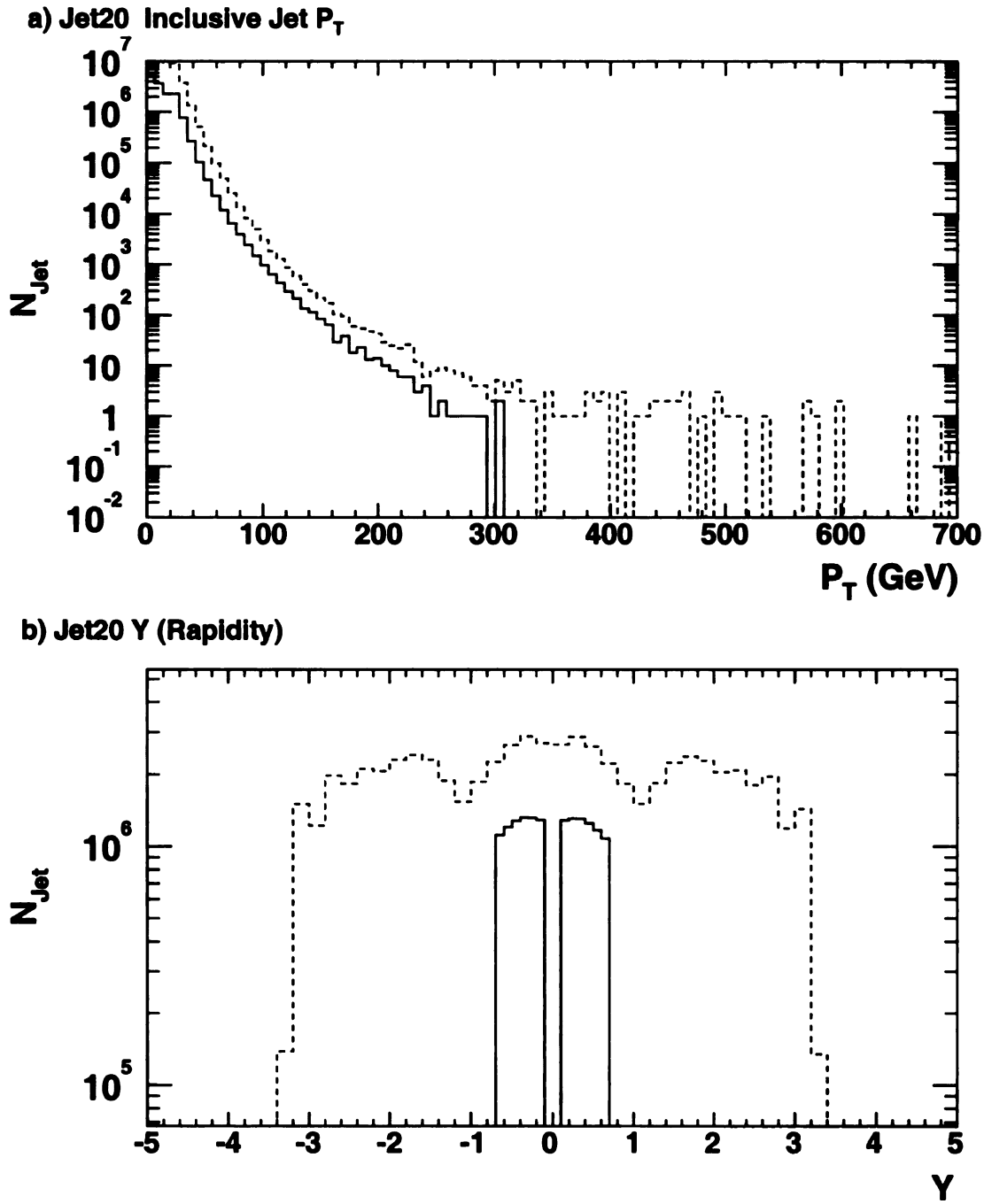

Figure 8.2: *Jet20 Kinematic variables. Inclusive P_T , Y and ϕ before cuts (dashed) and after cuts on $|Z| < 60cm$, $0.1 < |Y| < 0.7$, $E_{total} < 1960$ GeV and $\not\!\!E_T < 3.5$ (solid).*

figure 8.2 continued.

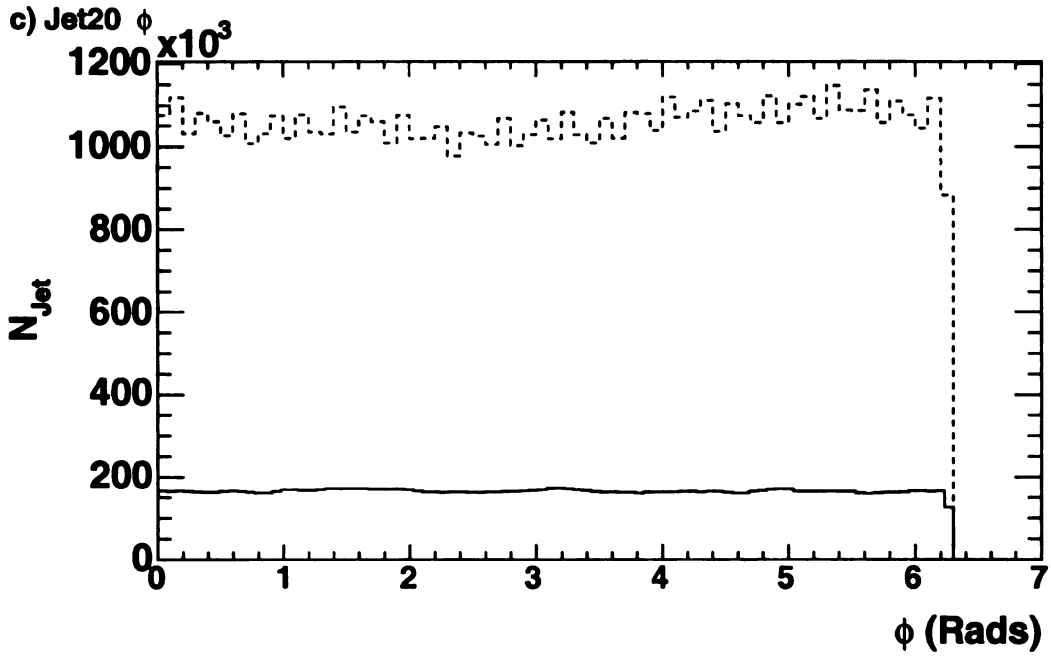

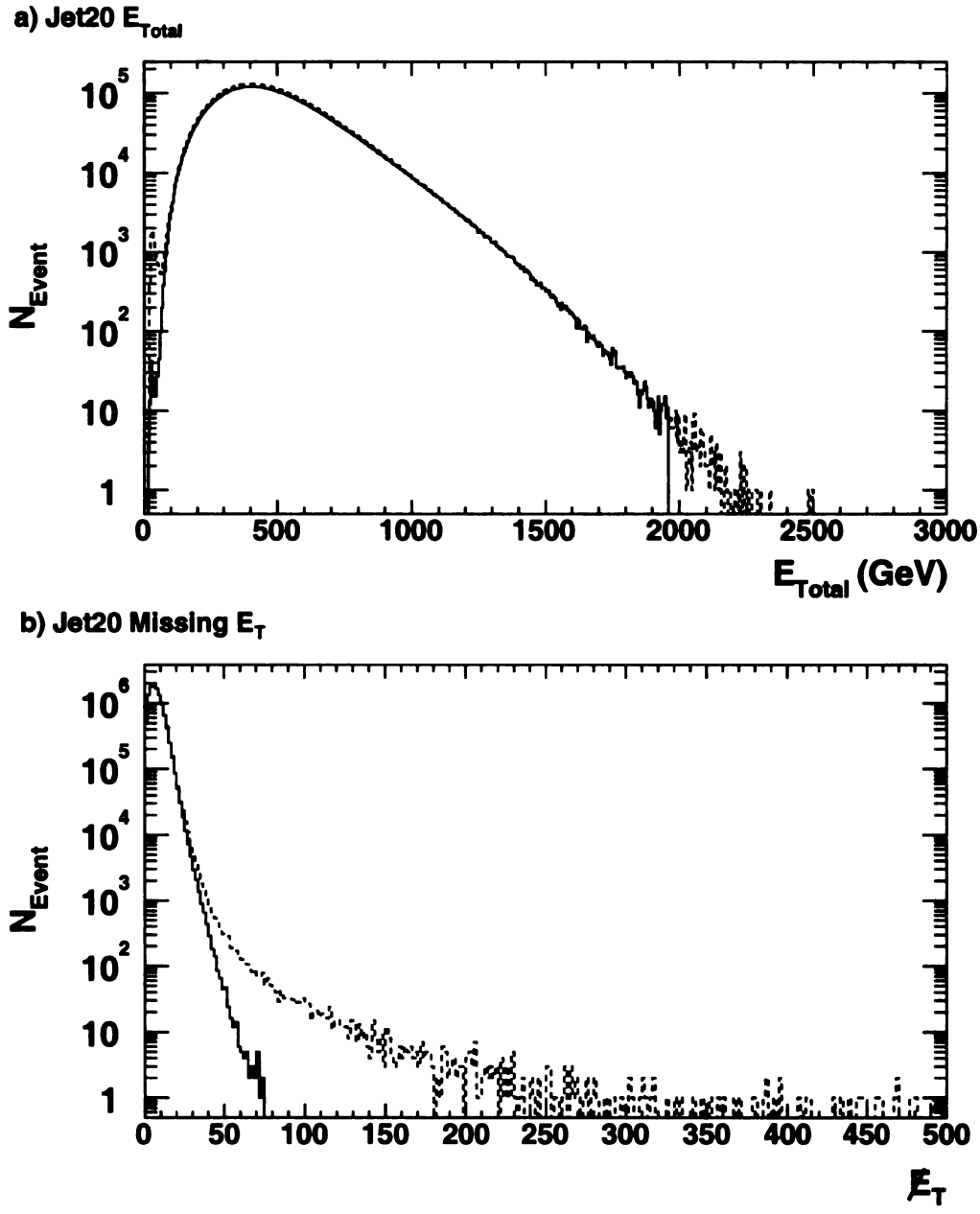

Figure 8.3: *Jet20 Kinematic variables:* E_{total}, $\not\!\!E_T$ *and* $\not\!\!\tilde{E}_T$ *before the selection cuts (dashed) and after (solid).*

figure 8.3 continued.

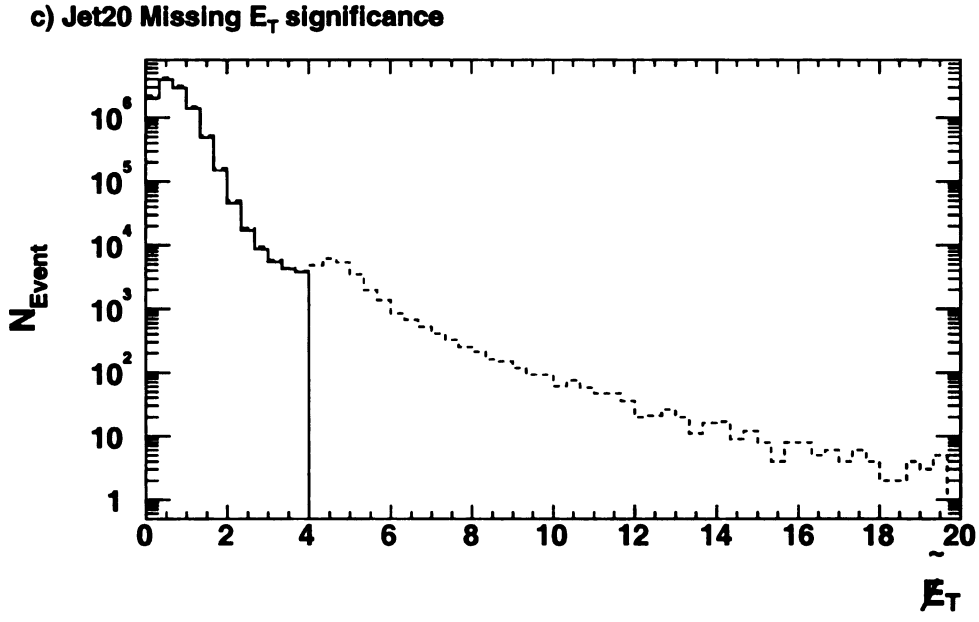

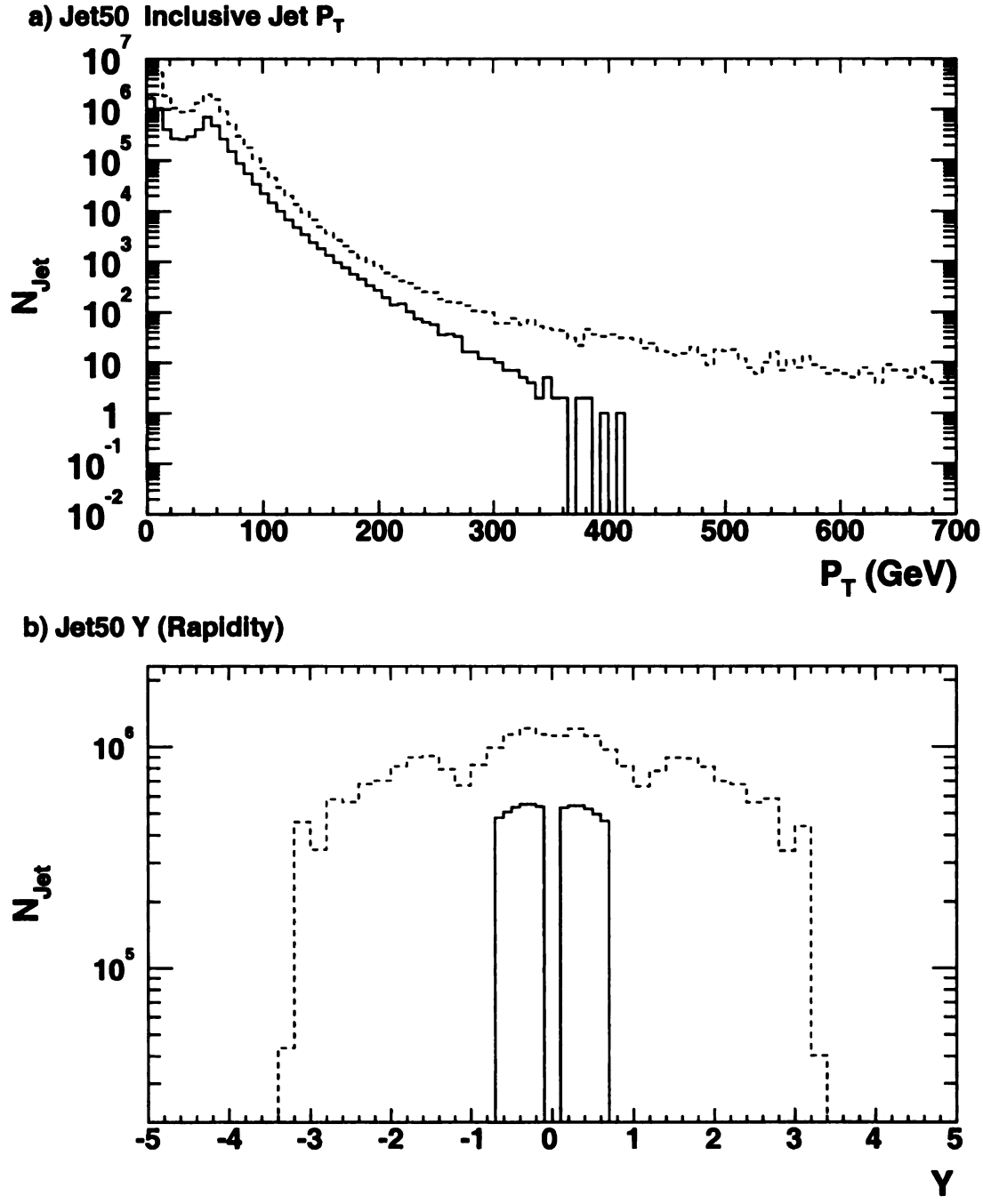

Figure 8.4: *Jet50 Kinematic variables: Inclusive P_T , Y and ϕ before cuts (dashed) and after cuts on $|Z| < 60cm$, $0.1 < |Y| < 0.7$, $E_{total} < 1960$ GeV and $\not\!\!E_T < 4$ (solid).*

figure 8.4 continued.

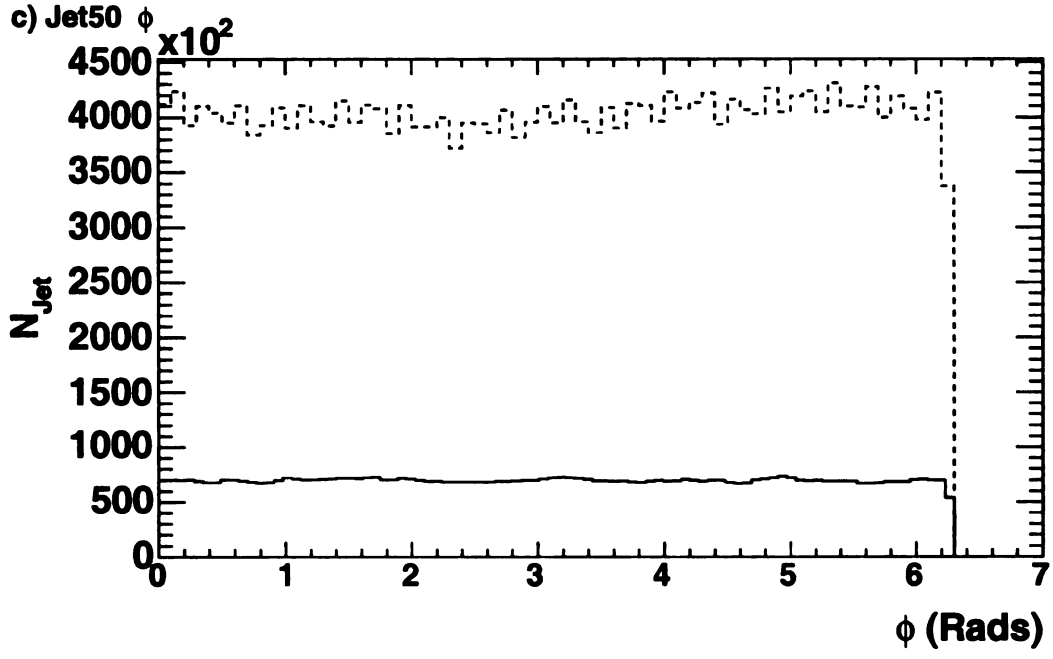

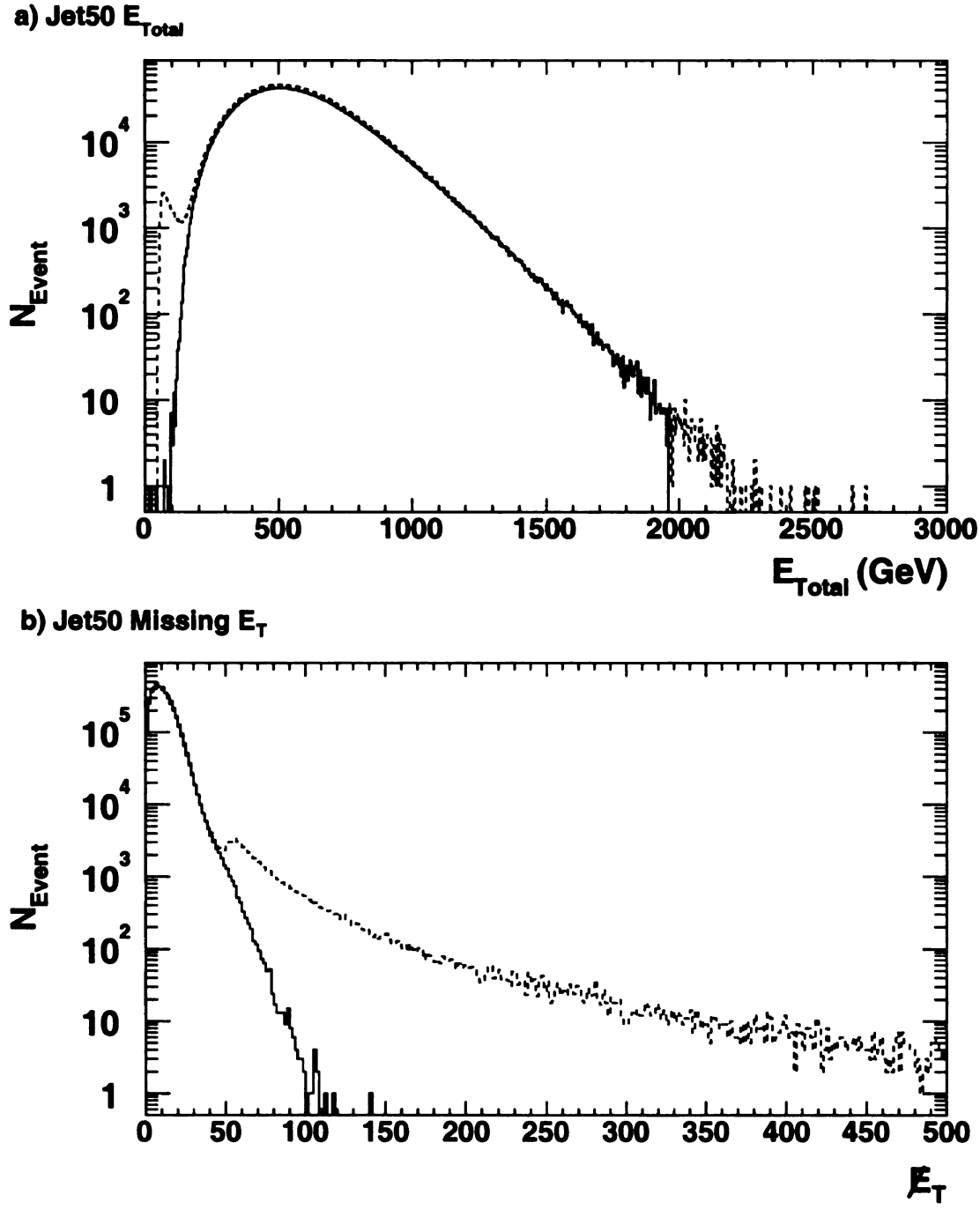

Figure 8.5: *Jet50 Kinematic variables.* E_{total}, $\not\!\!E_T$ *and* $\not\!\!\tilde{E}_T$ *before the selection cuts (dashed) and after (solid).*

figure 8.5 continued.

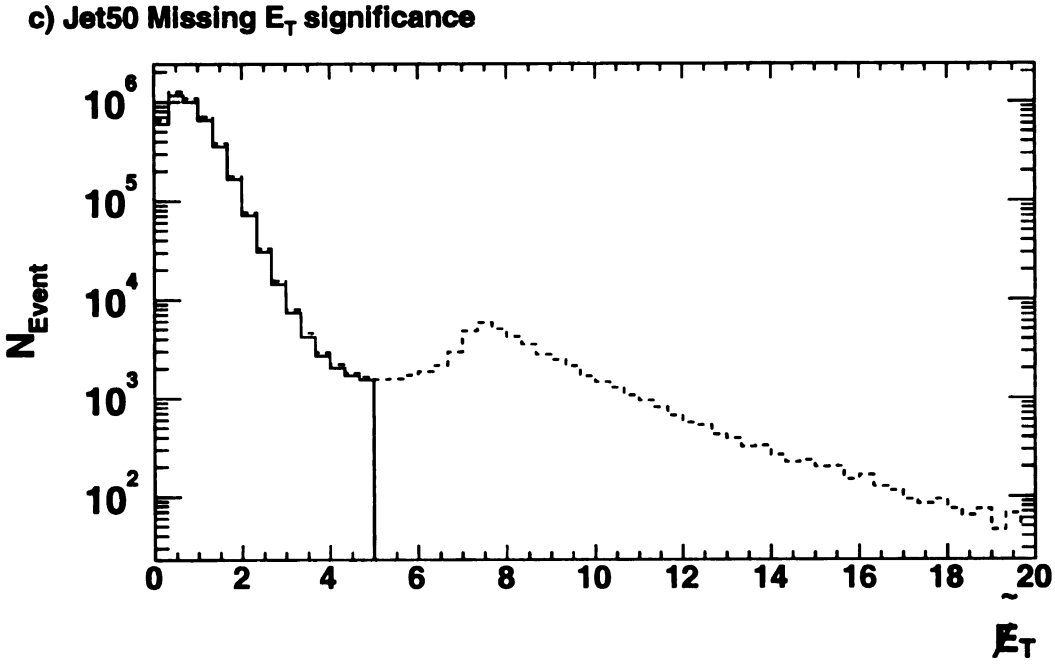

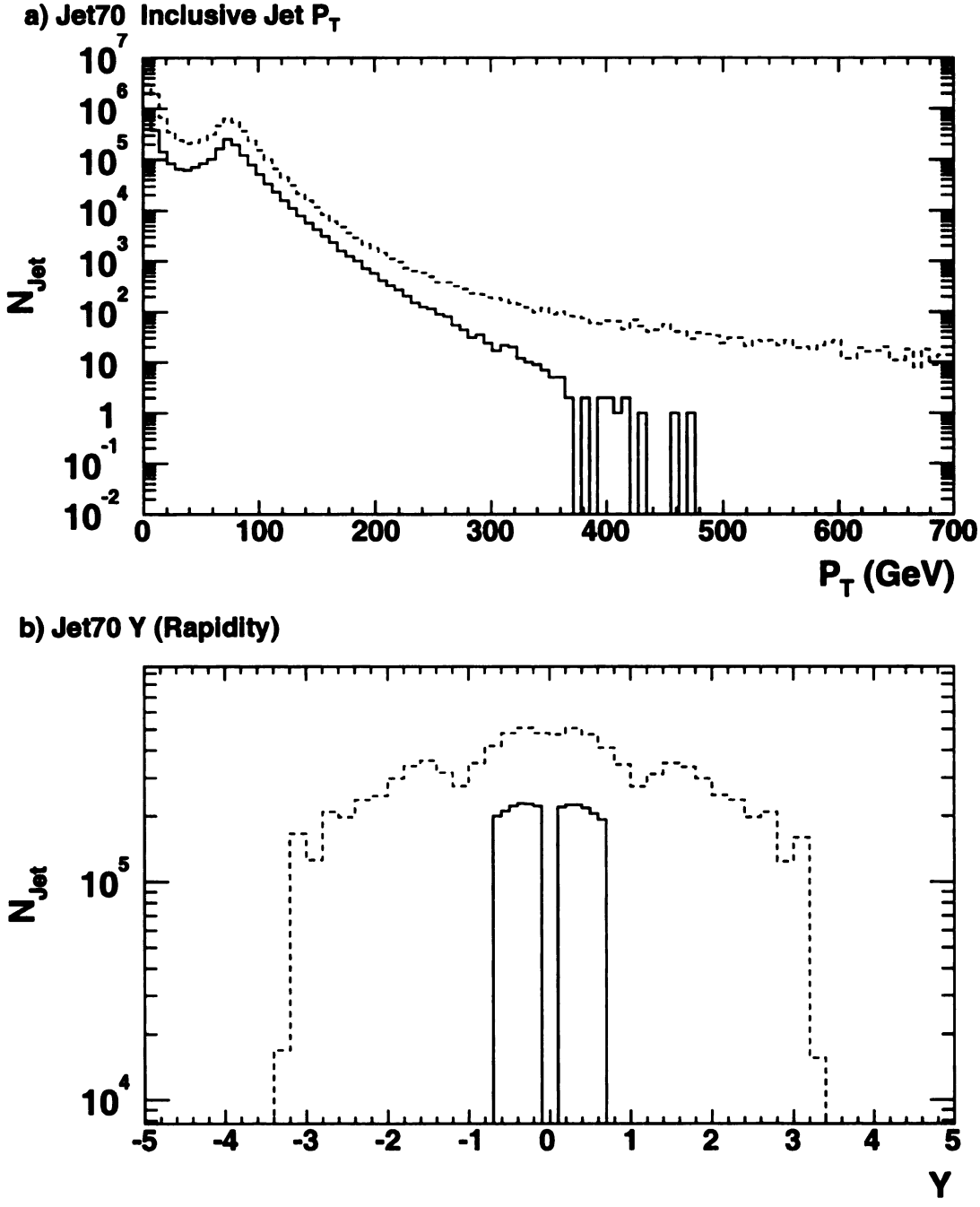

Figure 8.6: *Jet70 Kinematic variables: Inclusive P_T , Y and ϕ before cuts (dashed) and after cuts on $|Z| < 60cm$, $0.1 < |Y| < 0.7$, $E_{total} < 1960$ GeV and $\not\!\!E_T < 4$ (solid).*

figure 8.6 continued.

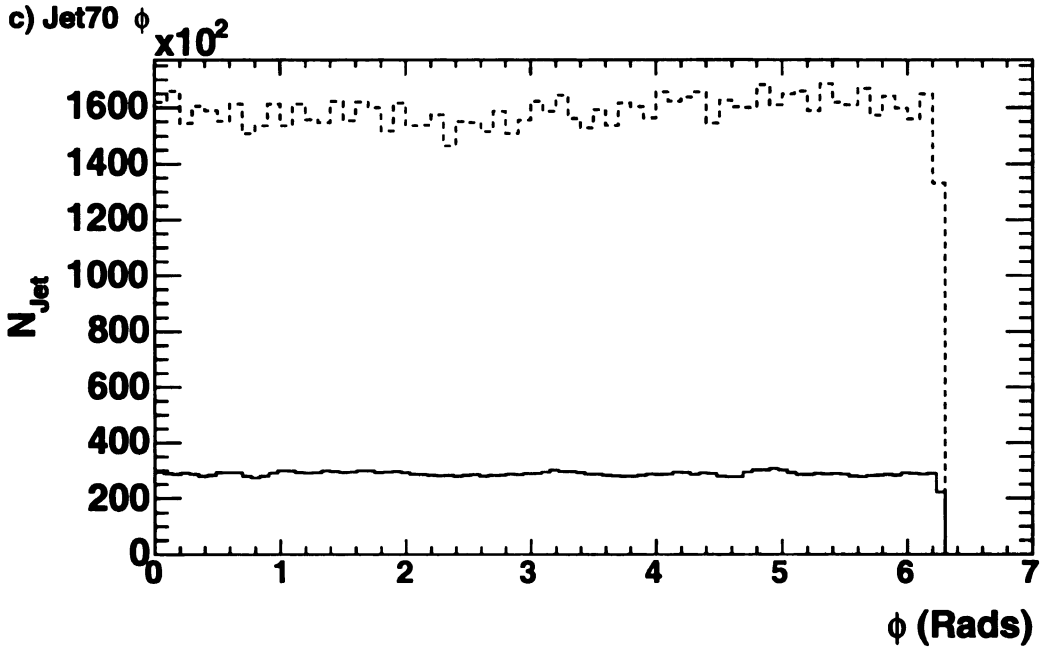

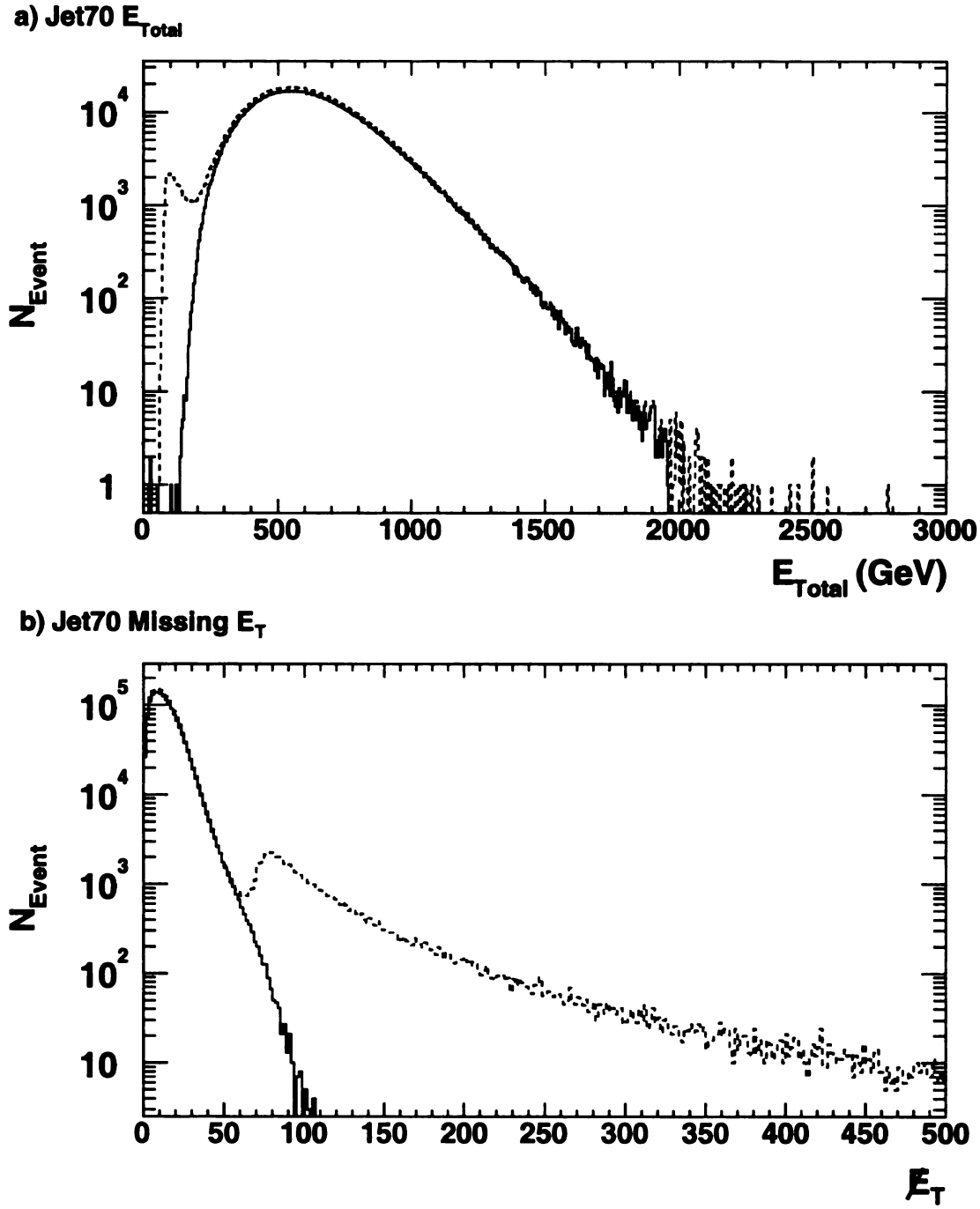

Figure 8.7: *Jet70 Kinematic variables.* E_{total}, $\not\!\!E_T$ *and* $\tilde{\not\!\!E}_T$ *before the selection cuts (dashed) and after (solid).*

figure 8.7 continued.

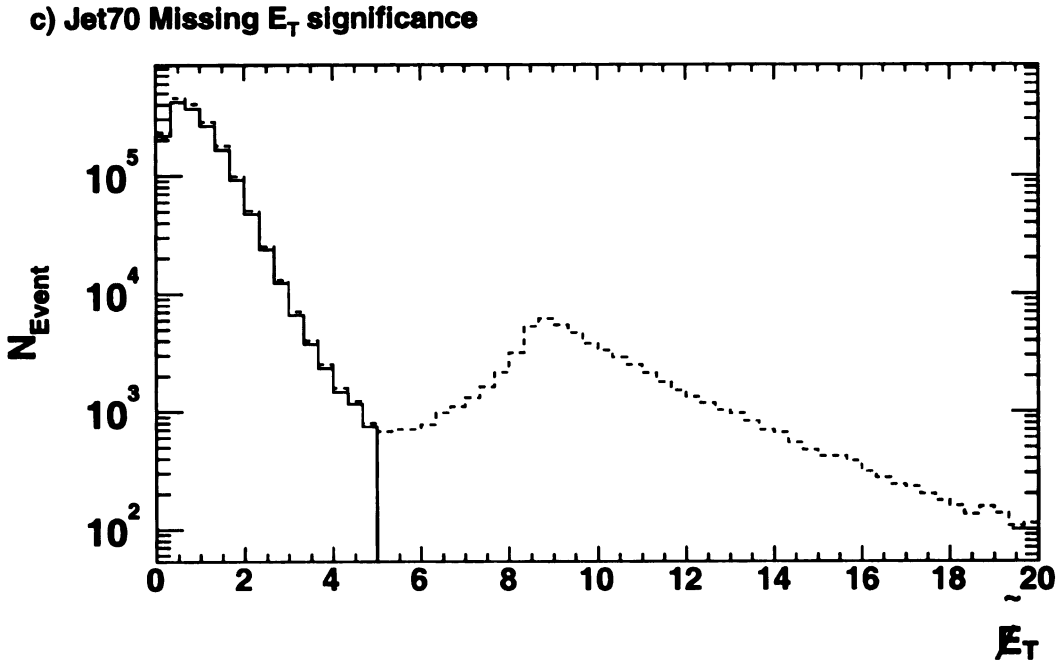

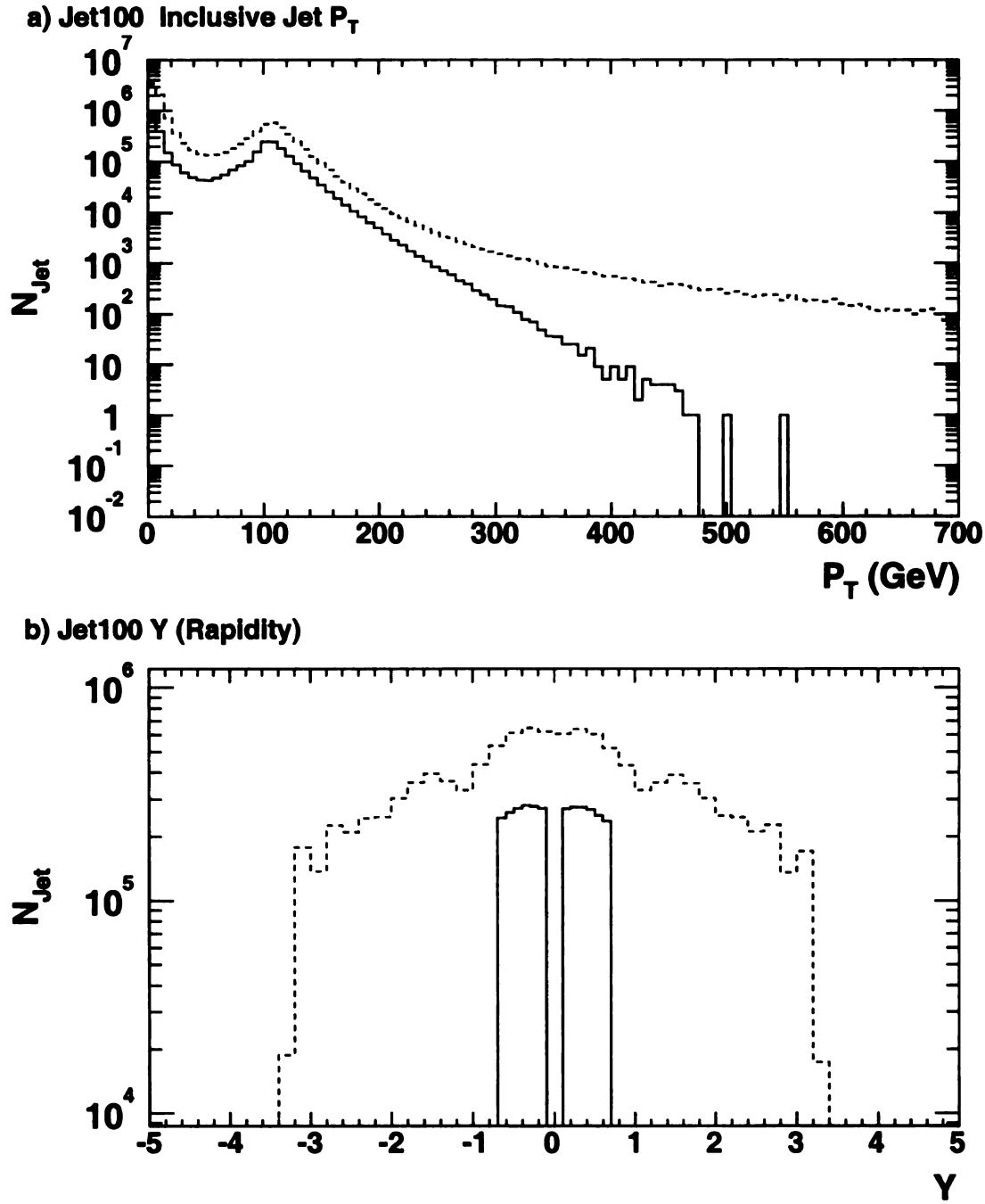

Figure 8.8: *Jet100 Kinematic variables: Inclusive P_T , Y and ϕ before cuts (dashed) and after cuts on $|Z| < 60cm$, $0.1 < |Y| < 0.7$, $E_{total} < 1960$ GeV and $\not\!\!E_T < 4$ (solid).*

figure 8.8 continued.

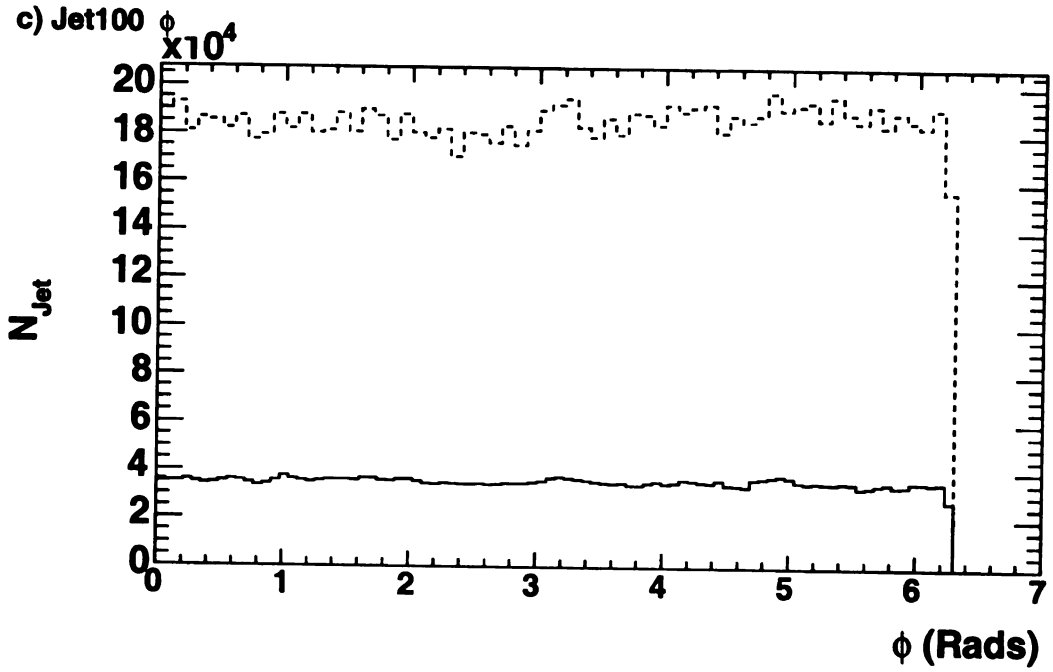

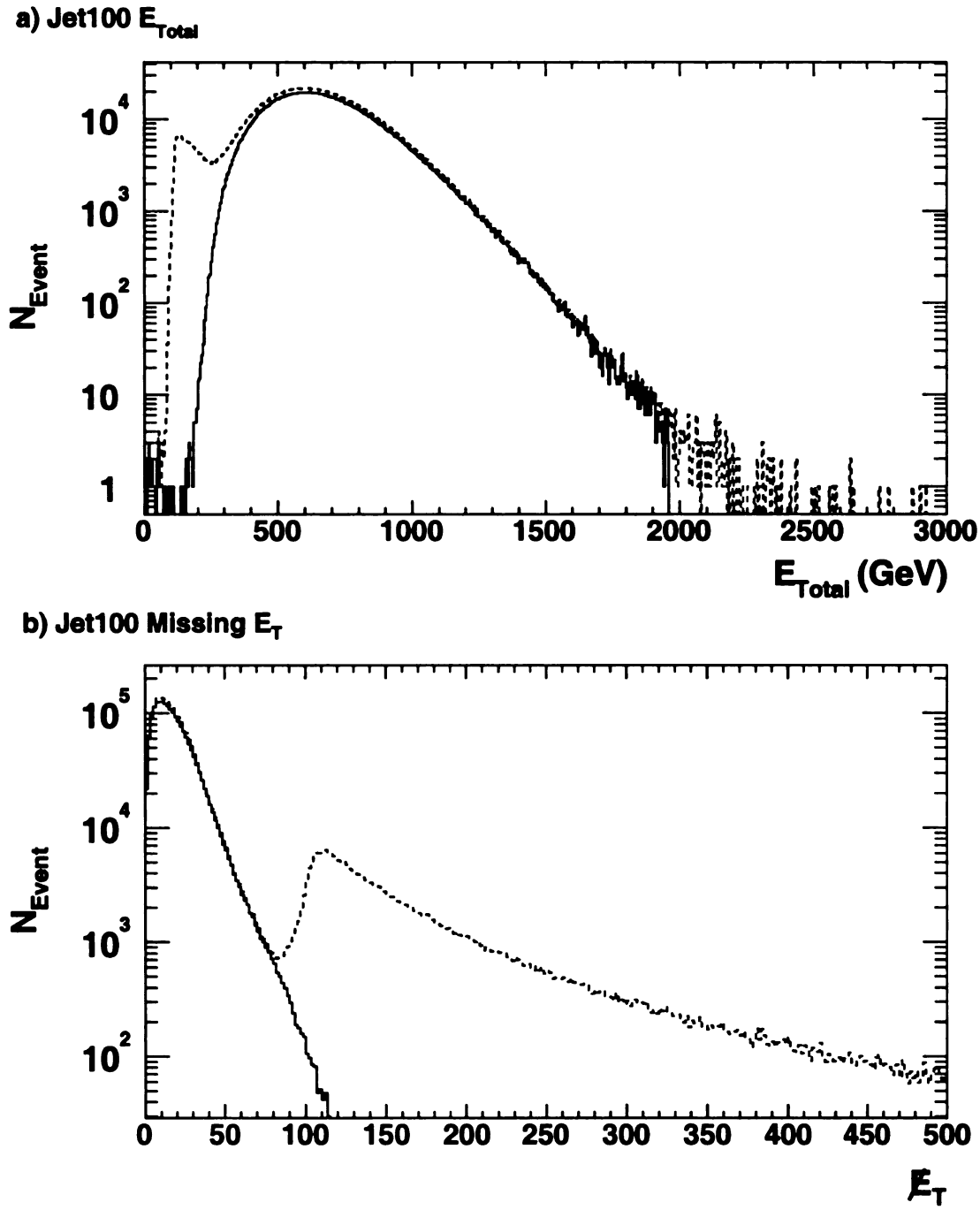

Figure 8.9: *Jet100 Kinematic variables.* E_{total}, $\not\!\!E_T$ *and* $\tilde{\not\!\!E}_T$ *before the selection cuts (dashed) and after (solid).*

figure 8.9 continued.

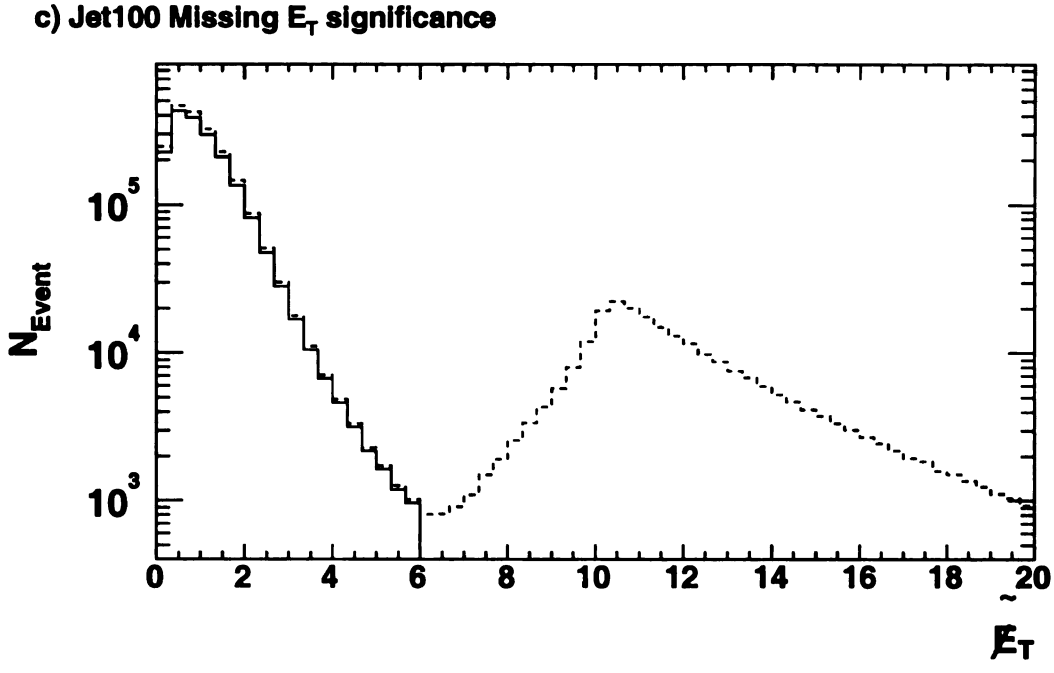

8.5 Backgrounds

Cosmic rays, accelerator loss backgrounds and detector noise were removed by cutting on the missing E_T significance, $\tilde{\not\!\!E}_T = \not\!\!E_T/\sqrt{\Sigma E_T}$, where the sum is over all towers in the calorimeter. The following figures show scatter plots of $\not\!\!E_T$ versus lead jet E_T and lead jet E_T versus ΣE_T. The plots show the quantities before the event selection cuts, after the $\tilde{\not\!\!E}_T$ and after all of the event selection cuts. No cut has been made on the rapidity of the individual jets in the figures that follow. From the figures we see that the Jet100 sample is the most affected by the cosmic background. The event and jet properties of jets in the three highest P_T cross section bins are scanned to make sure that we do not see cosmic events in the low statistics region of the cross section.

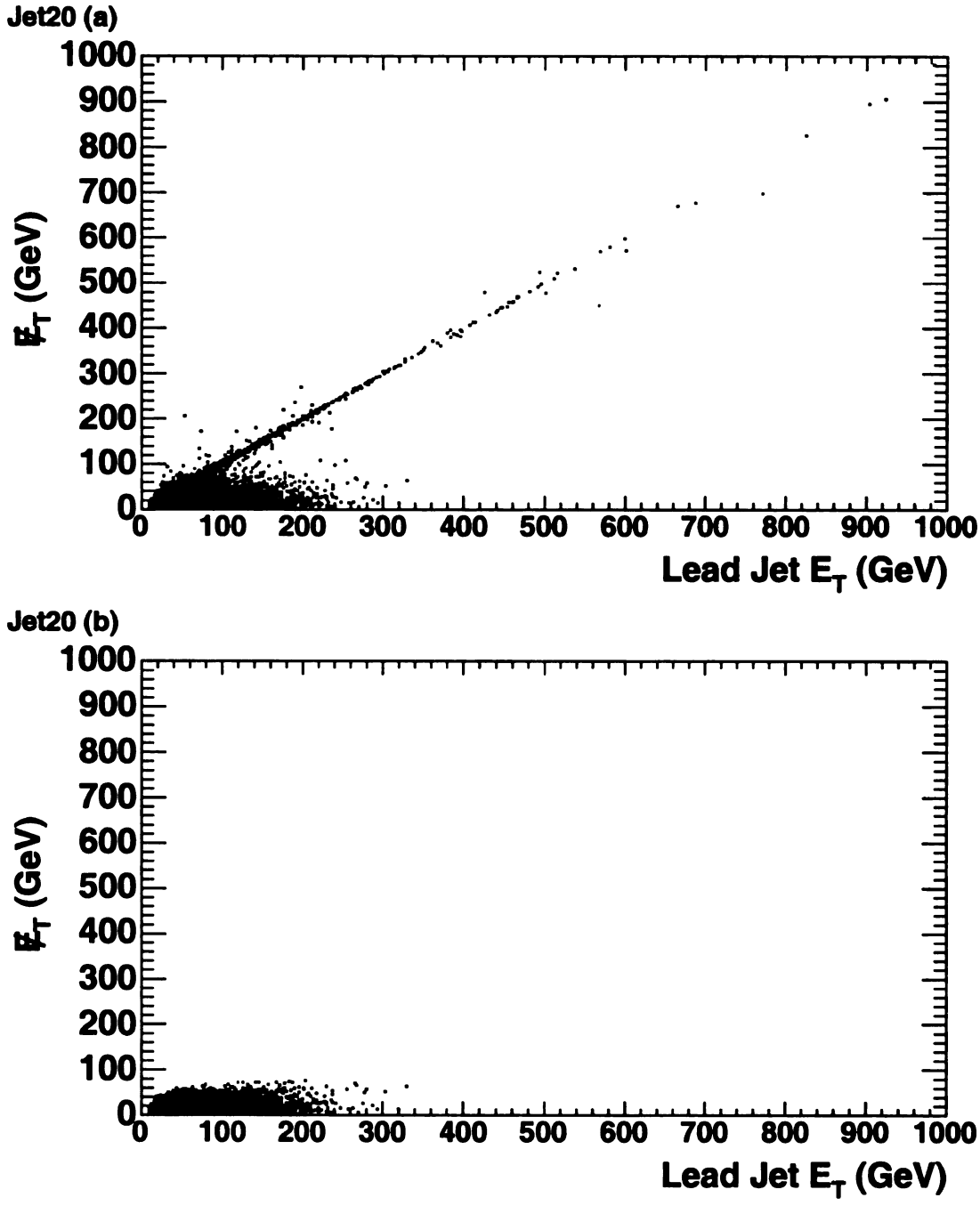

Figure 8.10: *Raw data distributions $\not\!\!E_T$ versus Leading jet for the jet20 trigger sample before selection cuts, after $\not\!\!\tilde{E}_T$ cut after all selection cuts.*

figure 8.10 continued.

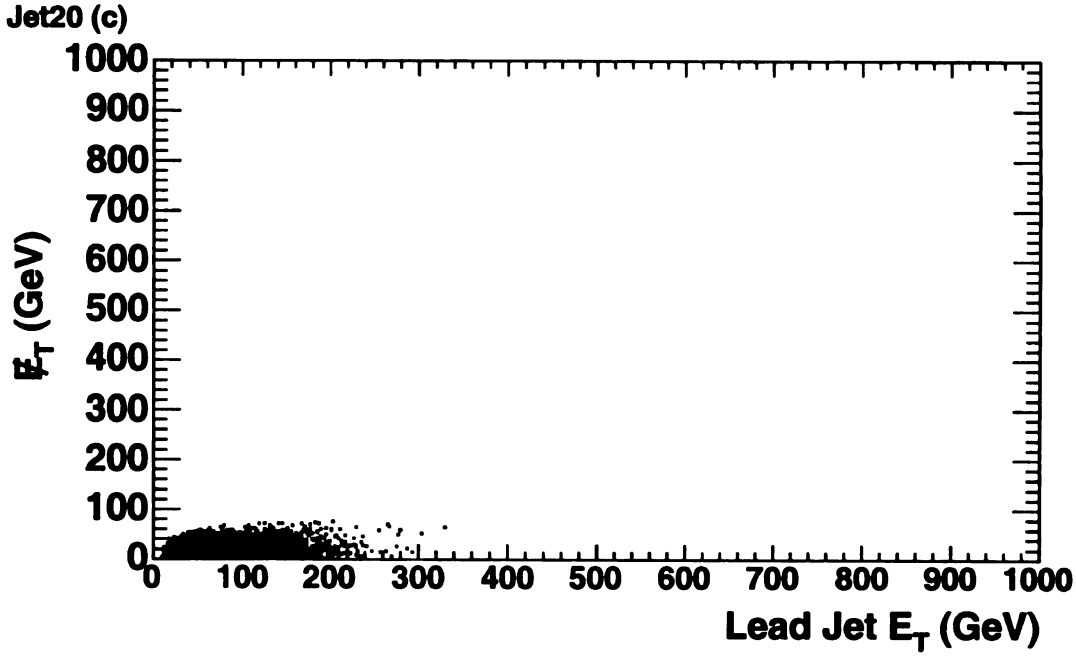

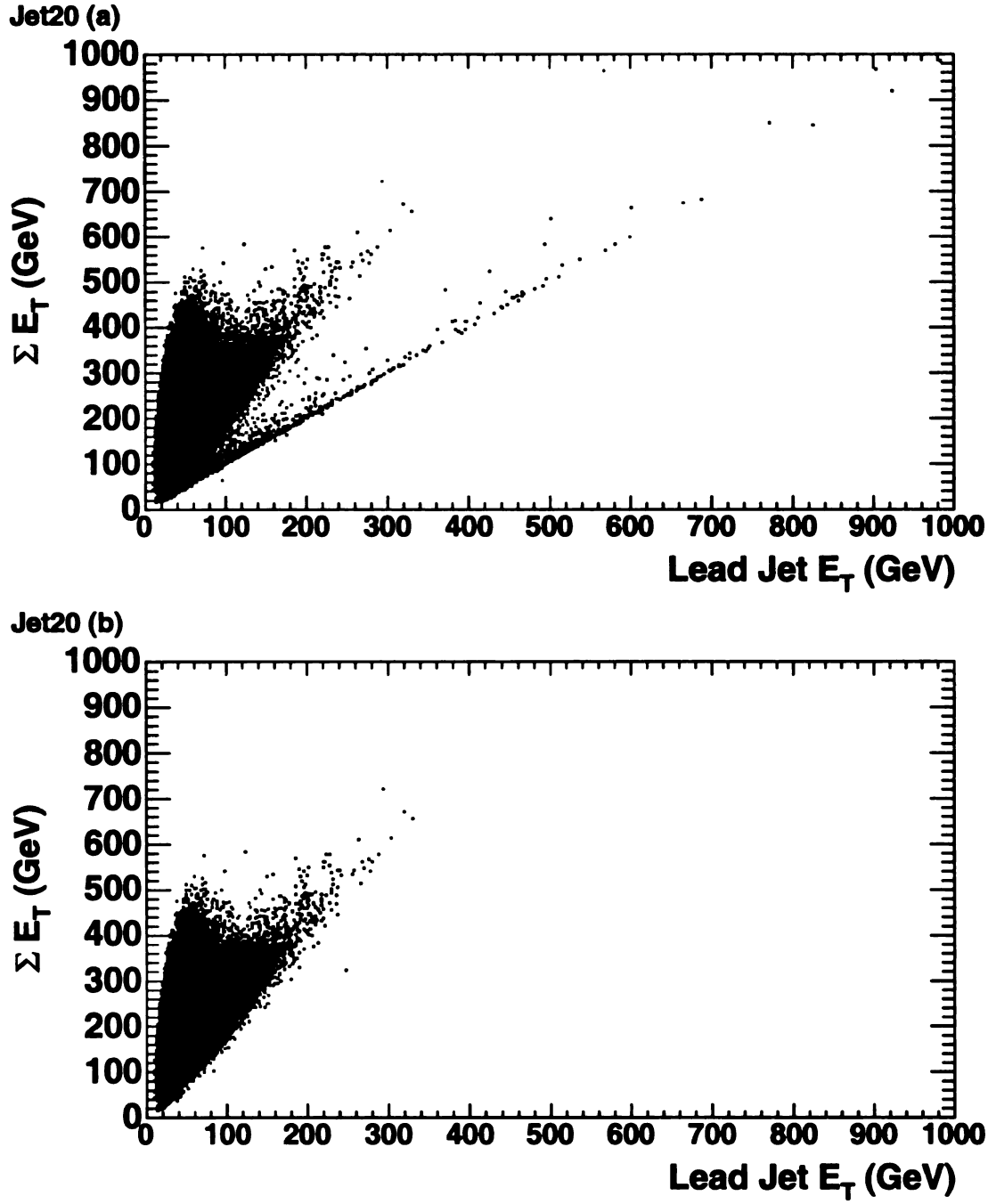

Figure 8.11: *Raw data distributions ΣE_T versus lead jet for the jet20 trigger sample before selection cuts, after $\not\!\!E_T$ cut after all selection cuts.*

figure 8.11 continued.

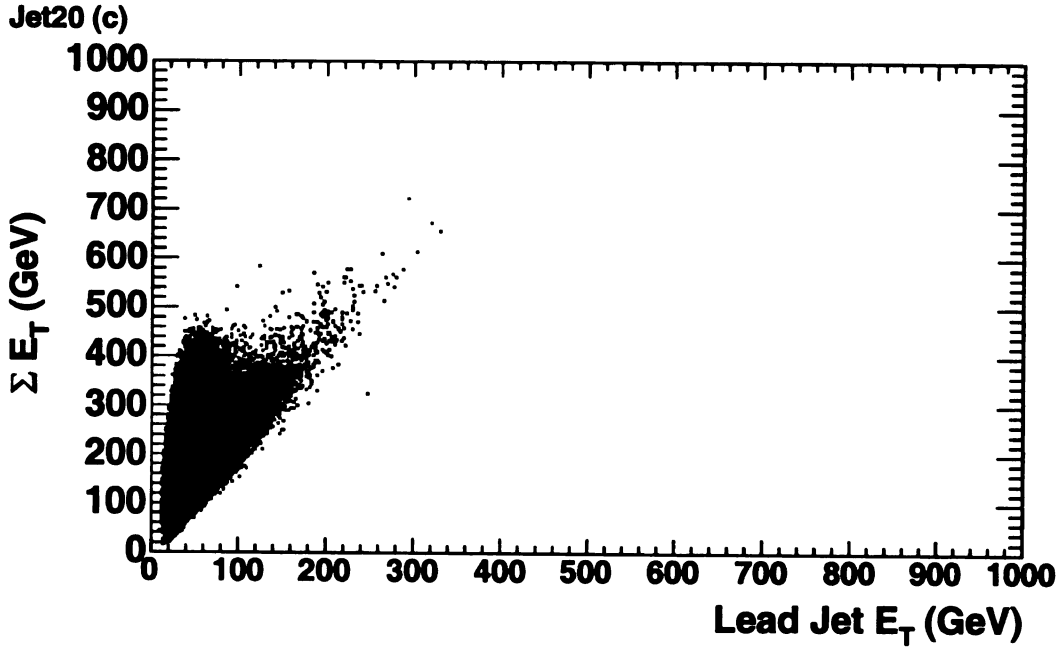

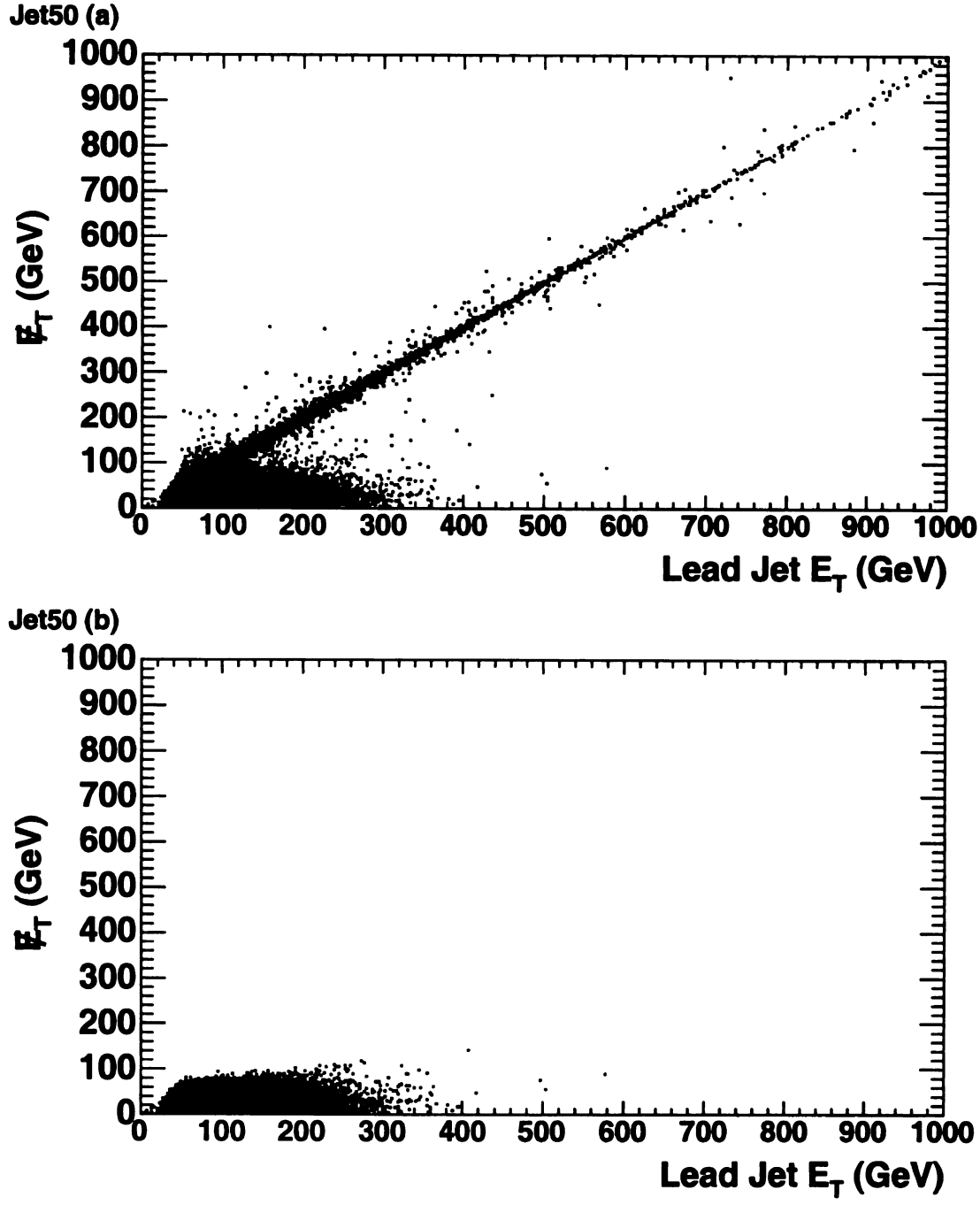

Figure 8.12: *Raw data distributions $\not\!\!E_T$ versus Leading jet for the jet50 trigger sample before selection cuts, after $\not\!\!\tilde{E}_T$ cut after all selection cuts.*

figure 8.12 continued.

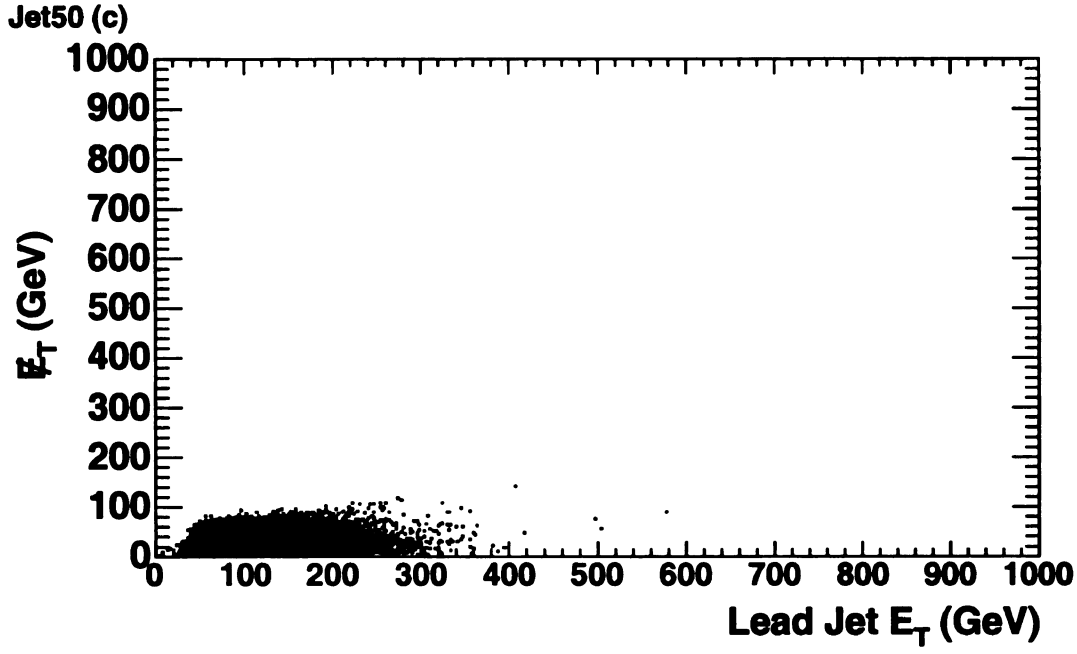

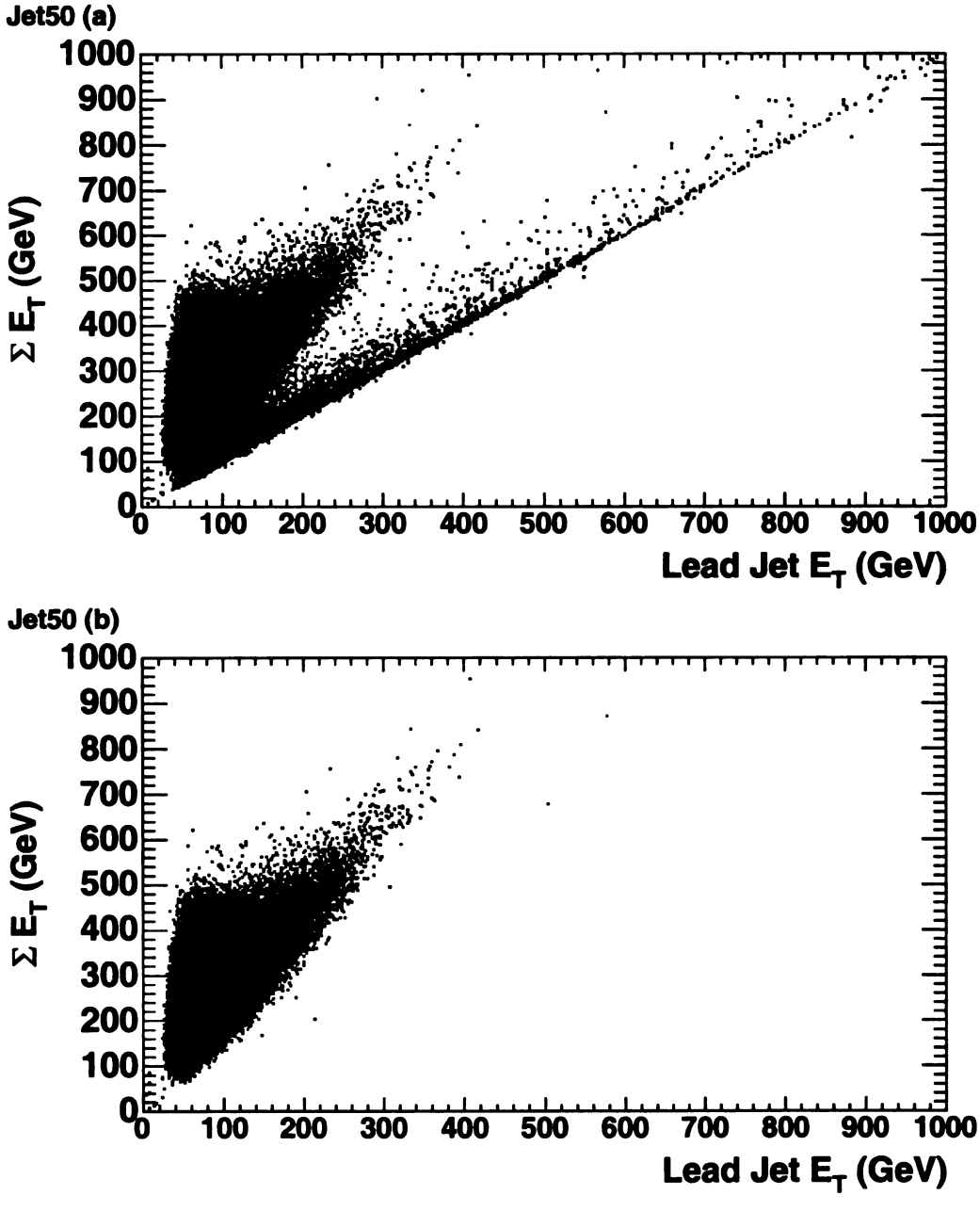

Figure 8.13: *Raw data distributions ΣE_T versus lead jet for the jet50 trigger sample before selection cuts, after $\not\!\!E_T$ cut after all selection cuts.*

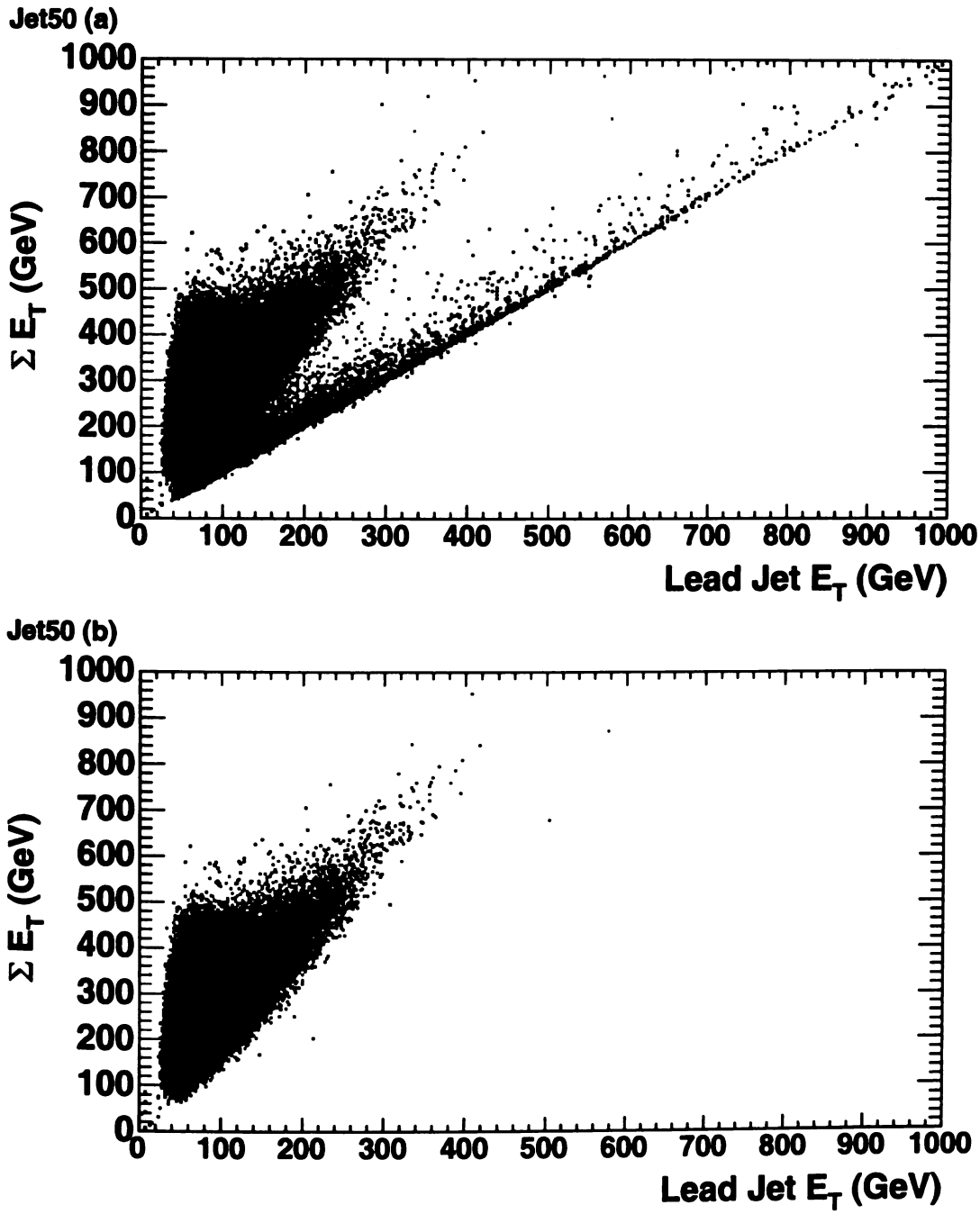

Figure 8.13: *Raw data distributions ΣE_T versus lead jet for the jet50 trigger sample before selection cuts, after $\not\!\!E_T$ cut after all selection cuts.*

figure 8.13 continued.

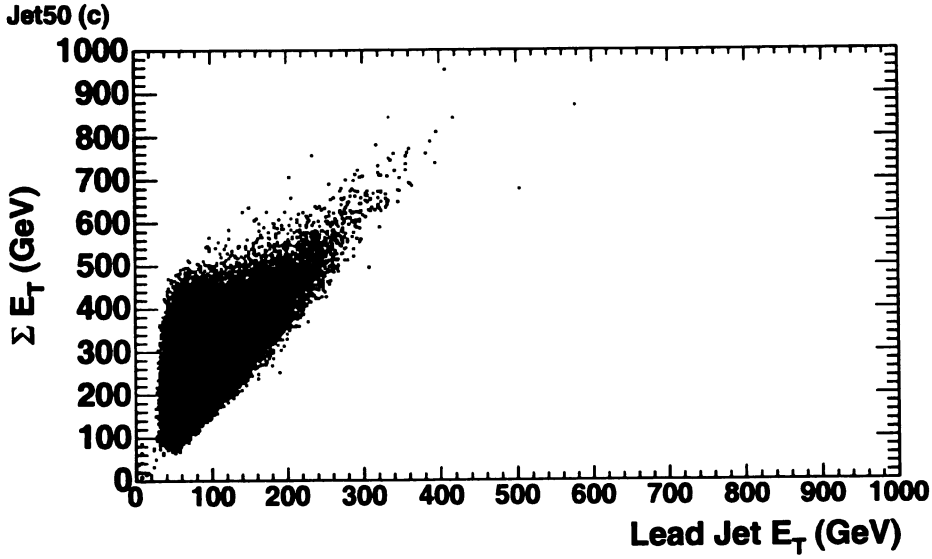

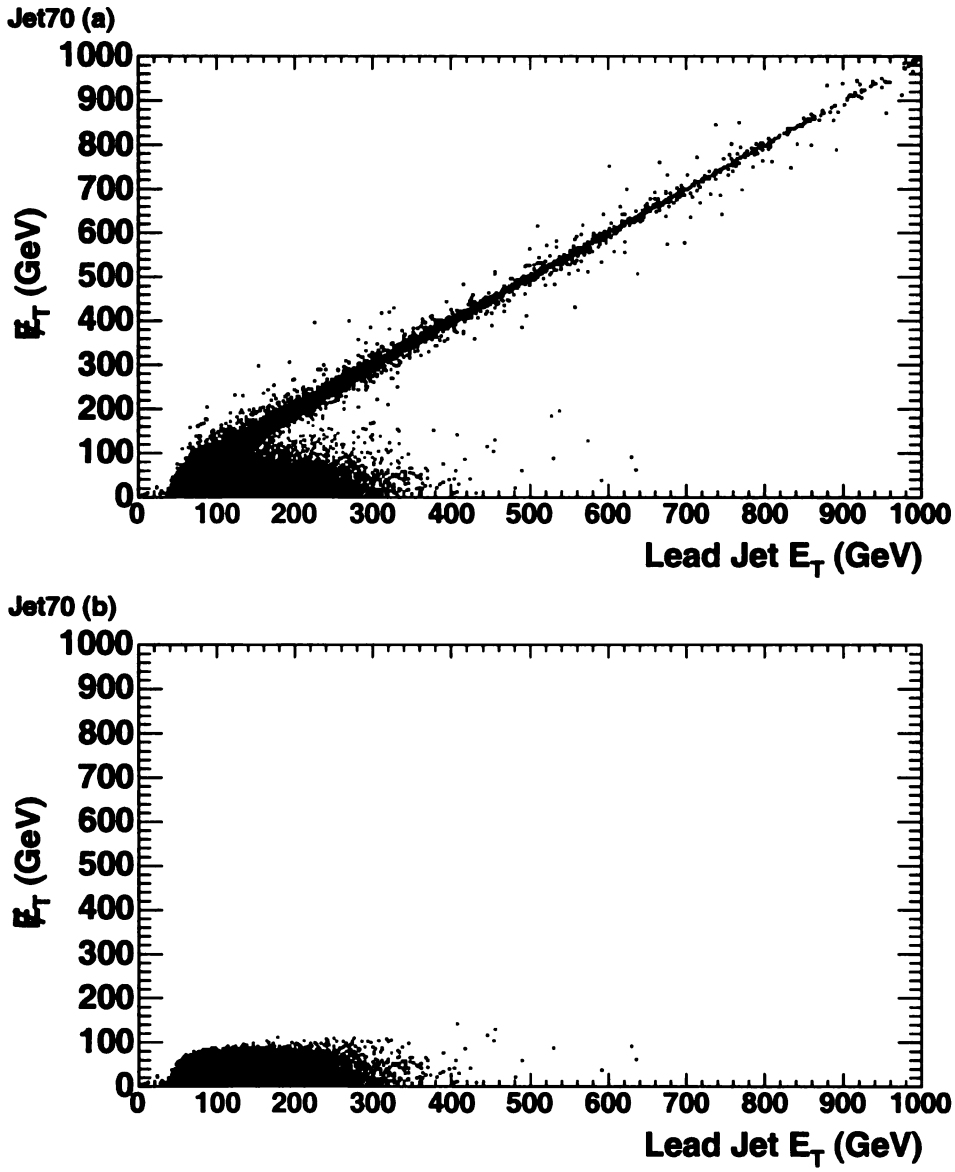

Figure 8.14: *Raw data distributions $\not\!\!E_T$ versus Leading jet for the jet70 trigger sample* ***before*** *selection cuts, after $\not\!\!\tilde{E}_T$ cut after all selection cuts.*

figure 8.14 continued.

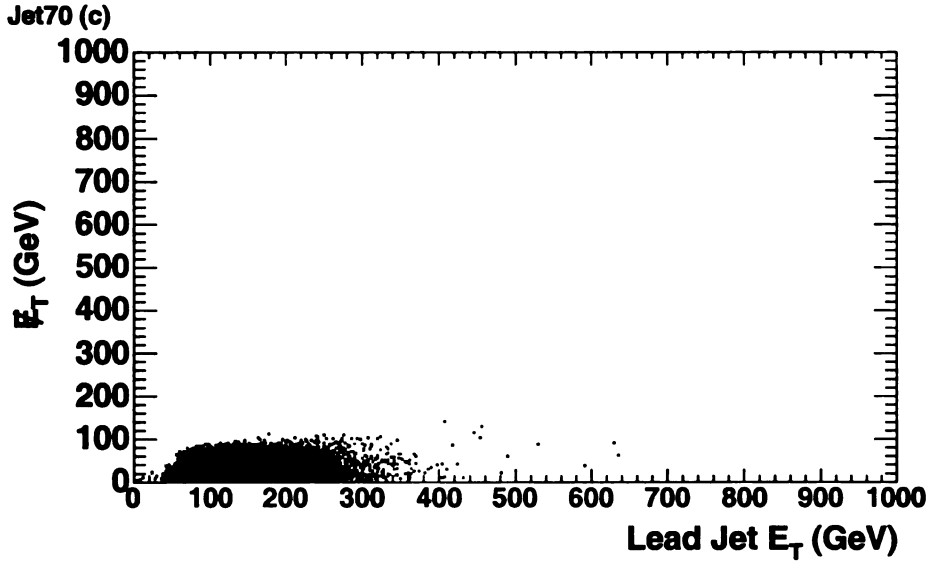

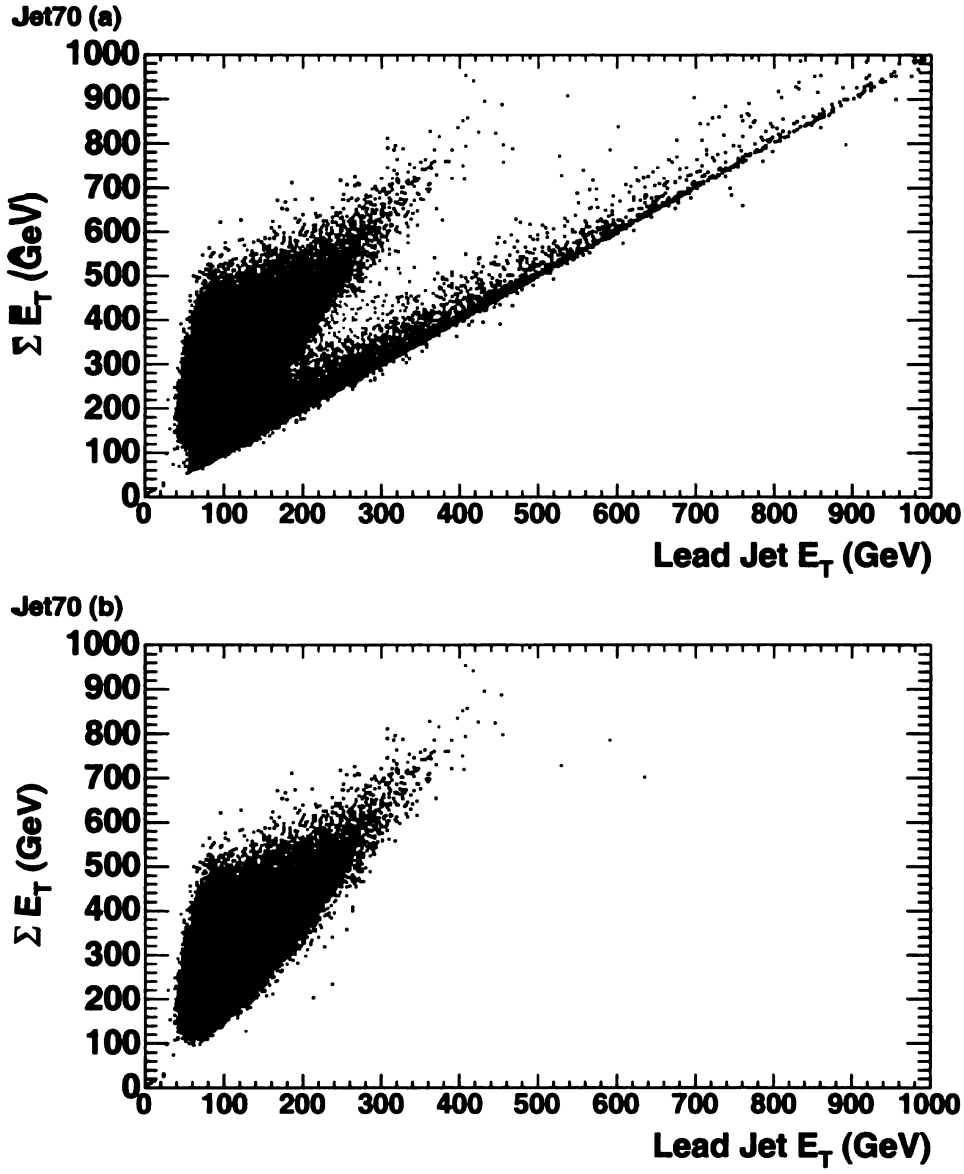

Figure 8.15: *Raw data distributions ΣE_T versus lead jet for the jet70 trigger sample* ***before*** *selection cuts, after $\not\!\!E_T$ cut after all selection cuts.*

figure 8.15 continued.

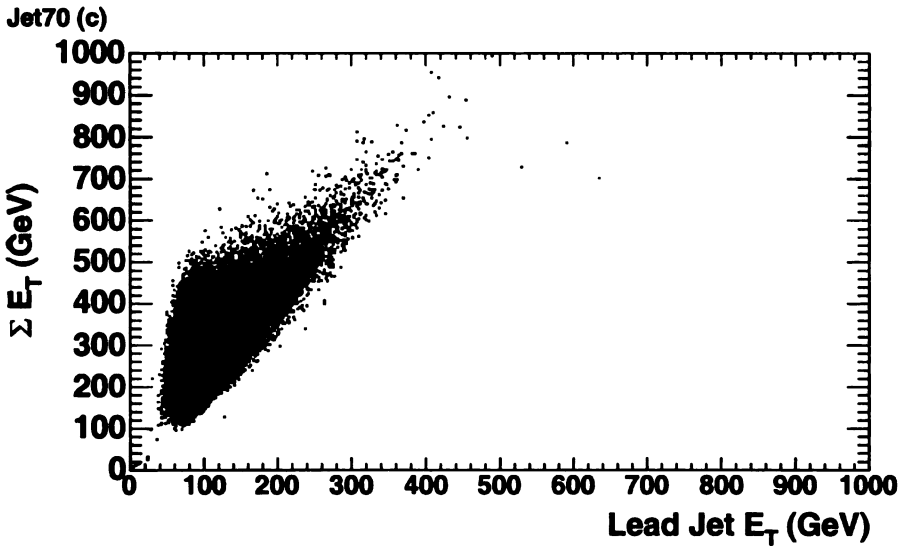

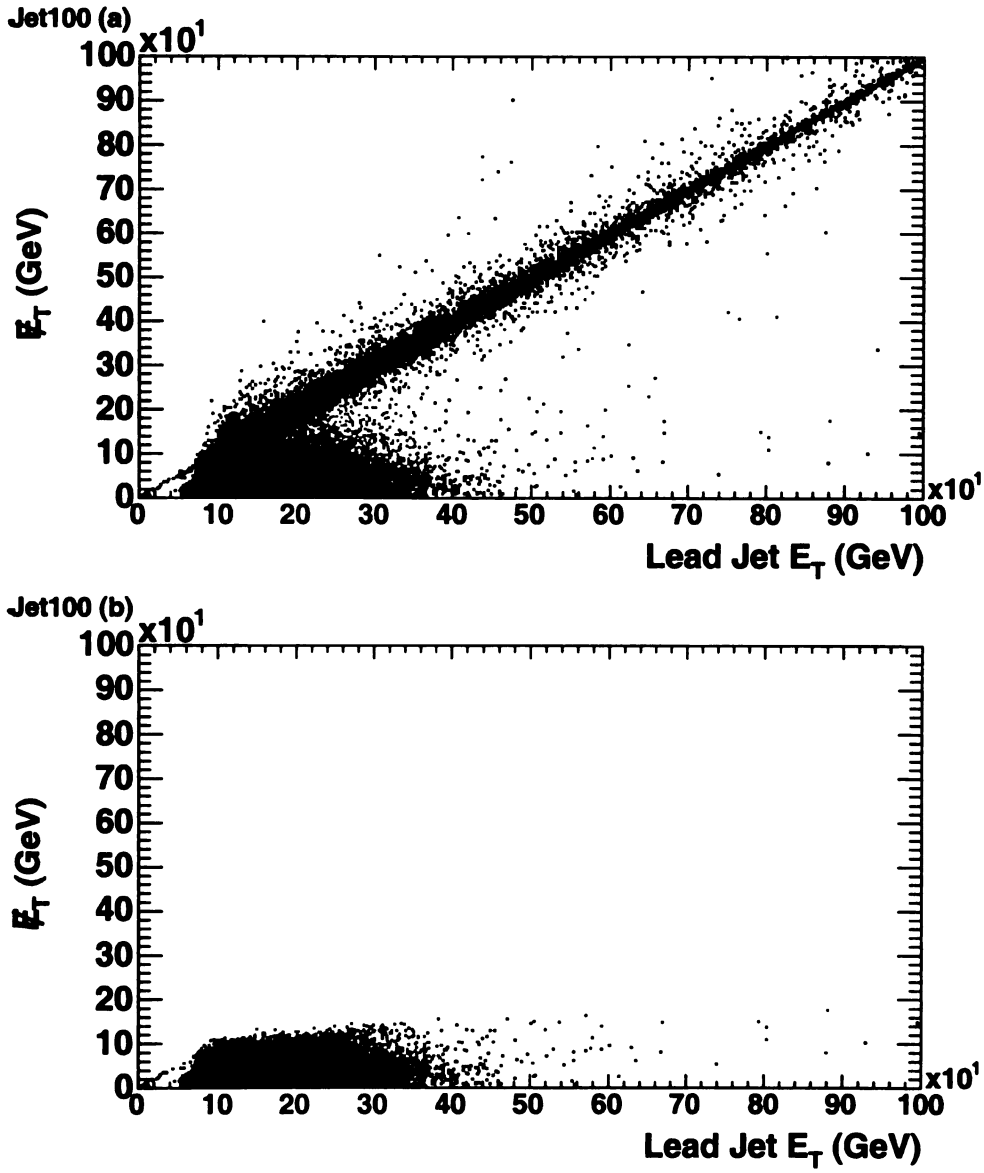

Figure 8.16: *Raw data distributions $\not\!\!E_T$ versus Leading jet for the jet100 trigger sample before selection cuts, after $\not\!\!\tilde{E}_T$ cut after all selection cuts.*

figure 8.16 continued.

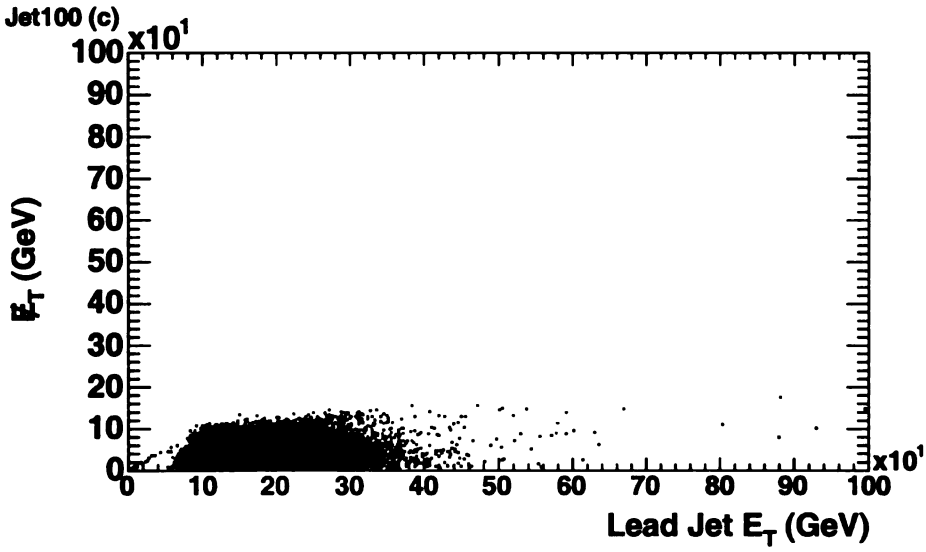

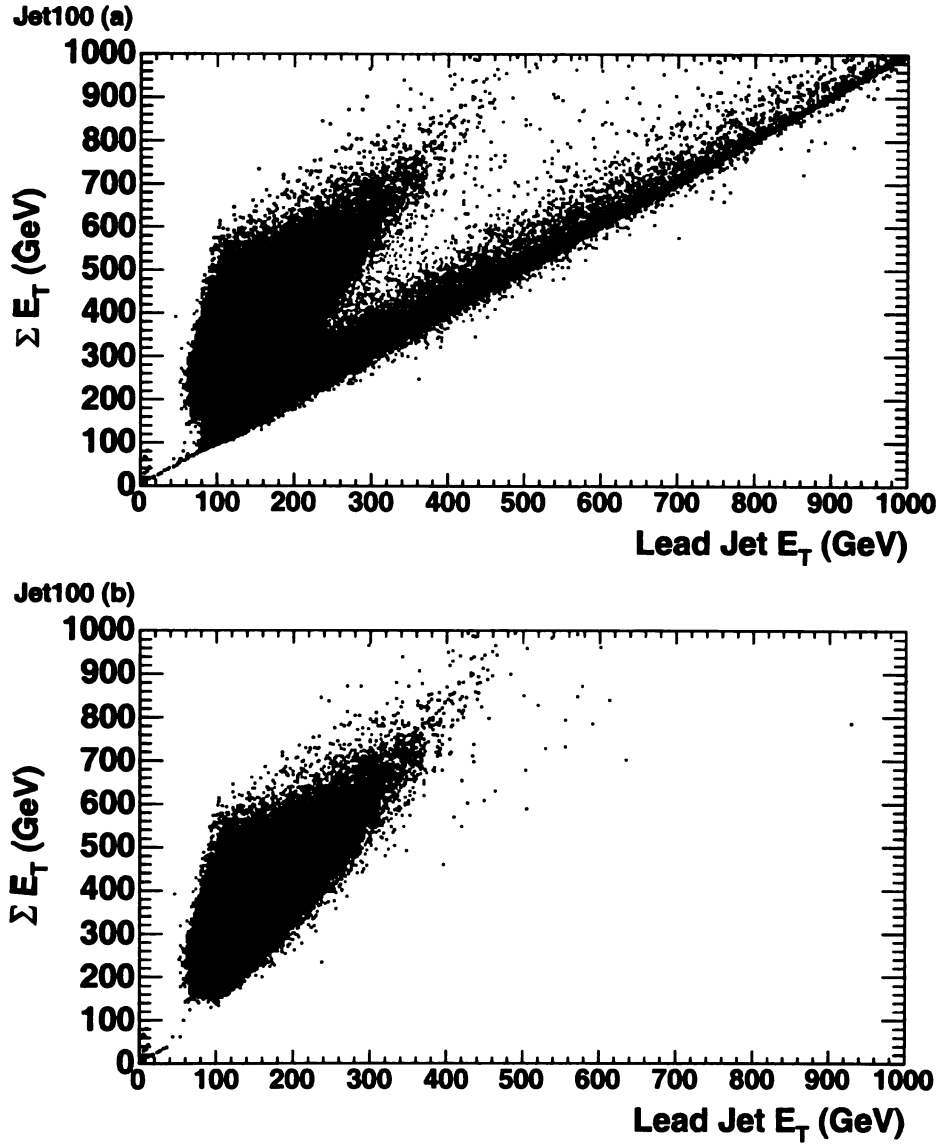

Figure 8.17: *Raw data distributions ΣE_T versus lead jet for the jet100 trigger sample* ***before*** *selection cuts, after $\not\!\!E_T$ cut after all selection cuts.*

figure 8.17 continued.

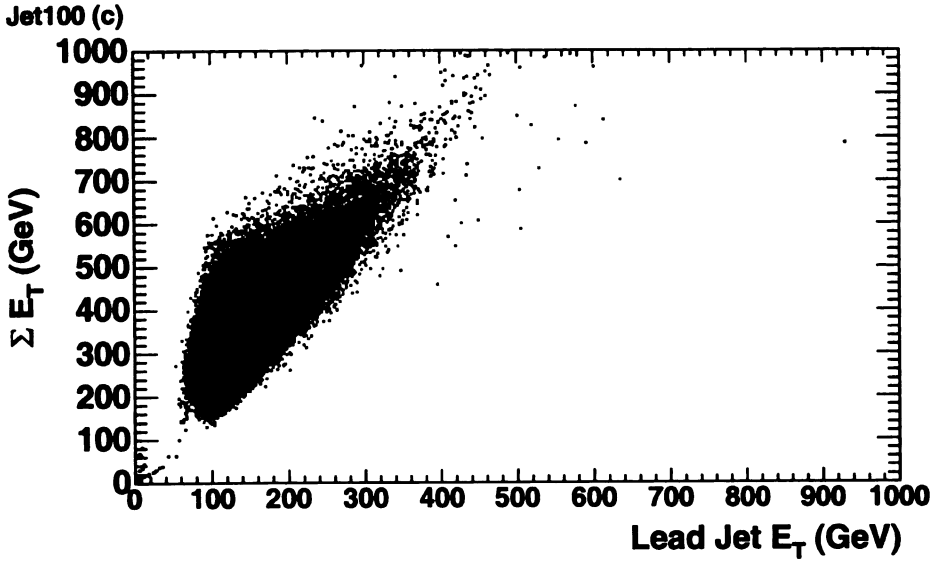

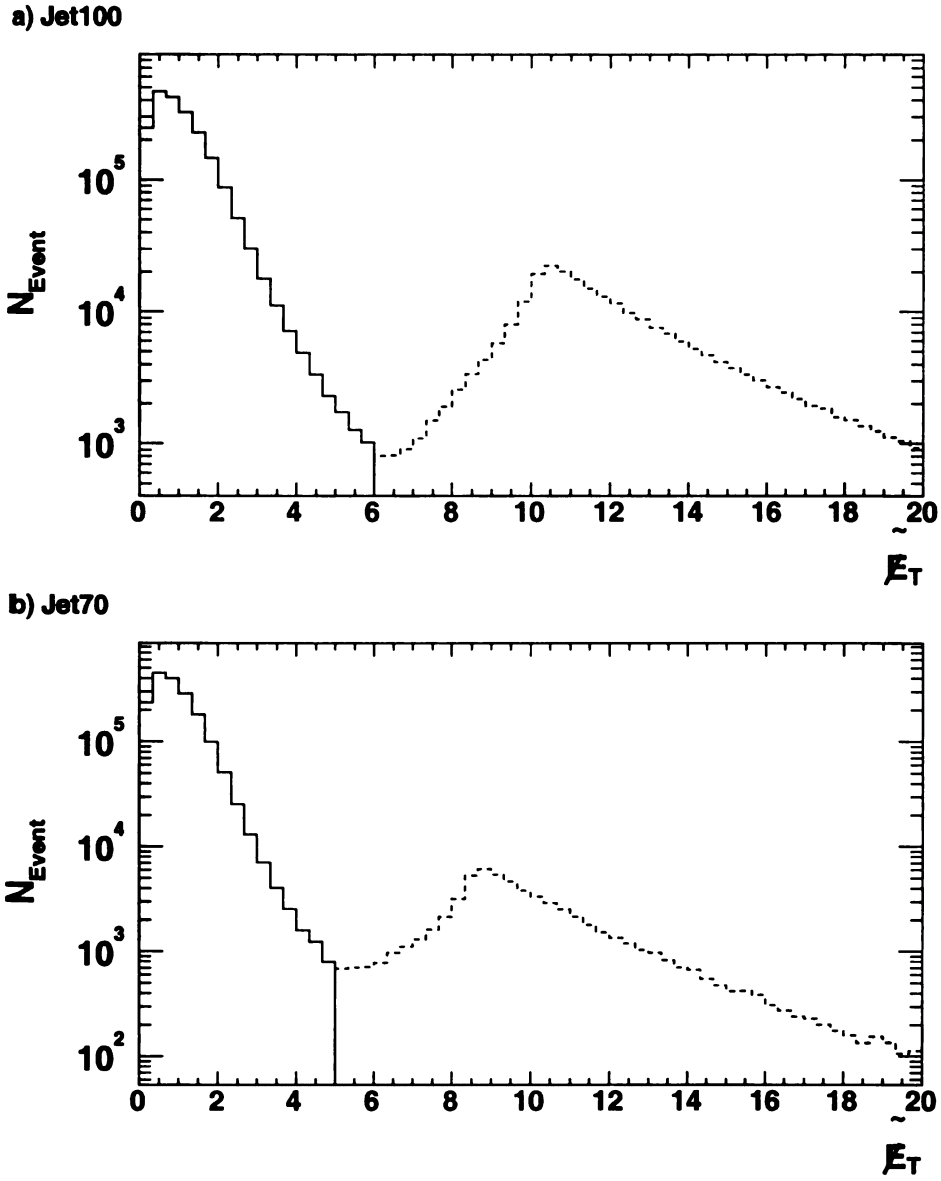

Figure 8.18: *$\tilde{\not{E}}_T$ before and after the $\tilde{\not{E}}_T$ cut for the jet20, jet50, jet70 and jet100 samples.*

figure 8.18 continued.

c) Jet50

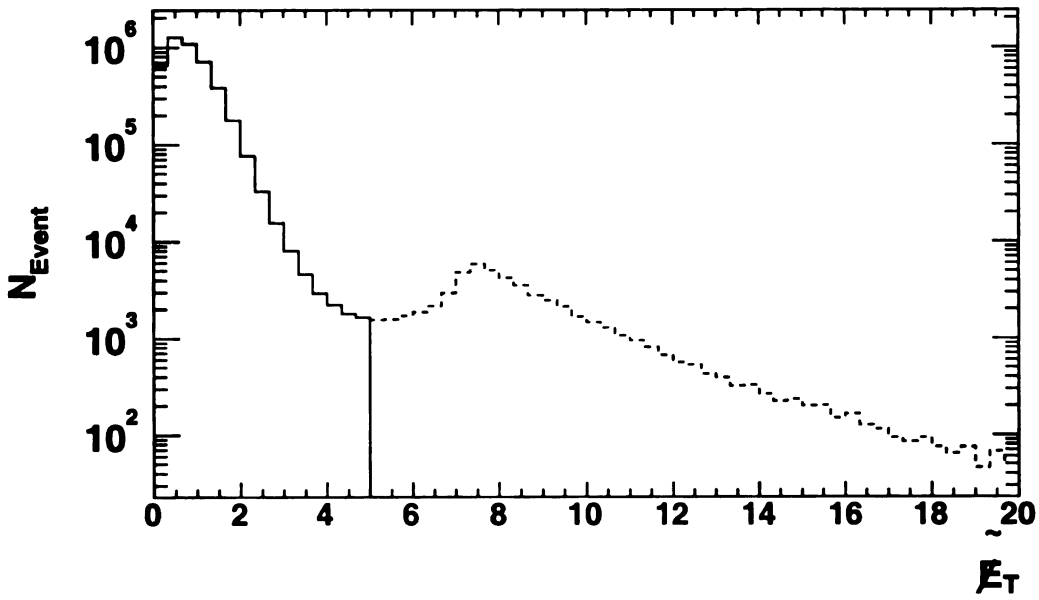

d) Jet20

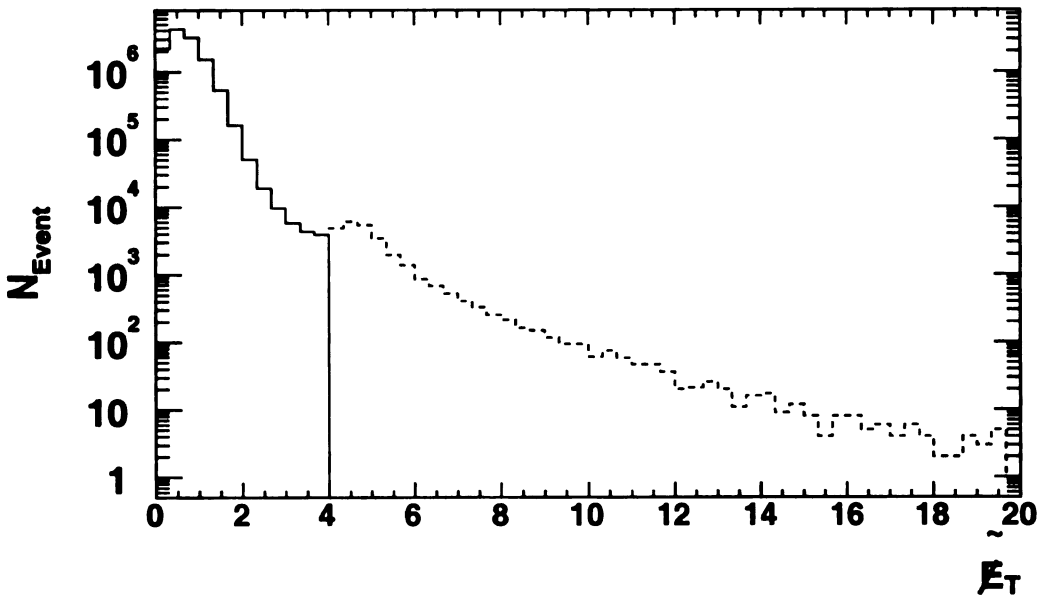

8.6 Raw Inclusive Jet Cross Section

The raw inclusive jet cross section is constructed by joining the inclusive jet cross sections found for the four jet triggers together into a single continuous cross section. Previously the trigger efficiency and prescales were measured for the jet trigger samples. The samples are combined by requiring that the trigger efficiency is greater that 995% and the prescales are used to scale the number of jets to that expected from the trigger path information. The inclusive cross section is defined as:

$$\frac{1}{\Delta Y}\int dY \frac{d\sigma}{dP_T dY} = \frac{1}{\Delta Y}\frac{1}{\int Ldt}\frac{N_{jet}/\epsilon}{\Delta P_T}, \tag{8.1}$$

where N_{jet}/ϵ is the number of jets in the P_T range ΔP_T corrected for trigger efficiency. $\int Ldt$ is the effective integrated luminosity including prescales and Z vertex correction. The rapidity range for the analysis ΔY is 1.2.

The statistical uncertainty on the measured cross section is calculated as

$$\begin{aligned}\delta\left(\frac{d^2\sigma}{dP_T dY}\right) &= \frac{\delta(N_{jet}/\epsilon)}{\int Ldt \Delta P_T \Delta Y} \\ &= \frac{d^2\sigma}{dP_T dY} \times \sqrt{(\delta N_{jet}/N_{jet})^2 + (\delta\epsilon/\epsilon)^2 + (\delta norm/norm)^2}, \end{aligned} \tag{8.2}$$

where $(\delta N_{jet}/N_{jet})$ comes from counting uncertainty in a given bin, $(\delta\epsilon/\epsilon)$ comes from the trigger efficiency calculation and $(\delta norm/norm)$ comes from the prescale calculation. The uncertainty on the luminosity is common for all data points and will be treated with the systematic errors.

P_T bin	N_{Jets}	Raw cross section (nb/GeV)	Stat. Err.
61-67	12615	3.67348	0.00156761
67-74	8250	2.0592	0.00108662
74-81	110696	1.22883	0.000839406
81-89	73903	0.717842	0.00060013
89-97	42896	0.416662	0.000457217
97-106	65610	0.247133	0.000331986
106-115	38731	0.145888	0.000255073
115-125	25838	0.0875914	0.000187502
125-136	138485	0.0505314	0.000135788
136-158	132231	0.0241247	6.63431e-05
158-184	55699	0.00859856	3.64336e-05
184-212	21570	0.00309203	2.10532e-05
212-244	8268	0.00103706	1.14052e-05
244-280	3115	0.000347302	6.22269e-06
280-318	1051	0.000111012	3.42428e-06
318-360	322	3.07722e-05	1.71487e-06
360-404	101	9.21341e-06	9.16768e-07
404-464	38	2.54205e-06	4.12375e-07
464-530	2	1.21629e-07	8.60048e-08
530-620	1	4.45973e-08	4.45973e-08

Table 8.4: *Raw inclusive jet cross section. Horizontal lines indicate trigger boundries. The Jet20 trigger is used in the P_T range* $50 - 74$ *GeV, Jet50:* $74 - 97$ *GeV, Jet70:* $97 - 125$ *GeV and Jet100 used for* $P_T > 125$ *GeV*

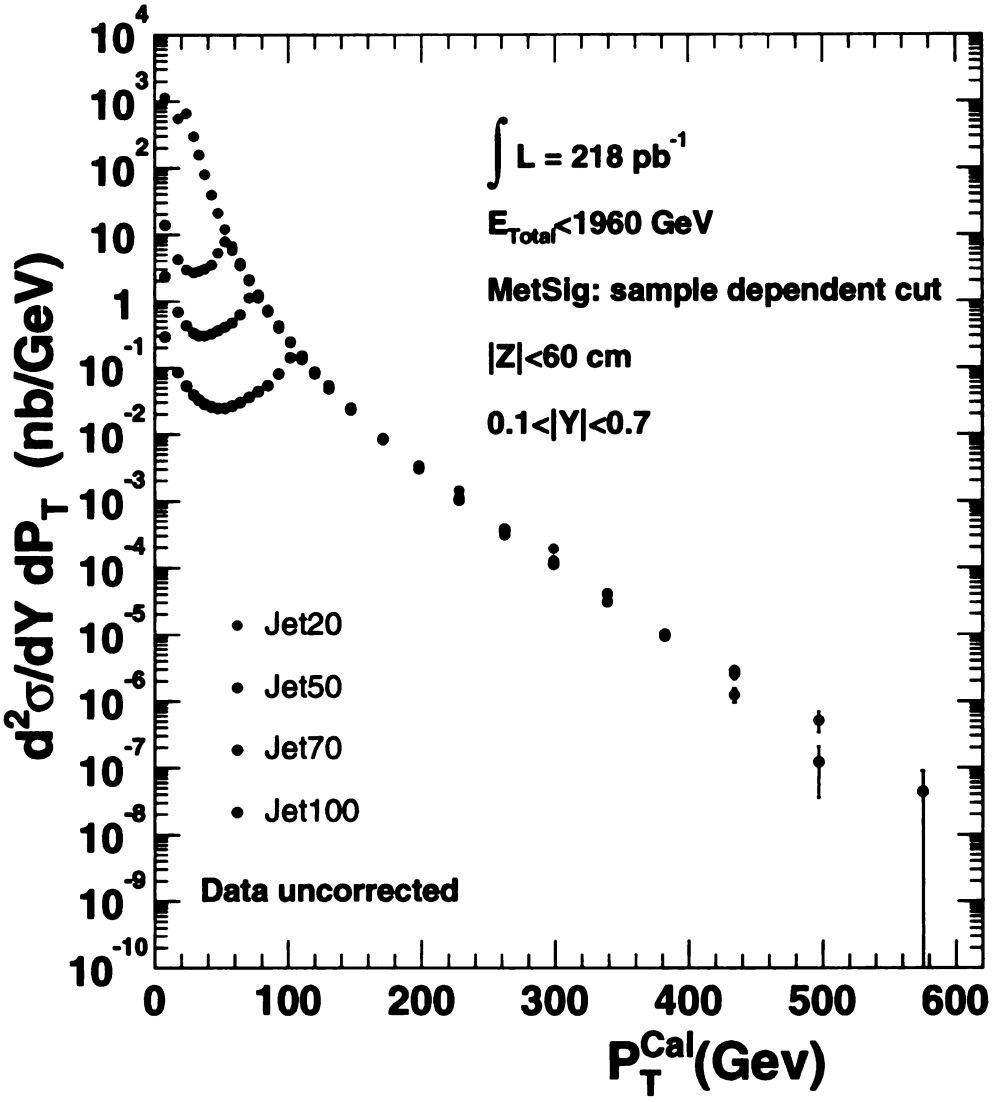

Figure 8.19: *Uncorrected inclusive jet cross section as a function of P_T, statistical errors only.*

Run	Event	P_T (GeV)	Y	EMF
143257	276943	401.184	0.398734	0.548158
145045	684636	412.519	-0.280769	0.12729
149387	4690452	437.213	-0.367935	0.354751
151555	1596656	411.366	0.100372	0.49213
152518	581053	457.819	0.116822	0.443789
153075	2273678	429.232	-0.65286	0.554674
153075	2273678	406.475	0.53179	0.5404
153374	1420764	400.446	0.260724	0.335107
153618	774625	455.659	-0.512773	0.966693
153447	4457374	410.003	-0.365903	0.467246
154208	885533	454.803	-0.407754	0.579744
154208	885533	415.526	0.237643	0.516058
155129	2465699	439.705	-0.282757	0.219059
155364	72998	549.186	-0.349703	0.826778
155997	1270890	403.824	0.233282	0.554097
156116	942464	416.51	-0.125138	0.511041
161633	4356826	463.062	0.181779	0.477635
161714	580900	426.88	-0.65474	0.761816
161714	580900	401.172	-0.195772	0.623039
162423	7395708	413.256	-0.134176	0.553815
162423	406758	444.049	-0.273213	0.466517
162423	406758	403.282	0.277389	0.363556
162423	2703418	403.149	0.305488	0.539976
162396	1039796	461.466	0.499424	0.398409
162498	4411694	453.453	0.372285	0.468243
162631	890671	409.185	-0.642414	0.723598
162631	10531661	418.287	-0.469212	0.558444
163130	531768	442.902	-0.36703	0.348904
164989	2549548	443.148	0.32768	0.477917
165064	108597	423.084	0.40578	0.350614
166328	378124	439.903	-0.54438	0.117618
166662	5668262	401.974	-0.169606	0.331801
166662	5668262	401.986	0.560265	0.614567
167023	1813038	413.845	0.548813	0.418639
166927	8320832	449.278	0.225822	0.615626
166927	8320832	432.747	0.570658	0.593227
167297	1155843	497.889	-0.206923	0.361894
167954	2035694	433.498	0.166443	0.556618

Table 8.5: *Jet properties for jets with P_T above 400 GeV.*

Table 8.5 continued

Run	Event	P_T (GeV)	Y	EMF
168089	144763	415.191	-0.612085	0.870442
175066	151109	404.304	0.210371	0.471045
177316	2847553	413.749	-0.417775	0.200374
177316	2847553	415.868	-0.106148	0.388122
177339	1691542	442.926	-0.254262	0.694501
177339	1691542	432.401	0.298508	0.291503
177418	407378	475.227	0.284872	0.590199
177624	2485205	413.335	-0.223299	0.33967
178758	682071	449.035	0.206208	0.310963
178758	682071	436.161	-0.664422	0.579327
178921	82234	430.563	-0.604363	0.486315
166927	8320832	449.278	0.225822	0.615626
166927	8320832	432.747	0.570658	0.593227
167297	1155843	497.889	-0.206923	0.361894
167954	2035694	433.498	0.166443	0.556618
168089	144763	415.191	-0.612085	0.870442
175066	151109	404.304	0.210371	0.471045
177316	2847553	413.749	-0.417775	0.200374
177316	2847553	415.868	-0.106148	0.388122
177339	1691542	442.926	-0.254262	0.694501
177339	1691542	432.401	0.298508	0.291503
177418	407378	475.227	0.284872	0.590199
177624	2485205	413.335	-0.223299	0.33967
178758	682071	449.035	0.206208	0.310963
178758	682071	436.161	-0.664422	0.579327
178921	82234	430.563	-0.604363	0.486315

Run	Event	NJets	NQ12Zv	Z (cm)	$\not\!\!E_T$ $(\sqrt{GeV})^{-1}$	E_{Total} (GeV)
143257	276943	3	1	-7.320	0.41908	1095.66
145045	684636	3	1	24.352	3.61982	1063.03
149387	4690452	8	1	5.662	3.82993	1082.47
151555	1596656	5	1	31.348	1.62779	1108.12
152518	581053	4	2	-7.958	0.371944	1123.27
153075	2273678	5	3	2.595	0.384346	1355.99
153075	2273678	5	3	2.595	0.384346	1355.99
153374	1420764	3	1	42.643	0.307279	1187.97
153618	774625	3	1	-10.838	4.54881	978.67
153447	4457374	4	2	13.980	0.303175	1138.04
154208	885533	8	2	-7.697	1.09069	1556.66
154208	885533	8	2	-7.697	1.09069	1556.66
155129	2465699	3	1	47.026	2.07085	1336.67
155364	72998	4	1	59.586	0.44107	1409.28
155997	1270890	4	1	-4.561	0.988793	1064.22
156116	942464	3	2	-46.612	1.71779	1142.24
161633	4356826	6	2	47.737	2.28901	1255.08
161714	580900	8	3	24.536	0.603169	1585.65
161714	580900	8	3	24.536	0.603169	1585.65
162423	7395708	3	1	4.765	1.43176	928.99
162423	406758	4	2	18.907	0.29795	1072.9
162423	406758	4	2	18.907	0.29795	1072.9
162423	2703418	2	1	31.102	0.394673	885.545
162396	1039796	6	2	8.199	0.283313	1197.74
162498	4411694	7	3	17.884	1.12226	1462.44
162631	890671	4	1	19.217	1.00378	1124.75
162631	10531661	4	1	-41.588	0.14247	1351.46
163130	531768	5	1	-16.563	1.41608	1160.1
164989	2549548	8	2	3.114	2.32176	1374.86
165064	108597	4	2	-50.157	1.65477	1144.98
166328	378124	7	1	-2.406	1.4873	1182.97
166662	5668262	8	3	26.036	0.873594	1484.85
166662	5668262	8	3	26.036	0.873594	1484.85
167023	1813038	3	1	0.246	1.39682	1008.47
166927	8320832	4	1	27.501	0.912677	1299.43
166927	8320832	4	1	27.501	0.912677	1299.43
167297	1155843	2	3	13.239	0.843306	1246.78
167954	2035694	4	1	-18.591	4.01535	1010.95

Table 8.6: *Event properties for jets with P_T above 400 GeV.*

Table 8.6 continued

Run	Event	NJets	NQ12Zv	Z (cm)	$\not\!\!E_T$ $(\sqrt{GeV})^{-1}$	E_{Total} (GeV)
168089	144763	6	1	37.156	2.76191	1362.88
175066	151109	4	1	20.595	0.855962	1068.8
177316	2847553	2	1	6.539	0.308571	930.435
177316	2847553	2	1	6.539	0.308571	930.435
177339	1691542	10	2	11.709	0.522452	1544.84
177339	1691542	10	2	11.709	0.522452	1544.84
177418	407378	8	2	-25.408	0.650897	1538
177624	2485205	8	2	16.594	1.58629	1268.15
178758	682071	2	1	-19.495	0.486888	1074.41
178758	682071	2	1	-19.495	0.486888	1074.41
178921	82234	12	2	6.503	0.966076	1510
166927	8320832	4	1	27.501	0.912677	1299.43
166927	8320832	4	1	27.501	0.912677	1299.43
167297	1155843	2	3	13.239	0.843306	1246.78
167954	2035694	4	1	-18.591	4.01535	1010.95
168089	144763	6	1	37.156	2.76191	1362.88
175066	151109	4	1	20.595	0.855962	1068.8
177316	2847553	2	1	6.539	0.308571	930.435
177316	2847553	2	1	6.539	0.308571	930.435
177339	1691542	10	2	11.709	0.522452	1544.84
177339	1691542	10	2	11.709	0.522452	1544.84
177418	407378	8	2	-25.408	0.650897	1538
177624	2485205	8	2	16.594	1.58629	1268.15
178758	682071	2	1	-19.495	0.486888	1074.41
178758	682071	2	1	-19.495	0.486888	1074.41
178921	82234	12	2	6.503	0.966076	1510

Chapter 9

Jet Corrections

9.1 Introduction

We wish to make a measurement of the hadron/parton level inclusive jet cross section as a funtion of jet P_T. In an *ideal* detector we could measure the jet P_T's in every event and the cross section would be given simply by normalising the resulting histogram for acceptance and luminosity. However, we do not have an *ideal* detector and the determination of the inclusive cross section is complicated by several effects:

- Background events from cosmics, detector noise and beam halo are present in the raw data.
- Not all jets are observed in the detector due to finite efficiency of the detector for hadron level jets at the calorimeter level.
- The measured transverse momentum P_T^{Cal} is smeared due to finite resolution of the detector. This smearing will cause migrations of jets in P_T.
- The measured P_T of a jet underestimates the original hadron level P_T by up to $\sim 20\%$. Like the previous point, this effect also leads to P_T smearing of the true hadron level cross section.

The background events are removed by the selection cuts applied when constructing the raw cross section (see section 8.5). No further correction needs to be made for background after that. The efficiency of the calorimeter for detecting jets was studied in Pythia. It was found that for hadron level jets with P_T above 25 GeV the detector is 100% efficient, *i.e.* there will always be a matching calorimeter level jet.

To facilitate comparison of the results to theory or other experiments we need to remove the detector effects. After the detector effects are removed we have a measure of the hadron level inclusive jet cross section. For comparison to NLO pQCD an additional correction to remove the underlying event contribution to the energy in the jet cone and the fragmentation losses from the jet cone will also be needed.

The jet corrections employed to remove the detector effects are based on Pythia events that have passed through a detector simulation. The calorimeter to hadron level jet corrections were made in two steps:

- Average P_T^{Jet} correction to remove the energy losses of hadrons going through the calorimeter; this is applied on a jet by jet basis.
- Bin by Bin unfolding to remove the effect of P_T smearing.

In the following chapter we outline the Monte Carlo generation, weighting and the jet correction procedure.

9.2 Monte Carlo Simulation

Jets are generated using Pythia 6.203 and Herwig 6.4. QCD ($2 \rightarrow 2$ processes) including initial and final state gluon radiation as well as secondary interactions between beam remnants. The jets are then passed through a detailed detector simulation (CDFSIM). The parton interactions are generated using LO QCD matrix elements.

The PDF set used to describe the proton and antiproton is CTEQ5l. This PDF set contains the CDF and D0 jet data from Run 1. The Pythia samples are generated using a tuned set of parameters that control the soft gluon emmision. The parameters were tuned to make Pythia reproduce the Run 1 underlying event properties.

9.2.1 Weighting the Monte Carlo

The Monte Carlo is generated using a number of $\hat{P_T}$ thresholds, where $\hat{P_T}$ is the tree level hard scattering momentum. The events are generated with an event weight and a fixed tree level cross section for the sample ($\sigma_{\hat{P_T}^{Min}} = \sigma(\hat{P_T} \geq \hat{P_T}^{Min})$). The samples can be joined into a continuous spectrum by applying to each event/jet the associated event weight. Figure 9.1 shows the number of events in the sample as a function of the tree level momentum $\hat{P_T}$ of the samples used in the following work after weighting. For both Pythia and Herwig we use 500K events from each of the $\hat{P_T}$ samples; $\hat{P_T}$ =18,40,60,90,120,200,300 and 400 GeV.

Figure 9.2 show the inclusive jet P_T distribution after the samples have been combined by weighting.

The lowest $\hat{P_T}$ threshold used in this study is 18 GeV, therefore the lowest P_T^{Cal} that can be used for this sample while still avoiding the generator level threshold bias is 35 GeV (figure 9.5).

Due to trigger efficiencies in the data, the inclusive cross section measurement begins at an uncorrected P_T of 50 GeV . This data threshold has a corresponding threshold in corrected P_T of 58 GeV. The corrected cross section will be presented with a lower corrected P_T bin edge of 60 GeV.

The calorimeter level inclusive jet distribution in figure 9.2 has two spikes/bumps around 320 – 350 GeV. These features come from jets that were generated from a

sample with a low $\hat{P}_T^{Min}$ (high weight) that fluctuate to a high P_T after passing through CDFSIM. These spikes/bumps do not have any significant effect on the corrections.

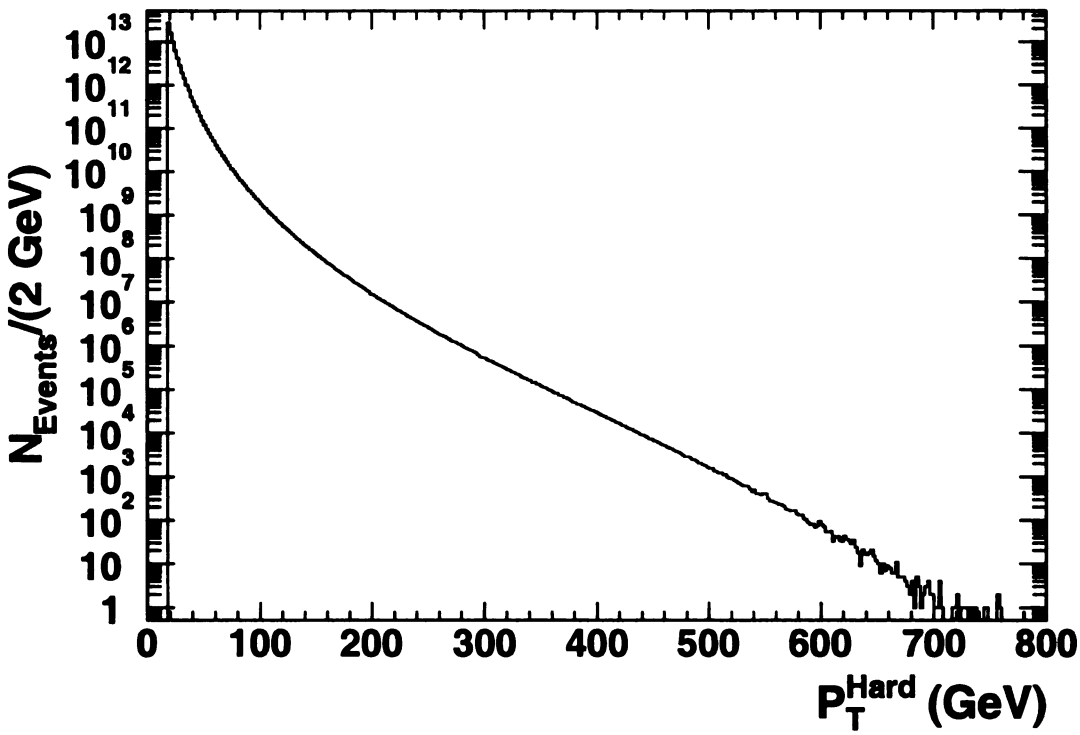

Figure 9.1: *Number of events as a function of $\hat{P}_T$ for Pythia after weighting. The smoothness of the plot indicates the weights have been found and applied correctly giving one continuous sample with a single threshold of $\hat{P}_T = 18$ GeV coming from the lowest of the samples.*

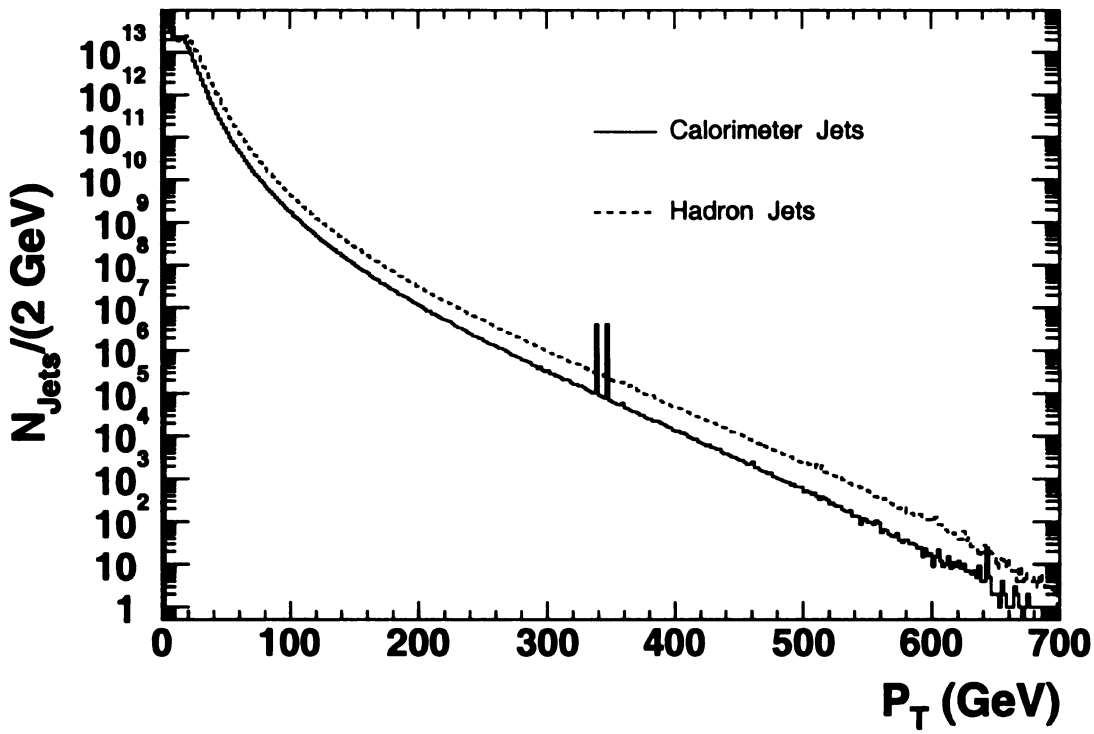

Figure 9.2: *Inclusive Pythia P_T distribution for hadron level and calorimeter level jets after weighting the events. The spikes/bumps around 300 GeV arise from jets from a low $\hat{P_T}$ (larger weight) sample fluctuating into a high P_T bin. They are associated with CDFSIM and therefore are not present in the hadron level distribution.*

9.3 Average P_T^{Jet} Correction

The average P_T^{Jet} correction is applied to the transverse momentum of each jet in order to compensate for the energy lost in the detector on average. The correction is derived from the Monte Carlo in the following way:

- The MidPoint jet algorithm is used to reconstruct jets at both the hadron and calorimeter level in the Monte Carlo. At the hadron level, 1 GeV seeds are used and no other requirements are made on the particles before clustering. At the calorimeter level, the standard clustering cuts/requirements were used.

- Hadron and calorimeter jets are matched into pairs. Jets are considered matched in (Y, ϕ) space if their separation $\Delta R = \sqrt{(\Delta Y)^2 + (\Delta\phi)^2}$ is less than $\Delta R = 0.7$. Figure 9.4 shows ΔR, $\Delta\phi$, ΔY and P_T^{Had}/P_T^{Cal} for the matched jet pairs for Pythia. The resolution of Y and ϕ are very good and no correction is required for these quantities. The P_T of the jet is underestimated by $\sim 20\%$ at low P_T improving to $\sim 10\%$ at high P_T. It is this scale that we wish to correct for with the average P_T^{Jet} correction before unfolding.

- From the Pythia jet pairs, the calorimeter P_T is fixed in 5 GeV bins; from the corresponding hadron distributions we find $\langle P_T^{Jet}(Had)\rangle$. This correlation is fit to a polynomial :

$$\langle P_T^{Had}\rangle = A + B \times P_T + C \times P_T^2 + D \times P_T^3 + E \times P_T^4. \qquad (9.1)$$

- The fit range is determined by the thresholds in the Monte Carlo sample, for the weighted sample this is the threshold associated with the lowest $\hat{P_T}^{Min}$ sample used.

9.3.1 Calorimeter Level Thresholds at Hadron Level

In the data there is a threshold (lower bin edge) from which all data below is disregarded. The location of this threshold is set by the trigger efficiency of the Jet20 sample. When a jet by jet correction is made the lower edge of the bin in uncorrected P_T is moved to a higher value in corrected P_T. When considering the inclusive jet distribution that has the Average P_T^{Jet} correction applied we must ensure that our first bin is away from the corrected P_T threshold. This prevents us having any bins that are underpopulated due to the calorimeter level trigger efficiency cut.

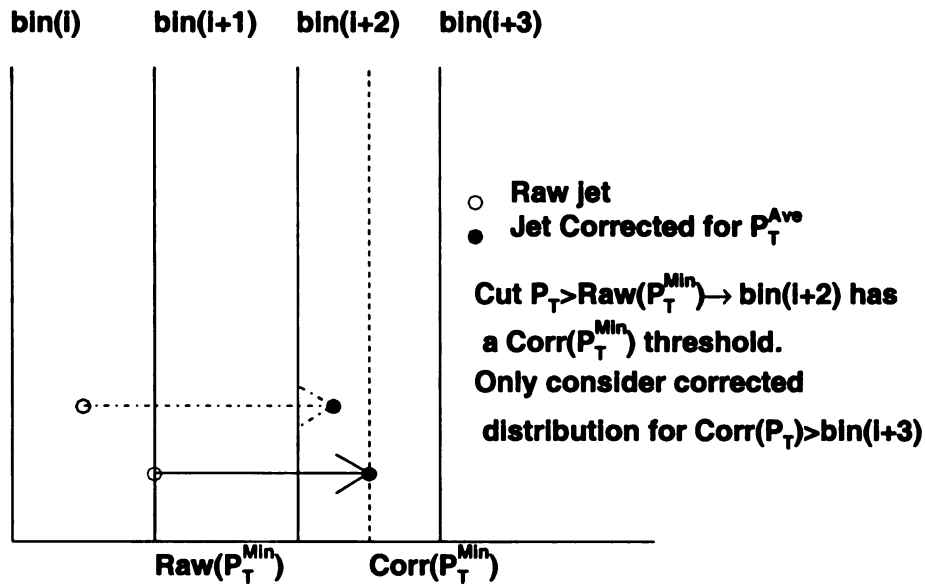

Figure 9.3: *Avoiding seeing the trigger efficiency cut in the P_T^{Ave} inclusive jet cross section.*

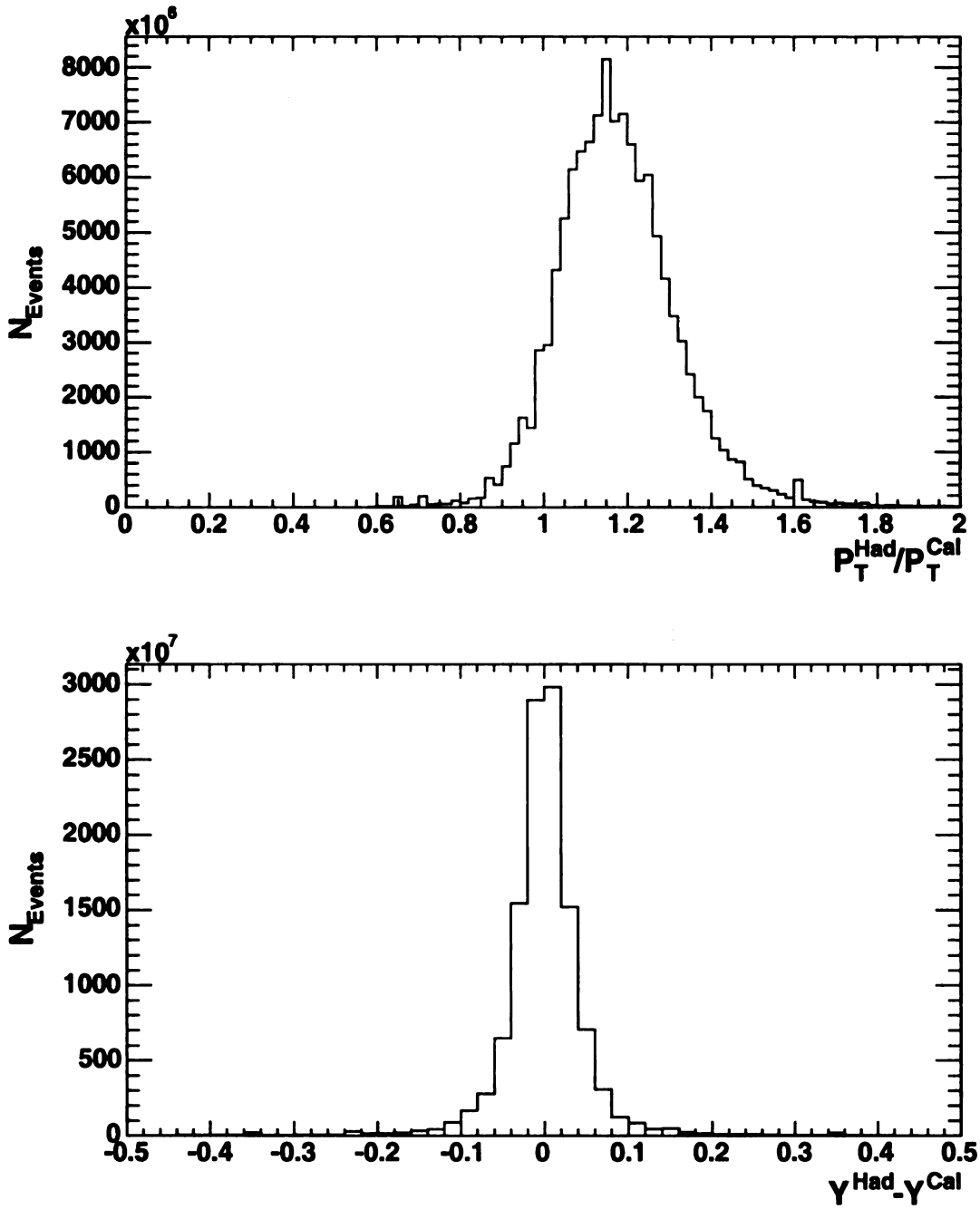

Figure 9.4: *Pythia* P_T^{Had}/P_T^{Cal}, $Y^{Had} - Y^{Cal}$ *and* $\phi^{Had} - \phi^{Cal}$. *From the plots it is clear the* Y *and* ϕ *resolutions are good, however the jet* P_T *is underestimated by* $\sim 20\%$ *with respect to the hadron level.*

figure 9.4 continued.

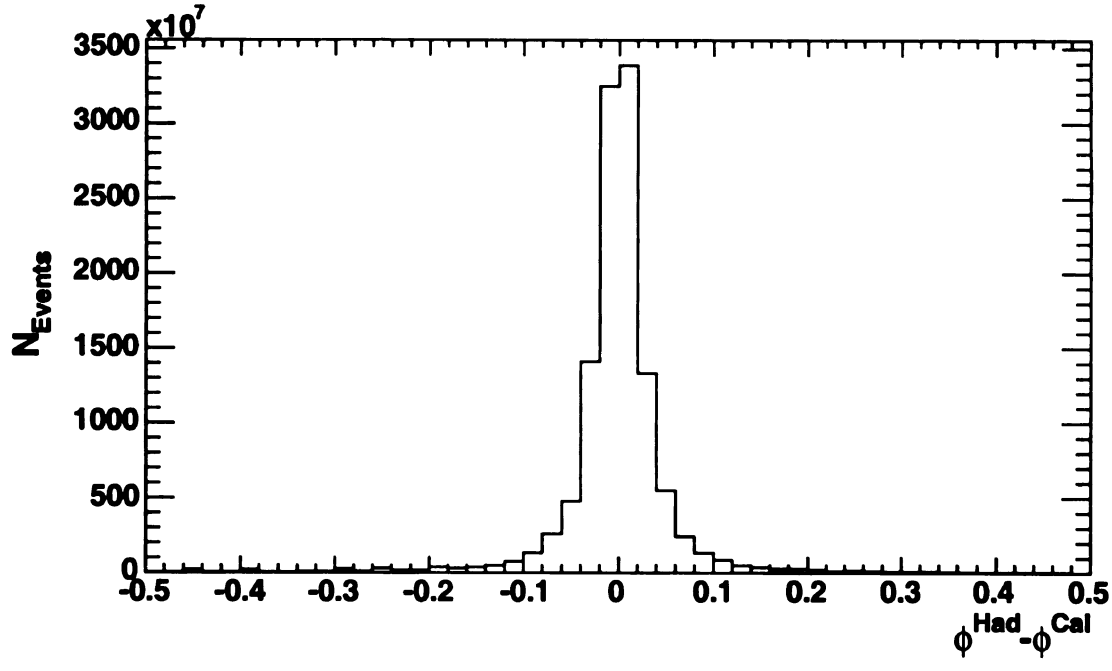

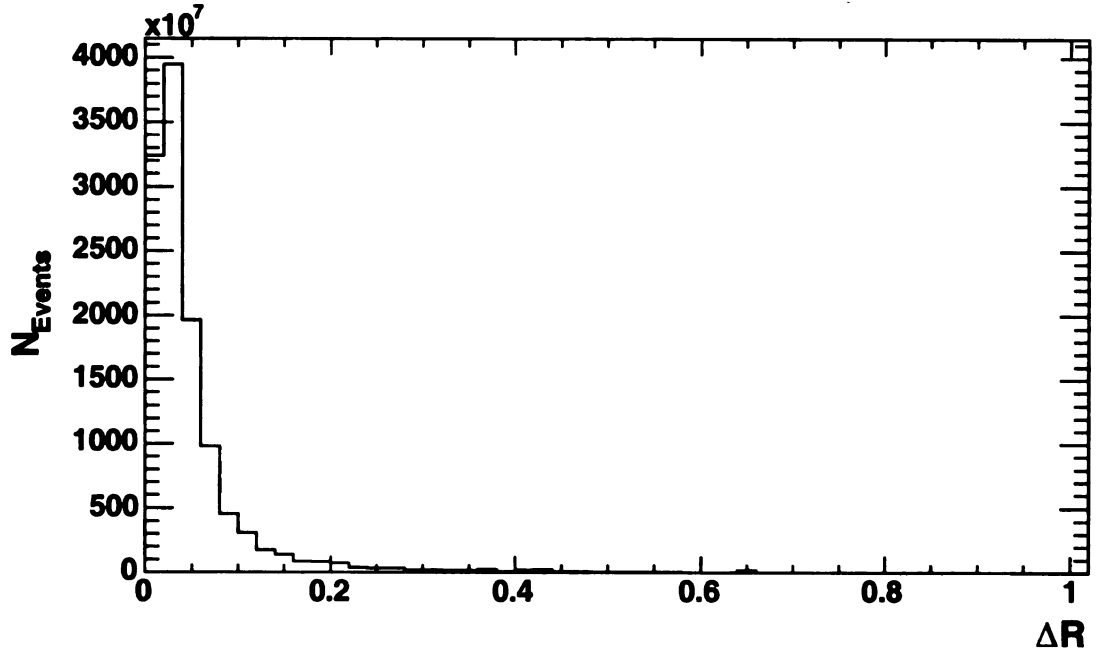

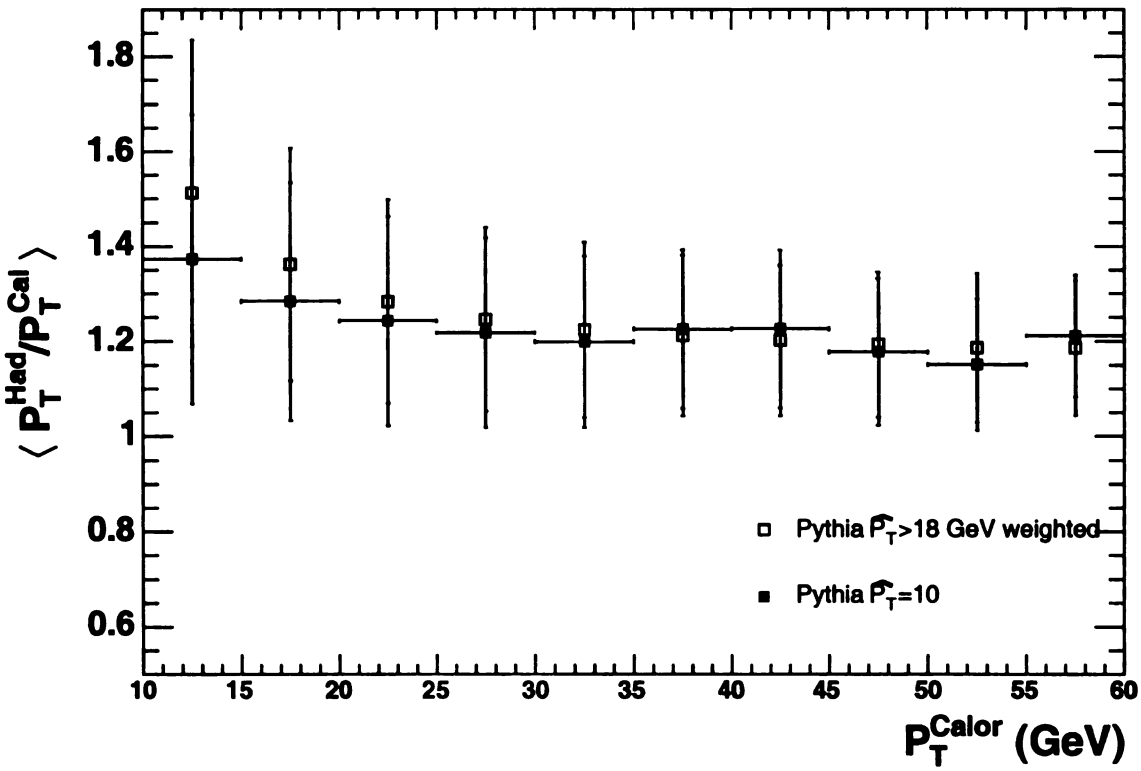

Figure 9.5: *It is clear there is a bias in the combined Pythia sample below 30 GeV. The bias is seen as a difference between the* $\langle P_T^{Had}/P_T^{Cal} \rangle$ *for the* $\hat{P}_T \geq 10$ *and all other samples with* $\hat{P}_T \geq 18$. *This bias is due to the generator level cut in the* $\hat{P}_T \geq 18$ *sample which is the only threshold present in the combined sample.*

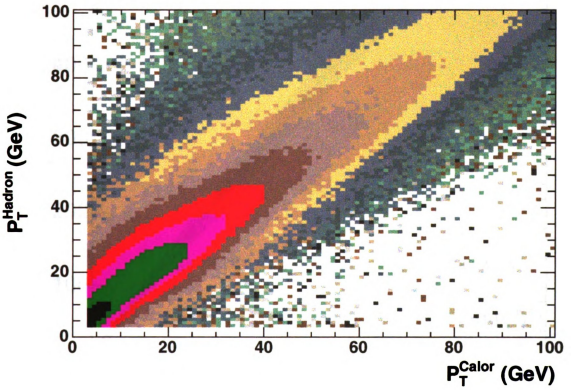

Figure 9.6: *Using the previous plot to set the lower limit of calorimeter P_T, we see that we do not truncate the tails of the hadron P_T distribution in the following work.*

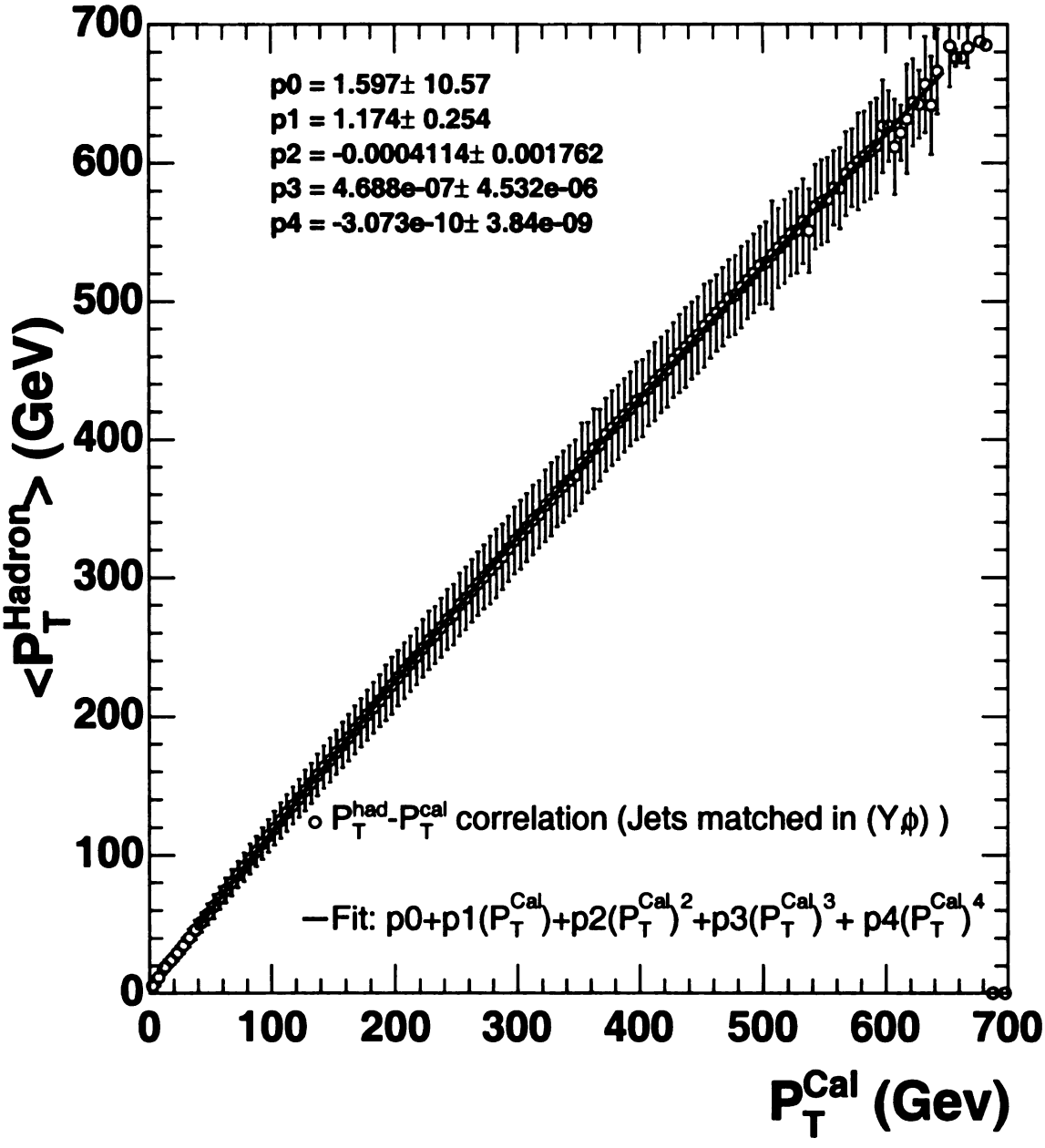

Figure 9.7: $\langle P_T^{Had} \rangle - P_T^{Cal}$ *correlation used to derive the* P_T^{Ave} *correction curve. The fit range is* $P_T^{Cal} > 35$ *GeV which is set by being in a region where Pythia 18 sample is unbiased.*

9.4 Smearing Correction

9.4.1 $P_T^{Cal}(Corr)$ Resolution and Bin Size

The smearing correction is applied to the average P_T^{Jet} corrected cross section on a bin by bin basis. We require the cross section bin sizes to be greater than or equal to the P_T resolution of the jets being measured/corrected. We measure from Pythia the P_T resolution of the calorimeter to the corrected jets. The resolution ($\sigma(f_b)$) is found as a function of $P_T^{Cal}(Corr)$ by fitting gaussians to the f_b distributions associated with fixed intervals of $P_T^{Cal}(Corr)$. The quantity f_b is defined as:

$$f_b = \frac{P_T^{cal}(Corr) - P_T^{had}}{P_T^{had}}, \tag{9.2}$$

where $P_T^{cal}(Corr)$ is the P_T of a jet that has had the average P_T^{Jet} correction applied to compensate for energy lost in the detector.

The mean of the fit (figure 9.9) gives a consistency check on the hadron scale correction. It should be close to zero: it is expected to differ from being exactly zero since the correction is found using the full distribution where as the gaussian used in the resolution study truncates the tails of the distribution. The standard deviation $\sigma(f_b)$ is the resolution of the calorimeter to corrected jet P_T (figure 9.10). The resolution multipled by the $P_T^{Cal}(Corr.)$ gives the 1σ bin width in corrected jet P_T.

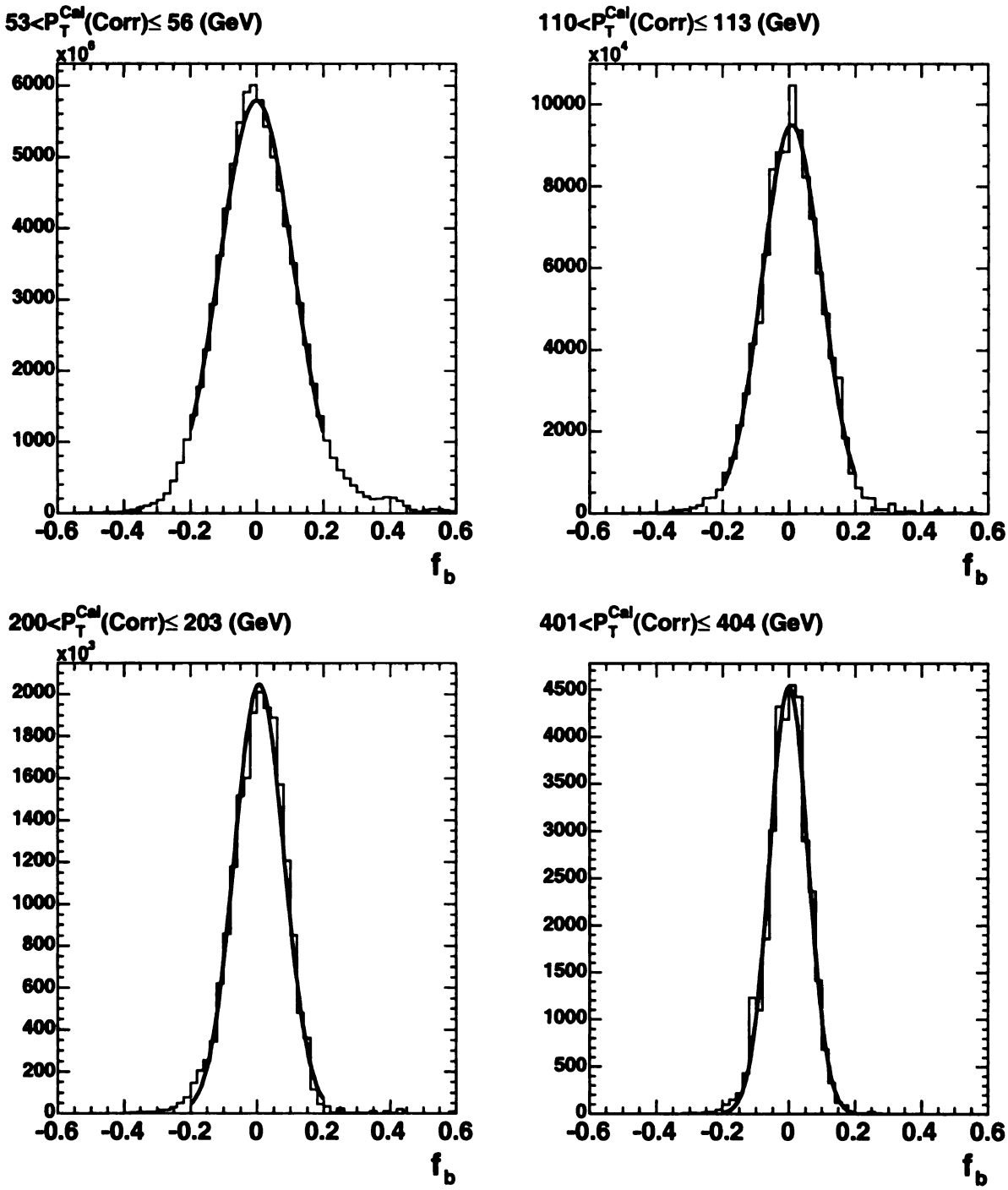

Figure 9.8: *Fixing P_T^{Cal} and plotting the corresponding f_b from these distributions we determine the resolution from a gaussian fit and set the bin widths according to this resolution.*

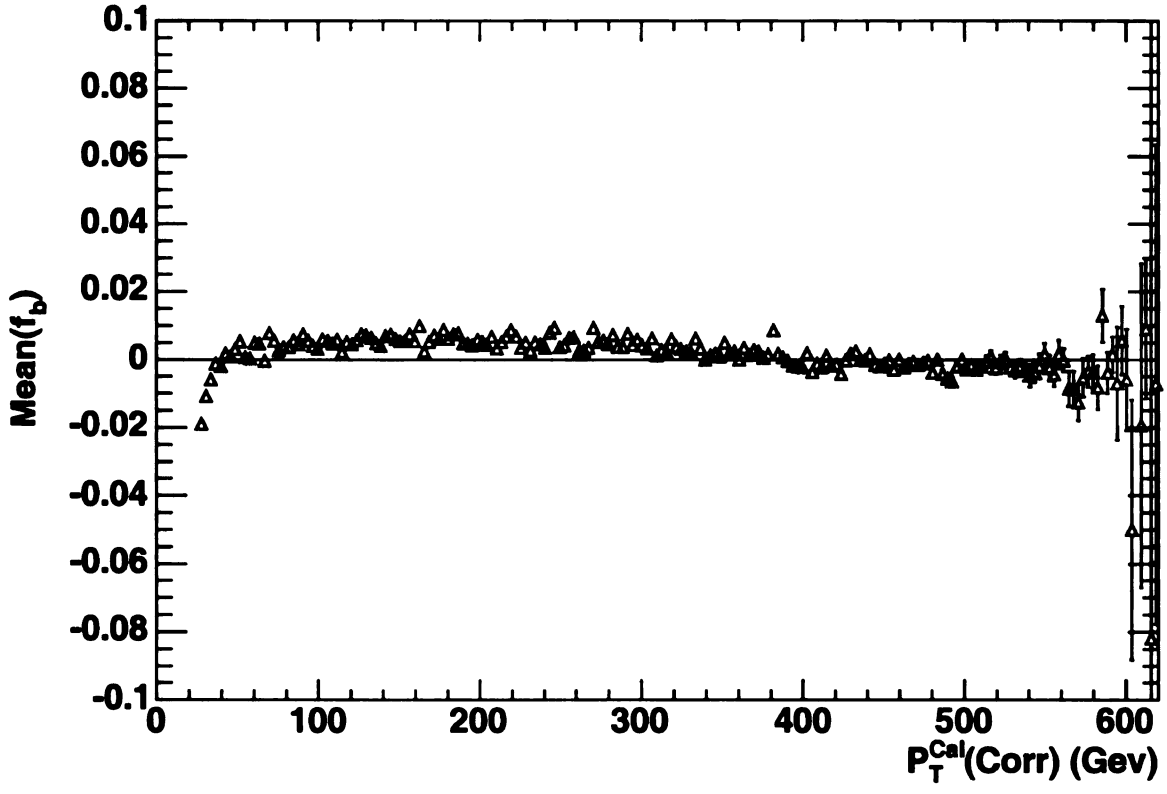

Figure 9.9: *mean(f_b)'s from gaussian fits to f_b distributions (e.g. 9.8). This value acts as a consistancy check for the P_T^{Ave} correction. We see the mean values are almost* 0.0 *which is what we expect if the correction is reasonable. The actual correction is derived from the statistical mean which includes the asymetric tails of the hadron distribution. The first unbiased $P_T^{Cal}(Cor)$ bin in the Monte Carlo sample is* 45.0 *GeV. Below this value we see the effect of the bias coming from P_T^{Cal}.*

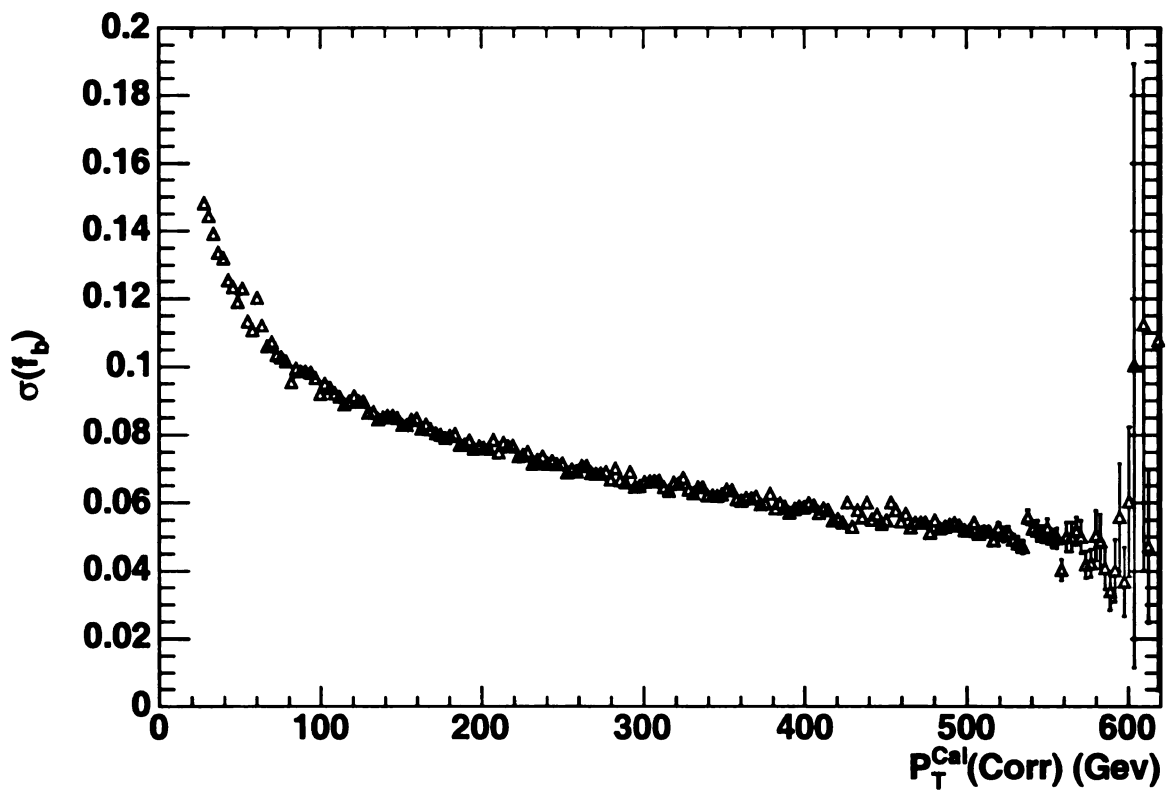

Figure 9.10: $\sigma(f_b)$ *from gaussian fit. This is* $P_T(Corr)$ *resolution which is used to set the bins of the cross section.*

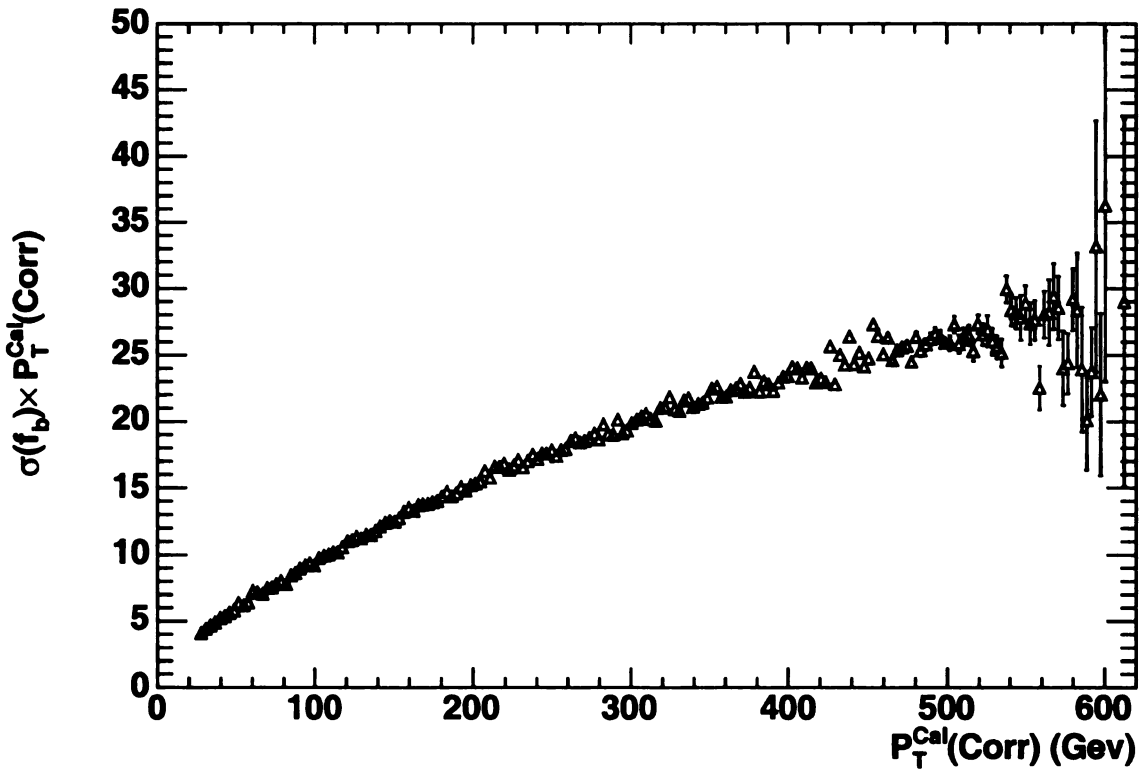

Figure 9.11: $\sigma \times P_T^{Cal}(Corr)$ *gives the bin widths in GeV. The bins are chosen to be* 1σ *for* $P_T^{Cal}(Corr) < 100$ *GeV,* 2σ *for* $P_T^{Cal}(Corr) < 200$ *GeV and* $\geq 3\sigma$ *for* $P_T^{Cal}(Corr) > 200$ *GeV depending on statistics.*

9.4.2 Bin by Bin Smearing Correction

The average P_T^{Jet} corrected jet cross section must still be corrected for the smearing effects of the calorimeter to give a hadron level inclusive jet cross section free of detector effects. The smearing correction is done with the following prescription:

- Jets are reconstructed at the hadron level using the HEPG final state particles. The ratio of the *true* hadron level cross section and the average P_T^{Jet} corrected cross section is taken. No matching requirement is made on either of these cross sections. The ratio of these cross sections gives the bin by bin correction factors:

$$C_i = \frac{N_{jets}^{Hadron}}{N_{jets}^{Calor}} \Big|_{bin(i)}, \quad (9.3)$$

  where N_{jets}^{Hadron} is the number of jets in a bin of the hadron level distribution and N_{jets}^{Calor} is the number of jets in a bin of the average P_T^{Jet} corrected distribution. All selection cuts are applied to the measured distribution; however only the rapidity cut is applied to the hadron level jets.

- Figure 9.12 shows the bin correction factors for Pythia ("smoothed" and raw) that are applied to the data.

The bin by bin corrections derived from Pythia are fitted to a smooth curve. The curve is then integrated over the bin and divided by the bin width to give a smoothed bin by bin correction. All figures where bin correction factors are shown include the original Pythia points with statistical errors and the smoothed correction. The statistical errors from Pythia were propagated into the cross section statistical error.

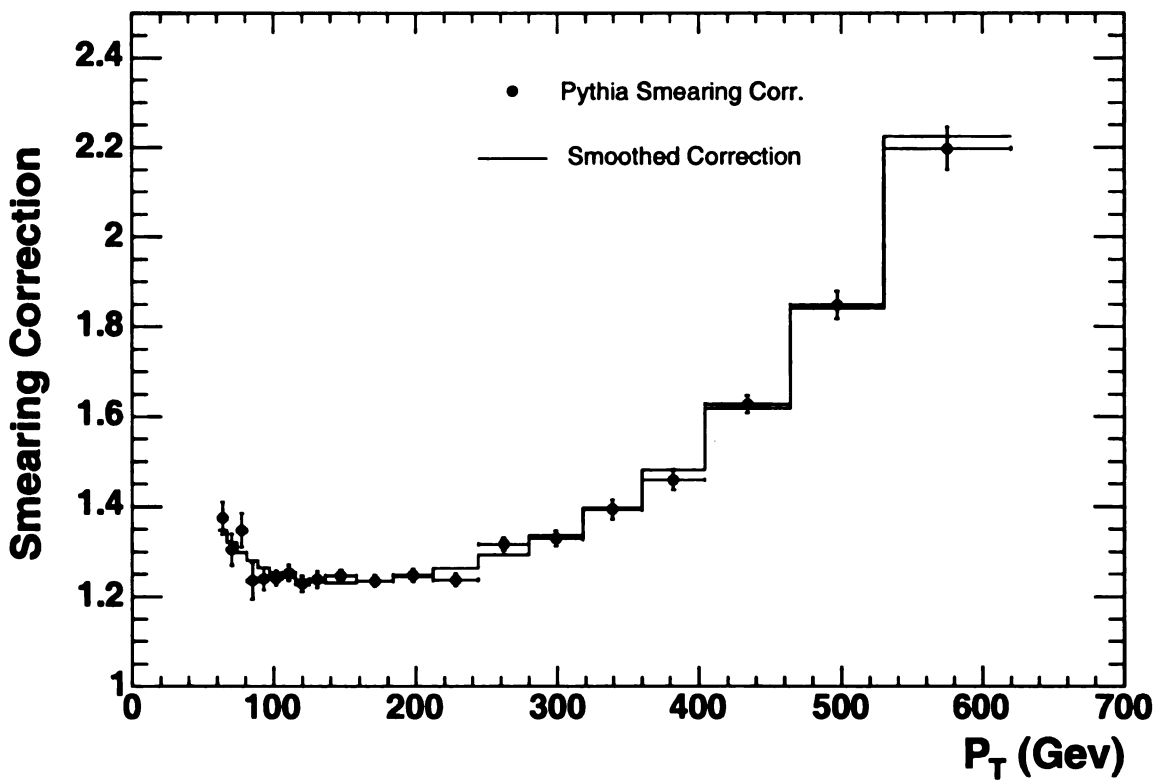

Figure 9.12: *Bin correction factors for Pythia. These correct the average P_T^{Jet} corrected calorimeter distribution for the smearing associated with detector resolution. The histogram is the smoothed correction that is applied in the data. The statistical errors from Pythia were propagated into the final cross section comparisons.*

9.4.3 Parton to Hadron Corrections

The corrections thus far describe how to correct the inclusive jet cross section to the hadron level. We must correct the cross section for hadronisation effects (fragmentation and underlying event) in order to make a fair comparison to NLO pQCD. These two contributions act in a competing manner. The hadronisation process acts to reduce the amount of energy clustered in a hadron level jet with respect to the original parton level jet. This effect is typically small in the P_T range for which we are currently measuring the inclusive jet cross section. The underlying event acts to add energy into the jet cone at hadron level. This energy is coming from beam-beam remnant and soft spectator interactions. As we go to lower P_T this effect becomes much larger that the hadronisation effect.

The hadron level to parton level correction is derived from the Monte Carlo. As with the calorimeter to hadron level corrections we derive the corrections using both Pythia and Herwig. However, we correct the data using the correction derived from Pythia as this provides a consistant correction scheme.

The full parton to hadron level correction is given by

$$C_i^{p \to h} = \frac{\sigma_i^{hadron(UE)}}{\sigma_i^{parton(no-UE)}}, \tag{9.4}$$

where $\sigma_i^{hadron(UE)}$ is the hadron level inclusive jet cross section in bin i with underlying event, $\sigma_i^{parton(no-UE)}$ is the parton level inclusive jet cross section, without underlying event. The fragmentation and underlying event corrections were also studied separately using:

$$C_i^{UE} = \frac{\sigma_i^{hadron(UE)}}{\sigma_i^{hadron(no-UE)}} \quad \text{and} \quad C_i^{frag} = \frac{\sigma_i^{hadron(no-UE)}}{\sigma_i^{parton(no-UE)}}, \tag{9.5}$$

where $\sigma^{hadron(UE)}$ and $\sigma^{parton(no-UE)}$ are defined as above, $\sigma_i^{hadron(no-UE)}$ is the hadron level cross section without underlying event. Using these definitions we see that $C_i^{p\to h} = C_i^{UE}.C_i^{frag}$ [36]. We should note here that Pythia and Herwig implement these effects is different ways. Pythia uses a multiple parton interaction model which contributes to the underlying event of jets at parton and hadron level. Herwig uses a beam-beam remnant model that only contributes to jets at the hadron level. When deriving these corrections with Herwig, the underlying event correction is underestimated and therefore so too is the full parton to hadron correction.

For Pythia we see that for $P_T > 60$ GeV the underlying event correction dominates the full hadron to parton correction. We present comparisons between NLO pQCD and both the inclusive jet cross section corrected to parton level and also corrected to hadron level with the underlying event correction.

We take as a systematic the difference between the Pythia and Herwig parton to hadron level corrections. This is a conservative estimate given that pythia is tuned to reproduce the CDF run 1 underlying event properties.

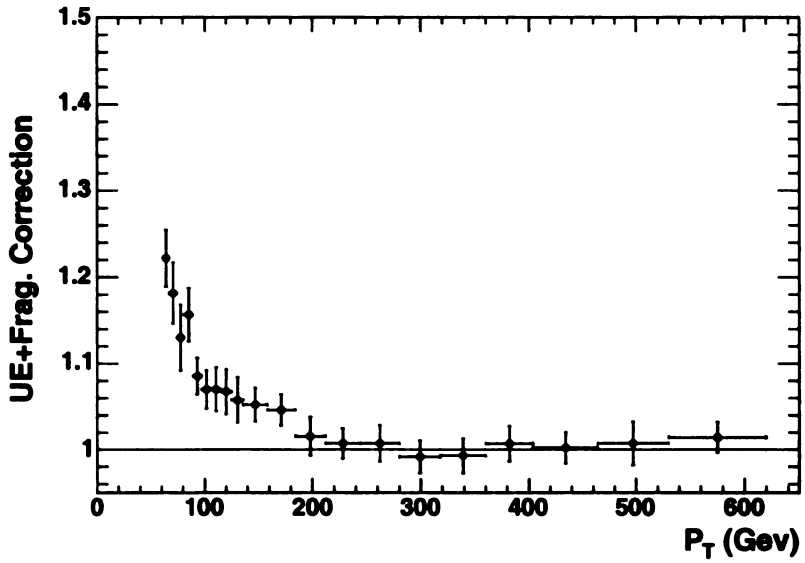

Figure 9.13: *Fragmentation + underlying event correction for Pythia.*

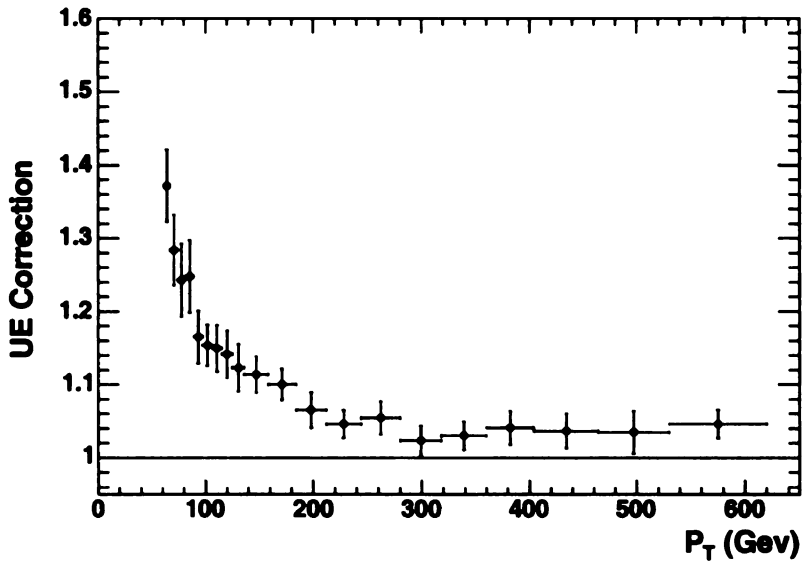

Figure 9.14: *Pythia underlying event correction.*

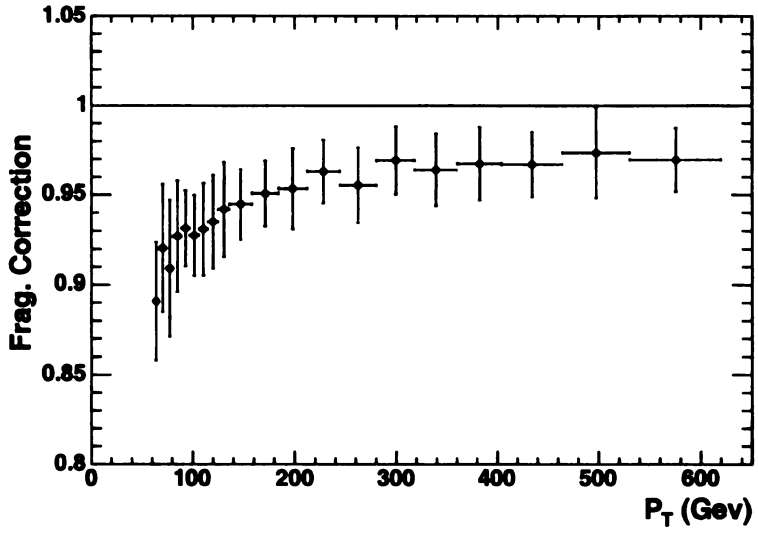

Figure 9.15: *Pythia fragmentation correction.*

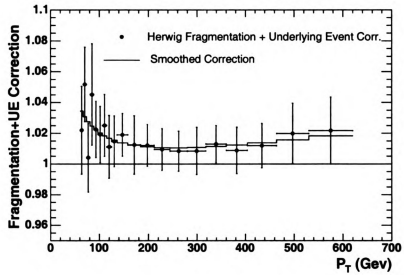

Figure 9.16: *Fragmentation + underlying event correction for Herwig.*

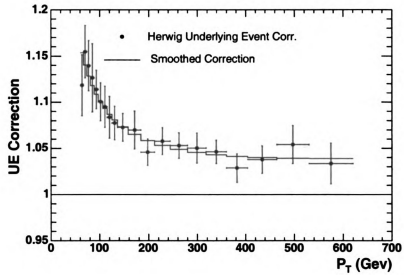

Figure 9.17: *Herwig underlying event correction.*

P_T (GeV)	Had Cor	Stat Err	UE Cor	Stat Err	Part Cor	Stat Err
61-67	1.347	0.036	1.372	0.049	1.222	0.033
67-74	1.321	0.035	1.284	0.048	1.182	0.035
74-81	1.298	0.038	1.243	0.050	1.130	0.038
81-89	1.280	0.041	1.248	0.050	1.157	0.031
89-97	1.265	0.025	1.165	0.036	1.085	0.021
97-106	1.253	0.016	1.153	0.028	1.070	0.022
106-115	1.244	0.018	1.149	0.032	1.070	0.026
115-125	1.238	0.017	1.141	0.032	1.067	0.026
125-136	1.233	0.019	1.123	0.033	1.058	0.026
136-158	1.231	0.013	1.114	0.025	1.052	0.020
158-184	1.234	0.013	1.100	0.022	1.046	0.018
184-212	1.245	0.014	1.065	0.024	1.016	0.023
212-244	1.264	0.014	1.046	0.019	1.007	0.018
244-280	1.293	0.014	1.054	0.022	1.007	0.021
280-318	1.336	0.017	1.023	0.021	0.992	0.019
318-360	1.397	0.022	1.030	0.019	0.993	0.020
360-404	1.482	0.023	1.041	0.023	1.007	0.021
404-464	1.618	0.019	1.036	0.024	1.002	0.018
464-530	1.840	0.031	1.035	0.030	1.007	0.025
530-620	2.225	0.047	1.046	0.020	1.014	0.018

Table 9.1: *Summary of Pythia bin correction factors: Had. Corr are the calorimeter level to hadron level correction factors, UE. Corr are the underlying event corrections and Part. Corr are the full parton level to hadron level correction factors.*

P_T (GeV)	$\sigma(P_T^{Corr})$ (nb/GeV)	$\delta\sigma(P_T^{Corr})$	$\sigma(had)$ (nb/GeV)	$\delta\sigma(had)$
61-67	8.54398	0.00239073	11.7442	0.304023
67-74	4.77716	0.00165505	6.23333	0.169222
74-81	2.71985	0.00124882	3.66377	0.102657
81-89	1.55688	0.00088381	1.92301	0.0638199
89-97	0.894061	0.000669753	1.10837	0.0219468
97-106	0.525822	0.000484255	0.652882	0.0084804
106-115	0.311059	0.000372457	0.389707	0.0055032
115-125	0.184461	0.0002721	0.226642	0.00324352
125-136	0.109076	0.0001995	0.135085	0.00204021
136-158	0.0514128	9.68501e-05	0.0640773	0.000679477
158-184	0.0184168	5.33208e-05	0.0227468	0.000242962
184-212	0.00642575	3.035e-05	0.00801484	9.75085e-05
212-244	0.00225774	1.68282e-05	0.0027944	3.70324e-05
244-280	0.000723146	8.9792e-06	0.000951761	1.57162e-05
280-318	0.000242093	5.05679e-06	0.000321771	7.88957e-06
318-360	7.263e-05	2.63457e-06	0.000101248	3.99794e-06
360-404	1.90654e-05	1.31878e-06	2.78288e-05	1.97373e-06
404-464	4.54893e-06	5.51639e-07	7.40197e-06	9.01978e-07
464-530	1.03385e-06	2.50745e-07	1.9109e-06	4.64583e-07
530-620	4.45973e-08	4.45973e-08	9.79972e-08	9.80198e-08

Table 9.2: *$\sigma(P_T^{Corr})$ is the average P_T^{Jet} corrected inclusive jet cross section. $\sigma(had)$ is the hadron level inclusive jet cross section (before UE or fragmentation corrections).*

Chapter 10

Comparison of the Data to Pythia+CDFSIM

10.1 Introduction

The raw data is corrected for hadron scale (average P_T^{jet} correction) and smearing using Pythia Tune A plus the detector simulation (CDFSIM). While the ultimate comparisons are to NLO pQCD predictions, which contain at most three partons in the final state, here we make some comparisons of the data to Pythia Tune A+(CDFSIM) using CTEQ5l PDF's. The fragmentation/hadronization of partons is well modelled for LO QCD predictions. Pythia uses LO matrix elements, plus a leading log approximation for the parton shower, then applies a string fragmentation model to convert partons into particles. The resulting particles are passed through the detector simulation. We compare Pythia to the four trigger samples in a region where both the data and Pythia are away from trigger and generator level thresholds. Pythia 18, 40 and 60 samples are used in the comparison to the Jet20 data sample. Only events in which the lead jet $P_T > 50.0$ GeV are used in the comparison. Pythia 40, 60 and 90 samples are used in the comparison to the Jet50 data sample. Only events in which the lead jet $P_T > 75.0$ GeV are used. Pythia 60, 90, 120 and 200 samples are used in the comparison to the Jet70 data sample. Only events in which the lead

jet $P_T > 100.0$ GeV are used in the comparison. Pythia 90, 120, 200, 300 and 400 samples are used in the comparison to the Jet100 data sample. Only events in which the lead jet $P_T > 150.0$ GeV are used in the comparison.

10.2 Quantities of interest

Figures 10.2 and 10.3 show the $\not\!\!E_T$ and $\not\!\!\tilde{E}_T$ comparisons for the jet trigger samples and Pythia. These quantities are sensitive to the simulation of both hard and spectator interactions. The inclusive jet analysis uses a cut on $\not\!\!\tilde{E}_T$ to reject background events. The MC distributions imply that $\sim 1\%$ of the good events are rejected. Figure 10.4 shows the transverse momentum difference in the two lead jets in the event (ΔP_T). This difference can result from: energy resolution of the detector and additional jets produced from the hard scattering. The agreement in this plot suggests the resolution and jet multiplicity are well modelled.

Figure 10.5 shows the difference in azimuthal angle between the events two leading jets ($\Delta\phi$). Like ΔP_T this quantity also depends on the number of jets in the event and resolution non-uniformities in ϕ. Again good agreement is observed. Both ΔP_T and $\Delta\phi$ are sensitive to detector resolution and additional radiation but these quantities do not distinguish between the two effects.

The effect of additional jets (QCD radiation) can be minimized by measuring the energy or momentum mismatch parallel to the axis defined by the leading two jets ($K_{T\|}$) (this work is included here for completness only, a more detailed discussion can be found in chapter 7). The direction of the parallel axis $\hat{\mathbf{n}}$ is defined as the perpindicular bisector, $\hat{\mathbf{t}}$, of the two jets:

$$\hat{\mathbf{t}} = \frac{\hat{\mathbf{n}}_1 + \hat{\mathbf{n}}_2}{|\hat{\mathbf{n}}_1 + \hat{\mathbf{n}}_2|} \tag{10.1}$$

where $\hat{\mathbf{n}}_{1,2}$ are the unit vectors along the two leading jets in the $(x-y)$ plane. From this $K_{T\|}$ is defined as $\vec{P}_{T1}.\mathbf{n} - \vec{P}_{T2}.\mathbf{n}$.

Figure 10.6 shows the $K_{T\|}$ comparisons for the jet triggers normalised to the average jet P_T. The good agreement indicates the jet resolution is well modelled by the simulation. The momentum imbalance along the $\hat{\mathbf{t}}$ direction, Figure 10.7 shows $K_{T\perp}$ which is sensitive to both energy resolution (non-uniformities in ϕ) and to additional jet production.

The CDF calorimeter measures the energy in two depth segments. The first (closest to the beam line) is the electromagnetic compartment. The second is the hadronic compartment. The electromagnetic calorimeter measures the electromagnetic particles (mainly π^0's) in the jets, along with some energy from hadronic particles. Figure 10.8 shows the fraction of the energy deposited in the electromagnetic compartment for jets.

Figures 10.11 and 10.12 show the comparison of the inclusive jet cross section between data and Pythia. In the plots the data has been corrected for multiple interactions, hadron scale and smearing. Both the data and Pythia have underlying event still present. On these plots the 5% systematic uncertainty on the energy scale (see discussion in chapter 12) is indicated by a shaded band. The Monte Carlo has been weighted according to the luminosity (as described earlier) to include Pythia samples with $\hat{P_T}$ 18, 40, 60, 90, 120, 200, 300 and 400 GeV. Table 10.1 gives the cross section values and the bin correction factors for each bin. In figures 10.1- 10.10 both data and Pythia have been normalised to a unit area.

10.3 Results

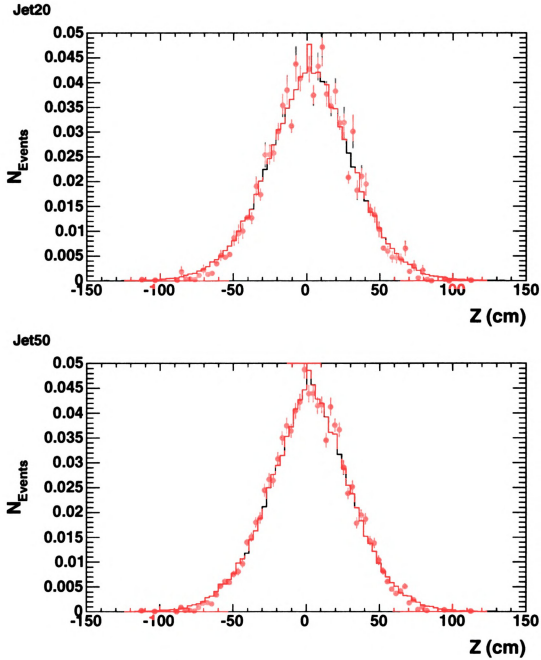

Figure 10.1: *Z vertex distributions for data (histogram) and Pythia (points).*

figure 10.1 continued.

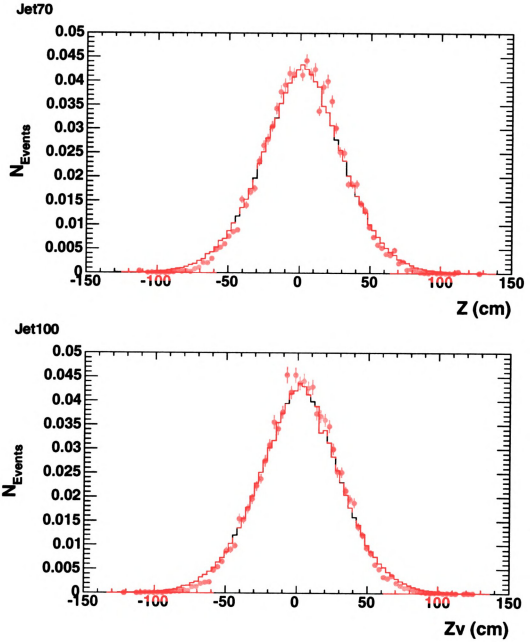

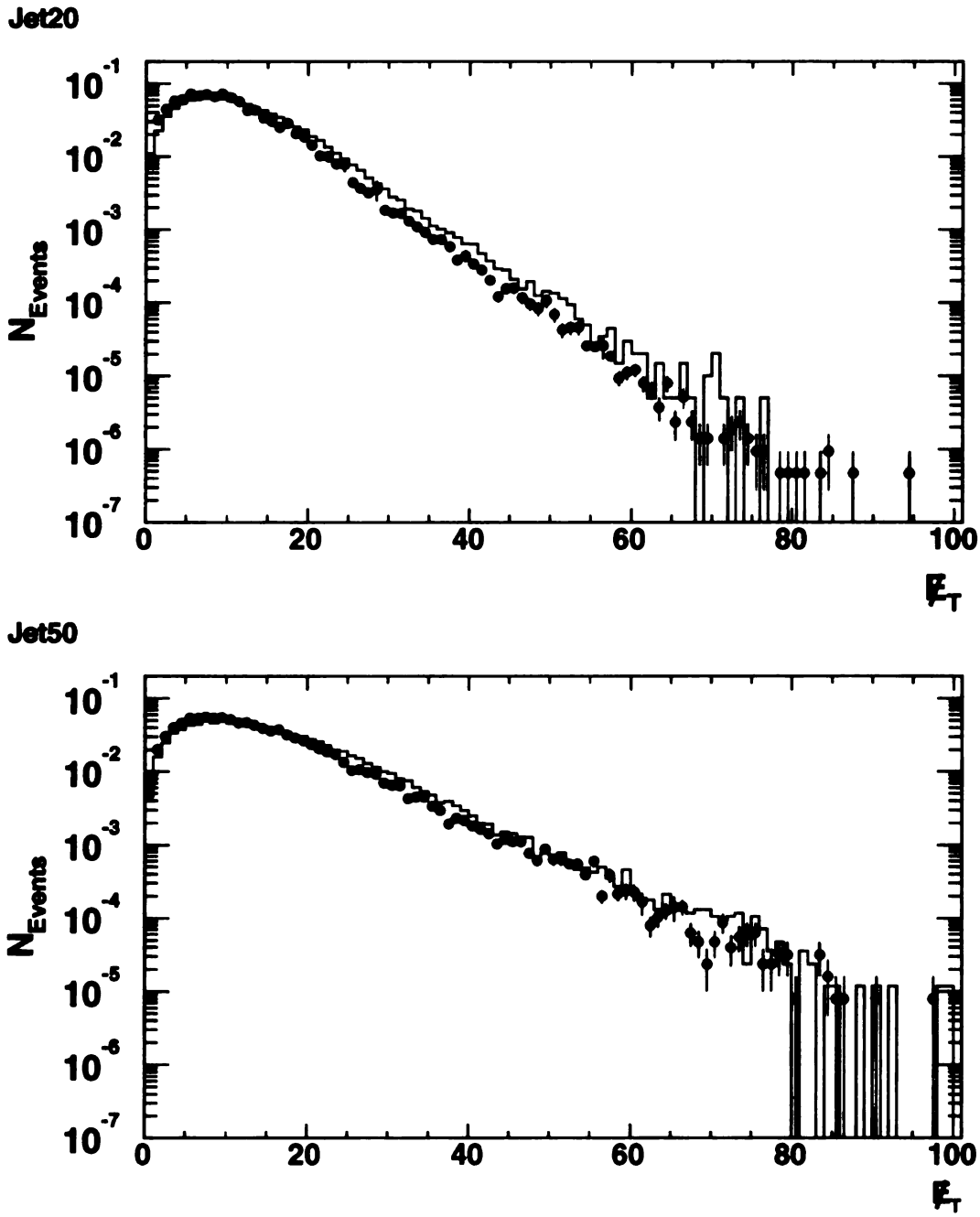

Figure 10.2: *$\not\!\!E$ distributions for data (histogram) and Pythia (points).*

figure 10.2 continued.

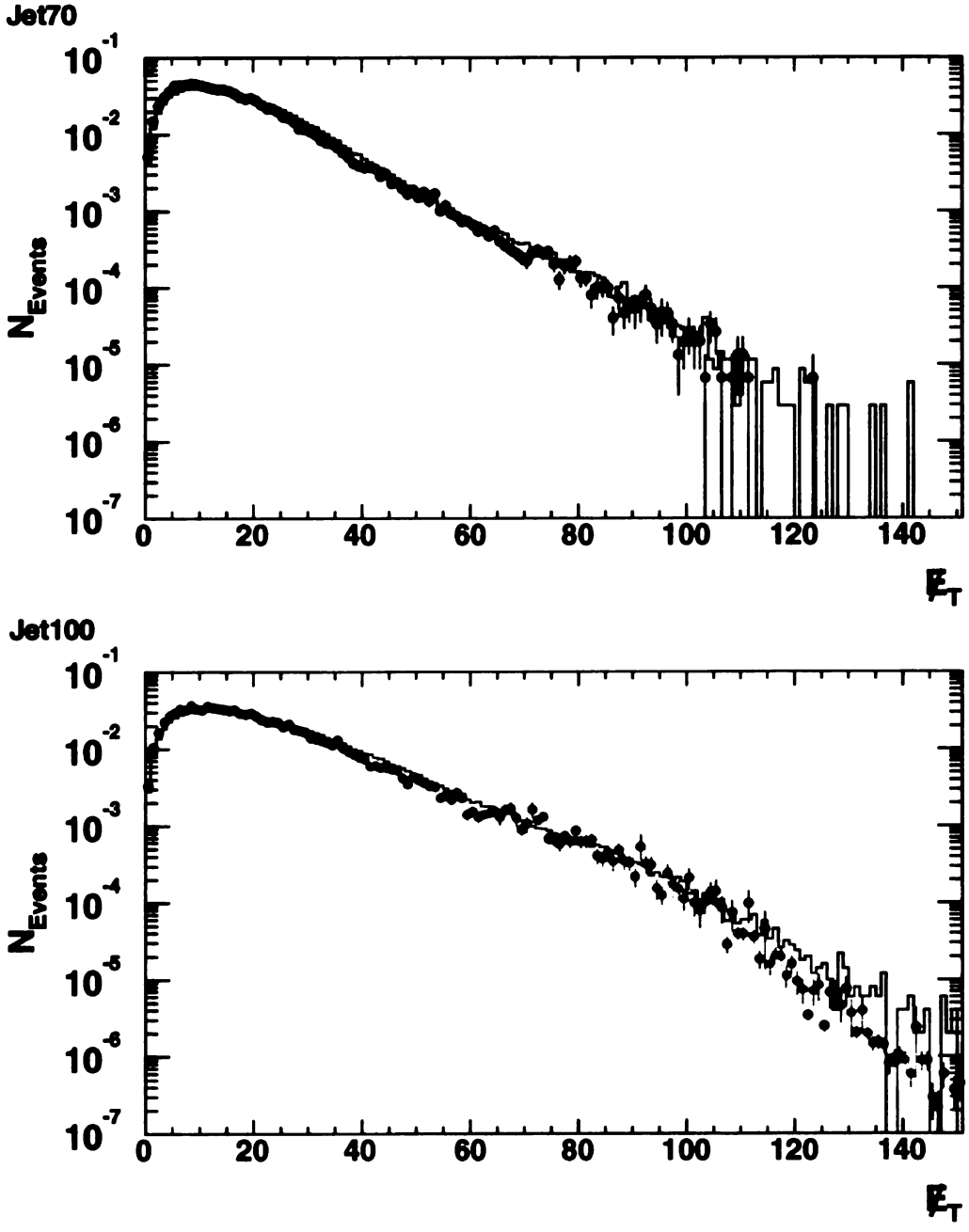

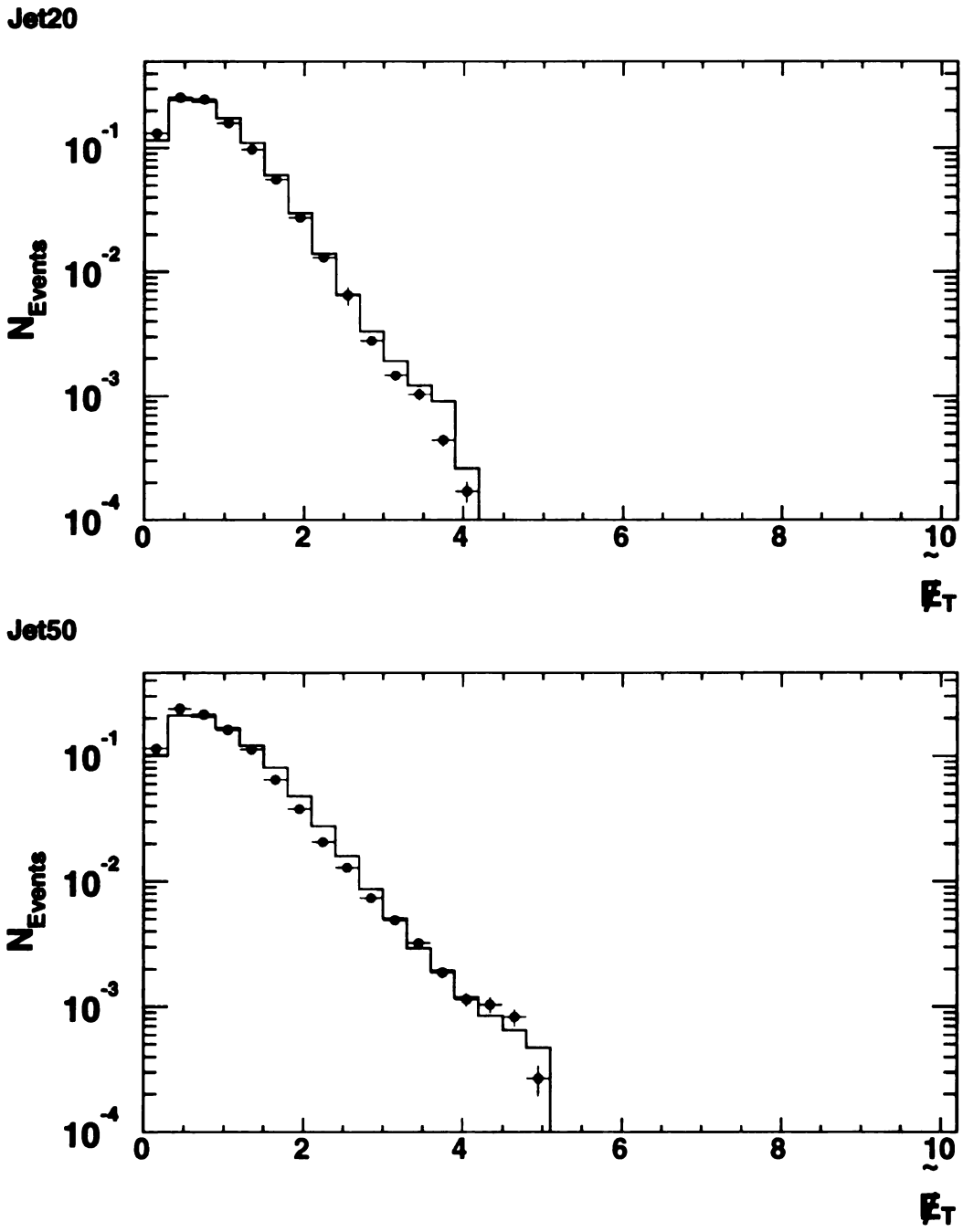

Figure 10.3: $\tilde{\not{E}}_T$ *distributions for data (histogram) and Pythia (points).*

figure 10.3 continued.

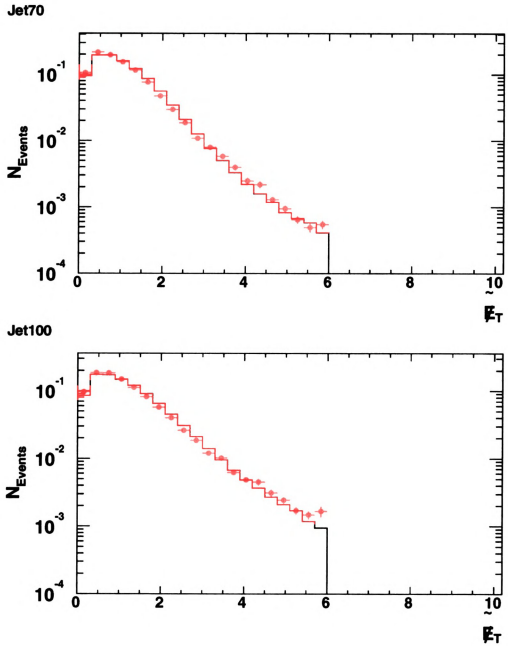

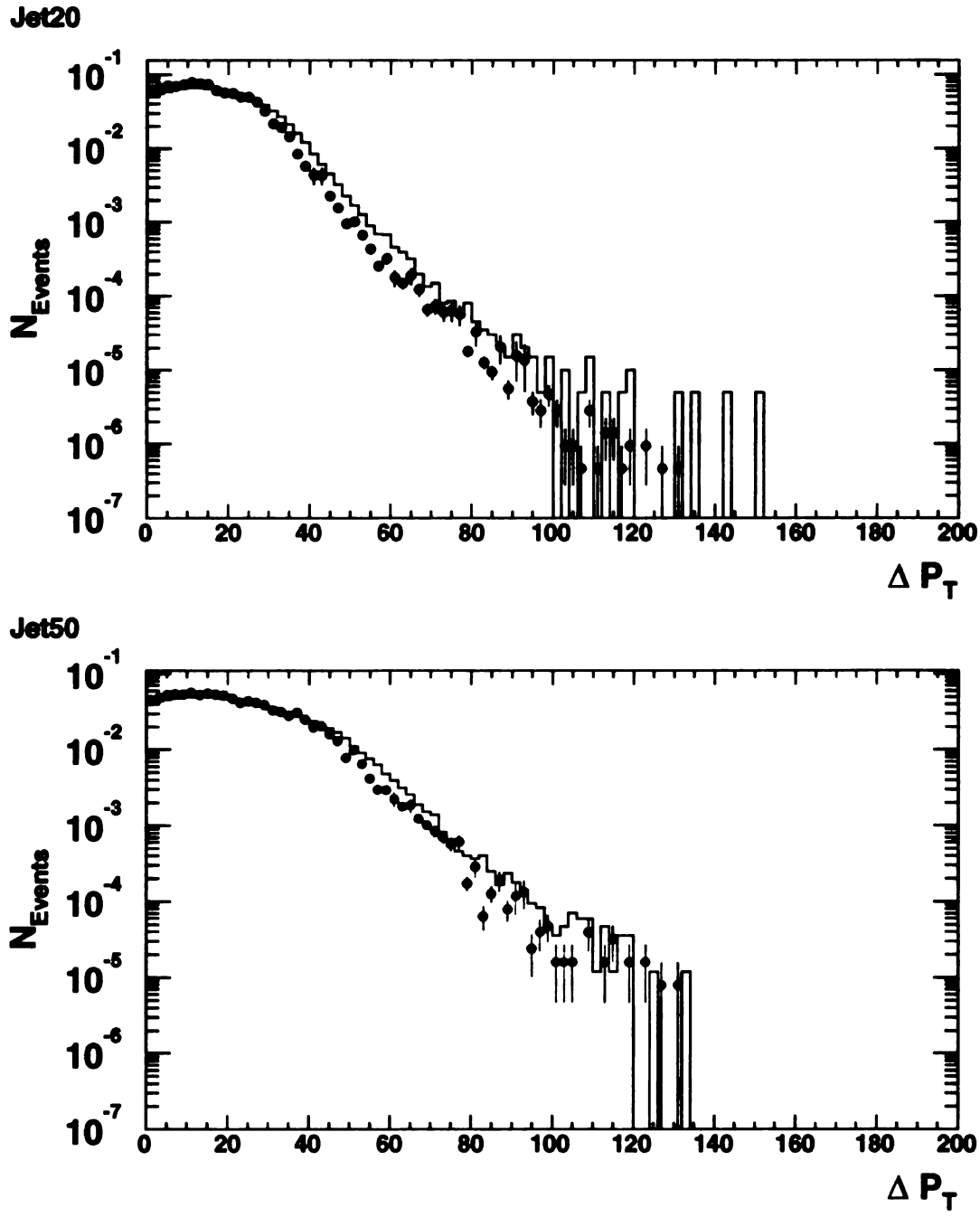

Figure 10.4: *ΔP_T distributions for data (histogram) and Pythia (points). This quantity is sensitive to radiation and non-uniformities in detector E_T resolution.*

figure 10.4 continued.

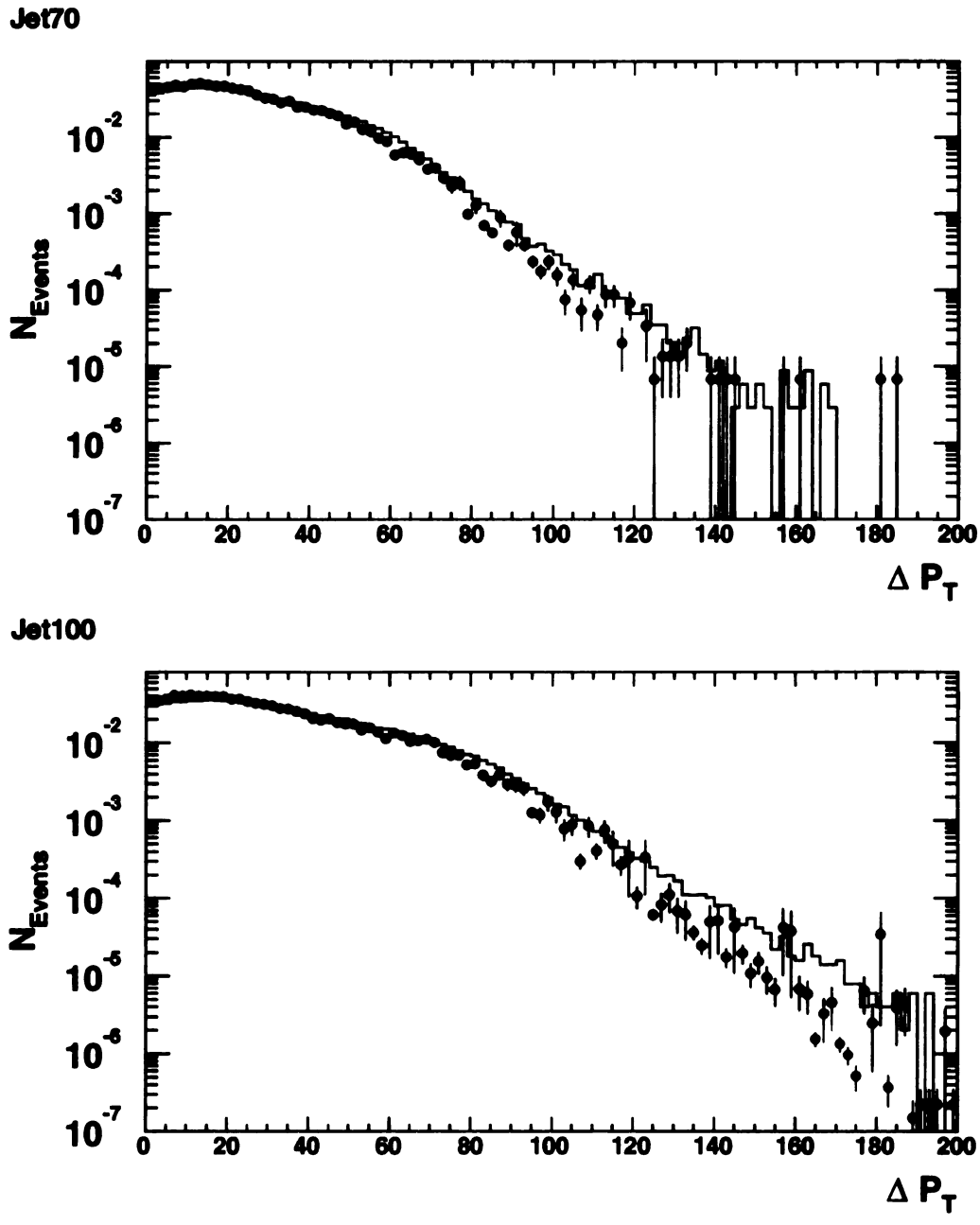

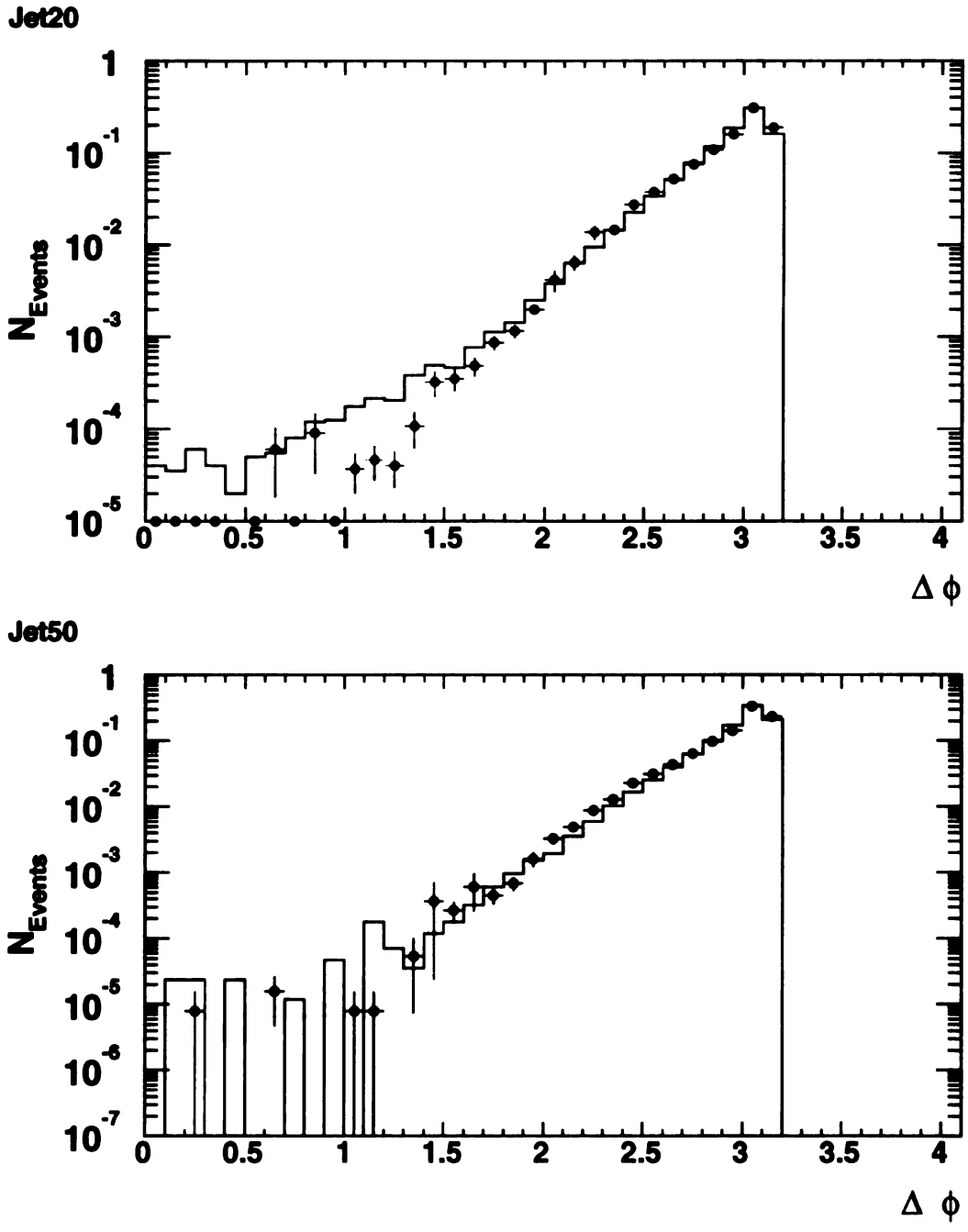

Figure 10.5: *$\Delta\phi$ distributions for data (histogram) and Pythia (points). This quantity is sensitive to radiation and non-uniformities in detector ϕ resolution.*

figure 10.5 continued.

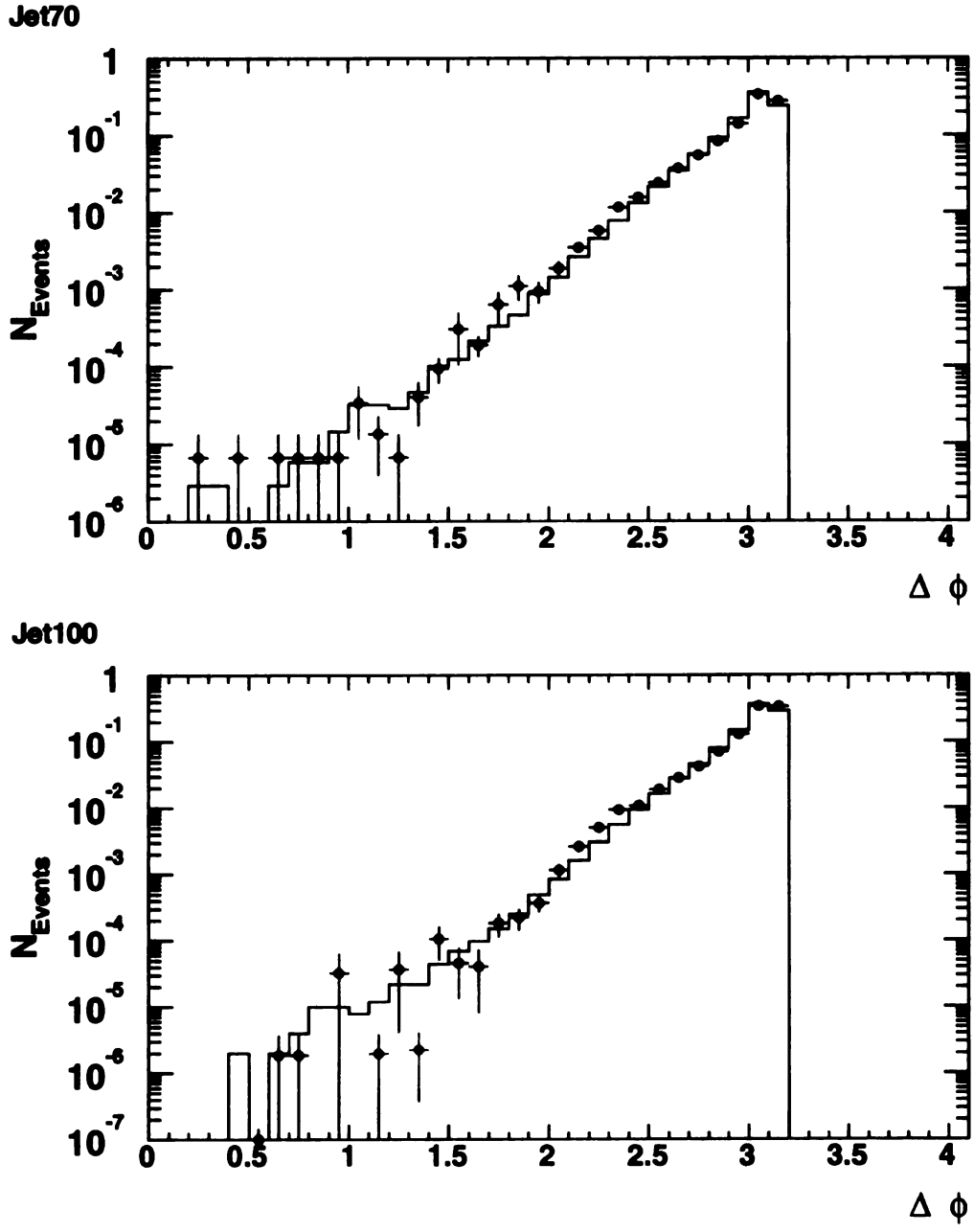

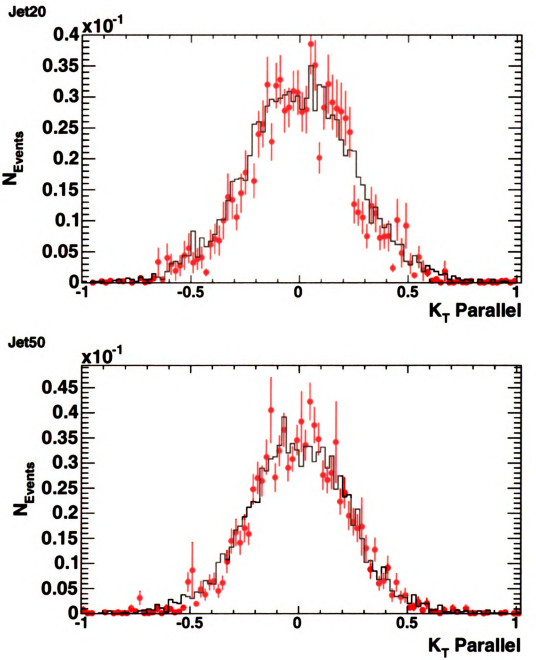

Figure 10.6: *$K_{T\|}$ distributions for data (histogram) and Pythia (points). This quantity is related to the detector E_T resolution.*

figure 10.6 continued.

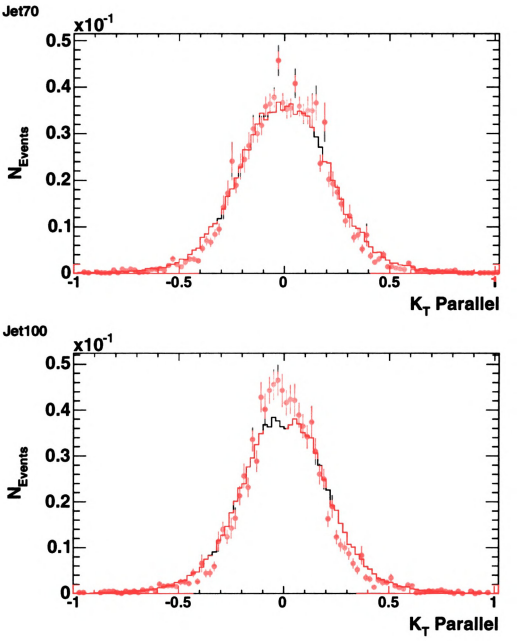

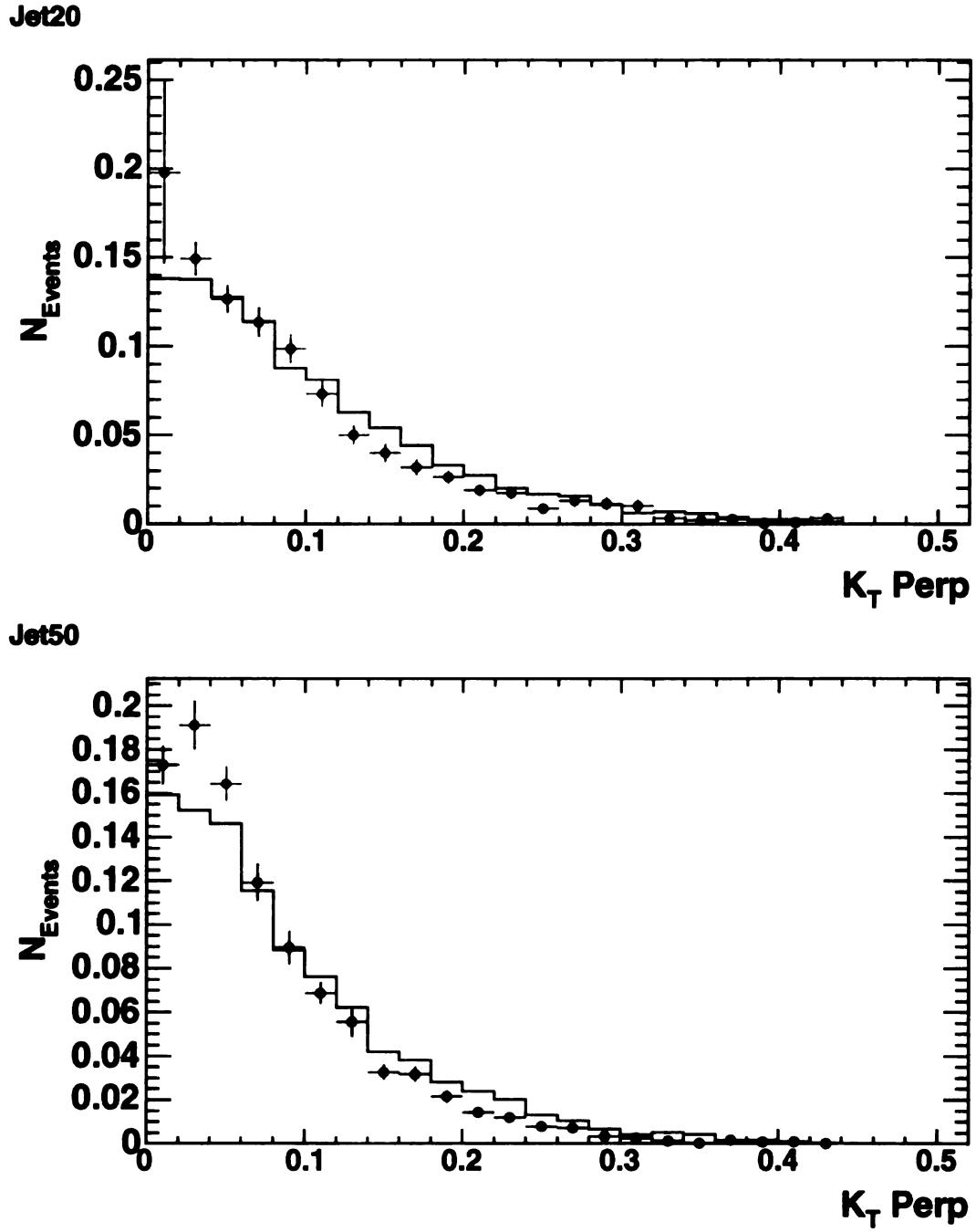

Figure 10.7: *$K_{T\perp}$ distributions for data (histogram) and Pythia (points). This quantity is related to the detector η resolution which is effected by radiation.*

figure 10.7 continued.

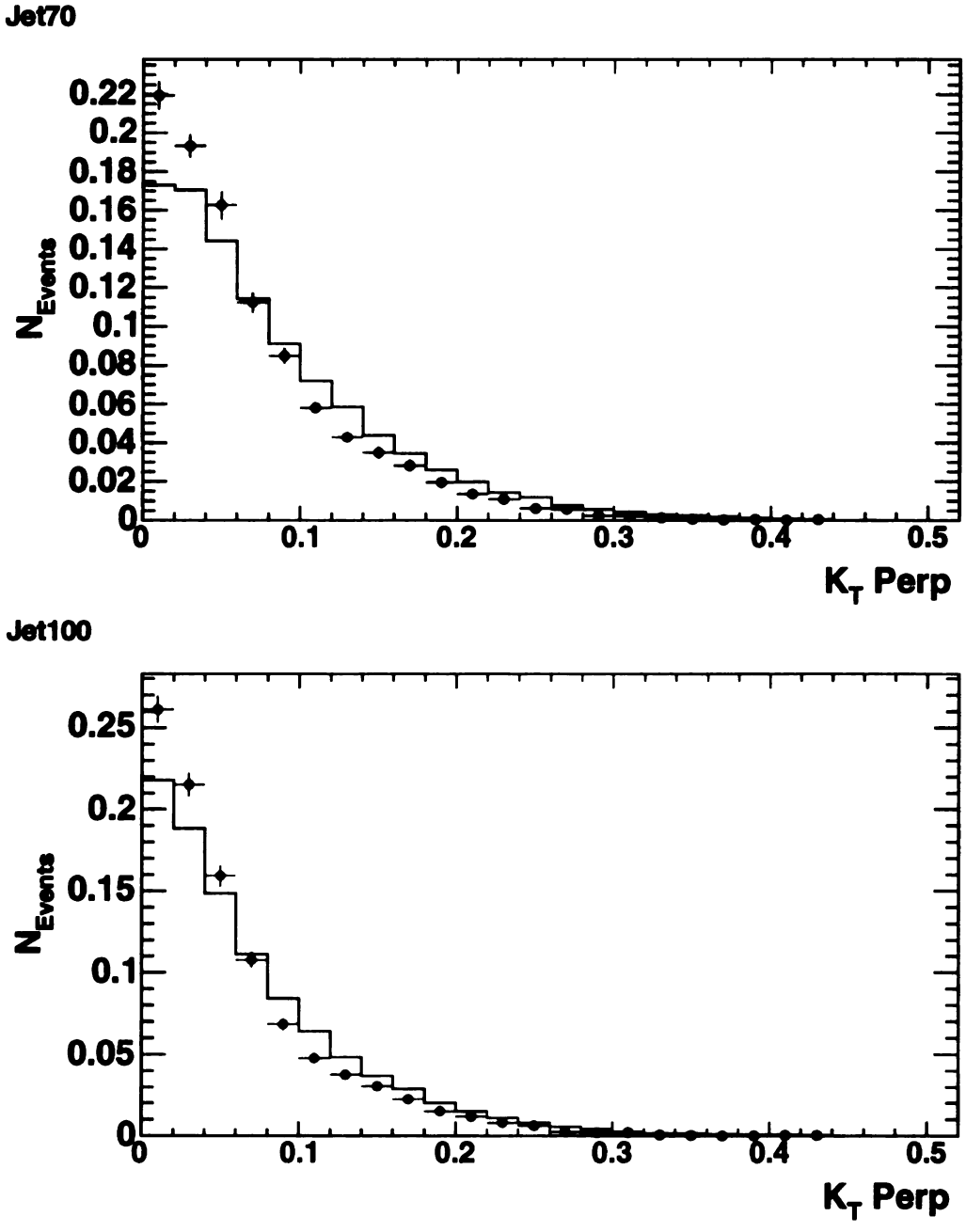

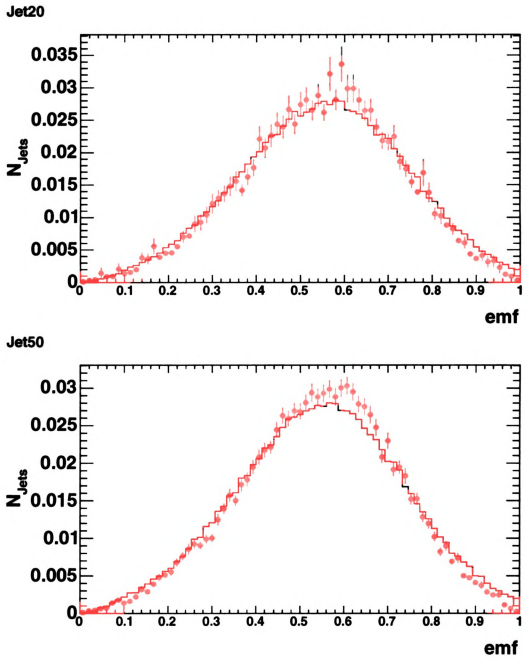

Figure 10.8: *Fraction of the total energy deposited in the electromagnetic compartment of the calorimeter for data (histogram) and Pythia (points).*

figure 10.8 continued.

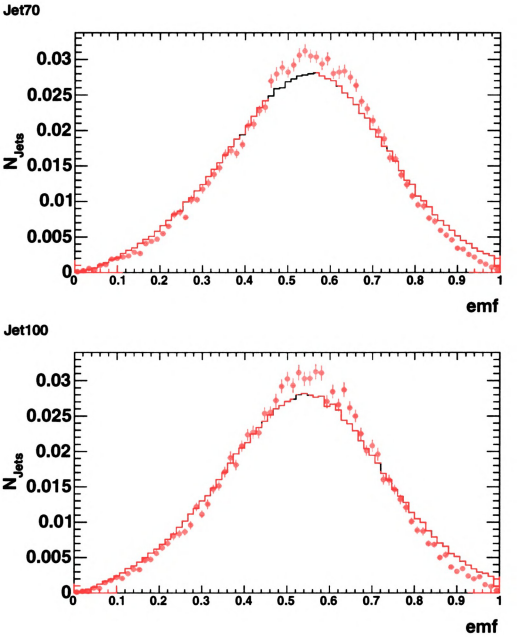

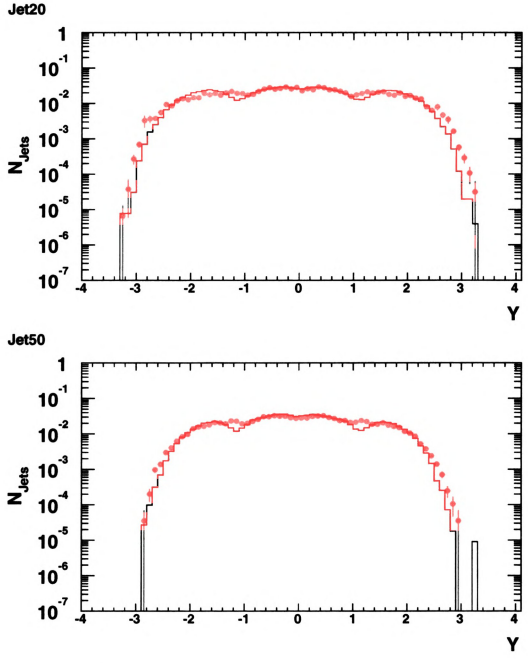

Figure 10.9: *Rapidity (Y) distribution for data (histogram) and Pythia (points).*

figure 10.9 continued.

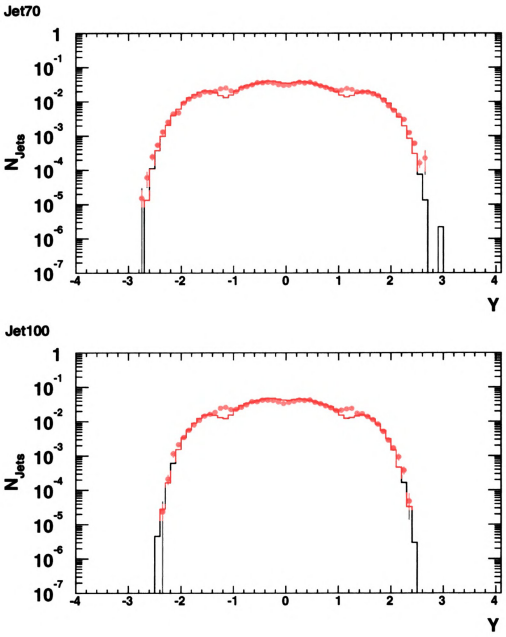

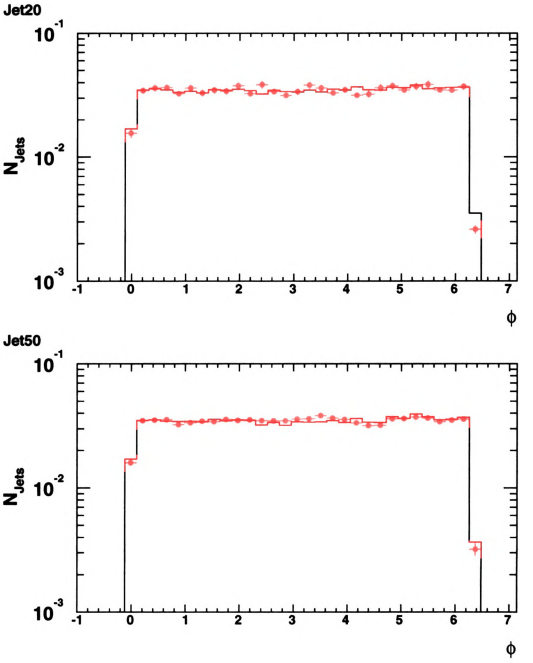

Figure 10.10: *Azimuthal angle (ϕ) distributions for data (histogram) and Pythia (points).*

figure 10.10 continued.

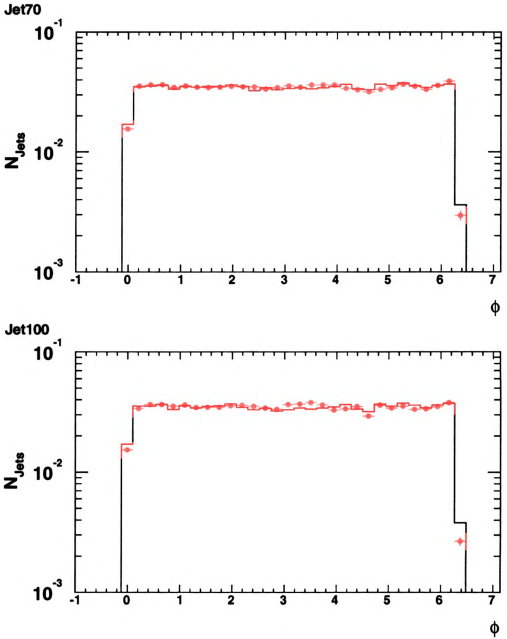

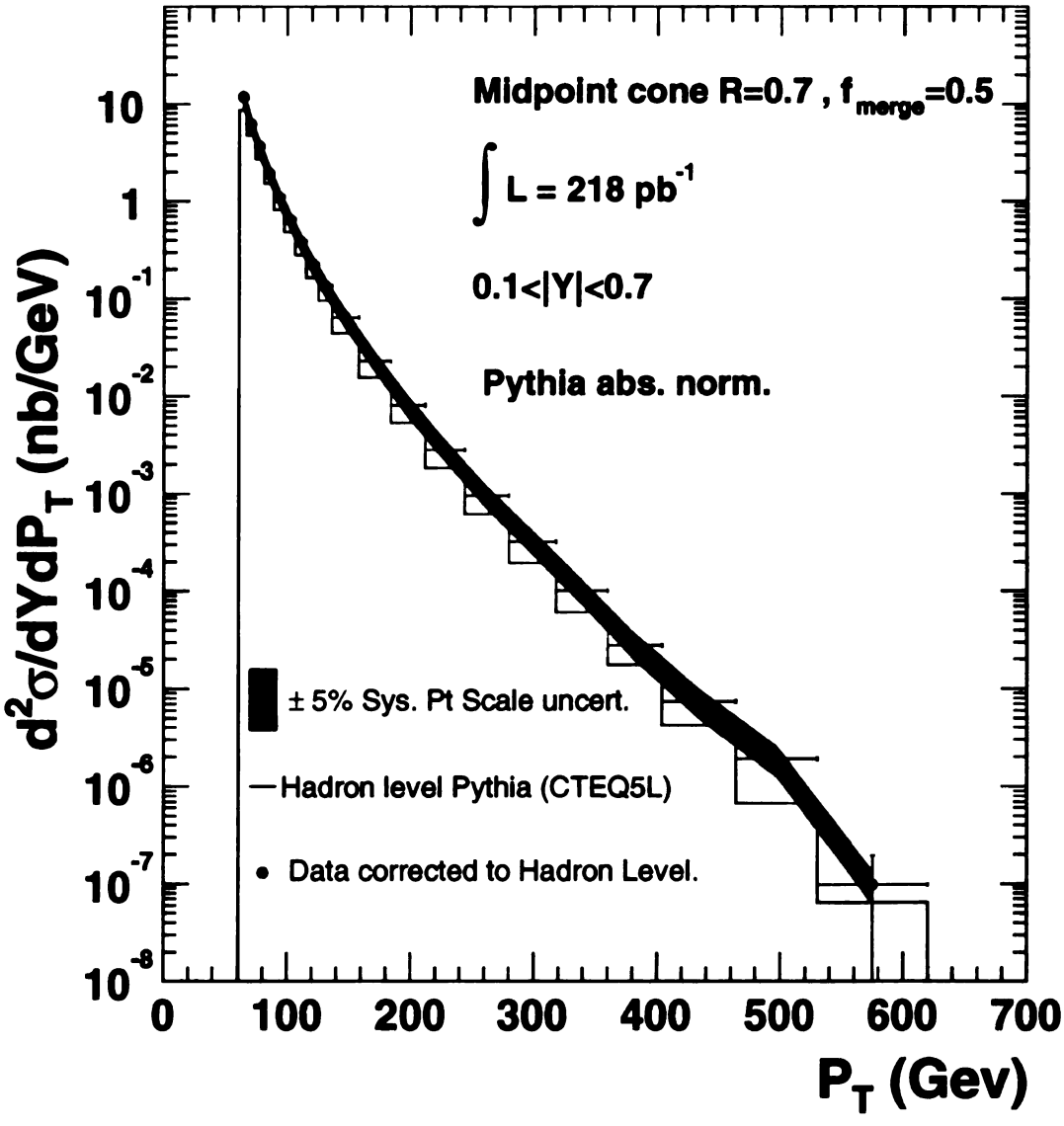

Figure 10.11: *Data corrected to hadron level versus hadron level pythia (CTEQ5L): log scale. The band represents the ±5% energy scale systematic uncertainty. Both the data and Pythia still have underlying event present.*

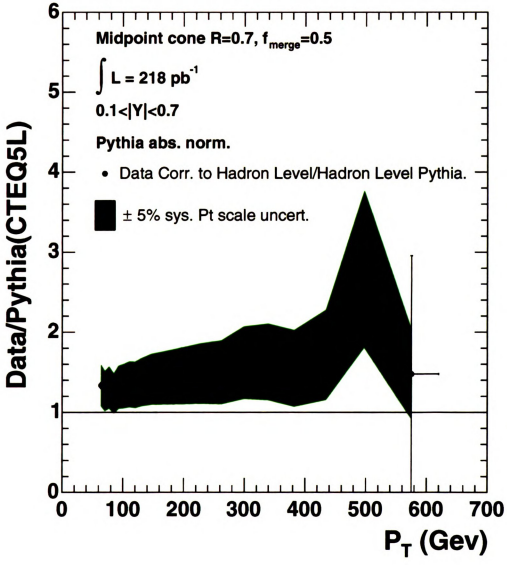

Figure 10.12: *Data corrected to hadron level versus hadron level pythia (CTEQ5L) linear scale. The band represents the ±5% energy scale systematic uncertainty. Both the data and Pythia still have underlying event present.*

$P_T^{Min} - P_T^{Max}$	$\sigma(hadron)/Pythia(CTEQ5l)$	Stat.Err
61-67	1.33421	0.0345388
67-74	1.26632	0.034378
74-81	1.31026	0.0367131
81-89	1.23448	0.0409693
89-97	1.31345	0.0260076
97-106	1.32763	0.0172449
106-115	1.35039	0.0190693
115-125	1.34406	0.0192351
125-136	1.37589	0.0207802
136-158	1.41256	0.0149788
158-184	1.43318	0.015308
184-212	1.45645	0.0177192
212-244	1.48374	0.019663
244-280	1.49944	0.0247599
280-318	1.62059	0.0397356
318-360	1.62995	0.0643615
360-404	1.54883	0.109849
404-464	1.71677	0.2092
464-530	2.78737	0.677675
530-620	1.47729	1.47763

Table 10.1: *Ratio of measured hadron level inclusive jet cross section over hadron level Pythia cross section. This cross section still contains underlying event.*

Chapter 11

Comparison of the Data to NLO pQCD

11.1 Introduction

The corrected inclusive jet cross section is compared to NLO pQCD predictions from the EKS program [29, 30, 31] using the CTEQ6.1 PDF set. In all comparisons that follow, the EKS prediction uses a renormalisation scale and factorisation scale of $P_T^{Jet}/2$. The CTEQ6.1 PDF's are an update to the published CTEQ6M PDF sets. The CTEQ6.1 PDF set contain the CDF and D0 Run 1 jet data and are thus the most complete/up to date set.

The predictions for NLO pQCD depend on input parameters such as the parton distribution functions, choice of factorisation/renormalisation scales and the choice of $\alpha_s(M_z)$.

As discussed previously it is desirable to have the clustering at parton level, hadron level and calorimeter level done in a consistent way. The clustering at the calorimeter level is performed over jets of hadrons (seen as calorimeter towers). The edges of these jets are not distinct. Some events will have jets that are close to one another, introducing ambiguities such as those seen with merging and splitting in jet algorithms. These ambiguities are not modelled in the NLO pQCD predictions as there

are, at most, 3 partons in the final state. The parameter R_{sep} was introduced into the theoretical prediction to approximate the effects of merging and splitting of clusters as done by experimental algorithms.

The choice of μ scale introduces an unavoidable uncertainty in a fixed order perturbative calculation. Traditionally, $\mu = P_T^{Jet}/2$ has been used but other scale choices such as $\mu = P_T^{Jet}$ are also acceptable.

11.2 Correcting NLO pQCD for Underlying Event

In order to compare NLO pQCD to the hadron level data the underlying event must be accounted for. This can be done either by subtracting the UE contribution from the data or adding it to the NLO predictions. Here the later method was used. The underlying event corrections were derived from both the Pythia and Herwig in the form of bin by bin corrections much like those used for the smearing correction. The corrections derived from Pythia were used to correct the data as these provided a consistent scheme with respect to the calorimeter to hadron level corrections.

There are two competing effects that make up the parton to hadron level correction: the first is fragmentation and the second is underlying event. Fragmentation causes energy to be lost from the jet cone whereas the underlying event adds additional energy into the jet cone. In Pythia the underlying event is the dominant process, especially at low P_T. In Herwig the underlying event contribution also dominates but not as much. The difference in the overall parton to hadron level correction is associated with two effects: Herwig underlying event is smaller than Pythia and Pythia has a more physical implementation of the underlying event (it is included at parton level).

11.3 Results

In this section we present a comparison of the data corrected to the hadron level and the parton level to the NLO pQCD prediction from the EKS program. The comparison of the hadron level cross section to the NLO pQCD prediction is done in three steps: the first is the comparison with no underlying event correction, the second is the comparison with the underlying event correction and the third is the comparison with the full parton to hadron correction. The results are organised in the following way:

- Figures 11.1 and 11.2 show the data (corrected to hadron level) compared to the NLO pQCD prediction. No correction has been made for the underlying event.

- Figures 11.3 and 11.4 show the data compared to the NLO pQCD prediction. The prediction has been corrected on a bin by bin basis to account for the underlying event only.

- Figure 11.5 shows data compared to the NLO pQCD prediction with the underlying event and fragmentation correction applied.

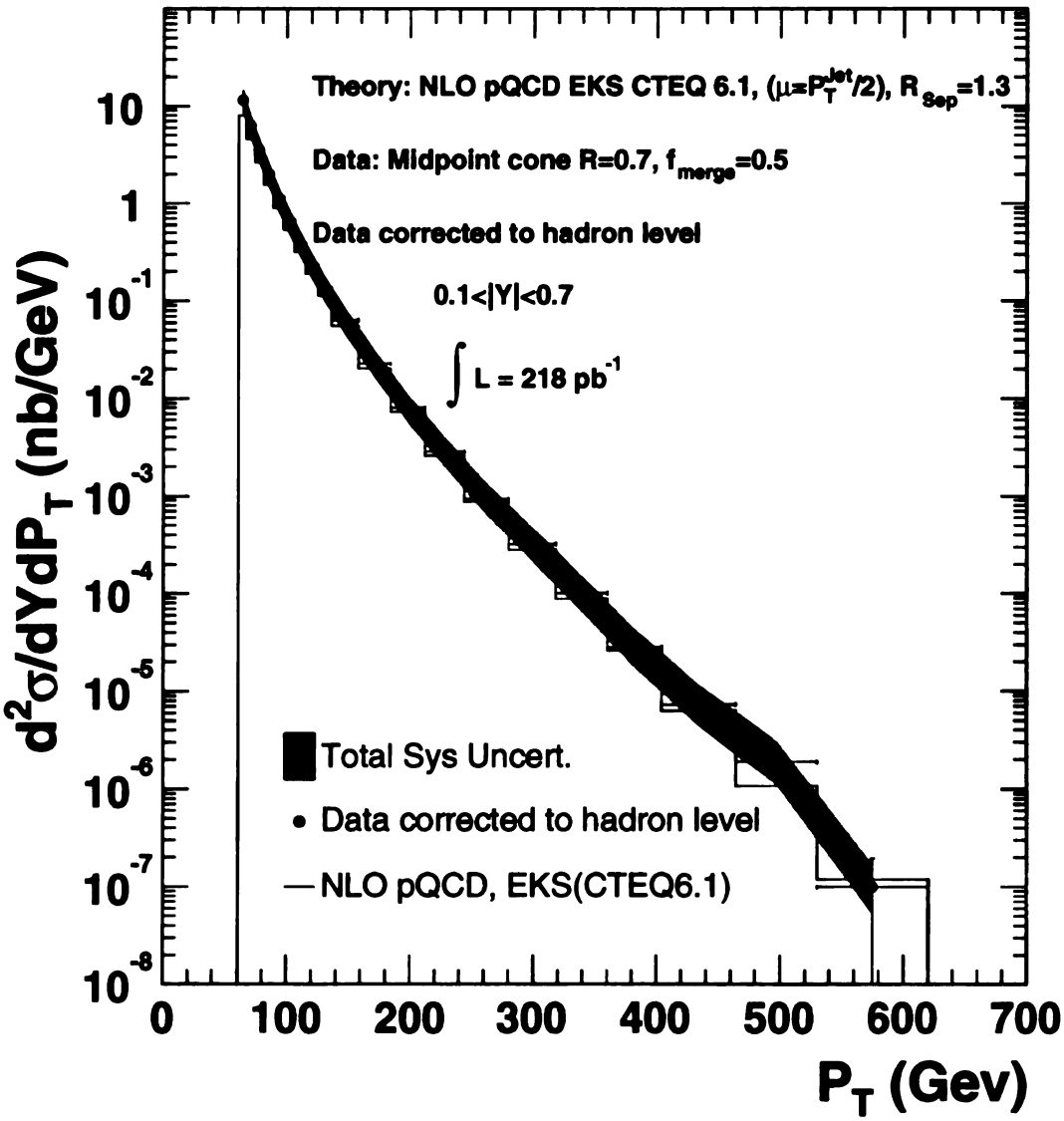

Figure 11.1: *Data corrected to hadron level versus NLO pQCD. The data is corrected for multiple interactions; however no correction for underlying event has been made.*

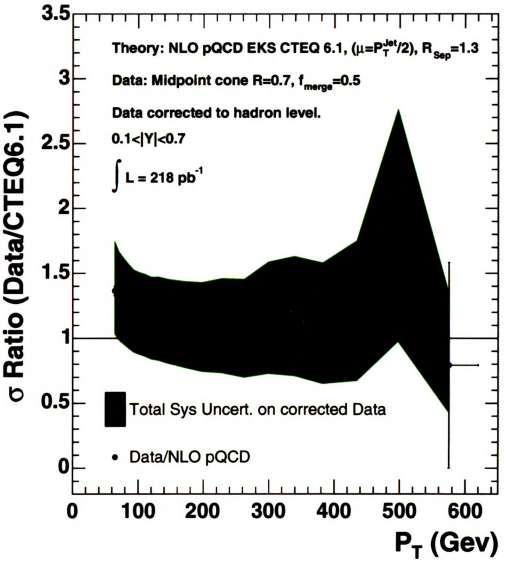

Figure 11.2: *Data corrected to hadron level versus NLO pQCD. (no underlying event correction)*

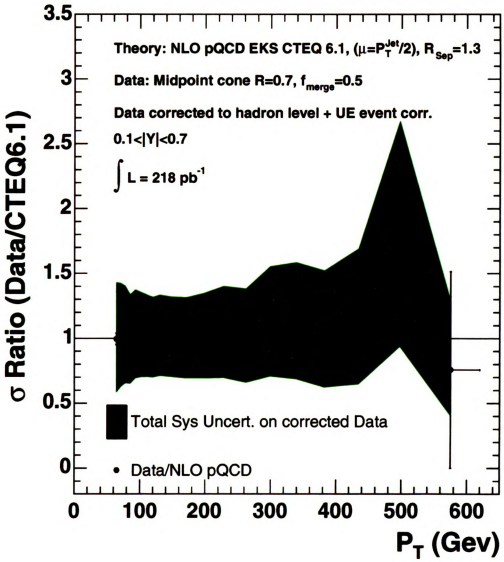

Figure 11.3: *Data corrected to hadron level and corrected for underlying event versus NLO pQCD.*

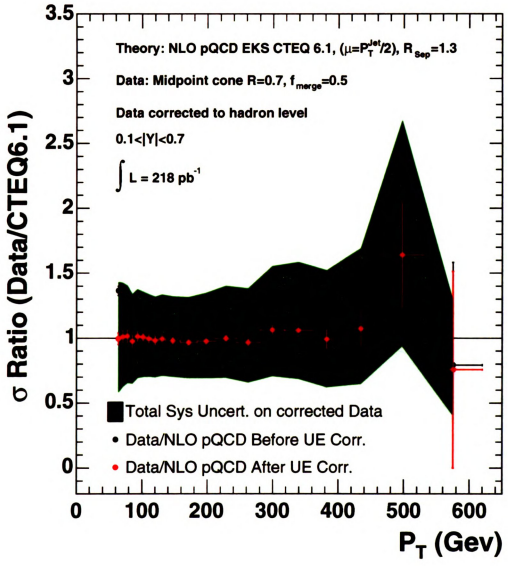

Figure 11.4: *Data corrected to hadron level before and after underlying event correction versus NLO pQCD.*

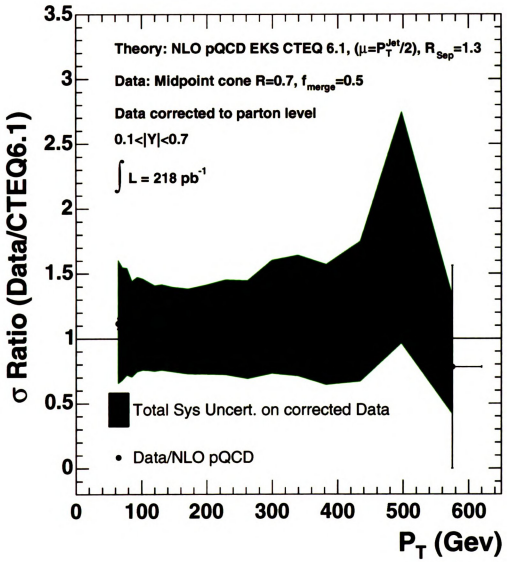

Figure 11.5: *Data corrected to parton level versus NLO pQCD.*

P_T Bin	Had. Level Data	Stat. Err.	UE Corr.	Part. Corr.	NLO pQCD
61-67	11.512	0.3040	1.2733	1.22425	8.03309
67-74	6.30843	0.1692	1.2404	1.19712	4.6274
74-81	3.5305	0.1026	1.2112	1.17312	2.6693
81-89	1.9922	0.0638	1.1857	1.15202	1.5570
89-97	1.1307	0.02194	1.1631	1.13341	0.9123
97-106	0.6588	0.008480	1.1434	1.11709	0.5407
106-115	0.3869	0.005502	1.1261	1.10272	0.3222
115-125	0.2283	0.003243	1.1109	1.09013	0.1940
125-136	0.1345	0.00204	1.0970	1.07857	0.1148
136-158	0.06329	0.0006792	1.0800	1.06435	0.05528
158-184	0.02273	0.0002429	1.0620	1.04918	0.02038
184-212	0.007999	9.7479e-05	1.0482	1.03747	0.007330
212-244	0.002853	3.728e-05	1.03831	1.02882	0.002604
244-280	0.0009352	1.5562e-05	1.03138	1.02259	0.0008745
280-318	0.0003234	7.9200e-06	1.02734	1.01869	0.0002834
318-360	0.0001014	4.0050e-06	1.02575	1.01674	8.8620e-05
360-404	2.8252e-05	2.0023e-06	1.02622	1.01644	2.6066e-05
404-464	7.3605e-06	8.9697e-07	1.02892	1.01782	6.3116e-06
464-530	1.9024e-06	4.6254e-07	1.03424	1.02118	1.0685e-06
530-620	9.9217e-08	9.9239e-08	1.04297	1.02709	1.1929e-07

Table 11.1: *The inclusive jet cross section corrected to the hadron level and NLO pQCD prediction. The additional columns are the underlying event correction factors (UE. Corr) and the parton to hadron correction factors (Part. Corr).*

P_T Low - P_T High	$\sigma_{Data}^{Hadron}/\sigma_{pQCD}^{NLO}$	Stat. Err	+Sys(-Sys)
61-67	1.365	0.036	+0.284(-0.243)
67-74	1.298	0.035	+0.286(-0.241)
74-81	1.260	0.037	+0.290(-0.241)
81-89	1.219	0.039	+0.294(-0.241)
89-97	1.180	0.023	+0.300(-0.243)
97-106	1.160	0.015	+0.306(-0.245)
106-115	1.144	0.016	+0.313(-0.248)
115-125	1.120	0.016	+0.322(-0.252)
125-136	1.115	0.017	+0.335(-0.256)
136-158	1.090	0.012	+0.354(-0.262)
158-184	1.062	0.011	+0.377(-0.273)
184-212	1.039	0.013	+0.402(-0.285)
212-244	1.043	0.014	+0.431(-0.298)
244-280	1.018	0.017	+0.462(-0.314)
280-318	1.087	0.027	+0.496(-0.331)
318-360	1.090	0.043	+0.533(-0.350)
360-404	1.032	0.073	+0.578(-0.370)
404-464	1.111	0.135	+0.632(-0.395)
464-530	1.696	0.412	+0.699(-0.425)
530-620	0.792	0.792	+0.701(-0.462)

Table 11.2: *Data corrected to the hadron level over NLO pQCD including full statistical and systematic errors (No underlying event correction has been applied).*

P_T Low - P_T High	$\sigma_{Data}^{Hadron+UE}/\sigma_{pQCD}^{NLO}$	Stat. Err	+Sys(-Sys)
61-67	0.995	0.044	+0.438(-0.413)
67-74	1.011	0.047	+0.409(-0.381)
74-81	1.014	0.050	+0.386(-0.354)
81-89	0.977	0.050	+0.369(-0.333)
89-97	1.013	0.037	+0.357(-0.316)
97-106	1.006	0.028	+0.349(-0.303)
106-115	0.995	0.031	+0.344(-0.294)
115-125	0.982	0.031	+0.343(-0.287)
125-136	0.993	0.032	+0.344(-0.283)
136-158	0.979	0.024	+0.350(-0.281)
158-184	0.966	0.022	+0.363(-0.284)
184-212	0.976	0.025	+0.382(-0.291)
212-244	0.998	0.022	+0.405(-0.303)
244-280	0.966	0.026	+0.433(-0.317)
280-318	1.062	0.034	+0.463(-0.333)
318-360	1.059	0.046	+0.497(-0.351)
360-404	0.992	0.074	+0.534(-0.371)
404-464	1.072	0.133	+0.579(-0.396)
464-530	1.639	0.401	+0.633(-0.426)
530-620	0.757	0.758	+0.701(-0.465)

Table 11.3: *Data corrected to the hadron level over NLO pQCD including full statistical and systematic errors. The ratio has been corrected for underlying event.*

P_T Low - P_T High	$\sigma_{Data}^{Parton}/\sigma_{pQCD}^{NLO}$	Stat. Err	+Sys(-Sys)
61-67	1.117	0.042	+0.438(-0.413)
67-74	1.099	0.044	+0.409(-0.381)
74-81	1.115	0.050	+0.386(-0.354)
81-89	1.054	0.044	+0.369(-0.333)
89-97	1.088	0.030	+0.357(-0.316)
97-106	1.085	0.027	+0.349(-0.303)
106-115	1.069	0.030	+0.344(-0.294)
115-125	1.050	0.030	+0.343(-0.287)
125-136	1.054	0.031	+0.344(-0.283)
136-158	1.036	0.022	+0.350(-0.281)
158-184	1.016	0.021	+0.363(-0.284)
184-212	1.023	0.026	+0.382(-0.291)
212-244	1.036	0.023	+0.405(-0.303)
244-280	1.011	0.027	+0.433(-0.317)
280-318	1.096	0.034	+0.463(-0.333)
318-360	1.098	0.049	+0.497(-0.351)
360-404	1.025	0.076	+0.534(-0.371)
404-464	1.108	0.137	+0.579(-0.396)
464-530	1.683	0.411	+0.633(-0.426)
530-620	0.781	0.781	+0.701(-0.465)

Table 11.4: *Data corrected to the parton level over NLO pQCD including full statistical and systematic errors.*

11.4 Conclusion

In summary, we have measured the inclusive jet cross section in the P_T range 61-620 GeV. The statistical uncertainty of the data is significantly better than the systematic uncertainty in the measurement. We see good agreement between the central values of data and NLO pQCD predictions. The systematic uncertainties quoted here very conservative. From the figures 11.1- 11.5 it is seen that within the systematic uncertainties the corrected data agree very well with the NLO pQCD prediction (CTEQ6.1). The NLO pQCD predictions use the CTEQ6.1 PDF set. These contain jet data both CDF and D0 run I jet data.

Chapter 12

Systematic Uncertainties

12.1 Introduction

The systematic uncertainties on the measured inclusive jet cross section come from three sources: calorimeter response, resolution and luminosity. The uncertainty on the luminosity has no P_T dependence: it only effects normalisation. Systematic uncertainties arising from the unfolding of the measured cross section to the hadron level contributes to the uncertainty on the corrected inclusive cross section. This contribution is in addition to the systematic uncertainty associated with the measured cross section. There are additional uncertainties on the NLO pQCD due to choice of μ scale, PDF uncertainty and the underlying event correction.

12.2 Jet P_T Scale Uncertainties

The uncertainties associated with jet energy scale include calorimeter response, fragmentation tuning, multiple interaction energy and the energy from the underlying event falling into the jet cone.

12.2.1 Calorimeter Response

The uncertainty on the calorimeter response is taken from a comparison of data and Pythia. The comparison is made between the quantity

$$R(P_T) = \sum P_T(Cal) / \sum P_T(Tracks) \tag{12.1}$$

for data and Pythia. The double ratio $R(P_T)^{Data}/R(P_T)^{Pythia}$ is then found. The deviation of this double ratio from unity is used to set the jet scale uncertainty. From this study the uncertainty is found to be 5% [35].

The non linearity of the central calorimeter to charged particles contributes to the energy loss of the calorimeter. Jet fragmentation is a measure of the distributions of the charged particles associated with tracks and therefore effects how well the simulation reproduces the jet energy and jet energy losses in the detector. The overall agreement between the data and Pythia is reasonably good (seen in jet shapes). The uncertainty on the cross section due to the fragmentation tuning is related to the track finding efficiency in the dense track environment of jets. The differences between track finding efficiencies in data and Pythia are not corrected for in the determination aformentioned 5% systematic, therefore this value is a conservative estimate of the systematic uncertainty.

12.2.2 Unfolding

In order to estimate the uncertainty associated with the hadronisation model used in the Monte Carlo corrections we treat the difference between the bin correction factors from Pythia and Herwig as a systemaic uncertainty. The difference is only significant below 100 GeV.

12.2.3 Multiple Interaction Uncertainties

The contribution to the jet energy due to multiple interactions is removed from the raw jets. For a given event if more than one quality 12 vertex is found 0.92 GeV is removed for each additional vertex. The systematic uncertainty on this correction is 30%: this systematic covers the luminosity dependence of the measurement and also the changes seen by increasing/decreasing the tower threshold by 50 MeV in the measurement definition.

12.2.4 Underlying Event

Underlying event corrections are derived from Pythia and Herwig. We used the correction derived from Pythia to correct the data as this provides a consistent correction scheme for calorimeter to hadron corrections and the parton to hadron corrections. Also Pythia includes the underlying event contribution at parton level which Herwig does not. This is important when deriving parton-hadron level corrections. The difference between Herwig and Pythia corrections are used as the systematic uncertainty. It is not combined with the uncertainties on the measured cross section. Instead it is treated as a systematic on the NLO pQCD prediction.

12.2.5 Integrated Luminosity and Z Vertex Uncertainty

The integrated luminosity enters the cross section expression as a normalisation factor. The uncertainty on the integrated luminosity contributes to the systematic uncertainty on the cross section as follows:

$$\delta\sigma = \frac{d\sigma}{dL}.\delta L = \sigma.\frac{\delta L}{L}. \tag{12.2}$$

The uncertainty on the luminosity is 6.0% common for all P_T values.

12.2.6 Results

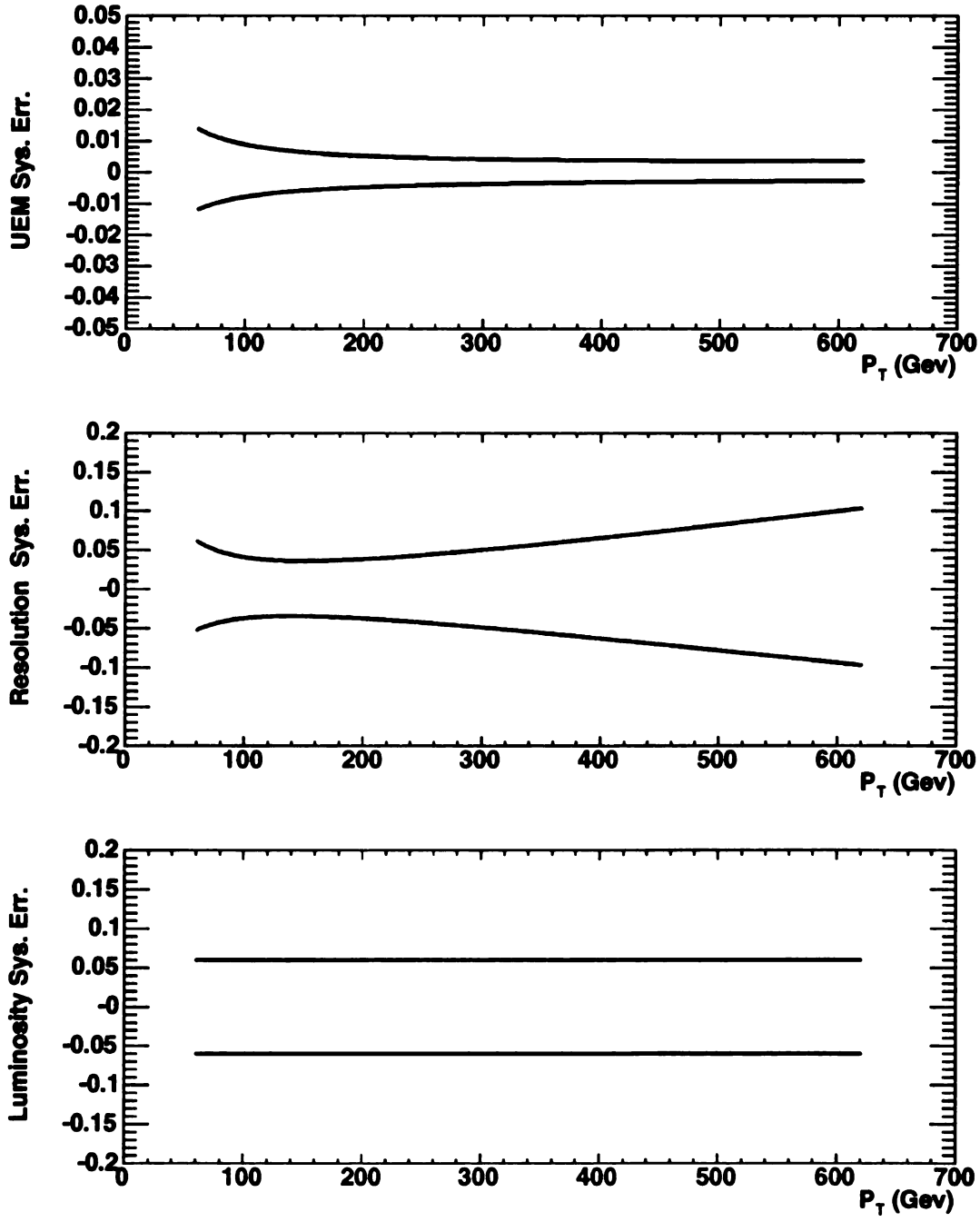

Figure 12.1: *Fractional contributions to the total systematic uncertainty on the inclusive jet cross section. We see that the energy scale and underlying event uncertainties dominate the total systematic uncertainty.*

figure 12.1 continued.

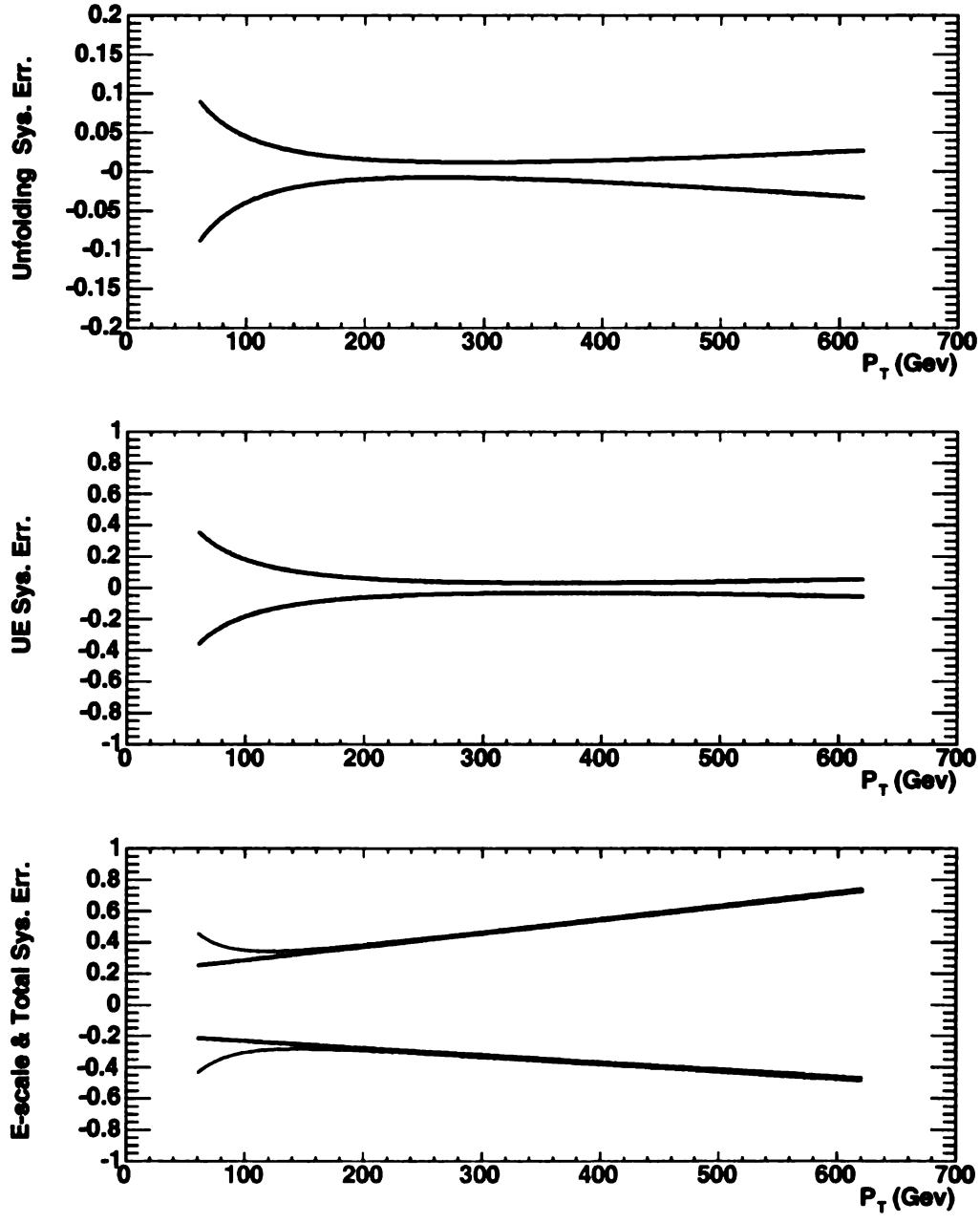

P_T Low - P_T High	E-scale(+)	E-scale(-)
61-67	0.255857	-0.214444
67-74	0.261371	-0.217418
74-81	0.267309	-0.220621
81-89	0.27367	-0.224053
89-97	0.280456	-0.227713
97-106	0.287666	-0.231603
106-115	0.2953	-0.235721
115-125	0.303359	-0.240067
125-136	0.312265	-0.244872
136-158	0.326261	-0.252422
158-184	0.346619	-0.263403
184-212	0.369521	-0.275757
212-244	0.394968	-0.289484
244-280	0.423809	-0.305041
280-318	0.455193	-0.321971
318-360	0.489123	-0.340274
360-404	0.525597	-0.359949
404-464	0.569706	-0.383742
464-530	0.623145	-0.412568
530-620	0.689307	-0.448258

Table 12.1: *Energy scale systematic uncertainty.*

P_T Low - P_T High	Unfolding(+)	Unfolding(-)
61-67	0.0840673	-0.082172
67-74	0.0737525	-0.0708698
74-81	0.064686	-0.0609694
81-89	0.056741	-0.0523296
89-97	0.0497957	-0.0448149
97-106	0.0437369	-0.0382995
106-115	0.0384625	-0.0326698
115-125	0.0338817	-0.0278248
125-136	0.0297355	-0.0234897
136-158	0.0246824	-0.0183037
158-184	0.019571	-0.0132506
184-212	0.0159109	-0.00989093
212-244	0.0135178	-0.00801959
244-280	0.0121957	-0.00744484
280-318	0.011868	-0.00805544
318-360	0.0123901	-0.00969023
360-404	0.0136477	-0.0122223
404-464	0.0158327	-0.0160229
464-530	0.0191441	-0.0213666
530-620	0.023914	-0.0287277

Table 12.2: *Hadronisation model systematic uncertainty.*

P_T Low - P_T High	UEM(+)	UEM(-)
61-67	0.0132962	-0.0112895
67-74	0.0121768	-0.010397
74-81	0.0111847	-0.00960322
81-89	0.0103068	-0.00889782
89-97	0.00953027	-0.00827081
97-106	0.00884327	-0.0077129
106-115	0.00823514	-0.00721573
115-125	0.00769638	-0.00677185
125-136	0.00719679	-0.00635643
136-158	0.0065646	-0.00582353
158-184	0.00587912	-0.00523199
184-212	0.00532653	-0.00473791
212-244	0.00488753	-0.00432619
244-280	0.00453533	-0.00397355
280-318	0.00426825	-0.00368092
318-360	0.00407113	-0.00343642
360-404	0.00393205	-0.00323069
404-464	0.0038333	-0.00303637
464-530	0.00378311	-0.00285541
530-620	0.00379103	-0.00268631

Table 12.3: *Multiple interaction systematic uncertainty.*

P_T Low - P_T High	UE(+)	UE(-)
61-67	0.334386	-0.334386
67-74	0.294689	-0.294689
74-81	0.25965	-0.25965
81-89	0.228791	-0.228791
89-97	0.20165	-0.20165
97-106	0.177801	-0.177801
106-115	0.156859	-0.156859
115-125	0.138479	-0.138479
125-136	0.121627	-0.121627
136-158	0.100669	-0.100669
158-184	0.0786399	-0.0786399
184-212	0.0617522	-0.0617522
212-244	0.0493094	-0.0493094
244-280	0.0404576	-0.0404576
280-318	0.0350219	-0.0350219
318-360	0.0324551	-0.0324551
360-404	0.0323262	-0.0323262
404-464	0.0346786	-0.0346786
464-530	0.0400378	-0.0400378
530-620	0.0492035	-0.0492035

Table 12.4: *Underlying Event systematic.*

12.3 Jet Energy Resolution Uncertainty

The uncertainty on the jet resolution is determined from the average deviation of the single jet resolution (σ_{RMS}) measured in the data from that measured in Pythia. The comparison is made over 12 bins of $\langle P_T \rangle$. This uncertainty is propagated into the cross section using the following procedure: the systematic uncertainty for the resolution is found by smearing the true hadron level inclusive jet P_T distribution by:

$$N_{Jet}^{Had}(P_T^{Had})' = N_{Jet}^{Had}(P_T^{Had})(1 + \sigma(\frac{P_T^{Cal}}{P_T^{Had}}) \times \alpha), \tag{12.3}$$

where $N_{Jet}^{Had}(P_T^{Had})$ and $N_{Jet}^{Had}(P_T^{Had})'$ are the number of hadron jets in a bin before and after smearing respectively. $\sigma(\frac{P_T^{Cal}}{P_T^{Had}})$ is the jet resolution as a function of P_T^{Had} and α is a random number generated from a gaussian distributions with $\mu = 0$ and $\sigma = 1, 1.08$ and 0.92: these are labelled $gaus(0,1)$, $gaus(0,1.08)$ and $gaus(0,0.92)$ respectively. The size of the variation of the σ's comes the average Pythia-Data σ^{Jet} discrepancy.

Having smeared the inclusive P_T distribution the overall change in cross section was determined from the ratio:

$$\left(\frac{N_{Jet}/N_{Jet}^{gaus(0,1)}}{N_{Jet}/N_{Jet}^{gaus(0,1.08)}} \right) = \left(N_{Jet}^{gaus(0,1.92)}/N_{Jet}^{gaus(0,1)} \right), \tag{12.4}$$

where N_{Jet} is the number of jets in a P_T bin without smearing, $N_{Jet}^{gaus(0,1)}$ is the number of jets in a P_T bin after the resolution has been smeared with a gaussian ($\mu = 0$ and $\sigma = 1$) and $N_{Jet}^{gaus(0,1.08)}$ is the number of jets in a P_T bin after the resolution has been smeared with a gaussian ($\mu = 0$ and $\sigma = 1.08$). This procedure is repeated with a ($\mu = 0$ and $\sigma = 0.92$) gaussian. These two ratio's give the fractional

uncertainty on the cross section due to the resolution difference in the data and Pythia.

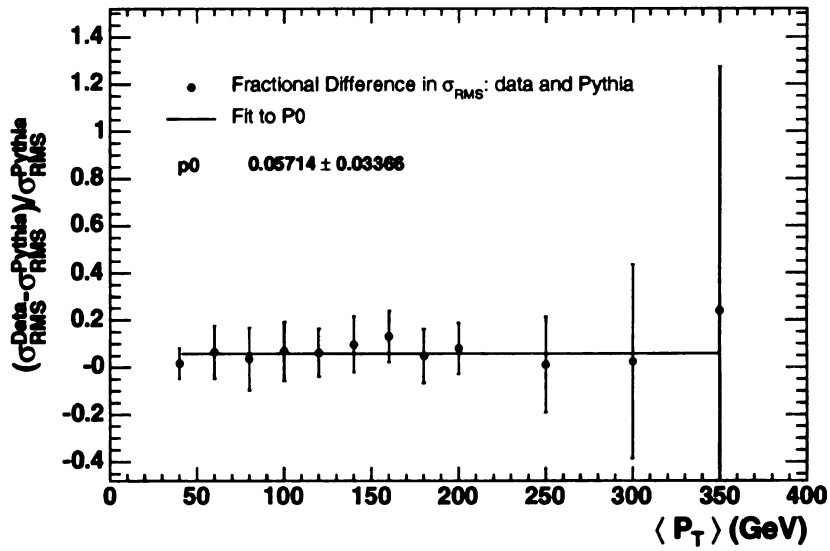

Figure 12.2: *Data-Pythia Resolution difference versus* $\langle P_T^{Dijet} \rangle$

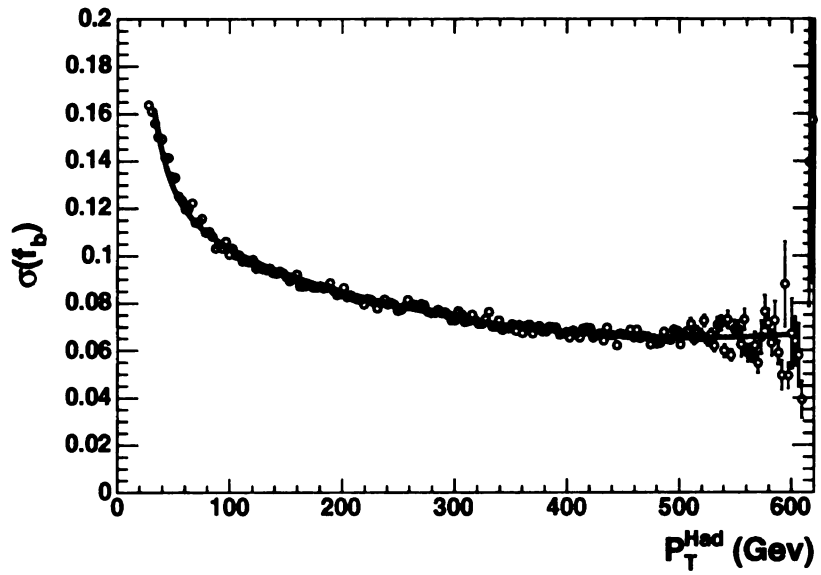

Figure 12.3: $\sigma(f_b)$ *versus* P_T^{Hadron}. *The errors are errors from the gaussian fit. This function is smeared with a gaussian to set the resolution uncertainty.*

P_T Low - P_T High	Resolution(+)	Resolution(-)
61-67	0.0585414	-0.0494923
67-74	0.0535827	-0.045816
74-81	0.0494036	-0.0427523
81-89	0.0459318	-0.0402457
89-97	0.0430981	-0.0382426
97-106	0.0408382	-0.0366936
106-115	0.039094	-0.0355538
115-125	0.0378138	-0.0347834
125-136	0.0369202	-0.034334
136-158	0.0363474	-0.034269
158-184	0.036787	-0.0351564
184-212	0.0384701	-0.0370714
212-244	0.0412917	-0.0399332
244-280	0.04528	-0.0437862
280-318	0.0502519	-0.0484666
318-360	0.0561252	-0.0539107
360-404	0.0628349	-0.0600686
404-464	0.0713266	-0.0678065
464-530	0.0819923	-0.0774728
530-620	0.0955784	-0.0897343

Table 12.5: *Resolution systematic uncertainty.*

P_T Low - P_T High	Total(+)	Total(-)
61-67	0.437662	0.413194
67-74	0.40892	0.380713
74-81	0.386293	0.354019
81-89	0.369156	0.332539
89-97	0.356856	0.315683
97-106	0.348746	0.302863
106-115	0.344213	0.293517
115-125	0.342695	0.287121
125-136	0.343805	0.283066
136-158	0.349505	0.281059
158-184	0.362905	0.283909
184-212	0.381734	0.291462
212-244	0.404899	0.302506
244-280	0.432516	0.316663
280-318	0.46337	0.333046
318-360	0.497207	0.351357
360-404	0.533898	0.371451
404-464	0.57855	0.396137
464-530	0.632942	0.426477
530-620	0.700633	0.464587

Table 12.6: *Total systematic uncertainty on the inclusive jet cross section.*

12.4 Sensitivity to Input PDF

In order to check the sensitivity of the jet correction method to the input PDF we would have liked to have had multiple Pythia samples generated with different PDF's. Generating a second complete set of Pythia samples was not practical so instead the standard Pythia CTEQ5l sample was re-weighted by the ratio of the LO pQCD cross section predictions from EKS using the CTEQ5l and CTEQml PDF sets. The re-weighting is performed on the $\hat{P_T}$ distribution. This re-weighting gives a new Pythia sample with a smaller high P_T cross section and a larger low P_T cross section with respect to Pythia CTEQ5l. We refer to the new/re-weighted Pythia sample as Pythia CTEQml.

Having re-weighted the distribution, the calorimeter and hadron cross sections were found using the CTEQml sample. The CTEQml calorimeter cross section was corrected using the standard CTEQ5l jet corrections and the corrected cross section compared to the expected/true CTEQml hadron cross section. Figure 12.8 shows that within the statistical uncertainty the correct hadron distribution is recovered.

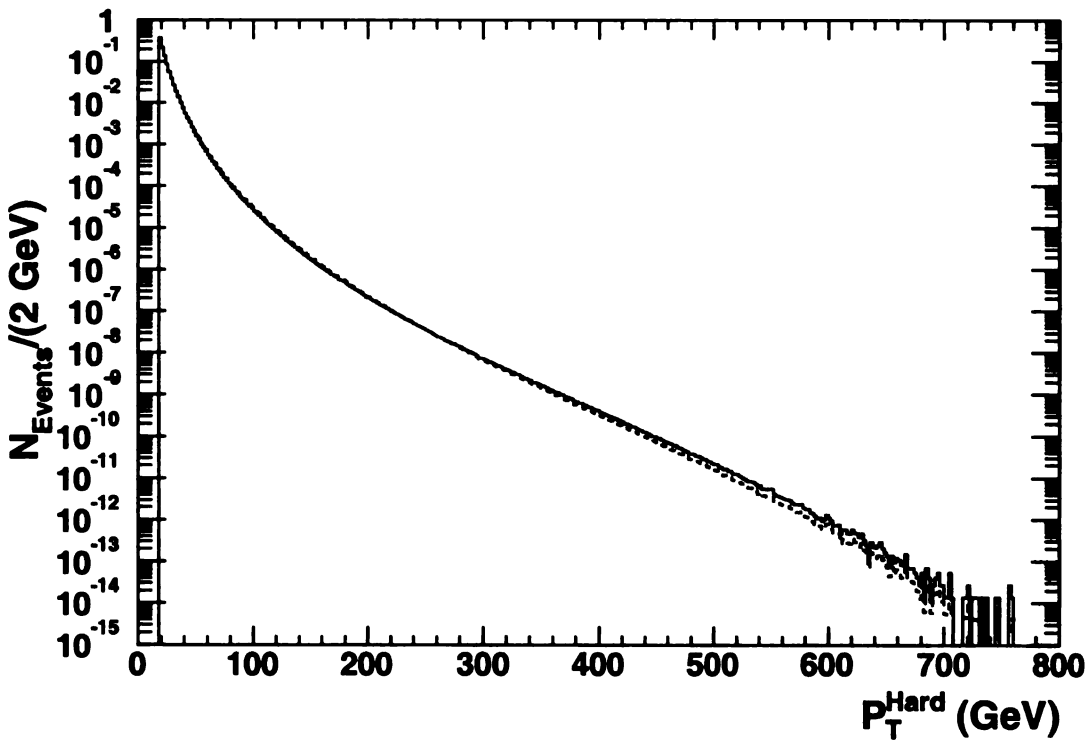

Figure 12.4: $\hat{P}_T$ *Pythia CTEQ5l Monte Carlo and Pythia re-weighted to resemble Pythia CTEQml.*

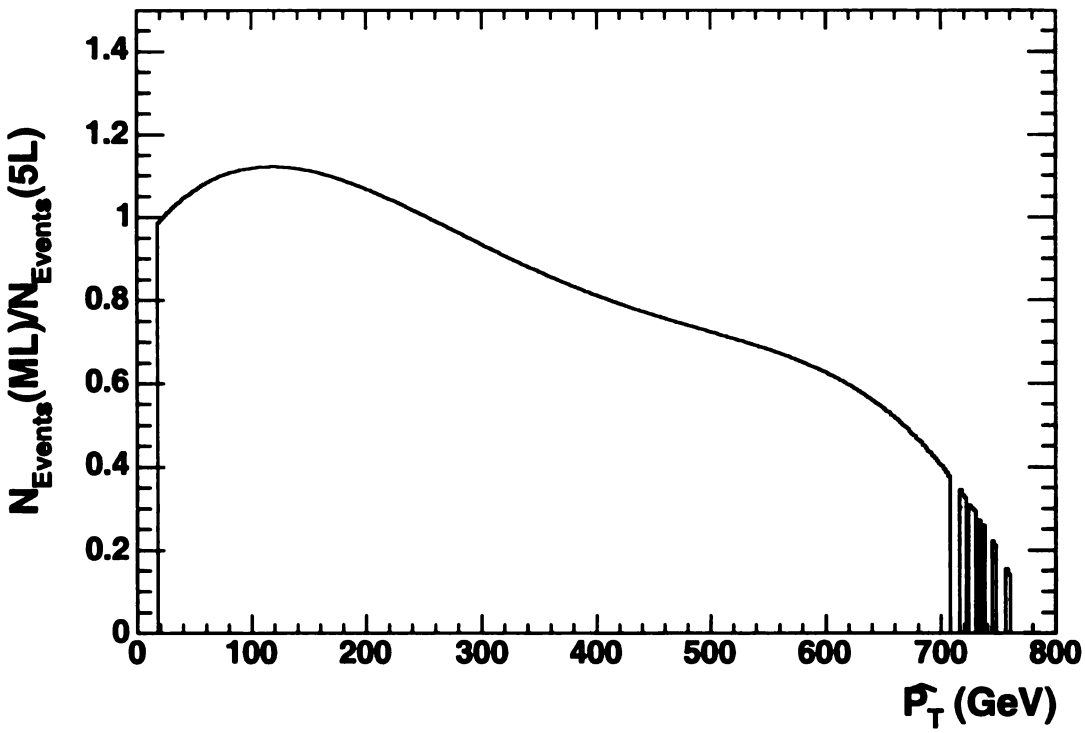

Figure 12.5: *Ratio of $\hat{P_T}$ Pythia CTEQ5l Monte Carlo and Pythia re-weighted to resemble Pythia CTEQml. It is clear that CTEQ5l has a much stiffer gluon distribution giving a larger high P_T cross section.*

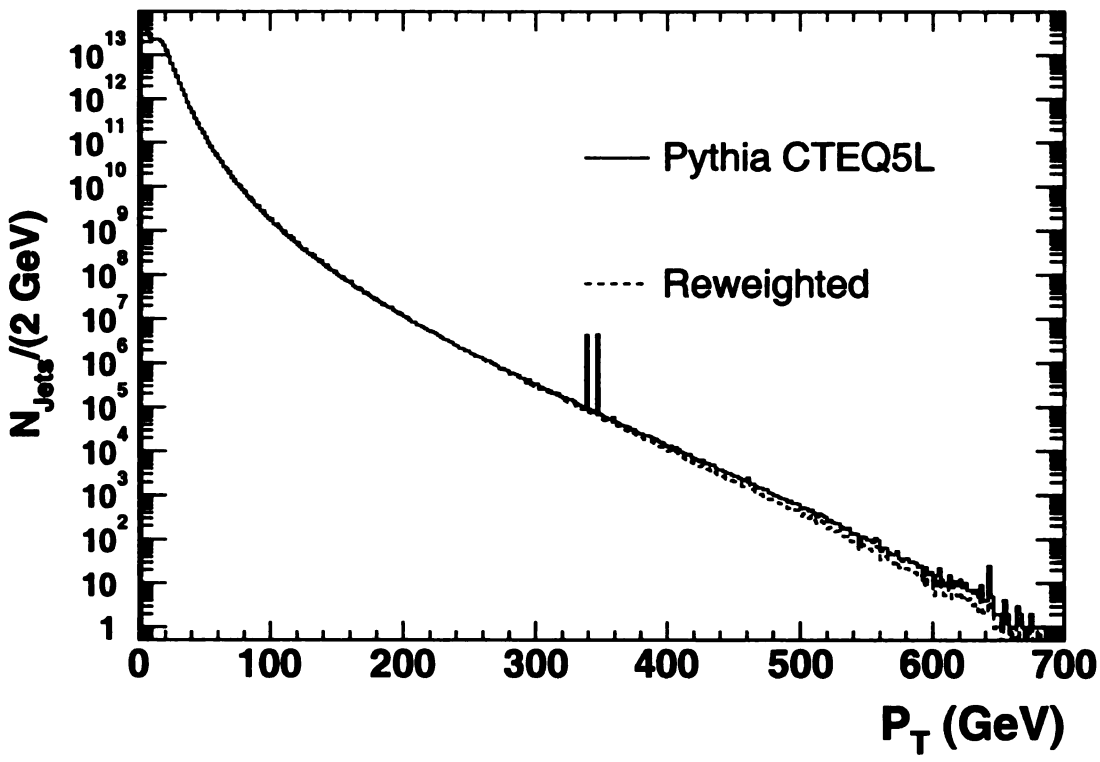

Figure 12.6: *Calorimeter level inclusive jet distribution for Pythia CTEQ5l and Pythia re-weighted by CTEQml*

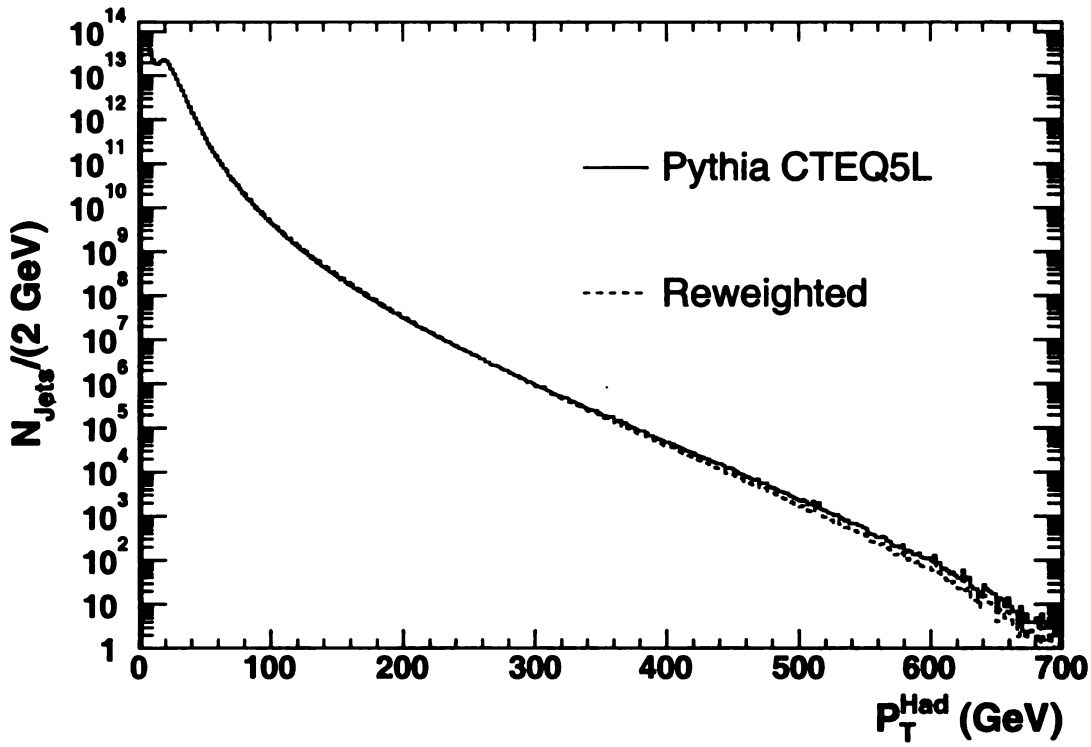

Figure 12.7: *Hadron level inclusive jet distribution for Pythia CTEQ5l and Pythia re-weighted by CTEQml*

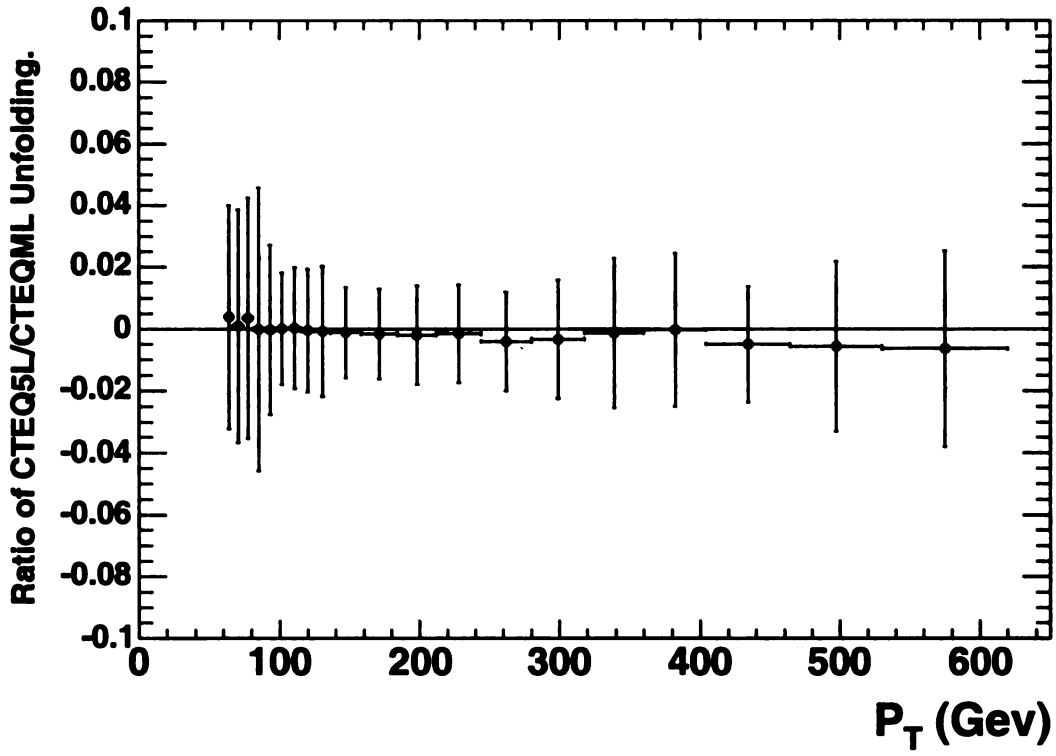

Figure 12.8: *The ratio of the Pythia re-weighted by CTEQml corrected to hadron level using Pythia CTEQ5l jet corrections over the true hadron level cross section. Within statistical uncertainties the true cross section is recovered.*

Bibliography

[1] C. N. Yang and R. L. Mills, Phys. Rev. **96** 191 (1954)

[2] R.K. Ellis, W.J. Sterling and B.R. Webber " QCD and Collider Physics" Cambridge Monographs on Particle Physics, Nuclear Physics and Cosmology, Cambridge Univ. Press, United Kingdom (1996). pp 8,9.

[3] R.K. Ellis, W.J. Sterling and B.R. Webber " QCD and Collider Physics" Cambridge Monographs on Particle Physics, Nuclear Physics and Cosmology, Cambridge Univ. Press, United Kingdom (1996). pp 260.

[4] R.K. Ellis, W.J. Sterling and B.R. Webber " QCD and Collider Physics" Cambridge Monographs on Particle Physics, Nuclear Physics and Cosmology, Cambridge Univ. Press, United Kingdom (1996). pp 17.

[5] R.K. Ellis, W.J. Sterling and B.R. Webber " QCD and Collider Physics" Cambridge Monographs on Particle Physics, Nuclear Physics and Cosmology, Cambridge Univ. Press, United Kingdom (1996). pp 27.

[6] R.K. Ellis, W.J. Sterling and B.R. Webber " QCD and Collider Physics" Cambridge Monographs on Particle Physics, Nuclear Physics and Cosmology, Cambridge Univ. Press, United Kingdom (1996). pp 18.

[7] R.K. Ellis, W.J. Sterling and B.R. Webber " QCD and Collider Physics" Cambridge Monographs on Particle Physics, Nuclear Physics and Cosmology, Cambridge Univ. Press, United Kingdom (1996). pp 248,249.

[8] R.K. Ellis, W.J. Stirling, B.R. Webber. http://www.hep.phy.cam.ac.uk/theory/webber/QC

[9] L.D. Faddeev and V.N. Popov, Phys. Lett. **B25**, 29 (1967).

[10] G. 't Hooft and M. Veltman, Nucl. Phys. **50**, 318 (1972).

[11] G. Leibbrandt, Rev. Mod. Phys. **59**, 1067 (1987).

[12] B.L. Combridge, J. Kripfganz and J. Ranft, Phys. Lett. **B70** (1977) 234.

[13] M.G. Albrow et al., Nucl, Phys. **B160** (1979) 1.

[14] A.L.S. Angelis et al., Phys. Scr. 19 (1979) 116.

[15] A.G.Clark et al., Nucl. Phys. 160 (1979) 397.

[16] D. Drijard et al., Nucl, Phys. **B166** (1980) 233.

[17] G. Sterman and S. Weinberg, Phys. Rev. Lett. **39**, 1436 (1977).

[18] Yu.L. Dokshitzer, D.I. Dyakanov and S.I. Troyan, Phys. Rep. **58C**, 269 (1980).

[19] P.Bagnaia et al, Measurement of Jet Production Properties at the CERN $p\bar{p}$ Collider, Phys. Lett. **144B** 283 (1984).

[20] M.Banner et al., (UA2 Collaboration), Phys. Lett. **118B**(1982) 203.

[21] G. Arnison et al., (UA1 Collaboration), Phys. Lett. **123B**(1983) 115.

[22] R.K. Ellis, W.J. Sterling and B.R. Webber " QCD and Collider Physics" Cambridge Monographs on Particle Physics, Nuclear Physics and Cosmology, Cambridge Univ. Press, United Kingdom (1996).

[23] S.Ellis, Z. Kunszt and D. Soper, Phys. Rev. Lett. **62** 2188 (1989); Phys. Rev. Lett. **64** 2121 (1990); Phys. Rev. D. **40** 2188 (1989)

[24] B.L. Combridge, J. Kripfganz and J. Rantf, Phys. Lett. **70B**(1977) 234.

[25] F. Aversa, P. Chiappetta, M. Greco, P. Guillet, Phys. Lett. **123B** 225 (1988);**211B**, 465 (1988); Nucl. Phys. **B327**, 107 (1995).

[26] W.K. Sakumoto and A. Hocker, *"Event $|Zvtx| < 60cm$ Cut Efficiency for Run II"*, CDF/ANAL/ELECTROWEAK/CDFR/6331.

[27] M.Banner et al., (UA2 Collaboration), Phys. Lett. **118B**(1982) 203.

[28] G.Marchesini et al., Comp.Phys. Commun. **67**, 465 (1992).

[29] S.Ellis, Z. Kunszt and D.Soper, Phys. Rev. Lett.**62** 2188 (1989).

[30] S.Ellis, Z. Kunszt and D.Soper, Phys. Rev. Lett.**64** 2121 (1990).

[31] S.Ellis, Z. Kunszt and D.Soper, Phys. Rev. D.**40** 2188 (1989).

[32] J.F. Arguin, B. Heinemann, A. Yagil. Z-vertex efficiency, CDF-Note 6238.

[33] Underlying Event Energy from Minimum bias Data. CDF/ANAL/JET/CDFR/5008 Anwar Ahmad Bhatti

[34] The CDF Collaboration, The CDF II Detector Technical Design Report. FERMILAB-Pub-96/390-E CDF

[35] *"Study of Jet Shapes in Inclusive Jet Production at CDF II"*, CDF/PHYS/JET/PUBLIC/6952 Mario Martinez.

[36] *"First Measurement of the Inclusive Jet Cross Section Using the Midpoint Algorithm"*, CDF/ANAL/JET/CDFR/7206 F. Chlebana, G. Flanagan, J.Huston, G. Latino